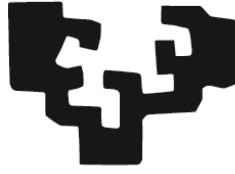


eman ta zabal zazu



Universidad
del País Vasco

Euskal Herriko
Unibertsitatea

Reliability Enhancement of Perovskite Solar Cells: Role of Low-Dimensional Materials for Interfacial Modifications

A thesis submitted in satisfaction of the requirements for the degree of Doctor of Philosophy

by

Naveen Harindu Hemasiri, Bastian Waduge

January 2023

Supervised by:

Prof. Dr. Shahzada Ahmad

Dr. Samrana Kazim

Tutor/Coordinator:

Prof. Luis Maria Lezama Diago

eman ta zabal zazu



Universidad
del País Vasco

Euskal Herriko
Unibertsitatea

Reliability Enhancement of Perovskite Solar Cells: Role of Low-Dimensional Materials for Interfacial Modifications

Naveen Harindu Hemasiri, Bastian Waduge

This research works for the degree of Doctor of Philosophy by the University of Basque Country [Universidad del País Vasco/Euskal Herriko Unibertsitatea (UPV/EHU)] has been carried out at the Basque Centre for Materials, Applications and Nanostructures (BCMaterials) and the Department of Organic and Inorganic Chemistry, the Faculty of Science and Technology of the UPV/EHU.



*This thesis is dedicated to the two who gave me life, for their
endless love, support and encouragement*

ACKNOWLEDGEMENT

The end of four years Ph.D. journey is approaching, and looking back, I see all the people who have helped me and accompanied me in each section. I owe a great deal of thanks to a number of people, without whom it would not have been possible to reach such a positive conclusion.


I will forever be thankful to my Ph.D. supervisor, Prof. Dr. Shahzada Ahmad for his constant support, guidance, and encouragement during my Ph.D. research program, and for his time to share his knowledge and effective discussions on the encountered problems in the experiments. Shahzada provided me the freedom I needed to become a self-standing researcher. I truly appreciated my Co-supervisor Dr. Samrana Kazim for being so generous with her time, knowledge, and ideas.

I am immensely grateful to my tutor and Ph.D. coordinator Prof. Luiz Lezama for being such a valuable mentor, collaborator, and after all a nice human. I also owe a great debt of gratitude to Dr. Rüdiger Berger for all the knowledge, incredible guidance, and support you provided during my research stay in your group at Max Planck Institute for Polymer Research (MPIP, Mainz). Rüdiger, your humility will never be forgotten. I would also appreciate Prof. Dr. Hans-Jürgen Butt, Prof. Dr. Stefan Weber, and Dr. Robert Graf for hosting and allowing me to access your laboratories and facilities during my time at MPIP. I also like to thank Kostas Bidinakis and Yenal Yalçinkaya for helping me out while my visit to the Department of Physics at Interfaces at MPIP. Needless to say, I owe a great debt of gratitude to Sunchon National University, South Korea and my Master's thesis supervisor Prof. Ji-Myon Lee for showing me how rewarding an academic career can be.

My heartfelt thanks to Dr. Rajasekhar Madugundo, Dr. Ana Maria Schönhöbel, and Dr. Alex Aubert for their great friendship and encouragement in the early time of my Ph.D. until you left BCMaterials. I am indebted to all the friends with whom I shared this period of my life, and who truly supported me at BCMaterials. I shall fondly remember the odd and fun things we did together in and out of the research. My gratitude also to Dr. Roberto Fernandez, Dr. Javier del Campo, Dr. Daniel Salazar, Dr. Javier Reguera, and Dr. Eduardo Fernandez for their assistance. I am also thankful to all the administrative staff, technical staff, and facility staff of BCMaterials for creating and maintaining a positive work environment. I must also be thankful to all the technical staff including Dr. Maria Belen, Dr. Alejandro Díez, Dr. Aitor Larrañaga, and Eng. Inaki Orue from SGIker at UPV/EHU. I would like to show my gratitude to the

European Union H2020 Programme under the ERC grant 726360 for the financial support of my research works. I also thank the ECOST STSM action CA16235 for providing financial assistance for my overseas visit and stay.

Finally, yet importantly, I am deeply grateful to my parents, my sisters, and Sanj, their support and encouragement allow me to tackle many challenges. I would not be where I am today without them.

A handwritten signature in black ink, appearing to read 'Naveen H. H. B. W.', with a long horizontal stroke extending to the right.

Naveen H. H. B. W.

Leioa

January 2023

ABSTRACT

The transition to low-carbon energy systems would be the main solution for global climate change, which deals with the long-term alteration of weather and temperature pattern. Sustainable energy, such as *solar power* set to play a larger role in the transition to renewable energy, accounting for a considerable amount of global energy production. *Photovoltaic* (PV) absorbs solar energy in the form of photons to knock electrons from semiconductor materials in a way that they can generate a flow of electricity. Conventional PV cells are dominated by silicon semiconductors, however, the absorption potential of crystalline silicon is limited to absorbing wavelengths higher than or equal to 1100nm due to its indirect bandgap. Among other PV technologies, *perovskite solar cells* (PSCs) have drawn a great deal of attention in the last decade, owing to several factors including their outstanding *power conversion efficiency* (PCE) within a short period of time, which has reached up to 25.7 % in single-junction devices as of today. Despite their rapid success, interfaces remain the weakest part of the complete device, holding their further improvement towards commercialization. This thesis focuses on a comprehensive understanding of the photo-induced charge transfer dynamics and the reliability enhancement of the PSCs based on interfacial modification through low-dimensional semiconductor materials.

In the first part of this thesis, the performance enhancement of PSCs is uncovered by the insertion of a 2D-MoS₂ interfacial layer. The phenomena of alkali metal intercalation of bulk MoS₂ is realized to achieve a predominantly existing 1T-phase in layered MoS₂, which escalates the device performance significantly when compared with 2H predominant MoS₂ synthesized via liquid phase exfoliation. It is found that the layered-MoS₂ interfacial layer reduces the energy required for detrapping the trapped charges, which results in prompt extraction of photo-induced charges at the interface of the perovskite/PTAA. Higher energy gap at the interface due to the shallow HOMO state of pristine PTAA w.r.t the valence band minimum of the perovskite was overcome by placing the 2D-MoS₂ interlayer, suppressing the charge recombination, resulting in boosted V_{oc} from 0.88 to 1.05 V, together with a higher FF of 79.9%. The fabricated-PSCs with 1T-rich TMD-based interface layer leads to superior PV performance, we further identified the saturation of photo-induced current density at a relatively low effective voltage in the devices upon the 1T-rich WS₂ layer. Low-temperature admittance spectroscopy is established to investigate the state-of-trap densities in the devices. The used protocol based on the 2D-WS₂ interlayer in a dopant-free PSC demonstrates a

stabilized PCE of over 19%. Third, we demonstrate the reduction of interface recombination and enhancement of charge transfer dynamics at the NiO_x nanocrystal/perovskite interface by application of an additional semiconductor layer, which can be either purely organic or inorganic in low-temperature inverted PSC. The molecularly engineered dithieno thiophene-based thin layer of organic semiconductor is deposited on NiO_x nanocrystal thin-film to reduce the surface defects and roughness, commonly associated with the layer of NiO_x, which indeed reduce interfacial recombination losses enabling enhancement in PV performances. The developed strategy is further extended with the implementation of an inorganic interface layer based on a 2D-C₃N₄ polymeric network. This interlayer enables greater V_{oc} and FF that deliver the PCE up to 19.3% with a minimal hysteresis by reducing non-radiative losses and faulty charge build-up at the NiO_x/perovskite interface. The MA⁺ cations in the perovskite have greater coordination via H-bonding with the unbound nitrogen electron pairs in the C₃N₄, which stabilizes the FA⁺ and MA⁺ cations at the interface as a passivation layer for the perovskite, overcoming the possible deprotonation of MA⁺ occurs with Ni^{>3+} in NiO_x. More significantly, the interlayer increases the device's stability.

A thorough grasp of the perovskite/electron transport layer interface is also essential to progress and increase the device's efficiency and stability. In this context, it is necessary to prevent any potential parasitic losses within the device. Due to the decreased non-radiative recombination at the perovskite/electron transport layer interface, we found that 2D-TiS₂ had a greater effect on PV performance when paired with PC₆₀BM under ideal addition, resulting in V_{oc} as high as 1.057 V and eventually the PCE up to 17.95%. When 2D-TiS₂ is added to PC₆₀BM, the current density reaches saturation at a relatively low V_{eff} , demonstrating that the device has a higher capacity to extract electrons while retaining a high fill factor of 78%. The results presented in this thesis offer unique insight into the interfacial modification using low-dimensional materials to achieve simultaneous high-efficiency and stability in PSCs.

LABURPENA

Karbono gutxiko energia-sistematarako trantsizioa izango litzateke klima-aldaketa globalaren irtenbide nagusia, eguraldiaren eta tenperaturaren epe luzeko aldaketaz arduratzen dena. Energia jasangarriak, hala nola eguzki-energiak, zeregin handiagoa izan zuen energia berriztagarriko trantsizioan, eta horrek mundu mailako energia-ekoizpen handia ekarri zuen. Fotovoltaikoak (PV) eguzki-energia xurgatzen du fotoi moduan material erdieroaleetako elektroiak kolpatzeko, elektrizitate fluxu bat sortzeko moduan. PV zelula konbentzionaletan siliziozko erdieroaleak dira nagusi; hala ere, silizio kristalinoaren xurgatze-potentziala 1100nm edo gehiagoko uhin-luzerak xurgatzera mugatzen da, zeharkako banda-arrakala dela eta. Euskal Autonomia Erkidegoko beste teknologia batzuen artean, eguzki-zelula perovskitoek (PSC) arreta handia piztu dute azken hamarkadan, hainbat faktoreren ondorioz, besteak beste, potentzia-bihurketaren eraginkortasuna (PCE) epe laburrean, gaur egun % 25,7ra iritsi baita gailu bakarretan. Arrakasta handia izan duten arren, interfazeak gailuaren zatirik ahulena dira oraindik ere, eta merkantilizazioari eusten diote. Tesi hau fotokondutoreak eragindako kargak transferitzeko dinamikaren eta PSCen fidagarritasunaren ulermenean oinarritzen da, dimentsio txikiko material erdieroaleen bidezko aurpegi-aldaketetan oinarrituta.

Tesi honen lehen zatian, PSCren errendimendua azaleratzen da aurpegi-arteko 2D-MoS₂ geruza bat txertatuz. MoS₂ solteko alkali metalen interkalizazioaren fenomenoak MoS₂ geruzan existitzen den 1T-fase bat lortzeko egiten dira, gailuaren errendimendua nabarmen handitzen duena 2H nagusi den MoS₂ rekin alderatuz fase likidoen esfoliazioaren bidez sintetizatua. Ikusten denez, MoS₂ aurpegi-arteko geruzak murriztu egiten du harrapatutako kargak askatzeko behar den energia, eta horrek azkar erauzten ditu fotoiak eragindako kargak perovskita/PTAA interfazean. Interfazean energia-arrakala handiagoa HOMO pristine PTAA w.r.t egoeraren ondorioz perovskitaren balentzia-bandaren minimoa gainditu zen 2D-MoS₂ intergeruza ezarriz, kargaren birkonbinazioa ezabatuz, V_{oc} 0,88 eta 1,05 V artean bultzatuz, eta FF % 79,9 altuago batekin batera. Tha fabrikatzaileak -PSCk 1T-rich TMDn oinarritutako interfaze geruzarekin PV errendimendu gorenera garamatza, gehiago identifikatu genuen fotoiak eragindako korrontearen dentsitatearen saturazioa 1T-rich WS₂ geruzaren gailuetan tentsio eraginkor baxu samar batean. Tenperatura baxuko espektroskopia ezartzen da gailuen azken tranpako dentsitateak ikertzeko. Dopinik gabeko PSC batean 2D-WS₂ intergeruzan oinarritutako protokoloak % 19tik gorako PCE egonkorra erakusten du. Hirugarrenik, NiO_x nanokristala/perovskita interfazean karga transferitzeko dinamikaren interfazearen

errekombinazioa eta hobekuntza erakusten dugu geruza erdieroale gehigarri bat aplikatuz, tenperatura baxuko PSC alderantzikatuan organikoa edo inorganikoa izan daitekeena. Ingeniari molekularra den dithieno thiofenoa erdieroale organikoko laer mehea NiO_x nanokristal mehearen gainean jartzen da azaleko akatsak eta zimurtasuna murrizteko, NiO_x en geruzarekin lotu ohi dena. Izan ere, PVren emanaldietan hobekuntza ahalbidetzen duten aurpegi-arteo birkonbinazio-galerak murrizten dituzte. 2D- C_3N_4 sare polimeriko batean oinarritutako interfaze ez-organiko baten inplementazioarekin garatutako estrategia are gehiago hedatzen da. Intergeruza honek V_{oc} eta FF handiagoak ahalbidetzen ditu, PCEa % 19,3ra arte ematen dutenak histeresi minimo batekin, galera ez erradiatiboak murriztuz eta karga akastunak metatuz NiO_x /perovskita interfazean. Perovskitazko MA^+ kateek koordinazio handiagoa dute C_3N_4 -ko lotu gabeko nitrogenu elektroiaren pareekin H bidez lotuz, eta horrek FA^+ eta MA^+ kateak egonkortzen ditu interfazean perovskitarentzako pasibatze geruza gisa, MA^+ en balizko deprotonazioa gaindituz Ni^{3+} rekin NiO_x en. Nabarmenago, intergeruzak gailuaren egonkortasuna areagotzen du.

Perovskita/elektroi-geruza garraiatzeko interfazea sakon hartzea ere funtsezkoa da aurrera egiteko eta gailuaren eraginkortasuna eta egonkortasuna handitzeko. Testuinguru honetan, gailuan gerta daitezkeen galera parasitoak saihestu behar dira. Perovskita/elektroi garraio geruzaren interfazean birkonbinazio ez-erradiatiboa gutxitu zenez, egiaztatu genuen 2D- TiS_2 eragin handiagoa izan zuela PVren errendimenduan PC_{60}BM gehigarri idealaren pean parekatzen zenean, V_{oc} 1.057 V-raino iritsiz eta, azkenik, PCEa % 17,95eraino. 2D- TiS_2 PC_{60}BM ari gehitzen zaionean, egungo dentsitatea aletasunera iristen da V_{eff} baxu samar batean, eta horrek erakusten du gailuak ahalmen handiagoa duela elektroiak ateratzeko, % 78ko betegarri handia mantentzen duen bitartean. Tesi honetan aurkeztutako emaitzek aurpegiaren arteko eraldaketa modu paregabearen ezagutzeko aukera ematen dute, material dimentsiogabeak erabiliz, aldi berean eraginkortasun eta egonkortasun handia lortzeko PSCn.

RESUMEN

La transición a sistemas energéticos sin o con bajas emisiones de carbono sería el principal remedio para el cambio climático global, que se refiere a la alteración a largo plazo del patrón de clima y temperatura. Los beneficios de los sistemas energéticos modernos y la tecnología deberían ser más fiables, más eficientes y asequibles para todas las partes. Como alternativa a la energía sostenible, la energía solar está llamada a desempeñar un papel más importante en la transición hacia las energías renovables, representando una cantidad considerable de la producción energética mundial. A nivel básico, las células fotovoltaicas (*photovoltaic*, *PV*) o solares funcionan permitiendo que la energía solar en forma de fotones libere los electrones de los átomos en el material semiconductor de manera que puedan generar un flujo de electricidad. En las células fotovoltaicas convencionales predominan los semiconductores de silicio, pero el potencial de absorción del silicio cristalino está limitado a la absorción de longitudes de onda superiores o iguales a 1100 nm debido a su banda prohibida indirecta. Entre otras tecnologías fotovoltaicas, las células solares híbridas orgánico-inorgánicas de perovskita han atraído una gran atención en la última década, debido a varios factores, entre ellos su extraordinaria eficiencia de conversión de energía (*power conversion efficiency*, *PCE*) en un corto período de tiempo, que en la actualidad, ha llegado a alcanzar hasta el 25,7% en dispositivos de unión simple.

La palabra "perovskita" se refiere a la forma mineral CaTiO_3 , que fue descubierta por el mineralogista alemán Gustav Rose en los Montes Urales y bautizada en honor del conde ruso Lev A. Perovski. En la actualidad, el término perovskita se refiere a una amplia gama de materiales con estructura cristalina ABX_3 como el CaTiO_3 y generalmente está compuesto por un catión monovalente orgánico o inorgánico (A) como el metil-amonio (MA^+ , CH_3NH_3^+), etilamonio (EA^+ , $\text{CH}_3\text{CH}_2\text{NH}_3^+$), formamidinio (FA^+ , $\text{CH}_3(\text{NH}_2)_2^+$), Cs^+ , y Rb^+ , un catión metálico divalente (B) como Pb^{2+} y Sn^{2+} . X, por su parte, representa un anión monovalente como Cl^- , Br^- , I^- , SCN^- , y PF_6^- . Se observa que, para la estructura cúbica de simetría ideal, los cationes del sitio A suelen ser más grandes que los cationes del sitio B, y el catión del sitio B centrado en el cuerpo está coordinado de forma octaédrica por el anión del sitio X centrado en la cara para formar una red tridimensional (3D) BX_6 que comparte las esquinas. Una nueva subclase de la familia de las perovskitas, a menudo denominada perovskitas híbridas orgánico-inorgánicas (HOIP), ha atraído una enorme atención en la última década debido a su enorme diversidad estructural y composicional, con una abundante variedad de componentes orgánicos

y sal metálica, más allá de sus sistemas puramente orgánicos o inorgánicos, ofreciendo potenciales aplicaciones tecnológicas.

Dependiendo de la incidencia de la luz, se pueden identificar dos tipos de configuración en las PSC de unión simple: la *n-i-p*, donde se puede separar aún más en heterounión planar o mesoporosa, y la *p-i-n* (invertidas). Aquí, *n* y *p* se refieren a los materiales transportadores de carga (CTM) de electrones y huecos, respectivamente, e *i* se refiere a la capa de absorción de perovskita intercalada entre la capa transportadora de electrones (*n*, ETL) y la capa transportadora de huecos (*p*, HTL). La definición anterior también se basa en el tipo de contactos de la capa de transporte de carga (CTL) con el sustrato conductor transparente. En las PSC *n-i-p* planas, la ETL se deposita sobre la capa de óxido conductor transparente (TCO) que funcionará como cátodo y será de óxido de estaño dopado con flúor (FTO) o de óxido de indio y estaño (ITO). Por otro lado, la configuración *p-i-n* tiene el HTL en el lado de entrada de la luz, depositado sobre el TCO, que se identifica como el ánodo. A diferencia de las PSCs *n-i-p* de estructura planar, las PSCs *n-i-p* mesoporosas comprenden un ETL compacto (c-ETL) formado sobre el sustrato TCO y luego se construye un ETL mesoporoso adicional (mp-ETL) sobre el c-ETL como ETL y andamio estructural. La fabricación del dispositivo se completa con la construcción de una capa metálica (oro, plata o aluminio) como electrodo superior.

A pesar de su gran éxito, las interfaces siguen siendo la parte más débil del dispositivo completo debido a las capas con cuatro interfaces diferentes, es decir, HTL/perovskita, ETL/perovskita, HTL/ánodo y ETL/cátodo, lo que frena su futura mejora hacia la comercialización. Esta tesis se centra en la comprensión exhaustiva de la dinámica de transferencia de carga fotoinducida y la mejora de la fiabilidad de las células solares de perovskita basada en la modificación interfacial mediante materiales de baja dimensión.

En la primera parte de la tesis, se desvela la mejora del rendimiento de las células solares de perovskita de triple catión (PSC) mediante la inserción de 2D-MoS₂ como capa interfacial. El 2D-MoS₂ es un dicalcogenuro de metales de transición (TMD) del grupo VI, cuya fórmula generalizada es MX₂, donde el átomo de metal de transición (M) está covalentemente intercalado por dos planos de átomos de calcogenuro (X). A diferencia de los TMDs a granel, los TMDs en capas pueden presentar una fase prismática trigonal (2H) o una fase octaédrica que se representa convencionalmente como 1T. En el caso del MX₂ monocapa, la fase prismática trigonal se indica como 1H. La 2H o 1H pertenece al grupo de puntos D_{3h} con simetría hexagonal que corresponde a la coordinación prismática trigonal de los átomos de

metales de transición, donde los átomos de calcogenuro están alineados verticalmente a lo largo del eje z con la secuencia de apilamiento $AbA BaB$ (b y a indican los átomos de metal mientras que A y B indican los átomos de calcogenuro). En cambio, la fase octaédrica 1T tiene una simetría tetragonal D_{3d} con coordinación octaédrica en los átomos del metal de transición. En este estudio, exfoliamos el MoS_2 a granel en capas 2D- MoS_2 utilizando intercalación de litio asistida por fase líquida, lo que dio lugar a una transformación de fase del MoS_2 desde la fase 2H, termodinámicamente estable, a la fase 1T, metaestable. La mencionada transición de fase estructural se atribuye a la transferencia efectiva de electrones desde el orbital de valencia s de los átomos del metal alcalino (Li) al orbital d del centro del metal de transición, lo que da lugar a un aumento del número de electrones en el orbital d del metal de transición con la densidad de estados en el nivel de Fermi. Encontramos que el 2D- MoS_2 preparado se encuentra predominantemente en la fase metálica 1T, alcanzando un 78,3%, lo que se investigó cuantitativamente a partir de la espectroscopia de fotoelectrones de rayos X. El 2D- MoS_2 rico en fase 1T exfoliado aumenta el rendimiento del dispositivo de forma significativa en comparación con el MoS_2 predominante en 2H sintetizado mediante exfoliación en fase líquida. Se ha comprobado que la capa interfacial de MoS_2 reduce la energía necesaria para eliminar las cargas atrapadas, lo que da lugar a una rápida extracción de las cargas fotoinducidas y a la mitigación de la posible recombinación interfacial. La implementación de una fina capa de 2D- MoS_2 reduce la brecha de nivel de energía entre la capa de perovskita y la capa de transporte de huecos (HTL), aumentando el voltaje de circuito abierto (V_{oc}) de 0,88 a 1,05 V, junto con un elevado factor de llenado (FF) del 79,9%.

Habiendo demostrado que el procesamiento de PSCs con una capa de interfaz basada en TMD rica en 1T conduce a un rendimiento fotovoltaico superior, identificamos además la saturación de la densidad de fotocorriente (J_{sat}) a un voltaje efectivo relativamente bajo (V_{eff}) en los dispositivos sobre la capa WS_2 rica en 1T en la interfaz entre la perovskita de triple catión $Cs_{0,1}(FA_{0,9}MA_{0,1})_{0,9}Pb(I_{0,9}Br_{0,1})_3$ y el pristine PTAA. El dispositivo de destino basado en la capa de interfaz presentaba una pronta recolección de carga foto-generada y disociación de excitaciones, dando lugar a una dinámica de foto-carga factible en el dispositivo. Se estableció una espectroscopia de admitancia a baja temperatura para investigar el estado de las densidades de trampa en los dispositivos, donde la reducción de la densidad de trampa en el dispositivo fue de aproximadamente un 25%. El protocolo presentado, basado en la introducción de 2D- WS_2 entre el PTAA no dopado y el absorbente de perovskita, permitió la demostración de PSCs

n-i-p con una eficiencia estabilizada de más del 19%, allanando el camino hacia la mejora de la fiabilidad en PSCs para su viabilidad comercial.

Las PSCs invertidas con una arquitectura positiva-intrínseca-negativa (a menudo denominada *p-i-n*) son atractivas para su futura comercialización, debido a varios factores, entre ellos, su fabricación de bajo coste, la diversificación de materiales, el funcionamiento fiable con histéresis insignificante y las menores pérdidas de absorción parasitaria respecto a la configuración normal *n-i-p*, lo que las hace compatibles con las células solares en tándem. Sin embargo, la eficiencia de conversión de potencia de la arquitectura *p-i-n* sigue estando por detrás de su homóloga estructural *n-i-p*, que contiene la misma capa activa. En el capítulo 3, demostramos la reducción de la recombinación de la interfaz y la mejora de la dinámica de transferencia de carga en la interfaz NiO_x nanocristal/perovskita mediante la aplicación de una capa orgánica semiconductor adicional en la PSC *p-i-n*. Se utilizó la capa fina de semiconductor orgánico a base de ditieno-tiofeno de ingeniería molecular como capa de interfaz depositada sobre NiO_x. La capa orgánica reduce eficazmente los defectos superficiales y la rugosidad comúnmente asociada a la capa de NiO_x, lo que efectivamente reduce las pérdidas por recombinación interfacial en el dispositivo. El efecto de transferencia de carga intermolecular de la capa semiconductor orgánica introducida mejora la movilidad de los huecos y la conductividad del NiO_x, su existencia reduce la brecha de energía entre las bandas de valencia de la perovskita y el NiO_x, potenciando una extracción de carga suave y rápida en la interfaz NiO_x/perovskita. Posteriormente, se observó una mejora en el Voc y en el FF, lo que permitió obtener el dispositivo objetivo con un PCE reforzado de más del 18%.

La estrategia desarrollada en la primera mitad del capítulo 3 se amplió aún más en el capítulo 4 con la implementación de una capa de interfaz inorgánica basada en semiconductores de nitruro de carbono 2D en PSC *p-i-n*. La acumulación de carga defectuosa y la recombinación de carga interfacial se minimizan, aumentando el V_{oc} y el FF hasta 1,06 V y 78%, respectivamente, lo que finalmente alcanzó un PCE del 19,33%. A pesar de la excelente estabilidad intrínseca observada en el NiO_x inorgánico, una posible reacción redox en el NiO_x/perovskita inicia y promueve la degradación de la capa activa y posteriormente la inestabilidad de los dispositivos. La naturaleza dual de aceptación de protones y electrones del Ni^{>3+} en el NiO_x podría ser la responsable de la oxidación del yoduro y la desprotonación de las aminas catiónicas (MA⁺) al entrar en contacto con la perovskita, dando lugar a la deformación de la red de la perovskita y produciendo barreras de extracción de huecos basadas en el PbI_{2-x}Br_x en la interfaz. Para averiguar la influencia de la capa de interfaz basada en

nitruro de carbono de baja dimensión para superar la posible degradación de la perovskita y las vías de defectos de NiO_x , se investigó la estabilidad operativa a largo plazo de las PSC sin encapsular con y sin la capa de interfaz mediante el seguimiento del punto de máxima potencia en condiciones de HR ambiental del 45-65%. El dispositivo de control perdió rápidamente el 20% de su PCE inicial tras 85h de funcionamiento continuo, mientras que el dispositivo objetivo mostró el 80% de su PCE inicial durante casi 300h de funcionamiento continuo.

Además, se evaluó el efecto de 2D-TiS₂, un material TMD de tipo *n*, sobre el rendimiento de las PSC. Entre las dos capas de transporte de carga (CTL), la capa de transporte de electrones (ETL) desempeña un papel crucial en la mejora del rendimiento fotovoltaico y la estabilidad ampliada en las PSCs *p-i-n*. Un derivado del fullereno, comúnmente conocido como PCBM, que es [6,6]-fenil-C61-isometil butirato, se considera la ETL más utilizada en la configuración *p-i-n* desde su primera aplicación en PSCs en 2013 por Chen y otros colaboradores. Sin embargo, la calidad de la película de PCBM depende en gran medida de la morfología de la superficie de la película de perovskita subyacente, en la que las películas de perovskita ásperas de la superficie pueden dar lugar a una capa de PCBM discontinua, lo que conduce a una corriente de fuga de recombinación no radiactiva interfacial. El 2D-TiS₂ se utilizó como capa de interfaz entre el PCBM y la perovskita o mezclado con el PCBM y aplicado como ETL en los dispositivos. Se comprobó que el efecto de la 2D-TiS₂ en el rendimiento fotovoltaico es mayor cuando se mezcla con PCBM en lugar de utilizarse como capa de interfaz. Tras la adición óptima de un 15 % en peso de 2D-TiS₂ en la ETL basada en PCBM, conseguimos preparar dispositivos con recombinación no radiactiva suprimida, lo que condujo a una V_{oc} tan alta como 1,057 V, un FF del 77,56 % y, finalmente, un PCE de hasta el 17,95 %. El dispositivo con PCBM + 15 wt% de 2D-TiS₂ muestra un J_{sat} a un V_{eff} relativamente bajo de 0,235 V comparado con el del dispositivo de control (0,398 V), lo que sugiere una mayor capacidad de extracción de carga tras la adición de 2D-TiS₂ en PCBM, proporcionando otra evidencia para la alta FF observada en el dispositivo basado en 2D-TiS₂ + PCBM. El dispositivo basado en PCBM de pristina muestra un tiempo de vida de los electrones de 13,91 mientras que el dispositivo con 2D-TiS₂ incorporado presenta un tiempo de vida de los electrones más largo de 37,27 μs , lo que indica una recombinación de carga mitigada en la interfaz perovskita/ETL tras la incorporación de 2D-TiS₂ en PCBM. Este trabajo pone en marcha un esquema facial y eficiente para ampliar los PCEs con una estabilidad operativa extendida.

Los resultados presentados en esta tesis ofrecen una visión única de la modificación interfacial utilizando materiales de baja dimensión para lograr simultáneamente alta eficiencia y

estabilidad a largo plazo en las PSC. Se utilizan diferentes técnicas optoelectrónicas fiables para entender la dinámica de la foto-carga en las interfaces.

CONTENTS

ACKNOWLEDGEMENT	iv
ABSTRACT.....	vi
LABURPENA.....	viii
RESUMEN	x
CONTENTS.....	xvi
ACRONYMS & ABBRIVATIONS	xxi
LIST OF SYMBOLS	xxiii
LIST OF FIGURES	xxv
LIST OF TABLES	xxxii
CHAPTER 1	2
INTRODUCTION	3
1.1 Overview.....	3
1.2 Photovoltaic Effect.....	4
1.3 Photovoltaic Fundamentals.....	6
1.3.1 Characteristics and Parameters of PV Cells.....	6
1.3.2 The External Quantum Efficiency	9
1.3.3 Energy Losses and Limitations of Energy Conversion.....	9
1.3.4 Shockley-Queisser Limit.....	10
1.4 Perovskite.....	11
1.5 Hybrid Organic-Inorganic Perovskites and Their Properties.....	12
1.6 Hybrid Organic-Inorganic Perovskite Solar cells	13
1.6.1 Device Architecture of PSCs	14
1.6.2 Deposition Techniques of HOIP Layer.....	15
1.6.3 Charge Transport Layers in PSCs.....	16
1.7 Charge Transfer Dynamics in PSCs.....	18
1.8 Carrier Recombination Mechanism in PSCs.	20
1.9 Causes of HOIP Solar Cell Degradation.....	22
1.9.1 Extrinsic Factors	22
1.9.2 Intrinsic Factors	23
1.10 Development Strategies of PSCs	24
1.10.1 Interface Engineering of PSCs.....	24
1.11 Low Dimensional Materials.....	26
1.11.1 Graphene and Reduced-Graphene Oxide.....	26

1.10.2 Two-Dimensional Transition-Metal Dichalcogenides (2D TMDs)	27
1.10.3 NiO _x Nano Crystals.....	31
Outline of the Thesis.....	32
BIBLIOGRAPHY	34
CHAPTER 2	44
METHODS	45
2.1 Low-Dimensional Materials Synthesis	45
2.1.1 Graphene Oxide (GO).....	45
2.1.2 Reduced Graphene Oxide (rGO).....	45
2.1.3 2D-Transition Metal Dichalcogenides (2D-TMDs).....	45
2.1.4 NiO _x Nanocrystals (NCs).....	46
2.2 Perovskite Precursor Synthesis	46
2.2.1 MAPbI ₃	47
2.2.2 (FAPbI ₃) _{0.85} (MAPbBr ₃) _{0.15}	47
2.2.3 Cs _{0.1} (FA _{0.9} MA _{0.1}) _{0.9} Pb(I _{0.9} Br _{0.1}) ₃	47
2.2.4 Rb _{0.05} [(FA _{0.83} MA _{0.17})] _{0.95} Pb(I _{0.83} Br _{0.17}) ₃	47
2.3 Device Fabrication.....	47
2.3.1 <i>n-i-p</i> planar PSCs	47
2.3.2 <i>n-i-p</i> mesoporous PSCs	48
2.3.3 <i>p-i-n</i> planar PSCs	49
2.4 Device Characterization.....	49
CHAPTER 3	52
MITIGATION OF TRAP DENSITY AND INTERFACIAL LOSSES BY INTRODUCING A TWO-DIMENSIONAL MOLYBDENUM DISULFIDE INTERFACE LAYER IN PEROVSKITE SOLAR CELLS	53
3.1 Abstract.....	54
3.2 Introduction.....	54
3.3 Results and Discussion	56
3.3.1 2D-MoS ₂ Characterization.....	56
3.3.2 SnO ₂ QDs ETL.....	58
3.3.3 Device and Photovoltaic Characterization.....	59
3.3.5 Admittance Spectroscopy and Mitigation of Trap Density.....	64
3.4 Conclusions.....	68
3.5 Experimental Section	68
3.5.1 Materials	68
3.5.2 Device fabrication.....	68

3.5.3 Materials characterization	69
3.6 Bibliography	69
CHAPTER 4	78
PHOTO-INDUCED CHARGE TRANSFER DYNAMICS IN DOPANT-FREE PEROVSKITE SOLAR CELLS UPON 1T-RICH WS ₂ INTERFACIAL LAYER	79
4.1 Abstract	80
4.2 Introduction	80
4.3 Results and Discussion	82
4.3.1 2D-WS ₂ Characterization	82
4.3.2 Thin-Film Characterization	84
4.3.4 Photo-Induced Charge Transfer Dynamics	88
4.3.5 Low-Temperature Admittance Spectroscopy	91
4.3.6 Long-Term Device Stability	94
4.4 Conclusions	95
4.5 Supporting Information	95
4.5.1 Materials	95
4.5.2 Device fabrication	95
4.5.3 Trap density measurements	95
4.5.4 Materials and thin-film characterization	96
4.6 Bibliography	97
CHAPTER 5	104
NiO _x NANOCRYSTAL ASSISTED INTERFACE MODULATION FOR THE PERFORMANCE BOOSTING OF INVERTED PEROVSKITE SOLAR CELLS	105
5.1 Abstract	106
5.2 Introduction	106
5.3 Results and Discussion	108
5.3.1 Materials and Thin-Film Characterization	108
5.3.3 Recombination and Charge-Transfer Kinetics	114
5.4. Conclusions	117
5.5 Supporting Information	118
5.5.1 Materials	118
5.5.2 NiO _x nanocrystals (NCs) synthesis	118
5.5.3 Device fabrication	118
5.5.4. Device and thin-film characterization	118
5.6 Bibliography	119
CHAPTER 6	125

INTERFACE TWEAKING OF PEROVSKITE SOLAR CELLS WITH CARBON NITRIDE-BASED 2D MATERIALS.....	126
6.1 Abstract.....	127
6.2 Introduction.....	127
6.3 Results and Discussion	128
6.3.1. g-C ₃ N ₄ and L-C ₃ N ₄ Characterization	128
6.3.2. Thin-Film Characterization.....	131
6.3.3 Interaction between C ₃ N ₄ and CsFAMA Perovskite.....	133
6.3.4 Device and Photovoltaic Characterization.....	136
6.3.5 Trap-Density Reduction & Charge Kinetics	139
6.3.6 Long-Term Device Stability	142
6.4 Conclusions.....	145
6.5 Supporting Information.....	145
6.5.1 Materials	145
6.5.2 Preparation of C ₃ N ₄ -based solutions	145
6.5.3 Device fabrication.....	146
6.5.4. Device characterization.....	146
6.5.5 Materials and thin film characterization	147
6.5.6 Sample preparation for solid-state NMR	147
6.6 Bibliography	148
CHAPTER 7	154
CURTAILEMENT OF INTERFACE RECOMBINATION FOR ENHANCED EFFICIENCY IN INVERTED PEROVSKITE SOLAR CELLS VIA 2D-TiS ₂ -PCBM ELECTRON TRANSPORT LAYER	155
CURTAILEMENT OF INTERFACE RECOMBINATION FOR ENHANCED EFFICIENCY IN INVERTED PEROVSKITE SOLAR CELLS VIA 2D-TiS ₂ -PCBM ELECTRON TRANSPORT LAYER	155
7.1 Abstract.....	156
7.2 Introduction.....	156
7.3 Results and Discussion	158
7.3.1 Exfoliated 2D-TiS ₂ Characterization.....	158
7.3.2 Thin-Film Characterization.....	159
7.3.3 Device and Photovoltaic Characterization.....	162
7.3.4 Exciton Generation and Photocharge Transfer Kinetics	166
7.3.5 Long-Term Device Stability	169
7.4 Conclusions.....	170
7.5 Experimental Section	170

7.5.1 Materials	170
7.5.2 Thin-film characterization.....	171
7.5.3 Device fabrication.....	171
7.5.4 Device characterization.....	172
7.6 Bibliography	172
CHAPTER 8	179
PERORATION & UPCOMINGS.....	180
PERORATION & UPCOMINGS.....	180
APPENDICES	187
APPENDIX A.....	188
APPENDIX B	192
APPENDIX C	194
APPENDIX D.....	196
Vita.....	201

ACRONYMS & ABBRIVATIONS

2D	Two-Dimensional
AFM	Atomic Force Microscopy
AM 1.5G	Air Mass 1.5 Global
BCP	Bathocuproine
BuLi	Butyl lithium/Hexane
CB	Conduction Band
CBZ	Chlorobenzene
CTL	Charge Transport Layer
DMF	<i>N, N</i> -dimethylformamide
DMSO	Dimethyl sulfoxide
EIS	Electrochemical Impedance Spectroscopy
EQE	External Quantum Efficiency
ETL	Electron Transport Layer
FF	Fill Factor
FTO	Fluorine-doped Tin Oxide
GO	Graphene Oxide
HI	Hysteresis Index
HF	High Frequency
HOIP	Hybrid organic-inorganic perovskite
HOMO	Highest Occupied Molecular Orbital
HTL	Hole Transport Layer
IF	Intermediate Frequency
IPA	Isopropanol
ITO	Indium Tin Oxide
Li-TFSI	Bis (trifluoromethane) sulfonimide lithium salt
LF	Low Frequency
LUMO	Lowest Unoccupied Molecular Orbital
MoS ₂	Molybdenum Disulfide
MPP	Maximum Power Point
NC	Nano Crystal
NiO _x	Nickel Oxide
NMP	N-Methyl-2-pyrrolidone

P3HT	Poly(3-hexylthiophene-2,5-diyl)
PC ₆₀ BM	[6,6]-phenyl-C ₆₁ -isomethyl butyrate
PCE	Power Conversion Efficiency
PEDOT:PSS	Poly (3,4-ethylenedioxythiophene): polystyrene sulfonate
PL	Photoluminescence
PSC	Perovskite Solar Cell
PV	Photovoltaics
PTAA	Poly(triaryl amine)
QD	Quantum Dot
rGO	Reduced Graphene Oxide
SEM	Scanning Electron Microscopy
SnO ₂	Tin Oxide
Spiro-OMeTAD	2,2',7,7'-tetrakis(N,N-di-p-methoxyphenylamine)-9,9'-spirobifluorene
<i>t</i> BP	4-tert-butylpyridine
TCO	Transparent Conducting Oxide
TEM	Transmission Electron Microscopy
TiO ₂	Titanium Oxide
TiS ₂	Titanium Disulfide
TMD	Transition Metal Dichalcogenides
UV	Ultraviolet
UV-Vis	Ultraviolet-Visible
VB	Valence Band
WS ₂	Tungsten Disulfide
XPS	X-ray Photoelectron Spectroscopy
XRD	X-ray Diffraction

LIST OF SYMBOLS

A	Device active area
J - V	Current density-Voltage
V_{oc}	Open-circuit voltage
I_{sc}	Short-circuit current
J_{sc}	Short-circuit current density
e_x	Electron affinity
E_C	Conduction band
E_F	Fermi level
E_V	Valence band
E_{vac}	Vacuum level
Φ_F	Work function
J_{int}	Integrated current density
R_{sh}	Shunt resistance
R_s	Series resistance
R_{rec}	Charge recombination resistance
R_{ctr}	Charge transport resistance
n_{id}	Ideality factor
e_n	Emission rate of electrons from a trap state
ν_0	Attempt-to-escape frequency
h	Planck constant
E_a	Activation energy
K_B	Boltzmann constant
T	Temperature
F	Frequency
f_{peak}	Peak frequency
C	Capacitance
v_{bi}	Built-in potential
W	Depletion layer thickness
q	Electron charge
ϵ	Dielectric constant
ϵ_0	Vacuum permittivity

N_T	Trap density
t_{DOS}	Trap density of state
N_{Defects}	Defect density
J_D	Dar current density
J_{ph}	Photocurrent density
J_{sat}	Saturation current density
V_{eff}	Effective voltage
V_{app}	Applied-bias voltage
τ	Charge lifetime
G_{max}	Maximum exciton generation rate

LIST OF FIGURES

Figure 1. 1 (a) Schematic illustration of the creation of neutral region/depletion of mobile ions region at a p-n junction by majority carrier diffusion from p-type to n-type and n-type to p-type. The energy level of a p-n junction under (b) thermodynamic equilibrium [q-electron charge, <i>v_{bi}</i> -built-in potential], (c) illumination/open circuit, and (d) illumination/short circuit conditions.....	5
Figure 1. 2 The equivalent circuit of (a) an ideal and (b) a real PV cell (redrawn ¹¹).	6
Figure 1. 3 (a) Characteristic <i>I-V</i> curve of a solar cell extracted from a typical perovskite solar cell (discuss later in this chapter). (b) AM 0 and AM 1.5 spectral distribution of solar radiation power (redrawn ¹¹).....	8
Figure 1. 4 (a) Intrinsic energy losses as a function of E_g under one sun illumination. (b) Fraction of incident power into intrinsic energy losses (redrawn ¹⁵).....	9
Figure 1. 5 The lattice representation of perovskite crystal structure ABX_3 , showing corner sharing network of BX_6 octahedral and larger A cation occupied in cubo-octahedral site, where A, B, and X represent monovalent cation, divalent cation, and monovalent anion, respectively.	11
Figure 1. 6 The schematic diagram of the different architectures of perovskite solar cells; (a) n-i-p mesoporous, (b) n-i-p planar, and (c) p-i-n planar (inverted) configuration.....	14
Figure 1. 7 Schematic illustrations of solution-based perovskite thin film deposition techniques. (a) Solvent engineering free one-step method, (b) solvent engineering-assisted one-step method, and (c) two-step methods.....	15
Figure 1. 8 Charge transfer process in (a) <i>n-i-p</i> and (b) <i>p-i-n</i> , PSCs. (c) The desirable and undesirable charge transfer kinetics in a typical PSC. TCO: transparent conductive oxide, ETL: electron transport layer, HTL: hole transport layer, CB: conduction band, VB: Valance band. HOMO: highest occupied molecular orbital; LUMO: lowest unoccupied molecular orbital (redrawn ⁵¹).....	19
Figure 1. 9 The photo-induced charge-carrier recombination dynamics: (a) radiative recombination, (b) defect-assisted or Shockley-Red-Hall (SRH) recombination, (c) Auger-direct recombination (<i>e-e-h</i>), (d) Auger-direct (<i>h-h-e</i>) recombination, and (e) Auger-indirect recombination. The origins of interface- induced recombination losses at perovskite/HTM interface (similar recombination processes could be possible at perovskite/ETM interface): (f) deep level defects-assisted, (g) incompatible energy level alignment at the interface together with defects in the perovskite, (h) back transfer-induced, and (i) defect-assisted in the HTL (redrawn ⁷⁰).....	21
Figure 1. 10 Structure of graphene: (a) honeycomb lattice structure of carbon atoms, (b) the unit, where A and B represent carbon atoms from different sub-lattices, a_1 and a_2 are unit cell	

vectors, (c) sp^2 hybridization with σ and π bonding, and (d) electronic band structure with Dirac cone (redrawn⁸⁹).26

Figure 1. 11 (a) Structure of graphene oxide (GO), (b) Scanning electron microscopy image (SEM), and (b) transition electron microscopy image of reduced graphene oxide (rGO) flakes.27

Figure 1. 12 The transition metals and three chalcogen elements that form TMDs. Those predominantly forming in layered structures are highlighted in transition metal groups.28

Figure 1. 13 (a) 1T (octahedral), 2H (trigonal prismatic), and 3R (trigonal prismatic) unit cell structures of MoS₂. (b) Band alignment of the monolayer TMDs (redrawn⁹⁹).29

Figure 1. 14 Atomic model structures of 2D-TMDs, (a) 2H-trigonal prismatic phase, and (b) 1T-octahedral phase.30

Figure 3. 1 (a) UV–Vis absorbance and photoluminescence spectra of spin coated 2D-MoS₂ on quartz substrate. (b) AFM topography of drop casted MoS₂ thin film on Si substrate, inset shows the thickness profile. XPS narrow spectrum of (c) Mo3d and (d) S2p of spin coated MoS₂ thin film.57

Figure 3. 2 SEM images of (a) FTO substrate, (b) SnO₂-QD layer on c-TiO₂/FTO and (c) the triple cation perovskite grown on SnO₂-QD/c-TiO₂/FTO.58

Figure 3. 3 (a) Architecture used for the device fabrication [FTO/c-TiO₂/SnO₂ QD/Cs_{0.1}(FA_{0.9}MA_{0.1})_{0.9}Pb(I_{0.9}Br_{0.1})₃/ MoS₂/PTAA/Au], (b) cross-sectional SEM image of the device with 2D-MoS₂ as interfacial layer and (c) energy level diagram of the fabricated PSCs.59

Figure 3. 4 (a) *J-V* curves of the CsFAMA devices (control and modified with 1T-predominant 2D-MoS₂) under simulated AM 1.5G illumination, (b) corresponding IPCE and integrated current density of devices. *J-V* hysteresis curve of forward and reverse scans of (c) control and (f) of modified device with 1T-predominant 2D-MoS₂ interfacial layer.60

Figure 3. 5 (a) *J-V* hysteresis curve and (b) corresponding IPCE and integrated current for the device with 2H-predominant 2D-MoS₂ as an interfacial layer.62

Figure 3. 6 (a) Continuous MPP tracking of the control and modified devices under constant 1 sun illumination at ambient atmosphere, (b) the stabilized power output of the devices under constant 1 sun illumination at ambient atmosphere, (c) normalized PCE with the storage time of control and modified devices.63

Figure 3. 7 Capacitance-frequency-temperature spectra obtained from (a) control device and (b) with 2D-MoS₂ interface layer. (c) Temperature-dependence low-frequency capacitance of

control and modified devices and (d) Arrhenius plot of $\ln(f_{\text{peak}}/T^2)$ versus $1/T$ for control and modified devices, extracted from $-fdC/df$ versus f spectra.65

Figure 3. 8 (a) Mott-Schottky analysis at 10 kHz and (b) trap density (N_T) of control and modified devices measured at 300 K.66

Figure 4. 1 Characterization of the synthesized 2D-WS₂. (a) TEM image of WS₂ flakes, (b) AFM image of selected WS₂ flakes. Inset represents the thickness profile of the selected flakes, (c) Statistical distribution of WS₂ flake thickness.82

Figure 4. 2 (a) XRD patterns of bulk and 2D-WS₂. (b) Optical absorption spectrum; inset shows the calculated optical band gap of WS₂ flakes from the Tauc plot. High-resolution XPS spectra of W4f (c) (and S2p (d)).83

Figure 4. 3 AFM topography images of (a) CsFAMA film and (b) 2D-WS₂/CsFAMA film. (c) XRD patterns of CsFAMA and 2D-WS₂/CsFAMA films. (d) UV-Vis absorption spectrum of perovskite and 2D-WS₂/perovskite.84

Figure 4. 4 High-resolution XPS spectra of (e) Pb4f and (f) I3d for perovskite and perovskite/2D-WS₂ layers.85

Figure 4. 5 (a) Device structure of planar perovskite solar cells incorporating the 2D-WS₂ interface layer, (b) cross-sectional SEM image of the PSC with 2D-WS₂ interface layer, and (c) energy band alignment of the corresponding layers.86

Figure 4. 6 (a) J - V curves of the champion PSCs with and without the interface layer, and (b) the corresponding EQE and integrated current. (c) J - V hysteresis curve of forward and reverse scans of the champion PSCs.87

Figure 4. 7 (a) Electrochemical impedance spectra of PSCs recorded with an applied voltage of 0.95 V and under dark conditions. (b) The equivalent circuit used for the fitting of the impedance spectra. The potential bias-dependent (b) charge transport resistance and (c) interfacial charge recombination resistance.88

Figure 4. 8 (a) The dark J - V curve of the PSCs and (b) photo-generated current density, J_{ph} vs. effective voltage (V_{eff}).89

Figure 4. 9 Temperature-dependent capacitance–frequency (c - f) measurements of the PSCs without (a) and with (b) the 2D-WS₂ interfacial layer. (c) Temperature-dependent low-frequency capacitance variation of the devices with and without 2D-WS₂.91

Figure 4. 10 $-fdC/df$ vs. frequency variation at low temperature for the devices without (a) and with (b) 2D-WS₂ interface layer. Arrhenius plot of the PSCs without (c) and with (d) the 2D-WS₂ interfacial layer. 92

Figure 4. 11 (a) Mott–Schottky analysis at 10 kHz and (b) trap density of states deduced from temperature-dependent $C-f$ spectroscopy for the PSCs without and with 2D-WS₂. 93

Figure 4. 12 (a) Normalized J_{sc} for 100 h of continuous MPP tracking for un-encapsulated PSCs under an ambient atmosphere. Initial 1000 s MPP tracking of (b) J and (c) PCE. 94

Figure 5. 1 (a) UV–vis absorption spectra, (b) Transition electron microscopy (TEM) of drop-casted NiO_x NC aqueous solution, and (c) X-ray diffraction (XRD) pattern of the NiO_x film. 108

Figure 5. 2 Surface SEM images of (a) NiO_x NC film, (b) DTT-EHDI₂ deposited on NiO_x NC film. Contact angle of perovskite on (a) NiO_x, and (b) DTT-EHDI₂/NiO_x NC films. Surface SEM images of CsFAMA grown on (e) NiO_x film and (f) DTT-EHDI₂/NiO_x NC film. To note here, images (a) and (b) are in 90 K magnification, while (e) and (f) are in 60 K magnification. 109

Figure 5. 3 Topography, 3D height, and phase images of the perovskite deposited on NiO_x (a, b, and c) and on DTT-EHDI₂/NiO_x (d, e, and f), respectively. 110

Figure 5. 4 XRD patterns of CsFAMA perovskite deposited on NiO_x film and DTT-EHDI₂/NiO_x film. (d) UV-Vis spectra of NiO_x/CsFAMA with and without DTT-EHDI₂ interface layer (c) $I-V$ curves for conductivity measurements in the configuration of FTO/NiO_x/Au and FTO/NiO_x/DTT-EHDI₂ in the dark. (d) $J-V$ curves for hole-mobility measurements with the hole-only device with the configurations of FTO/PTAA/NiO_x/Au and FTO/PTAA/NiO_x/DTT-EHDI₂/Au in the dark. 111

Figure 5. 5 (a) Chemical structure of DTT-EHDI₂ (2,6-bis(5,10,15-tris(2-ethylhexyl)-10,15-dihydro-5H-diindolo[3,2-a:3',2'-c]carbazol-3-yl)dithieno[3,2-b:2',3'-d]thiophene). (b) Energy band alignment at the NiO_x/CsFAMA interface. (c) p-i-n device structure and (d) cross-sectional SEM image of the fabricated PSC. 112

Figure 5. 6 (a) $J-V$ curve of the champion device without and with DTT-EHDI₂ interface layer in reverse scan under simulated AM 1.5G illumination. (b) The corresponding IPCE and integrated current density. (c) $J-V$ hysteresis curve of forward and reverse scans of the champion PSCs. (d) Stabilized initial 400 s MPP tracking of J_{sc} under ambient conditions. 113

Figure 5. 7 (a) Electrochemical impedance spectra of PSCs measured at an applied voltage of 950 mV in the dark (raw and fitted data). The potential bias-dependent (b) charge transport

resistance, (c) interfacial charge recombination resistance extracted from Nyquist plots in the dark. 115

Figure 5. 8 (a) Bode spectra of PSCs measured at an applied voltage of 950 mV in the dark, (b)) applied bias-dependent charge lifetime in the dark, and (c) dark J - V curves for the PSCs with and without the interfacial layer. (d) Photogenerated current density (J_{ph}) versus effective voltage (V_{eff})..... 116

Figure 6. 1 (a) Chemical structure of tri-s-triazine-based graphitic- C_3N_4 . XRD pattern (b), FTIR spectra (c), and Raman spectra (d) for g- C_3N_4 and L- C_3N_4 129

Figure 6. 2 DR-UV-Vis spectra (a) Inset: obtained powders of CN materials, and $[F(R)h\nu]^2$ vs. $h\nu$ plot (b) for g- C_3N_4 and L- C_3N_4 . High-resolution X-ray photoelectron spectroscopy (XPS) of C1s of (c) g- C_3N_4 and (d) L- C_3N_4 , N1s of (e) g- C_3N_4 and (f) L- C_3N_4 130

Figure 6. 3 SEM image of (a) FTO, (b) NiO_x /FTO, (c) g- C_3N_4 / NiO_x /FTO, and (d) L- C_3N_4 / NiO_x /FTO films. SEM image and the corresponding histogram of grain size (length) distribution of CsFAMA perovskite deposited on (e and e') NiO_x /FTO, (f and f') g- C_3N_4 / NiO_x /FTO, and (g and g') L- C_3N_4 / NiO_x /FTO, respectively. 132

Figure 6. 4 (a) XRD patterns of CsFAMA deposited on NiO_x , g- C_3N_4 / NiO_x , and L- C_3N_4 / NiO_x . (b) UV-Vis spectra of CsFAMA perovskite deposited on different bottom layers. 132

Figure 6. 5 High-resolution XPS of (a) Pb4f and (b) I3d, and (c) Cs3d detected from CsFAMA, CsFAMA/g- C_3N_4 , and CsFAMA/L- C_3N_4 . . High-resolution XPS of C1s (d, e, and f) and N1s (g, h, and i) found from CsFAMA, CsFAMA/g- C_3N_4 , and CsFAMA/L- C_3N_4 , respectively [here CsFAMA denotes $Cs_{0.1}(FA_{0.9}MA_{0.1})_{0.9}Pb(I_{0.9}Br_{0.1})_3$]. 133

Figure 6. 6 FTIR spectrum of CsFAMA, CsFAMA/g- C_3N_4 , and CsFAMA/L- C_3N_4 134

Figure 6. 7 Solid-state NMR results of CsFAMA perovskite samples with and without C_3N_4 addition: (a,b) 1H MAS and (d,e) ^{13}C CP-MAS NMR spectrum of CsFAMA perovskite, pure and blended with C_3N_4 material, respectively, and the resulting 1H (c) and ^{13}C (f) difference spectra. (g) 1H - ^{13}C CP-MAS correlation spectrum of the perovskite + C_3N_4 material acquired with 5ms CP-contact and (h) the 1H DQ correlation spectrum of the same material with 1 rotor period BABA-xy16 DQ excitation at 25 kHz MAS. 135

Figure 6. 8 (a) Device configuration and (b) corresponding cross-section SEM image of the PSC incorporating L- C_3N_4 interface layer. (c) J - V curve of the champion devices without and with g- C_3N_4 or L- C_3N_4 interface layer measured in reverse scan under simulated AM 1.5G illumination, (d) IPCE and integrated current density of the corresponding devices, (e) steady-state power output of PSCs. 137

Figure 6. 9 Statistical distribution of PV parameters extracted from *J-V* curves of the PSCs from different batches. 139

Figure 6. 10 (a) Dark *J-V* curves and (b) photo-generated current density vs. effective voltage of PSCs. (c) Electrochemical impedance spectra of PSCs measured at an applied voltage of 900 mV under dark conditions (raw and fitted data). Inset: the equivalent circuit diagram used for EIS data fitting. (d) Bode spectra of PSCs measured at an applied voltage of 900 mV under dark conditions. 140

Figure 6. 11 Space-charge-limited current (SCLC) vs voltage of hole only devices with the structure of (a) FTO/NiO_x/perovskite/PTAA/Au, (b) FTO/NiO_x/g-C₃N₄/perovskite/PTAA/Au, and (c) FTO/NiO_x/L-C₃N₄/perovskite/PTAA/Au. 142

Figure 6. 12 (a) The normalized current density of continuous MPP tracking for un-encapsulated PSCs under atmospheric conditions (RH 45-65 %, 300 K). (b) XRD of fresh perovskite on NiO_x and thermal/light stressed perovskite films deposited on NiO_x, g-C₃N₄/NiO_x, and L-C₃N₄/NiO_x. (c) Zoom in view of XRD patterns of around 2θ=10.5°-15° and (d) Zoom in view of XRD patterns of (202) peak around 2θ=28.5°. # and * represent the δ-phase of FAPbI₃ and the cubic PbI₂, respectively. 143

Figure 6. 13 UV-Vis spectra of fresh perovskite on NiO_x (A) and thermal/light stressed perovskite films deposited on NiO_x (B), g-C₃N₄/NiO_x (C), and L-C₃N₄/NiO_x (D). Images of each perovskite film are shown on the right side. 144

Figure 7. 1 (a) UV-Vis absorption spectrum of exfoliated 2D-TiS₂ in isopropanol, insert shows the suspension of 2D-TiS₂ in isopropanol. (b) XRD patterns of bulk and exfoliated TiS₂. TEM (c) and AFM (d) images of exfoliated 2D-TiS₂, insert of (d) shows the thickness profile along the line. 158

Figure 7. 2 XPS narrow spectrum of Ti 2p (a) and S 2p (b). 159

Figure 7. 3 SEM images of (a) CsFAMA perovskite, (b) PCBM on CsFAMA perovskite, and (c) PCBM + 15 wt% 2D-TiS₂ on CsFAMA perovskite. AFM topography and 3D height images of CsFAMA perovskite (d and e), PC_BM on CsFAMA perovskite (f and g), and PCBM + 15 wt% 2D-TiS₂ on CsFAMA perovskite (h and i), respectively. 160

Figure 7. 4 (a) Device configuration for the conductivity: FTO/PCBM(with or without 15 wt% 2D-TiS₂)/Ag. (b) Device configuration for the mobility and space-charge-limited current (SCLC): FTO/SnO₂/PCBM(with or without 15 wt% 2D-TiS₂)/Ag. (c) *I-V* curves for conductivity measurements in the dark. (d) *J-V* curves for electron-mobility measurements with the electron-only device in the dark. (e) SCLC for devices with electron-only device in the dark. 161

Figure 7. 5 Schematic of the proposed device architecture. FTO: fluorine-doped tin oxide/PTAA: poly(triaryl amine)/CsFAMA: $\text{Cs}_{0.1}(\text{FA}_{0.9}\text{MA}_{0.1})_{0.9}\text{Pb}(\text{I}_{0.9}\text{Br}_{0.1})_3$ /PCBM: [6,6]-phenyl-C61-isomethyl butyrate + 2D-TiS₂/BCP: bathocuproine/Ag. 162

Figure 7. 6 *J-V* curves of the champion devices under simulated AM1.5G light at reverse scan with 100 mV/s scan rate (a) and the corresponding EQE and integrated current (b). (c) Reverse and forward *J-V* curves of the champion devices. (d) Stabilized initial 600 s MPP tracking of J_{sc} under ambient conditions. 163

Figure 7. 7 Reverse and forward *J-V* curves of the device with the 2D-TiS₂ as an interface layer in the device structure of FTO/PTAA/CsFAMA/2D-TiS₂/PCBM/BCP/Ag (a) and the corresponding EQE and integrated current density (b). 165

Figure 7. 8 Reverse and forward *J-V* curves of (a) 5 wt% addition of 2D-TiS₂ into PCBM, (b) 20 wt% addition of 2D-TiS₂ into PPCBM. 165

Figure 7. 9 (a) The dark *J-V* curve of the PSCs with and without 15 wt% 2D-TiS₂ addition. (b) photo-generated current density, J_{ph} vs. effective voltage (V_{eff}) curve. 166

Figure 7. 10 (a) Electrochemical impedance spectra of PSCs recorded with an applied bias voltage of 0.95 V under dark conditions in the frequency range of 1 Hz - 2 MHz with 20 mV perturbation ac signal, and the raw data were fitted with the equivalent circuit inserted in the figure. (b) The potential bias-dependent interfacial charge recombination resistance. The Bode plot of the impedance spectrum of (c) pristine PCBM and (d) PCBM + 15 wt% 2D-TiS₂-based devices. 168

Figure 7. 11 Frequency-dependent series capacitance extracted from the EIS at 0.95 V under dark conditions. 169

Figure 7. 12 The normalized current density of continuous MPP tracking for un-encapsulated PSCs under atmospheric conditions (RH 45-65 %, 300 K). 169

LIST OF TABLES

Table 3. 1 PV parameters of the fabricated PSCs with and without 1T-predominant 2D-MoS ₂ interfacial layer.	61
Table 4. 1 PV parameters of the champion devices with or without the 2D-WS ₂ interfacial layer.....	87
Table 4. 2 Data extracted from the electrochemical impedance spectroscopy at an applied voltage of 0.95 V in dark conditions.....	90
Table 4. 3 Photoelectrical parameters of the devices.....	90
Table 5. 1 PV parameters of the champion devices with and without the organic interfacial layer.....	114
Table 5. 2 Extracted electrochemical parameters of the PSCs with and without the interface layer at 950 mV bias voltage under dark conditions.....	116
Table 6. 1 Summary of the PSC performances using with and without different C ₃ N ₄ interlayers.....	138
Table 7. 1 Electrical parameters of the electron only devices.....	162
Table 7. 2 PV parameters of the champion devices with and without 15 wt% 2D-TiS ₂ addition.	164
Table 7. 3 Photo-charge kinetic parameters extracted from dark current and J_{ph} - V_{eff} curves.	167
Table 7. 4 Electrochemical parameters of the PSCs with and without 2D-TiS ₂ at 950 mV applied bias in the dark.	169

CHAPTER 1

INTRODUCTION

In this chapter, the fundamentals of photovoltaic (PV), perovskite solar cells, and low-dimensional materials for interface engineering are discussed. Starting from the comprehensive and characteristic features of PV cells, the thermodynamic limitation and losses in solar cells are introduced. Next, perovskites, the evolution of hybrid organic-inorganic perovskite (HOIP) as an absorber in solar cells, basic considerations of photo-induced charge transfer dynamics, and recombination mechanisms are debated. Finally, the development strategies of PSC in particular interface engineering are briefly explored before introducing the low-dimensional materials with which the results in the following chapters are obtained.

1.1 Overview

The global energy demand continues to evolve owing to the rapid growth and modernization of the world economy and technology. Unprecedented consumption sets the non-renewable fossil energy, such as oil, gas, and coal diminish from the Earth within the next few decades. Coal was regarded as a dominant energy source in the energy system until the first half of the 20th century and then oil became from the 1970s.¹ Aside from the scarcity, the major problem with fossil fuel is atmospheric heat-trapping carbon dioxide emission, which has a direct impact on the earth's environment, causing global warming, ozonosphere destruction, acid rain, and pollution of water resources.² In an era of accelerating change in sociological, political, and technological, the imperative to achieve sustainable growth with minimal effect on climate is strengthening the momentum of the global energy transformation from traditional non-renewable to renewable green energy sources.³ The growing importance of sustainable development, rapid decline in renewable energy costs, and improving energy efficiency together with well-organized strategies, guiding energy transformation, moving towards a clean energy future.^{1,3,4}

As a renewable energy source, in a single hour, the sun provides a total of around 173,000 TW power, which is more than the world's energy needs for an entire year.⁵ Today, solar energy is increasingly becoming an economical, green, and sustainable energy choice as prices continue to fall. In practice, solar energy conversion has three categories; photo-thermal, photocatalytic, and photovoltaic. Photo-thermal devices convert solar energy into heat, which is then used as an energy source or further transformed into electricity. Photocatalytic cells work based on artificial photosynthesis where solar energy is used to catalyze chemical reactions and produce

Chapter 1

fuels. Photovoltaic (PV) technology directly produces electrical power through the photovoltaic effect. Since the first invention of the crystalline silicon solar cell at Bell Labs by Calvin Fuller and Daryl Chapin together with Gerald Pearson in 1954, PV cells have become a hotspot for the large-scale production of solar electricity. In 2019, solar PV accounted for 3.1% of global electricity production (IEA analysis, 2022), which is projected to lead the power generation, reaching 10% by 2050.⁶ The only limitation of solar power is our ability to transfer it into electricity efficiently and sustainably, consequently, there is an urgent demand for PV technologies.

1.2 Photovoltaic Effect

The PV effect is the principle of producing electricity from solar radiation, which was first reported by French scientist Alexandre Edmund Becquerel as early as 1839 from a silver-coated platinum electrode immersed in the electrolyte.⁷ Later in 1873, the PV effect was observed in solid selenium bars followed by William G. Adams and Richard E. Day in 1876, the system was further developed, demonstrating the first PV effect in a solid-state system.^{8,9} Since then, many studies have attempted to generate electricity based on this phenomenon.

Figure 1 illustrates the principle of the PV working, which is fabricated from *p*-type and *n*-type semiconductor materials and forms a *p-n* junction. When *p* and *n*-type semiconductor layers are brought into contact, an electric field is created between two semiconductors, and due to potential difference electrons and holes travel across the junction to the corresponding opposite-type semiconductor through charge diffusion, creating a depletion zone at the *p-n* junction where there is no more chance of any charge carrier migration. Thus, a balance between the charge diffusion and the built-in electric field at the junction generates a stable thermal equilibrium (Figure 1.1a). In this equilibrium, a flat Fermi level (E_F) is developed through the bending of conduction (E_C) and valence band (E_V) of *n*-type and *p*-type semiconductors, respectively (Figure 1.1b). When the semiconductor absorbs photons, the electrons move to the conduction band leaving holes in the valence band. The generated electron-hole pairs which are far from the depletion region recombine rapidly due to the electric field, losing their energy by heat. Others excited within and close to the depletion region can be separated and migrate, leading to a photocurrent across the junction. Figure 1.1c shows the illuminated *p-n* junction under open-circuit conditions, where the electron and hole Fermi levels are separated in the *p* and *n* region, creating a measurable potential difference (V_{oc} ,

Chapter 1

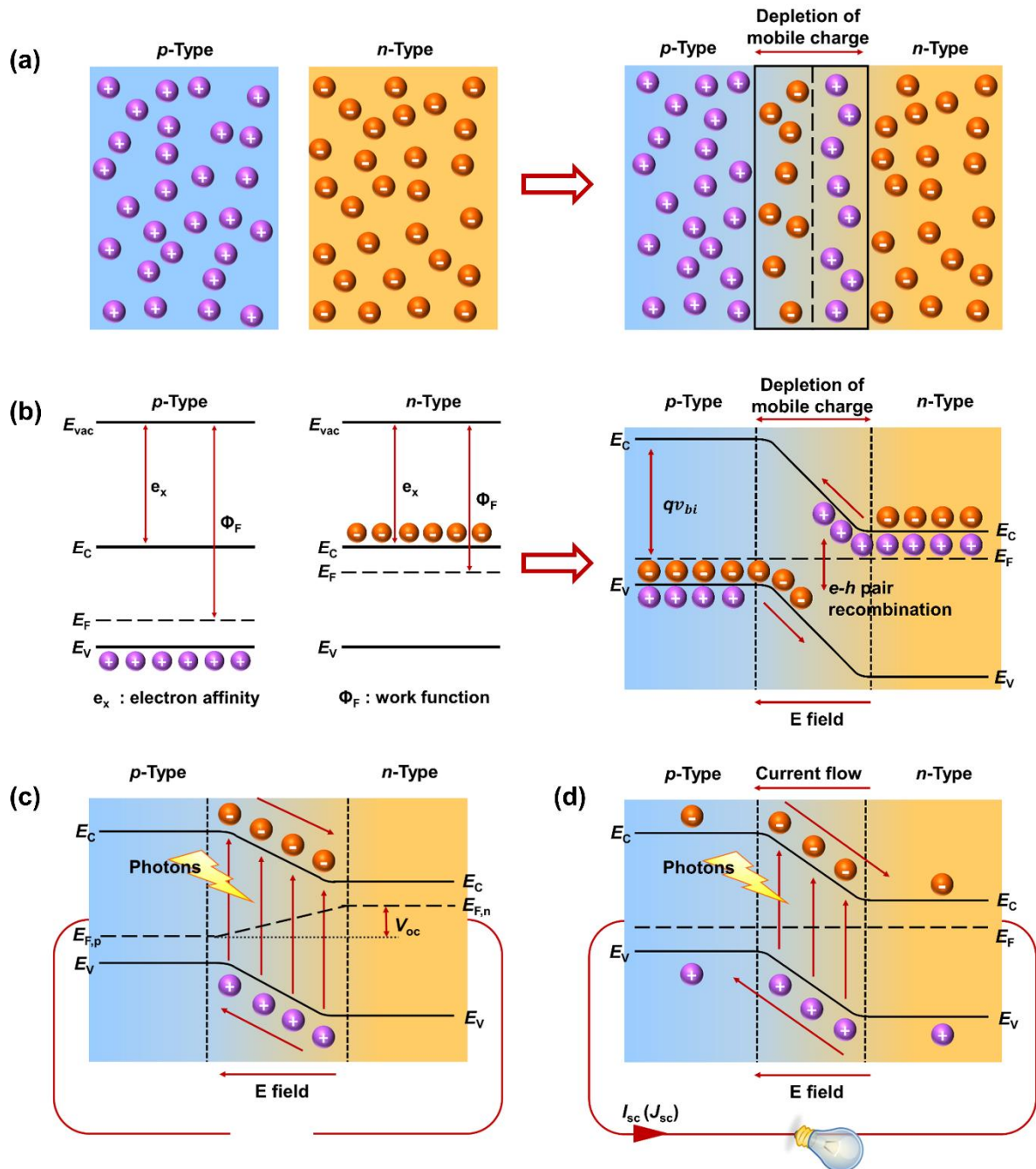


Figure 1. 1 (a) Schematic illustration of the creation of neutral region/depletion of mobile ions region at a p-n junction by majority carrier diffusion from p-type to n-type and n-type to p-type. The energy level of a p-n junction under (b) thermodynamic equilibrium [q -electron charge, v_{bi} -built-in potential], (c) illumination/open circuit, and (d) illumination/short circuit conditions.

open-circuit voltage) across the junction.¹⁰ Under the short-circuit condition, photogenerated current (I_{sc} , *short-circuit current*) flows freely (Figure 1.1d). A detailed elaboration of the V_{oc} and J_{sc} (*short-circuit current density*) will be discussed in the next section.

Chapter 1

1.3 Photovoltaic Fundamentals

1.3.1 Characteristics and Parameters of PV Cells

The ideal PV cell can be modelled by a light-induced current, I_{PV} as a current source in parallel with a diode, connected to an external load, as illustrated in Figure 1.2a. However, in real conditions, PV cells tend to imperfections in the $p-n$ junction such as unwanted recombination, finite refractive indices or electrical transport limitations, and imperfect absorption, resulting in parallel resistance (R_{sh}) across the junction with a series resistance (R_s) between the $p-n$ junction, which reduces the actual power output (Figure 1.2b).^{10,11}

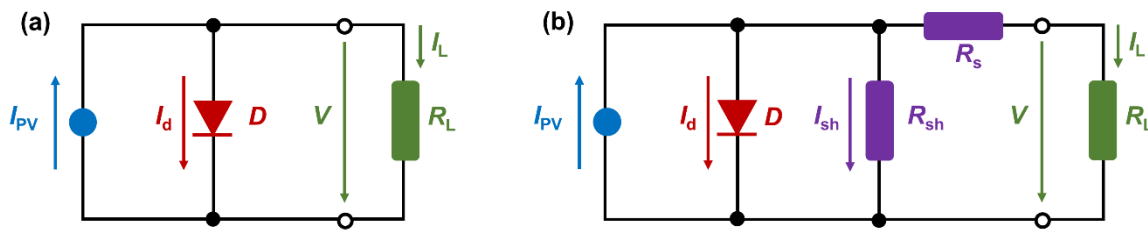


Figure 1. 2 The equivalent circuit of (a) an ideal and (b) a real PV cell (redrawn¹¹).

When the PV cell is irradiated, the current I_{PV} is generated, which follows the relation $I_{PV} = A_{light}J_{PV}$, where A_{light} and J_{PV} represent the active irradiated area and the generated current density of the PV cell, respectively. According to the $p-n$ junction theory, the voltage across the junction V_J and the generated current density $J(V_a)$ through the junction are connected to diffusion and generation-recombination reverse current density as,^{11,12}

$$J(V_a) = J_0 \left[\exp\left(\frac{eV_J}{n_1 K_b T}\right) - 1 \right] + J_{GR} \left[\exp\left(\frac{eV_J}{n_2 K_b T}\right) - 1 \right], \quad (1.1)$$

$$J_0 = n_i^2 e \left(\frac{D_n}{L_n} \frac{1}{N_D} + \frac{D_p}{L_p} \frac{1}{N_A} \right) \quad (1.2)$$

$$J_{GR} = \frac{en_i W}{2\tau} \quad (1.3)$$

where, n_1 and n_2 are so-called diode factors ($1 \leq n_1 \leq 2$; $n_2 \geq 2$), J_S is reverse saturation current density, L_n and D_n are the electron diffusion coefficient and diffusion length, L_p and D_p are the hole diffusion coefficient and diffusion length, N_D and N_A are n -side and p -side carrier concentrations. W and $1/\tau$ represent the depletion region width and capture probability in the

Chapter 1

combination center, respectively. The expression above (1.1) can be generalized by introducing the ideality factor n_{id} ;

$$J(V) = J_0 \left[\exp\left(\frac{eV}{n_{id}k_bT}\right) - 1 \right]. \quad (1.4)$$

If I is the output current, V is the output voltage, and R_s is the series resistance, the forward bias voltage across the p - n junction is $V + IR_s$. A part of the photo-generated current travels through the diode (I_d) while a part of the generated current flows through the parallel resistance (shunt resistance) R_{sh} . Therefore, the output current can be expressed by,^{10,11}

$$I = I_{PV} - I_d - I_{sh}. \quad (1.5)$$

By considering Eq. (1.1) and Eq. (1.5);

$$I = A_{\text{light}}P_{PV} - I_0 \left[\exp\left(e \frac{V+R_s I}{n_1 k_b T}\right) - 1 \right] - I_{GR} \left[\exp\left(e \frac{V+R_s I}{n_2 k_b T}\right) - 1 \right] - \frac{V+R_s I}{R_{sh}}. \quad (1.6)$$

The typical $I - V$ characteristic curve of the PV cell is shown in Figure 1.3a. The *open-circuit voltage* (V_{oc}) can be derived with the open-circuit conditions, where $V = V_{oc}$, $I = 0$, and with the assumption that $R_{sh} \gg R_s$,

$$V_{oc} = \frac{n k_b T}{e} \ln\left(\frac{J_{PV}}{J_0} + 1\right) \approx \frac{n k_b T}{e} \ln\left(\frac{J_{PV}}{J_0}\right) \quad (1.7)$$

where the approximation is justified because of $J_{PV} \gg J_0$.

The diffusion current is predominant in the device and the carrier recombination in the depletion region becomes negligible (or zero) when $n = 1$. The phenomena will be vice versa with $n = 2$. However, the PV cell exhibits both recombination and diffusion current under real conditions, thus, $1 \leq n \leq 2$. The *short-circuit current density* (J_{sc}) is used to describe the maximum current delivered by a PV cell, which strongly depends on the optical properties of the cell and the spectrum of the incident light. In ideal conditions with low R_s , J_{sc} is equal to J_{PV} .

The concept of *Fill-factor* (FF) has been introduced for characteristics evaluation, as it quantifies the fraction of maximum usable power versus internally generated power,¹¹

Chapter 1

$$FF = \frac{V_{MPP}I_{MPP}}{V_{oc}I_{sc}}. \quad (1.8)$$

The subscript MPP in expression (1.8) denotes the *maximum power point* of the solar cell (Figure 1.3a), which is the point on the I - V profile of the cell at which the solar cell generates the maximum power output. The FF can be further represented in terms of V_{oc} , with the assumptions of known n , zero R_s , and infinite R_{sh} ,¹³

$$FF = \frac{u_{oc} - \ln(u_{oc} + 0.72)}{u_{oc} + 1} \quad (1.9)$$

$$u_{oc} = V_{oc} \frac{e}{k_b T} \quad (1.10)$$

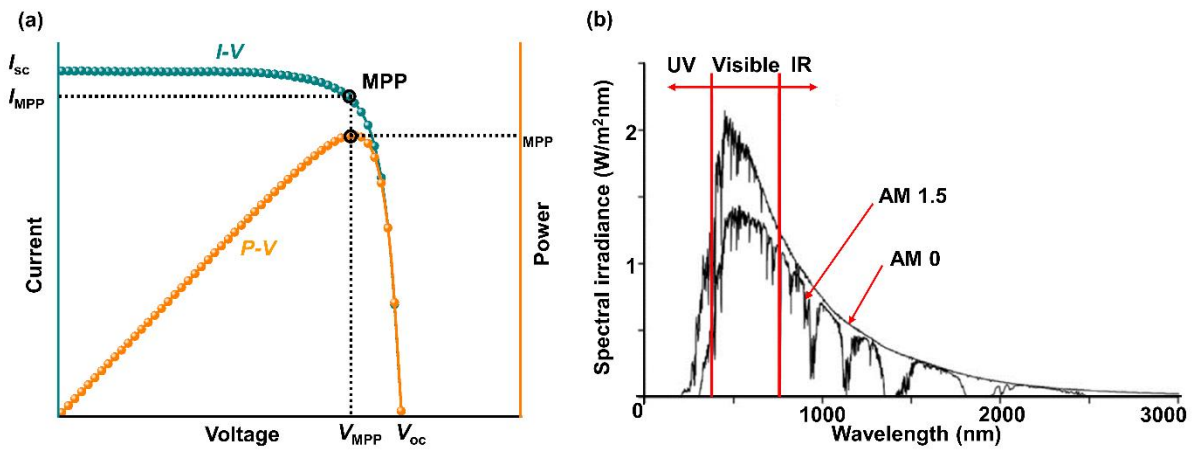


Figure 1.3 (a) Characteristic I - V curve of a solar cell extracted from a typical perovskite solar cell (discuss later in this chapter). (b) AM 0 and AM 1.5 spectral distribution of solar radiation power (redrawn¹¹).

The *power conversion efficiency* (η) can be calculated as the ratio between the maximal generated power and the incident power (P_{in}) on the cell area,

$$\eta = \frac{P_{max}}{P_{in}} = \frac{V_{MPP}I_{MPP}}{P_{in}} = \frac{V_{oc}I_{sc}FF}{P_{in}} \quad (1.11)$$

Since the spectral distribution and incident power control all the above parameters, reliable measurements of the J - V characteristics are given under *standard test conditions* (STCs), this means, that the total incident power on the solar cell should be measured is equal to 1000 W/m^2 . Further, the spectrum should resemble the AM 1.5G (Figure 1.3b), which is defined in the International Standard IEC 60904/3 under the solar spectral distribution tilted at 42 degrees to

Chapter 1

the horizontal.¹⁴ In this regard, the temperature of the solar cell should be maintained constant at 25°C.

1.3.2 The External Quantum Efficiency

The incident-photon-to-current-efficiency (IPCE), alternatively called external quantum efficiency (EQE) is the proportion of the created electron-hole pairs in the absorber collected by photons incident on the solar cell. The EQE is wavelength dependent, thus, it is measured by illuminating the solar cell with monochromatic light or light at individual wavelengths, and measuring the photocurrent through the solar cell. The EQE at a particular wavelength (λ) can be given as,¹⁰

$$EQE_{\lambda} = \frac{I_{ph,\lambda}}{q\psi_{ph,\lambda}} \quad (1.12)$$

where $I_{ph,\lambda}$ is the photocurrent at a given wavelength, q is the elementary charge, and $\psi_{ph,\lambda}$ is the spectral photon flow incident on the solar cell at a particular given wavelength.

1.3.3 Energy Losses and Limitations of Energy Conversion

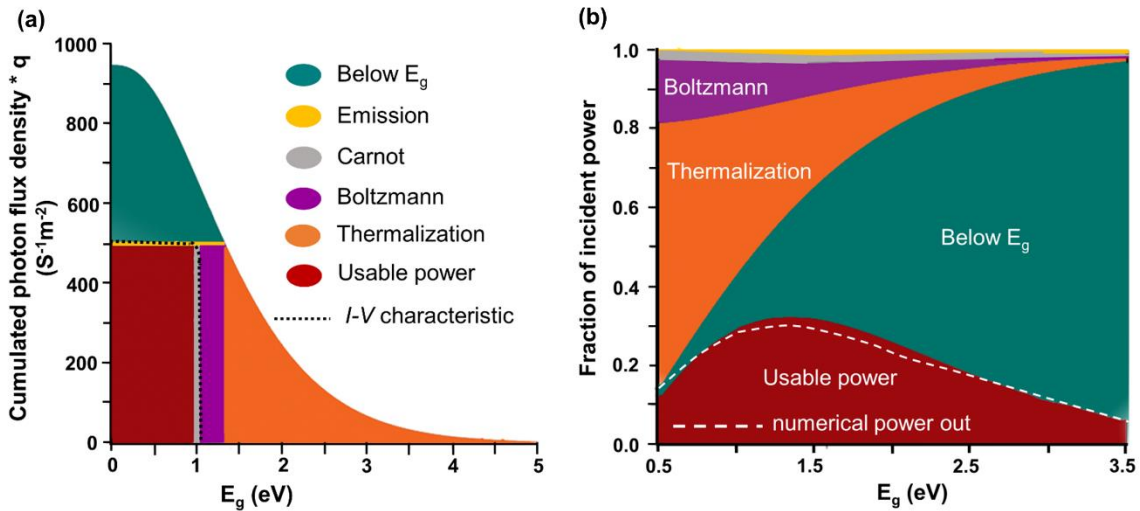


Figure 1. 4 (a) Intrinsic energy losses as a function of E_g under one sun illumination. (b) Fraction of incident power into intrinsic energy losses (redrawn¹⁵).

Limitation mechanisms of solar energy conversion in a typical solar cell under standard test conditions can be divided into two distinct categories; i.e extrinsic losses and intrinsic losses. Series resistance, shunt resistance or parasitic recombination, and contact shadowing are known to be extrinsic losses, which can subsequently limit the device's efficiency; however,

Chapter 1

they can be theoretically overcome.^{15,16} In contrast, unavoidable intrinsic losses that remain in the device are five types, which result in either a reduction in voltage or a reduction in current, thus, limiting the overall efficiency of solar cells (Figure 1.4a). Below E_g loss indicates unabsorbed photons with energy below the bandgap due to the mismatch between the broad solar spectrum and mono-energetic absorption. The conversion efficiency can be further reduced through emission loss according to Kirchoff's law where absorbers must also be emitters. Below E_g loss and emission loss are recognized as current drop mechanisms as they limit the number of available free charge carriers. Excited carriers with an excess amount of energy due to high-energy photons relax their excess energy down to the band edge, which is lost as heat, leading to the thermalization loss in the device.¹⁵

Some energy must be given up to transform thermal energy into electrical work; this energy loss is known as the Carnot loss.^{17,18} There is an additional energy loss known as Boltzmann loss that occurs owing to the inequality of absorption and emission angles, resulting in an entropy generation via photon modes expansion. Thermalisation, Boltzmann, and Carnot losses are responsible for voltage drop in the solar cells. In principle, the current-voltage characteristic of the solar cell is derived by considering all the intrinsic current and voltage drop processes.⁹ A numerically driven maximum power out for a given bandgap is compared alongside the analytical solution that is shown in Figure 1.4b.

1.3.4 Shockley-Queisser Limit

The free charge carrier generation is strongly dependent on the band gap and band structure of the semiconductor, only photons with energy higher than bandgap ($hc/\lambda > E_g$) can generate carrier pairs. A part ($\frac{hc}{\lambda} - E_g$) of absorbed energy is deprived due to thermalization. Hans-Joachim Queisser calculated and named in the honor of William Shockley a bandgap-dependent theoretical limitation of efficiency, referred to as the Shockley-Queisser limit (SQ-limit) based on the assumptions: the entire irradiation power $\int_{\lambda_{min}}^{\infty} \frac{hc}{\lambda} \Phi_0(\lambda) d\lambda$ is absorbed by the PV cell, the irradiation power $\int_{\lambda_{min}}^{hc/E_g} E_g \Phi_0(\lambda) d\lambda$ is converted into free-charge pair generation, only radiative recombination in an ideal PV cell with ideal junction characteristics and no parasitic resistances.^{10,11,19} According to the SQ criteria, the maximum theoretical limit for the conversion efficiency η_m can be represented as,

Chapter 1

$$\eta_m = \frac{\int_{\lambda_{min}}^{\frac{hc}{E_g}} E_g \Phi_0(\lambda) d\lambda}{\int_{\lambda_{min}}^{\infty} \frac{hc}{\lambda} \Phi_0(\lambda) d\lambda} \quad (1.13)$$

The maximum SQ limit for any solar cell is limited to 33.7% with a 1.36 eV band gap of an absorbing material under AM 1.5G solar radiation.^{11,19}

1.4 Perovskite

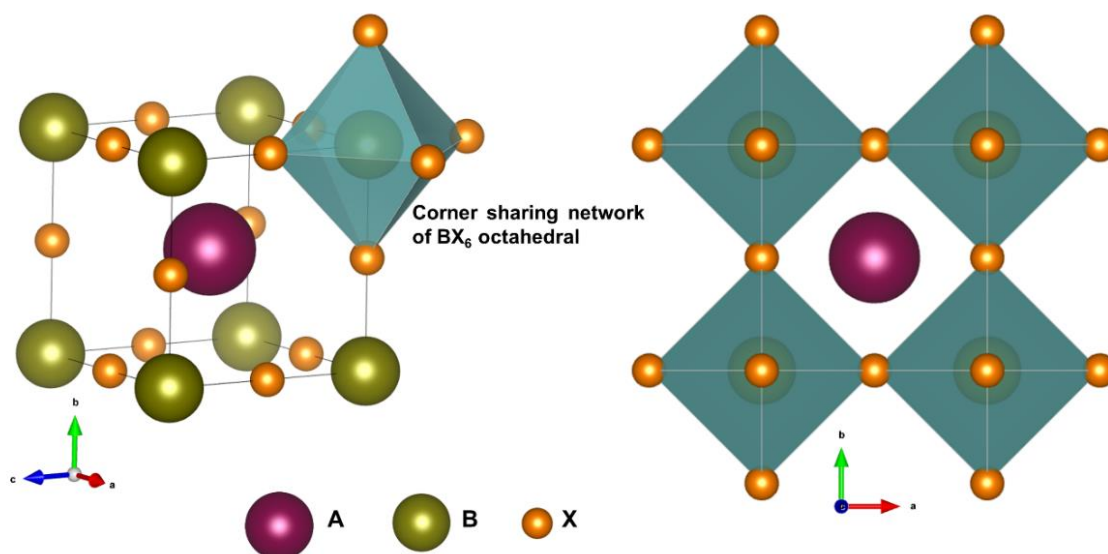


Figure 1. 5 The lattice representation of perovskite crystal structure ABX₃, showing corner sharing network of BX₆ octahedral and larger A cation occupied in cubo-octahedral site, where A, B, and X represent monovalent cation, divalent cation, and monovalent anion, respectively.

The word ‘perovskite’ refers to the mineral form CaTiO₃, which was discovered by the German mineralogist Gustav Rose in the Ural Mountains and named in honor of the Russian Count, Lev A. Perovski.²⁰ The term perovskite now refers to a wide range of materials with an ABX₃ crystal structure similar to CaTiO₃ and is generally composed of an organic or inorganic monovalent cation (A) such as methyl-ammonium (MA⁺, CH₃NH₃⁺), ethylammonium (EA⁺, CH₃CH₂NH₃⁺), formamidinium (FA⁺, CH₃(NH₂)₂⁺), Cs⁺, and Rb⁺, a divalent metal cation (B) such as Pb²⁺ and Sn²⁺. X represents a monovalent anion such as Cl⁻, Br⁻, I⁻, SCN⁻, and PF₆⁻. It is noted that for the ideal symmetry cubic structure, the A-site cations are usually larger than the B-site cations, and the body-centered B-site cation is octahedrally coordinated by the face-centered X-site anion to form a corner-sharing BX₆ three-dimensional (3D) network as shown in Figure 1.5.^{21,22}

Chapter 1

The Goldschmidt tolerance factor (t) is an indicator of evaluation of the crystal structure and the compositional space spanned by A, B, and X constituents, which is defined by the equation;

$$t = \frac{R_A + R_X}{\sqrt{2}(R_B + R_X)} \quad (1.14)$$

where, R_A , R_B , and R_X represent the ionic radii of A, B, and X, respectively.²³

Empirically, any molecular cation could be possible as long as it has sufficient space to fit within the cavity. The 3D perovskite network is distorted when the cation size is too large.²¹ A significant number of tolerance factors could be found in the range of $0.8 < t < 1$ for ideal cubic perovskite structures. The tilting of the BX_6 octahedral units and the displacements of the A and B sites primarily control the structural distortion.^{21,25}

1.5 Hybrid Organic-Inorganic Perovskites and Their Properties

A new subclass of the perovskite family, often referred to as hybrid organic-inorganic perovskites (HOIP) has attracted enormous attention in the last decade owing to their enormous structural and compositional diversity with an abundant variety of organic components and metal salt beyond their purely organic or inorganic systems, offering potential technological applications. In principle, HOIP can be categorized into three subclasses from a structural perspective: i.e. ABX_3 perovskite, $A_2BB'X_6$ double perovskites where the B cations are replaced by two or more cations heterovalently, and A_3BX antiperovskite.²⁶ However, $A_2BB'X_6$ double perovskites and A_3BX antiperovskites are not discussed herein. In 1978, the first known halide HOIPs with the cubic structure of $MAPbX_3$ were structurally investigated by Weber.²⁷ Generally, many intrinsic properties of perovskites including ferroelectricity, multiferrocity, and magnetism are varied depending on the phase transition.²⁸ Under the temperature perturbation, HOIPs undergo a successive phase transition, many of them first order with three distinct symmetries, evolving from cubic to tetragonal, and then to orthorhombic on cooling.^{29,30} The rotation of the A-site organic amine cation in HOIP is limited and only possible around the C-N axis when it is in the lowest temperature phase.^{24,31} Apart from the electrostatic force, the interaction of the perovskite framework with FA and MA cations through N-H...I hydrogen bonding ultimately influences the octahedral tilting, phase-transition mechanism, and disorder of the perovskite.^{24,32}

Chapter 1

Based on the preliminary consideration of HOIP as PV absorber material originates from the superior semiconducting properties associated with them. These include a suitable direct bandgap with experimentally observed bandgaps ranging from ~ 1.2 - 2.8 eV.³³ Owing to the strong contribution of the halide p orbitals to the optical transition, the halides in HOIP predominantly regulate their bandgap, which can also be tuned by differing the B-site metal. A-site organic cations, on the other hand, have a minor contribution in determining the bandgap of HOIP due to the negligible influence of the $2p$ orbitals of C and N together with the $1s$ orbitals of H on the density of state near the Fermi level. However, the steric effect of the A-site cation could influence the bandgap by distorting B-X bond length and bond angle through hydrogen bonding and van der Waals interaction.^{33,34}

HOIPs are recognized as promising light absorbers, comprising strong absorption, which significantly reduces the thickness of the absorber layer to hundreds of nanometres to achieve better efficiency. These materials also demonstrate low active defect density, which is potentially related to the low-temperature solution processing of the materials. The long diffusion length (up to 23 and 650 μm in films and crystals, respectively), the long carrier lifetimes (up to 30 μs for polycrystalline films and 2.7 ms for single crystals), in combination with high radiative efficiencies in HOIPs necessitate consideration of efficient photo charge transfer dynamics in thin films under illumination.³⁵ The exciton binding energy (E_B) to dissociate electron-hole pairs in HOIPs is as low as ≤ 25 meV, facilitating free charge forming rather than bound excitons.³⁶

1.6 Hybrid Organic-Inorganic Perovskite Solar cells

The application of hybrid perovskites in PVs was started back in 2006 with the incorporation of MAPbI_3 as a visible-light sensitizer, by Miyasaka and co-workers, which gave them light-to-electricity conversion efficiency of $\sim 2.2\%$. Later in 2009, the same group was able to reach the PCE up to $\sim 3.8\%$ by replacing I with Br.^{25,37} Despite the low initial PCE by that time, rapid progress has been made following the development of solid-state perovskite devices. Owing to the advancement in device architecture and materials processing, PSCs have shown great consideration, with their certified PCEs reaching 25.7% in just over 12 years of research.³⁸

Chapter 1

1.6.1 Device Architecture of PSCs

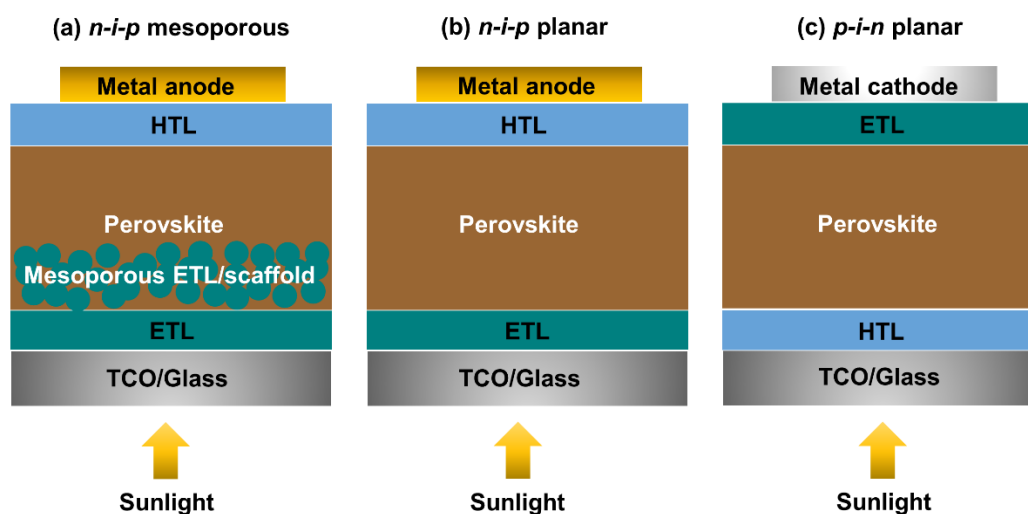


Figure 1. 6 The schematic diagram of the different architectures of perovskite solar cells; (a) $n-i-p$ mesoporous, (b) $n-i-p$ planar, and (c) $p-i-n$ planar (inverted) configuration.

Depending on the light incidence, two types of configuration can be identified in single-junction PSCs, which comprise either $n-i-p$, where it can be separated further into planar or mesoporous heterojunction and $p-i-n$ (inverted) architectures as illustrated in Figure 1.6. Here, n and p refer to electron and hole carrier charge transporting materials (CTMs), respectively, and i refers to the perovskite absorption layer sandwiched between electron transporting layer (n , ETL) and hole transporting layer (p , HTL). The aforementioned definition is also based on the type of charge transport layer (CTL) contacts with the transparent conductive substrate. In planar $n-i-p$ PSC, the ETL is deposited on the transparent-conductive oxide (TCO) layer that will function as the cathode and will be either fluorine-doped tin oxide (FTO) or indium tin oxide (ITO). On the other hand, $p-i-n$ configuration has the HTL at the light incoming side, deposited on TCO, which is identified as the anode. In contrast to the planar $n-i-p$ type PSCs, the mesoporous $n-i-p$ type PSCs comprise a compact ETL (c-ETL) formed on TCO substrate and then an additional mesoporous ETL (mp-ETL) is constructed on the c-ETL as both the ETL and structural scaffold. The device fabrication is finished with the deposition of a metal contact layer (gold, silver, and aluminium) as the top electrode.^{39,40}

Chapter 1

1.6.2 Deposition Techniques of HOIP Layer

Depositing techniques influence and control the morphology, crystallinity, and thickness of the perovskite layer. The quality of the perovskite layer is known to be one of the main factors for high-performance PSCs with longer lifetimes, thus, choosing the appropriate depositing techniques is paramount for achieving an appropriate perovskite film. The fabrication techniques for the fabrication of HOIP thin films can be classified into three main categories: solution-based, hybrid, and vacuum-based.⁴¹ However, the experiments in this thesis were constructed with the solution-based spin-coating method, only that technique is described in detail in the following section.

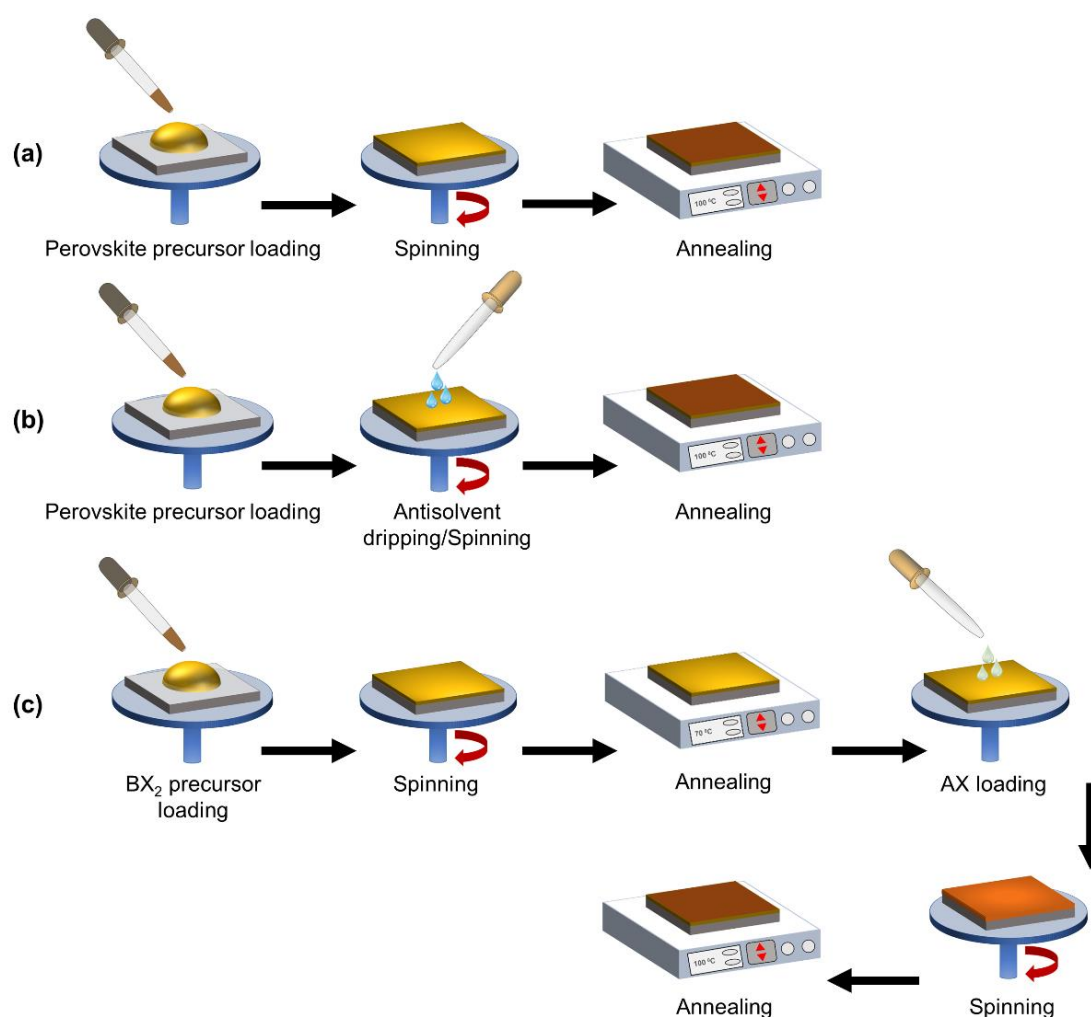


Figure 1. 7 Schematic illustrations of solution-based perovskite thin film deposition techniques. (a) Solvent engineering free one-step method, (b) solvent engineering-assisted one-step method, and (c) two-step methods.

Chapter 1

1.6.2.1 Solution-Based One-Step Coating:

The very first fabrication technology for solution-processed PSCs to be developed was the one-step deposition. In this process, the perovskite precursor solution containing the mixture of AX (eg: MAI, FAI, MAI/FAI, CsI) and BX_2 (eg: PbI_2 , $PbBr_2$, $PbI_2/PbBr_2$) in a solvent such as dimethylformamide (DMF) and dimethyl sulfoxide (DMSO) is loaded on the target substrate and spin-coated the thin film. The film is subsequently transferred onto a pre-heated hot plate and annealed for the desired time to obtain a crystallized perovskite film (Figure 1.7a). However, at the early stage of this research field, simple spin coating of the perovskite precursor solution introduces several drawbacks including inhomogeneity and pinholes on the perovskite film, which result in low performances of the PSCs.^{42,43} Later, the aforementioned shortcomings were overcome with solvent engineering, which is first introduced by Xiao and co-workers in 2014, by which a smooth, uniform and pinhole-free perovskite film can be achieved.⁴⁴ The technique involves dropping the antisolvent during the spinning of perovskite precursor on the spin coater before the end of the process (Figure 1.7b). Anti-solvent refers to a solvent, which should not dissolve the perovskite.

1.6.2.2 Solution-Based Two-Step Coating:

The sequential two-step coating protocol was first proposed by Mitzi's group to control the film morphology and overcome the choice of solvent involved with the one-step method in 1988.⁴⁵ Later, Grätzel and co-workers introduced the method in the PSCs field as an alternative technique that has the ability to fabricate high-quality perovskite films.⁴⁶ Generally, BX_2 film is first deposited by spin coating on the target substrate, followed by a heat treatment for an appropriate time. Once the BX_2 films reach room temperature, an isopropanol solution of AX is spun on it followed by annealing at the desired temperature for the relevant time (Figure 1.7c). Some protocols involve vacuum evaporation for BX_2 film formation and dipping of BX_2 films in AX solution to form ABX_3 .

1.6.3 Charge Transport Layers in PSCs

1.6.3.1 Electron Transport Layer (ETL):

The ETL in PSC plays an essential role in collecting and transferring electrons from perovskite while blocking holes, which can be achieved by maintaining a large energy barrier for hole transfer through offsets in the valence band. High-temperature sintered titanium oxide (TiO_2)

Chapter 1

has been widely used as an ETL in PSCs owing to their high bandgap and chemical resistance. Typically, a combination of spray pyrolysis or spin-coated TiO₂ (as a blocking layer) and spin-coated TiO₂ (as a mesoporous layer) is used as ETL. However, defects at the TiO₂/perovskite interface, which act as recombination centers for photo charge carriers, high temperature, and time-consuming fabrication of the TiO₂ layer, motivate the PSCs community to research alternative ETLs.⁴⁷ Recently a tin oxide (SnO₂) is upcoming rapidly due to its moderate synthesis temperature, lower charge accumulation, and fast charge extraction at the interface thanks to its deep conduction band and high electron mobility.⁴⁸ Several reports have also been studied using a combined layer of TiO₂ and SnO₂ as ETL. Besides, doped metal oxides, such as Cl-doped TiO₂, Li-doped TiO₂, and Y-doped TiO₂ demonstrated a proper energy level alignment with perovskite, which result in high FF or V_{oc} in PSCs.⁴⁹⁻⁵¹ Alternatively, complex bilayer ETLs, incorporating organic materials and metal oxides such as TiO₂/PCBM ([6,6]-Phenyl-C61-butyric acid methyl ester), SnO₂/PCBM, SnO₂/C₆₀ (Buckminsterfullerene) have also been constructed, showing enhanced energy alignment and better conductivity, and subsequently upgraded performances in PSCs.⁵²⁻⁵⁴

The aforementioned SnO₂ and TiO₂-based ETLs can only be possible in the *n-i-p* configuration as the perovskite layer does not survive under the conditions applied during the fabrication of these layers such as high temperature and solvents used. In this regard, either PCBM, C₆₀, or a mixture of both is applicable as an ETL atop the perovskite active layer in *p-i-n* configuration.

1.6.3.2 Hole Transport Layer HTL:

The hole transporting materials (HTM) that can be used must possess a few qualities, but are not limited to intrinsically high hole mobility, energy level alignment with the perovskite layer, and long-term photochemical and thermal stability. Spiro-OMeTAD [2,2',7,7'-tetrakis(*N,N*-di-*p*-methoxyphenylamine)-9,9'-spirobifluorene] remains the most popular HTM for high-performance PSCs.⁵⁵ However, they must be doped with *p*-type dopants, typically, bis(trifluoromethane) sulfonimide lithium salt (Li-TFSI) and 4-*tert*-butylpyridine (*t*BP) to achieve sufficient hole mobility and conductivity. Polymeric HTMs such as PTAA [poly(triaryl amine)], P3HT [poly(3-hexylthiophene-2,5-diyl)] have also been developed and utilized either in their pristine form or with *p*-type additives depending on the configuration of the PSC.⁵⁵⁻⁵⁷ PTAA and P3HT in their pristine form are widely used in inverted PSCs, whereas doped conditions are commonly utilized in *n-i-p* PSCs. However, the hygroscopic nature of these

Chapter 1

additives negatively affects the long-term stability through moisture-induced degradation of the active perovskite layer.

PEDOT:PSS [poly (3,4-ethylenedioxythiophene): polystyrene sulfonate] is also a conventional HTM developed in inverted PSCs due to its low cost and low-temperature processability, yet the hygroscopic and acidic nature associated with it degrades and corrodes the perovskite and TCO layer, resulting in lower device stability.^{58,59} Inorganic HTLs including NiO_x, CuS, CuCrO₂, MoO_x, CuO_x, CuI, Ta-WO_x, and CuSCN have been successfully integrated into PSCs with long-term operational stability.⁶⁰ With the advantage of bandgap tunability, several two-dimensional (2D) materials including but not limited to transition metal dichalcogenides (TMDs) and Mxene were employed as HTM by several reports, however, the poor continuous film-forming ability of such materials limit their use as individual HTL in high-performance PSCs.⁶¹⁻⁶⁶

1.7 Charge Transfer Dynamics in PSCs

A typical photovoltaic process in PSCs can be described in four fundamental steps:

- i. Photon absorption and exciton formation
- ii. Charge separation
- iii. Charge transportation
- iv. Charge extraction

Upon illumination, photons are absorbed by the perovskite layer and excitons are formed. When the electrostatic binding energy associated with the opposite charge pairs break, the excitons are dissociated into free charge carriers, i.e. electrons and holes.^{21,67} Once the free charge formation starts, charge separation occurs by injecting electrons and holes to their corresponding CTL, which has been demonstrated to happen on a similar timescale.⁶⁸ Then, electrons are transferred from the perovskite/ETL interface to the interface of ETL/electrode by ETL, while holes at perovskite/HTL to the HTL/electrode by HTL. Finally, the charge carriers are extracted by the respective electrodes, which are connected to an external circuit for completing an electrical circuit and generating electricity.

Chapter 1

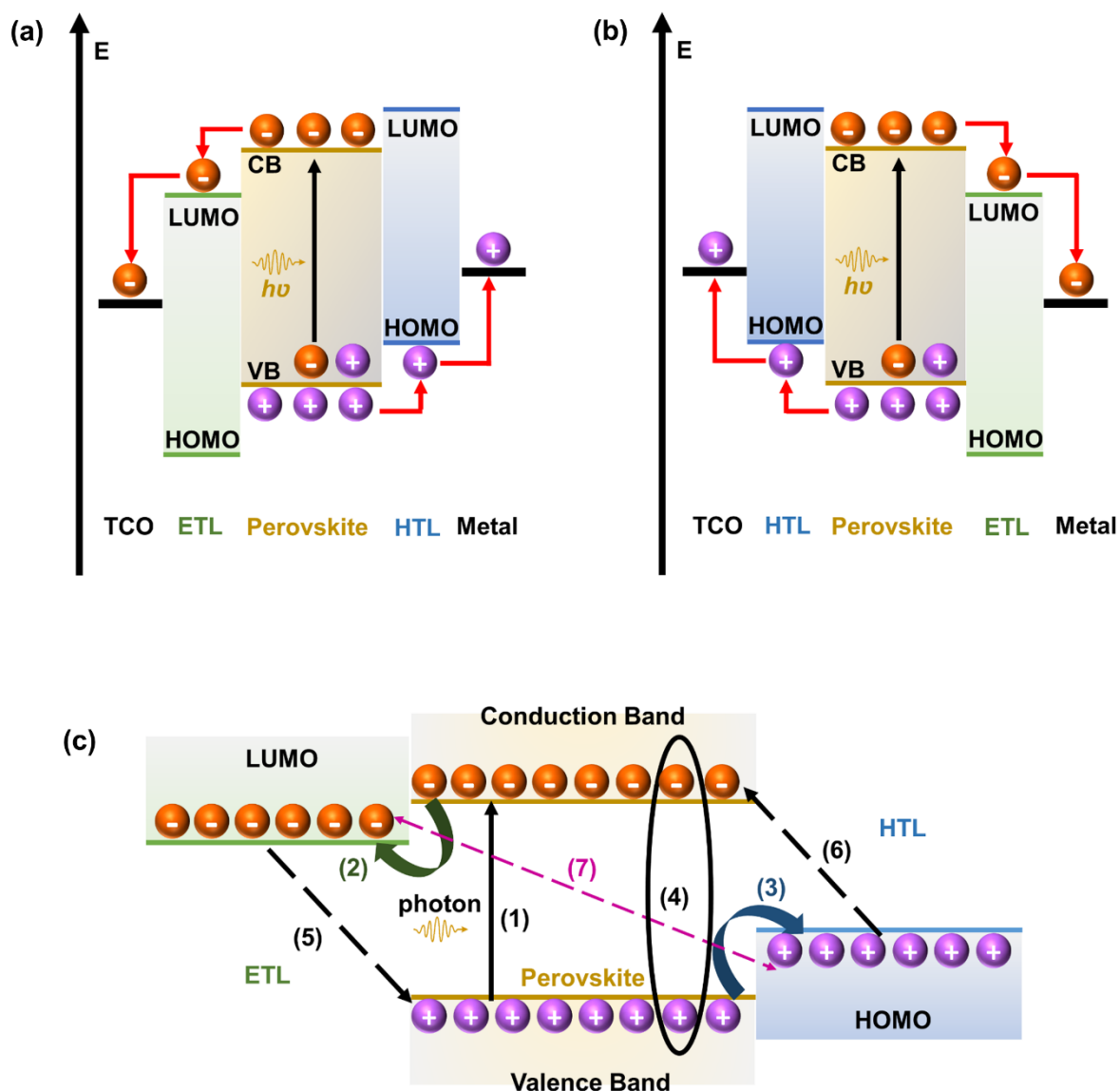


Figure 1. 8 Charge transfer process in (a) *n-i-p* and (b) *p-i-n*, PSCs. (c) The desirable and undesirable charge transfer kinetics in a typical PSC. TCO: transparent conductive oxide, ETL: electron transport layer, HTL: hole transport layer, CB: conduction band, VB: Valance band. HOMO: highest occupied molecular orbital; LUMO: lowest unoccupied molecular orbital (redrawn⁵¹).

The charge carrier kinetics of *n-i-p* and *p-i-n*-based PSCs are shown in Figure 1.8a and b, respectively. However, in real operating conditions, due to the imperfection nature of perovskite and the complexity of the device architecture, undesirable charge carrier kinetics within the device through various pathways also take place, which adversely influence the overall device performance. The possible charge kinetics are illustrated in Figure 1.8c. The

Chapter 1

desirable processes include:⁶⁸ (1) the generation of electrons and holes in the perovskite via photo-excitation; (2) electrons are injected into the ETL, and (3) holes are injected into the HTL. At the same time, a series of behaviours that are detrimental to the cell's performance can be recognized as: (4) bulk recombination of photo-generated species; (5) back charge transfer at the interfaces of ETL/perovskite, and (6) back charge transfer at the interface of HTM/perovskite; and (7) charge recombination between the ETL and the HTL.

1.8 Carrier Recombination Mechanism in PSCs.

Following light absorption, meta-stable hot carriers thermalize, where they exchange energy with one another and cool down to the conduction band minimum and release thermal energy.⁶⁹ Eventually, meta-stable electrons stabilize back down to a lower energy position in the valence band and recombine with holes while losing energy in the form of either heat or light, which is known as recombination. The main carrier recombination processes can broadly be categorized as follow,^{70,71}

i. Radiative recombination: This is often called band-to-band recombination, where electrons and holes recombine directly, thus resulting in the emission of photons (Figure 1.9a).

ii. Defect-assisted recombination: A type of non-radiative recombination, which is also known as Shockley-Red-Hall (SRH) recombination, where electron-hole recombination occurs via a trap level or deep-level defects in the band gap and the energy released by recombination gets dissipated to phonons (Figure 1.9b).

iii. Auger recombination: This is also a non-radiative recombination mechanism, involving three carriers. Rather than emitting energy from electron-hole recombination as a photon, the energy is captured by a third carrier that can be either electron (electron-electron-hole process, Figure 1.9c) or hole (hole-hole-electron process, Figure 1.9d) to a higher energy state within the CB or VB and subsequently thermalizes back down to the CB edge or VB edge depending on the process type. This mechanism can be either direct or indirect (Figure 1.9e).

The evolution of photo-generated carrier density (n) with time (t) is related to the whole recombination process as;^{71,72}

$$\frac{dn}{dt} = -K_1n - K_2n^2 - K_3n^3 \quad (1.15)$$

Chapter 1

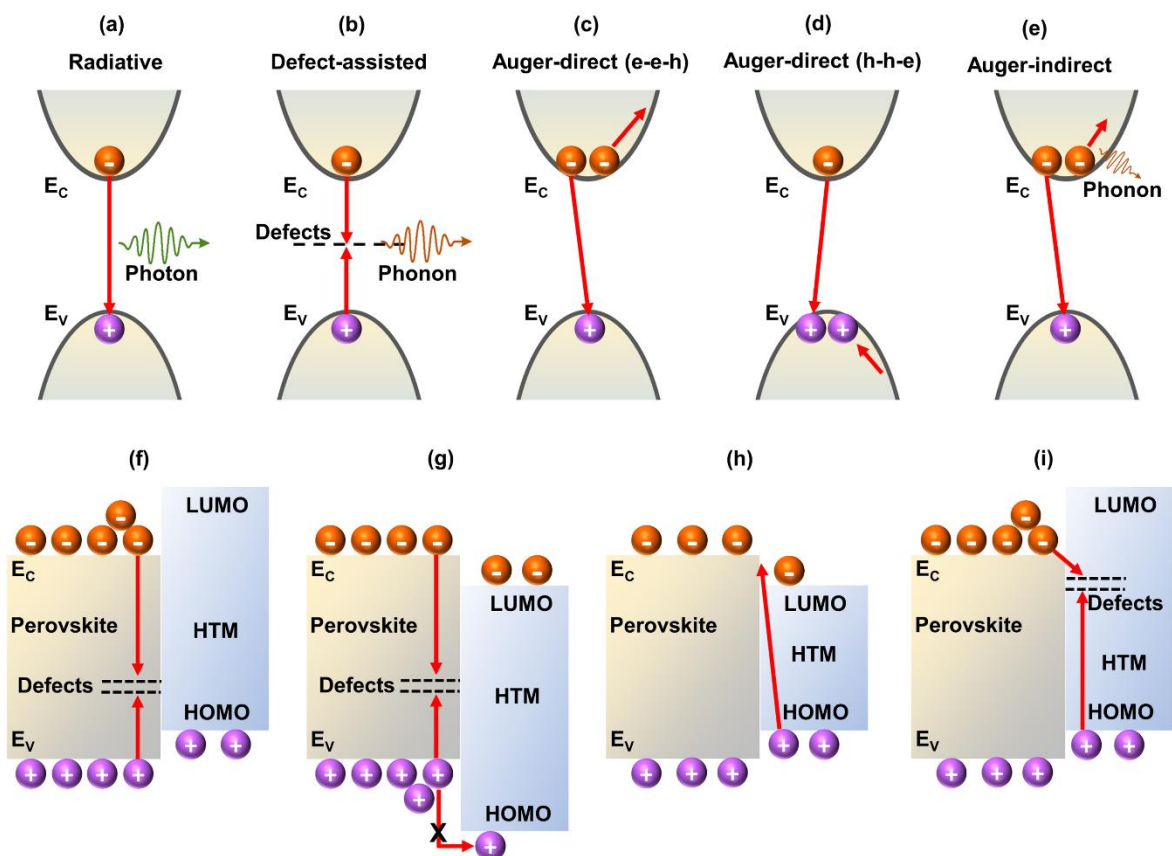


Figure 1. 9 The photo-induced charge-carrier recombination dynamics: (a) radiative recombination, (b) defect-assisted or Shockley-Red-Hall (SRH) recombination, (c) Auger-direct recombination ($e-e-h$), (d) Auger-direct ($h-h-e$) recombination, and (e) Auger-indirect recombination. The origins of interface- induced recombination losses at perovskite/HTM interface (similar recombination processes could be possible at perovskite/ETM interface): (f) deep level defects-assisted, (g) incompatible energy level alignment at the interface together with defects in the perovskite, (h) back transfer-induced, and (i) defect-assisted in the HTL (redrawn⁷⁰).

where K_1 , K_2 , and K_3 are coefficients corresponding to defect-assisted, radiative, and Auger recombination methods, respectively. The radiative recombination process of free charge carriers is minor in PSCs, whereas non-radiative recombination processes are predominantly contributed to the overall recombination in PSCs, limiting the PCEs.^{73,74} The energy depths and the density of defects govern the defect-assisted recombination in polycrystalline perovskite films. On the other hand, Auger recombination dominantly occurs for perovskite with high carrier concentrations above 10^{17} cm^{-3} and can be secondary with carrier concentrations in the range of $\sim 10^{13}$ - 10^{15} under AM 1.5G illumination.^{74,75}

Chapter 1

iv. Surface, grain boundary, and interface-induced recombination

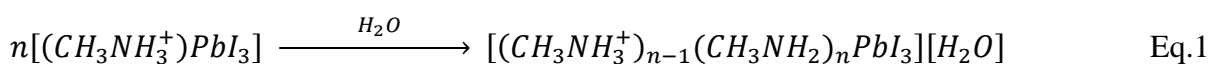
Owing to the polycrystalline nature, crystal imperfections are likely to be concentrated at film surfaces and grain boundaries (GBs). Further, in devices, dangling bonds exist on the surfaces of semiconducting materials, which can be identified as recombination sites, attracting photo-induced electrons or holes.⁷⁶ The surface states, interface states, and high-angle GBs in polycrystalline semiconductors in PSCs behave as infinite sinks or sources for carrier recombination and generation, and the recombination mechanism can be identified similarly to defect-assisted recombination. However, due to the different chemical nature of the recombination sites, the rate of surface recombination is dependent on the surface density and capture cross-section. Moreover, interface-induced recombination (Figure 1.9f-i) caused by ill-assorted energy level alignment, charge carrier back transfer, and surface imperfections is another source of non-radiative recombination losses, which severely influence the PSC performances.⁷⁰

1.9 Causes of HOIP Solar Cell Degradation

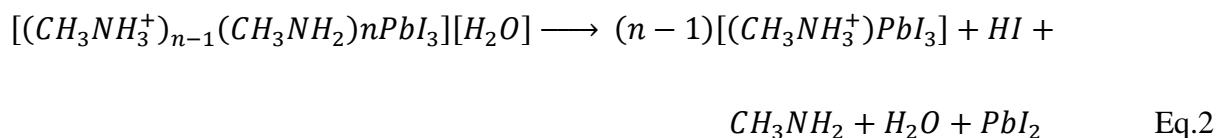
Despite its many advantages including excellent PCEs, the operational stability of HOIP solar cells remains of foremost concern. A better understanding of the exact causes of the device instability is paramount to improve the operational stability of the device while bringing this technology closer to industrial standards. In principle, factors that cause the perovskite crystal to undergo degradation and thus the collapse of the overall device can broadly be split into two categories - extrinsic and intrinsic factors.⁷⁷

1.9.1 Extrinsic Factors

i. Moisture: A major source of hybrid perovskite degradation through the decomposition of chemical constituents of the material. H₂O is considered a Lewis base, which forms weak hydrogen bonds with hygroscopic organic cations, leading to the formation of a reversible hydrated perovskite phase.⁷⁸ However, enough moisture penetration is responsible for metal salt solubility and irreversible degradation of HOIP film in the device. The rapid degradation of perovskite can occur when humidity is combined with high temperature, UV light, or the application of an electric field. The possible decomposition pathway of HOIP under moisture can be explained as follows where MAPbI₃ is considered due to simplicity of explanation.⁷⁸



Chapter 1



ii. Light: Light-induced degradation of PSCs is most significant when combined with other factors such as moisture and oxygen. Under light and oxygen, photo-generated electrons in the HOIP form superoxide, which can deprotonate cations, leading to the degradation of perovskite. Additionally, ultraviolet light can negatively influence the stability of common ETL, TiO₂, and forming trap states, which dramatically reduces the performance of PSCs.^{77,79} Under illumination, photo-induced holes can oxidize iodide atoms, which creates iodide vacancies in the perovskite lattice, thus increasing of ionic mobility in the excited state of perovskite. The transformation of iodide to iodine causes a reduction of ionic/atomic size and formation of interstitial vacancies in the lattice, and subsequently leads to the irreversible decomposition of perovskite, resulting in reducing the durability of PSCs.

iii. Temperature: During the thermal-induced degradation process, the organic cation MA⁺ and halide anion I⁻ synchronously release from HOIP and form PbI₂, which leads to a decomposition of the perovskite layer. It has been reported that inorganic cations such as Cs⁺, and organic cations such as FA⁺, and Br⁻ show more stability under heat, thus, choosing a complex multi-ion mixed perovskite system provides high thermal stability to PSCs.⁸⁰ Further, ion diffusion in the perovskite occurs under thermal activation, which is a key issue for the viability of PSCs. A high temperature in combination with humidity, oxygen, and UV light causes rapid degradation of HOIP, and ultimately the instability of the device.

1.9.2 Intrinsic Factors

i. Ion migration: It is typical to have defects like vacancies in the perovskite lattice during film formation, which later can encourage ion migration through the perovskite lattice. Ion migration within the perovskite layer can be identified as a source of hysteresis and fluctuation of performance in PSCs. Under applied bias conditions, ions drift within the perovskite layer and accumulate at the interfaces in PSCs, which acts as a barrier to current flow and degrades the performance of PSCs.^{81,82} Further, a conductivity reduction of HTL such as Spiro-OMeTAD can occur when it reacts with migrating iodine ions that quickly hampers the performance of PSCs. Ion migration is also a source of local electric field formation at the perovskite interface, which results in the deprotonation of the organic cations and subsequently

Chapter 1

deteriorates the PSC. Moreover, ion migration initiates and promotes halide segregation under illumination in HOIP, which is detrimental to the PV performance in PSCs.^{82,83}

1.10 Development Strategies of PSCs

PV performance, stability, cost, and scalability are four pivotal foundations for the development of PSCs and their successful laboratory-to-industry translation. Each component of the device plays an important and unique role in improving the overall device PV performance and long-term operational stability. Recent progress has been mainly attributed to the development of key strategies that effectively reduce the defects of the perovskite layer, enhances the photo-induced charge-transfer kinetics throughout the layers and interfaces, and minimize possible mechanisms of device degradation, thereby enhancing device efficiency. The development strategies for PSCs from the lab into the market to commercialization can be broadly categorized into three fronts:⁸² *i. compositional engineering* enables high-quality perovskite crystal synthesis with a desirable bandgap and optimized opto-electronic properties that are in line for satisfactory PV device fabrication. This strategy further engages with an addition of additives into perovskites to control the crystallization, defect passivation, bandgap tuning, lattice strain relaxation, and stability enhancement in perovskites. *ii. Device engineering*: innovating and engineering device configurations play a significant role in addressing the limitation of PV performances and stability issues in PSCs. Over the last decade, different device architectures have been immersed, which are not only engaging with designing new materials for CTLs and electrodes but also consisting of simple thin-film deposition techniques and encapsulation techniques.³⁹ It is important to maintain the key advantages of low cost, large area processability, and simple fabrication in any device engineering as the PSC structure continues its evolution to higher efficiency and extended stability. *iii. Interface engineering*: this part is discussed in the following section.

1.10.1 Interface Engineering of PSCs

PSCs are composed of several layers with four different interfaces, namely perovskite/HTL, ETL/perovskite, HTL/anode, and cathode/ETL, which ultimately play a crucial role in ruling device performance and stability. Interface charge collection and transfer, charge/ion accumulation at the interfaces, interfacial defects and vacancies, interface band alignment, interaction and compatibility between layers, and energy barriers not only have a strong impact on device performances but also have a great influence on the device stability.⁸⁴ In this regard,

Chapter 1

interface engineering has recently gained a pivotal role in the PSCs field that effectively manages the photo-induced charge transfer dynamics at the interfaces, thereby enhancing device efficiency.^{85,86} It is an effective approach to tune the interlayers and interfaces to overcome the interfacial losses in PSCs. Stabilizing perovskites from degradation is another important benefit of interface engineering, which could largely enhance device stability.

For clarity, the interface is known to be a junction between two adjacent layers, which can be either homo or hetero dependent on whether similar or different materials are elaborated. On the other hand, the interfacial layer is regarded as a layer of material that forms an interface with, e.g. the perovskite film. Apart from CTLs, the interfacial layers may include thin interlayers, which modify and tune the interface properties.⁸⁵ Inappropriate energy band alignment introduces a charge extraction barrier at interfaces, which leads to undesired charge accumulation, charge recombination, and reduction of charge collection efficiency, and subsequently a voltage and FF drop at the interface. Energy level alignment with the adjacent layers is the primary concern of interface engineering, which closely links with carrier dynamics, hysteresis, Voc, and FF of PSCs. Different techniques are available in interface engineering including but not limited to placing a new interface layer, introducing bilayer CTLs, and incorporating additives to CTLs. In any method, the interface layer must be conductive enough and thin as much as possible to reduce the interfacial resistance loss and form Ohmic contact with adjacent layers but thick enough to avoid defects.⁸⁷ Beyond interfacial band alignment, the interface layer should show intrinsic thermal and chemical stability, control the morphology of perovskite film if it is formed on the interface layer, and minimize the interfacial defects. Recently, low dimensional materials have been studied in the field, which can be incorporated as inter or buffer layers by modifying the intrinsic properties of involved layers at the interface, and eventually annihilating the energy barrier while improving photo-induced charge transfer kinetics at perovskite/CTLs interfaces.⁸⁸ Since the experiment works in this thesis are based on low-dimensional materials including 2D (two-dimensional) TMDs (transition metal dichalcogenides) as interface layer, in the following section, we discuss these materials.

Chapter 1

1.11 Low Dimensional Materials.

1.11.1 Graphene and Reduced-Graphene Oxide

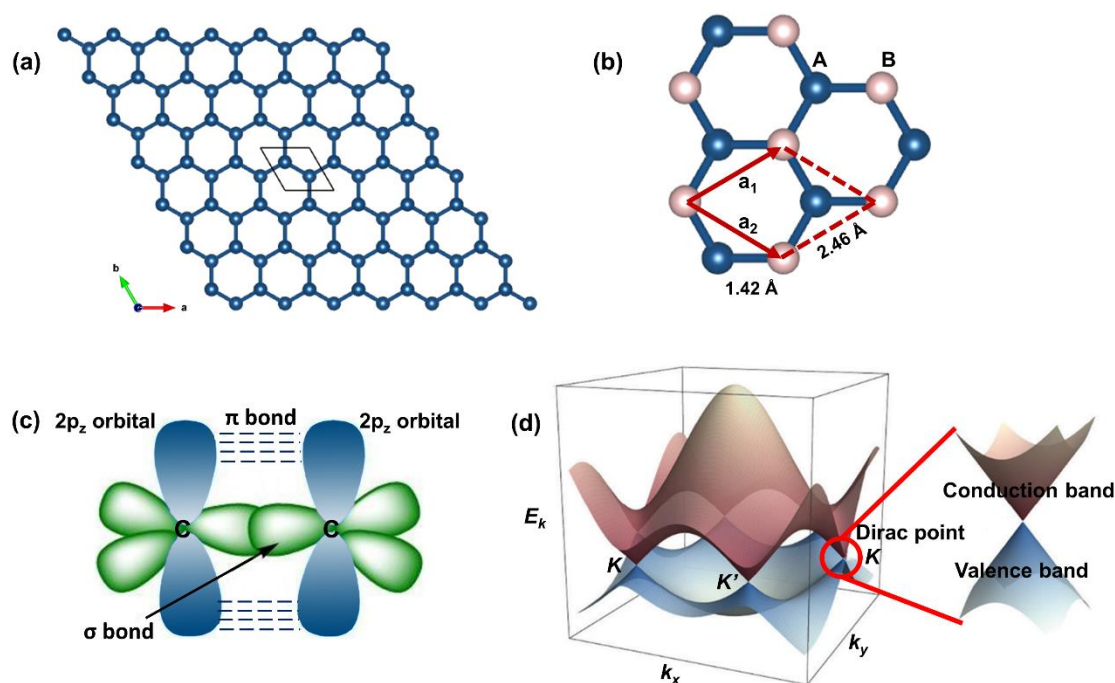


Figure 1. 10 Structure of graphene: (a) honeycomb lattice structure of carbon atoms, (b) the unit, where A and B represent carbon atoms from different sub-lattices, a_1 and a_2 are unit cell vectors, (c) sp^2 hybridization with σ and π bonding, and (d) electronic band structure with Dirac point (redrawn⁸⁹).

Graphene is a 2D carbon allotrope successfully exfoliated from graphite through micromechanical cleavage by Geim and Novoselov in 2004, which has opened a new field in the scientific community, so-called 2D materials. Graphite, a 3D crystal consists of atomically thin graphene sheets, presenting weak out-of-plane van der Waals interactions and strong in-plane covalent bonding.⁹⁰ A single layer of carbon atoms positioned in a hexagonal honeycomb design (Figure 1.10a) constructs a freestanding mono sheet of graphene, showing distinctive and extraordinary optoelectronic properties that cannot be found in their bulk form. Each carbon atom in graphene is bonded to another three carbon atoms through covalent σ bonds with a short interatomic length of $\sim 1.42 \text{ \AA}$, which are generated by sp^2 hybridization of two carbon atoms on the graphene layer (Figure 1.10b and c), thus resulting in outstanding mechanical strength with 1 TPa Young's modulus and 130.5 GPa intrinsic tensile strength.⁹¹ The conduction band and valence band meet at the Dirac point in monolayer graphene due to

Chapter 1

the half-filled π band (Figure 1.10d), making it a zero bandgap semiconductor or semimetal that permits electrons freely move with high mobility ($120,000 \text{ cm}^2/\text{Vs}$ at 240 K) that is higher than any other material.⁹² Although graphene shows outstanding optoelectronic features, its practical application in PV devices should be properly adjusted, as its overall properties are highly sensitive to the number of layers and quality of the crystal lattice.⁹³

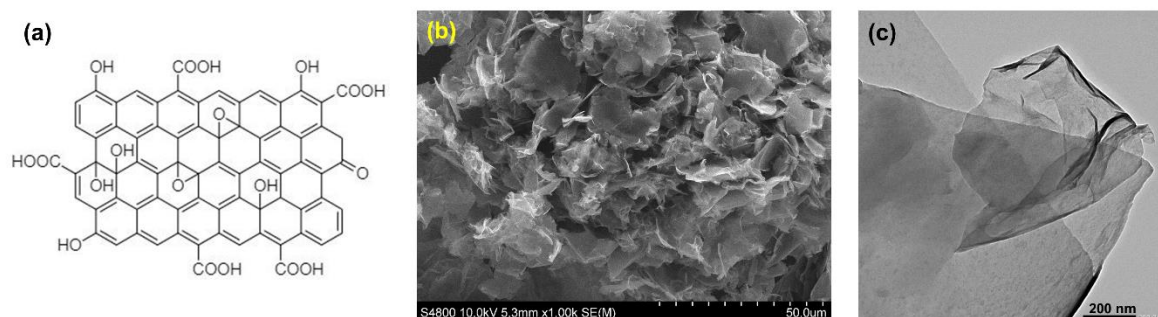


Figure 1. 11 (a) Structure of graphene oxide (GO), (b) Scanning electron microscopy image (SEM), and (b) transition electron microscopy image of reduced graphene oxide (rGO) flakes.

Chemically driven graphene derivatives such as graphene oxide (GO) and reduced graphene oxide (rGO), synthesized by modification of graphite oxide have shown promising results in PV applications, which further overcome the limitation of direct usage of graphene in solution-processed PSCs. Apart from a widely used solution-based intercalation, derivatives of free-standing GO can also be synthesized via covalent or non-covalent chemical functionalization, where each synthetic protocol creates a different GO with different properties.⁹³ The oxygenated functionalities attached to the interior aromatic domains in GO (Figure 1.10a) can be removed by direct reduction of GO using a reduction agent (e.g. hydrazine) or heat treatment, resulting in rGO with a restored π -network. The resulting rGO (Figure 1.11b and c) is physically and structurally more similar to graphene, however, the reduction efficiency controls the degree of π -network restoration with different properties.⁹⁴

1.10.2 Two-Dimensional Transition-Metal Dichalcogenides (2D TMDs)

2D layered transition-metal dichalcogenides (TMDs) consist of over 40 compounds, which are identified as sulfides, selenides, and tellurides with lamellar structures similar to that of graphene have been the subject of research in a growing number of fields including energy conversion, energy storage, catalysis, optics, biomedical, super-capacitors, and electromagnetic interference shielding applications.⁹⁵⁻⁹⁷ Monolayer 2D-TMDs, whose generalized formula is MX_2 , is a plane of transition metal atoms (M) covalently sandwiched

Chapter 1

by two planes of chalcogen atoms (X). Particularly, group 4B-7B transition metals predominantly form layered structures whereas group 8B-10B TMDs are generally found in non-layered structures (Figure 1.12).⁹⁵ The layered TMDs are stable against reactions with external species owing to their dangling bond-free structure and the termination of lone-pair electrons of the chalcogen atoms from the surfaces of the layers. The oxidation states of the transition metal and chalcogen atoms are +4 and -2, respectively in TMDs, in which the d orbital electrons vary between 0 to 6 depending on the group of transition metal.⁹⁸

The figure shows a periodic table with the following elements highlighted in blue (transition metals) and green (chalcogens):

Group	1	2	3	4	5	6	7	8	9	10	11	12	13	14	15	16	17	18
1	H																	He
2	Li	Be											B	C	N	O	F	Ne
3	Na	Mg											Al	Si	P	S	Cl	Ar
4	K	Ca	Sc	Ti	V	Cr	Mn	Fe	Co	Ni	Cu	Zn	Ga	Ge	As	Se	Br	Kr
5	Rb	Sr	Y	Zr	Nb	Mo	Tc	Ru	Rh	Pd	Ag	Cd	In	Sn	Sb	Te	I	Xe
6	Cs	Ba	La...Lu	Hf	Ta	W	Re	Os	Ir	Pt	Au	Hg	Tl	Pb	Bi	Po	At	Rn
7	Fr	Ra	Ac...Lr	Rf	Db	Sg	Bh	Hs	Mt	Ds	Rg	Cn	Uut	Uuq	Uup	Uuh	Uus	Uuo

A red arrow labeled MX_2 points to the transition metal groups 4, 5, 6, and 7, and the chalcogen elements S, Se, and Te.

Figure 1. 12 The transition metals and three chalcogen elements that form TMDs. Those predominantly forming in layered structures are highlighted in transition metal groups.

Unlike graphite, bulk TMDs consist variety of polymorphs with different stacking orders, most common polymorphs are identified as 1T, 2H, and 3R where the digits stand the number of MX_2 units in the unit cell while letters indicate for trigonal, hexagonal, and rhombohedral, respectively (Figure 1.13a).⁹⁵ In contrast to bulk TMDs, layered TMDs can exhibit a trigonal prismatic phase (2H) or an octahedral phase that is conventionally represented as 1T. In the case of monolayer MX_2 , the trigonal prismatic phase is indicated as 1H. 2H or 1H belongs to the D_{3h} point group with hexagonal symmetry (Figure 1.14a) corresponding to trigonal prismatic coordination of the transition metal atoms, where the chalcogen atoms are vertically aligned along the z-axis with AbA BaB stacking sequence (b and a indicate metal atoms while A and B indicate chalcogen atoms).^{95,98} In contrast, the 1T octahedral phase has a D_{3d} tetragonal symmetry (Figure 1.14b) with octahedral coordination in the transition metal atoms. In this geometry, the AbC stacking sequence can be recognized as one of the chalcogen atom layers

Chapter 1

is shifted compared to the others as shown in Figure 1.14b (A and C indicate chalcogen atoms while b represents transition metal atom).⁹⁸

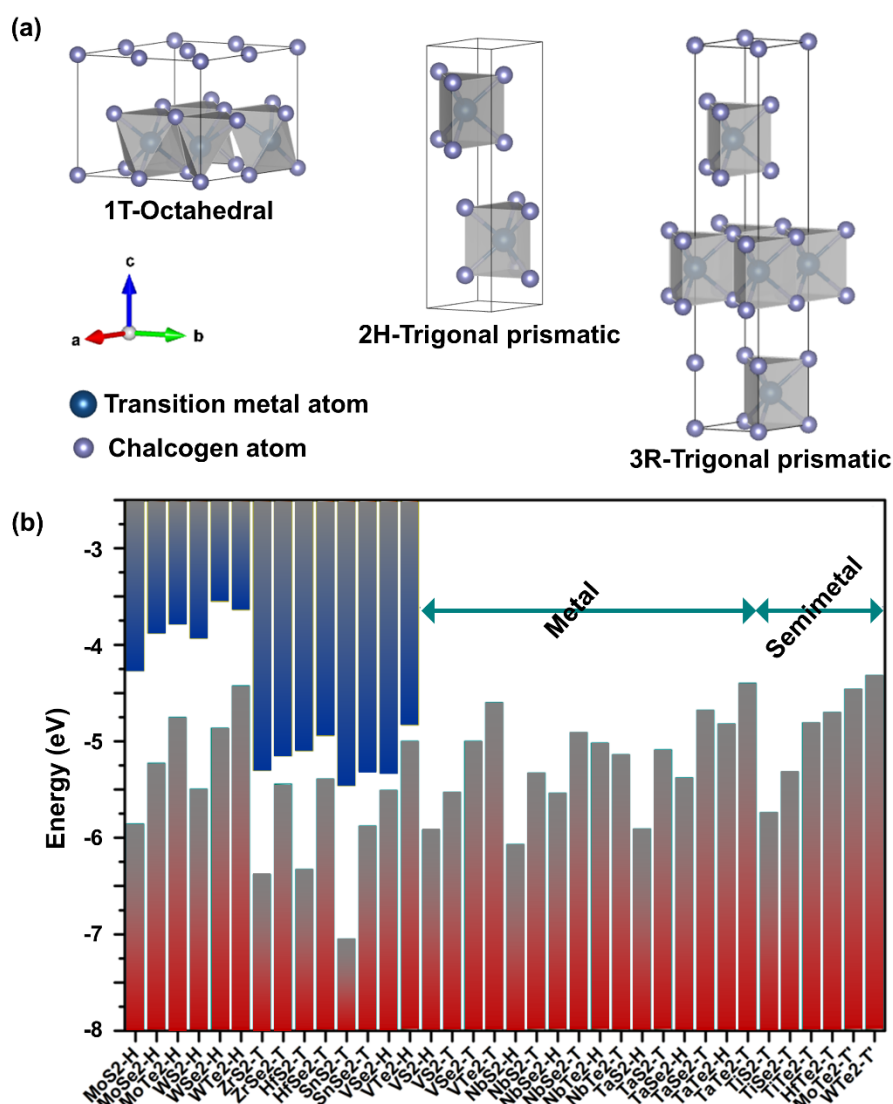


Figure 1. 13 (a) 1T (octahedral), 2H (trigonal prismatic), and 3R (trigonal prismatic) unit cell structures of MoS₂. (b) Band alignment of the monolayer TMDs (redrawn⁹⁹).

Disordered octahedral coordination is also possible in metal atoms, thus resulting in a disordered 1T phase commonly expressed as 1T' (trigonal-antiprismatic). In 2D-TMDs, one of the two possible coordination modes is thermodynamically stable while the other can often be metastable, which is primarily dependent on the *d*-electron count of the transition metal.^{95,100} For instance, under ambient conditions, 2D-TMDs that belong to group-4B that have *d*⁰ transition metal centers such as TiS₂ and ZrS₂ are thermodynamically stable in the octahedral 1T phase. Both 1T and 2H phases are seen in 2D-TMDs formed from group 5B elements,

Chapter 1

which have d^1 transition metal centers. In the case of 2D-TMDs formed from group-6B where the transition metal centers are d^2 such as MoS_2 and WS_2 usually show trigonal prismatic 2H phase.¹⁰¹

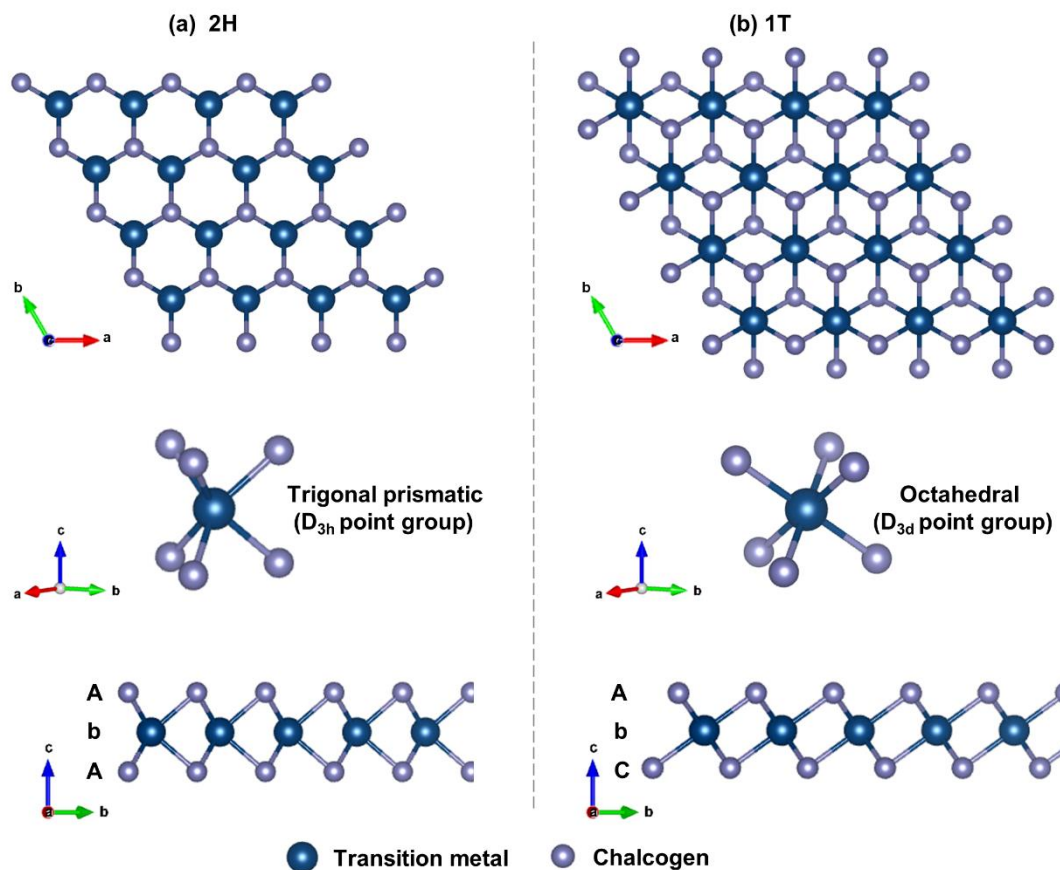


Figure 1. 14 Atomic model structures of 2D-TMDs, (a) 2H-trigonal prismatic phase, and (b) 1T-octahedral phase.

The ability to induce different phases in 2D-TMDs is predominantly controlled by the synthesis protocol. Among several synthesis techniques, alkali metal-based intercalation is well known for efficient mass production together with phase transition of 2D layered TMDs.^{96,102,103} The lithium intercalation of thermodynamically stable 2H- MoS_2 results in phase transformation to metastable 1T- MoS_2 . The aforementioned structural phase transition is attributed to the effective electron transfer from the valence s orbital of the alkali metal atoms to the d orbital of the transition metal center, resulting in increased electron counts on the transition metal d orbital with the density of states at the Fermi level.^{95,104} In the case of lithium intercalation of TaS_2 , the reverse scenario of 1T to 2H structural phase transition could be observed. However, alkali metal intercalation-assisted phase transition is partial and, thus results in a hybrid 2H-1T mixture.¹⁰⁵ It should be highlighted that the 2H (or 1H) phase is generally semiconducting

Chapter 1

whereas 1T is metallic (and 1T' is semimetal). Trigonal prismatic coordinated d orbital of transition metal in 2H-TMDs split into three groups; fully occupied d_{z^2} ; $d_{x^2-y^2,xy}$, and unoccupied $d_{xz,yz}$, rendering 2H phase semiconducting. Particularly, the octahedrally coordinated d orbital of transition metal in 1T-TMDs split into two groups; partially occupied $d_{xy,yz,xz}$, and unoccupied d_{z^2,x^2-y^2} , making the 1T phase metallic with high conductivity when compared with their 2H counterpart, and beneficial for many applications based on charge transfer processes.⁹⁶

1.10.3 NiO_x Nano Crystals

NiO_x is identified as a nonstoichiometric cubic rock-salt with the structure of octahedral Ni²⁺ and O²⁻ sites.¹⁰⁶ NiO_x is a wide bandgap p -type semiconductor with a VBM of ~ -5.21 eV. p -type semiconducting features in NiO_x originated from two positive charge compensation that favored Ni²⁺ vacancies.¹⁰⁷ The solution process method is a cost-effective technique to synthesize highly soluble well-crystallized NiO_x nanocrystals, which can directly be employed to make a thin film of NiO_x at low temperatures. Apart from using NiO_x as HTL in many planar PSCs with promising PV performances, the inclusion of NiO_x as interlayers has also been demonstrated to enhance the charge transfer kinetics at the interfaces, thus resulting in improved efficiency.

Chapter 1

Outline of the Thesis

This thesis targets to contribute to the field by addressing two objectives: i. understanding of interfacial photo-induced charge transfer dynamics, given its strong impact on the performance of hybrid organic-inorganic perovskite solar cells, and the role of low dimensional materials in interfacial engineering to enhance the device performances, and ii. escalating the device operational stability. The focus hereby lies in discovering the charge kinetics at the interfaces upon introduction of low dimensional materials, which ultimately influence the device overall performance and stability.

After laying out the basic concepts of PV and the introduction of low dimensional materials as an interfacial modification for the PSCs in **Chapter 1** followed by the experimental procedures in **Chapter 2**, the rest chapters have been gathered according to the experimental results in the following manner.

Chapter 3 describes the impact of the layered 2D-MoS₂ as an interfacial layer for the reliability enhancement of PSCs. This tendentious topic comprehensively addresses the preparation of 1T and 2H-phase predominant 2D-MoS₂, minimization of energetic mismatch between triplecation-perovskite and dopant-free PTAA (as HTM) based on 2D-MoS₂, which preliminary controls the charge build-up and possible non-radiative recombination at the interfaces and thus enhanced V_{oc} . We noted that the 2D-MoS₂ interfacial layer reduces the energy required for detrapping the trapped-charges, by providing prompt extraction of photo-generated charges while mitigating the interfacial charge recombination, thus enabling us to demonstrate 18.54% PCE from dopant-free PSC along with enhanced long-term operational stability.

Chapter 4 establishes the enhancement of PV performances and stability of PSCs upon 1T-rich WS₂, through preliminary stimulating the photo-induced charge transfer dynamics and suppressing the trap density at the interface of perovskite/HTM. The placement of the 2D-WS₂-based interface layer between the undoped-PTAA and the perovskite absorber reduces the trap density in the device by 25% with a saturation of photocurrent at a relatively low V_{eff} (0.3V), and thus the presented protocol enables to demonstrate over 19% stabilized PCE while paving the way toward reliability enhancement in PSCs approaching commercial viability.

Chapter 5 elaborates on the versatility of NiO_x nanocrystals in PSCs, particularly in low-temperature processable inverted architecture. We demonstrate an effective interface reform at

Chapter 1

NiO_x/perovskite by introducing an organic semiconductor (DTT-EHDI₂), which is composed of dithienothiophene (DTT) as the core and a planar triazatruxene incorporating an alkyl chain as the side group. Since the DTT-EHDI₂ is less wettable, it controls the nucleation sites in the perovskite and more room for larger grains to form during crystallization, which reduces the possibility of trap states and recombination pathways in the device. The origin of the boosted PCE was identified as the enhanced V_{oc} and FF by reducing the energy gap between the valence bands of the perovskite and NiO_x via the organic semiconductor layer.

Although inorganic NiO_x is quite stable by nature, a possible redox reaction at NiO_x/perovskite develops and promotes the degeneration of the active layer, which causes the devices to become unstable. In **Chapter 6**, a metal-free C₃N₄ 2D-polymeric material that has a highly stable tri-s-triazine architecture with a conjugated electronic structure was introduced at the interface of NiO_x/perovskite to enhance the stability of the perovskite. The novel interlayer enables greater enhancement in PV performances, delivering the PCE up to 19.3% with a negligible hysteresis by reducing non-radiative losses and faulty charge buildup at the NiO_x/perovskite interface.

In **Chapter 7**, the superior features of 2D-TiS₂ were studied in inverted PSCs. The 2D-TiS₂ had a higher effect on PV performance when paired with PC₆₀BM under ideal addition, resulting in an uplifted PCE of up to 17.95%. A higher capacity to extract electrons from the device is indicated by the inclusion of 2D-TiS₂, which results in a saturation of current density at a relatively low effective voltage while retaining a high fill factor. Beyond PCE, the operational-stability of the device was prolonged, opening the door to resolving the frequent instability noted in inverted PSCs.

The main achievements of the thesis together with the overall outlook are concluded in **Chapter 8**.

Chapter 1

BIBLIOGRAPHY

1. *BP Energy Outlook*, 2022 edition (Retrieved: September 2022).
2. *Global Energy Review 2021 – Analysis – IEA* (Retrieved: September 2022).
3. *Global energy transformation: A roadmap to 2050*, 2019 edition – IRENA (Retrieved: September 2022).
4. *Global Energy Perspective 2022*. McKinsey & Company (Retrieved: September 2022).
5. Archer, D. *Global Warming: Understanding the Forecast* (second edition), 2011, Wiley.
6. *Electricity Market Report - July 2022 – Analysis – IEA* (Retrieved: September 2022).
7. Becquerel, E. Mémoire sur les effets électriques produits sous l'influence des rayons solaires. *Comptes Rendus*, 1839, 9, 561-567.
8. Effect of light on Selenium during the passage of an electric current, *Nature*, 1873, 7(173), 303–303.
9. Grylls A. W. & Day R. E. The action of light on selenium. *Proc. R. Soc. Lond.*, 1877, 25, 113–117.
10. Smets, A., Jäger, K., Isabella, O., Swaaij, R. V., & Zeman, M. *Solar Energy: The Physics and Engineering of Photovoltaic Conversion, Technologies and Systems*. UIT Cambridge Ltd 2016.
11. Benda, V. *Photovoltaics: The Basics. A Comprehensive Guide to Solar Energy Systems*, 2018, 151–179.
12. Kasap, S. O., & Tannous, C. The pedagogy of the p-n junction: diffusion or drift? arXiv:physics/0306153.
13. Green, M. A. Accurate expressions for solar cell fill factors including series and shunt resistances. *Appl. Phys. Lett.*, 2016, 108(8), 081111.
14. *Photovoltaic devices - Part 3: Measurement principles for terrestrial photovoltaic (PV) solar devices with reference spectral irradiance data*. International Standard, IEC. (Retrieved: September 2022)
15. Hirst, L. C., & Ekins-Daukes, N. J. Fundamental losses in solar cells. *Prog. Photovolt.*, 2010, 19(3), 286–293.
16. Arefinia, Z. Modelling of intrinsic loss processes in the intermediate band solar cells. *Z Naturforsch A*, 2018, 74(1), 51–58.
17. Fermi E. *Thermodynamics*. Dover: New York, Dover Publications, New York, 1956, 29-45 ©1937.

Chapter 1

18. Landsberg, P. T., & Markvart, T. The carnot factor in solar-cell theory. *Solid State Electron.*, 1998, 42(4), 657–659.
19. Shockley, W., & Queisser, H. J. Detailed Balance Limit of Efficiency of p-n Junction Solar Cells. *J. Appl. Phys.*, 1961, 32(3), 510–519.
20. Rose G. De perowskite, fossili novo. In de novis quibusdam fossilibus quae in montibus uraliis inveniuntur. AG Schade: Berlin, 1839; pp 3–5.
21. Park, N.G, Grätzel, M., & Miyasaka, T. Organic-Inorganic Halide Perovskite Photovoltaics: From Fundamentals to Device Architectures (first edition), 2016, Springer.
22. Park, N. G. Perovskite solar cells: an emerging photovoltaic technology. *Mater. Today*, 2015, 18(2), 65–72.
23. Goldschmidt, V. M. Die Gesetze der Krystallochemie. *Die Naturwissenschaften*, 1926, 14(21), 477–485.
24. Li, W., Wang, Z., Deschler, F., Gao, S., Friend, R. H., & Cheetham, A. K. Chemically diverse and multifunctional hybrid organic–inorganic perovskites. *Nat. Rev. Mater.*, 2017, 2(3).
25. Green, M. A., Ho-Baillie, A., & Snaith, H. J. The emergence of perovskite solar cells. *Nat. Photonics*, 2014, 8(7), 506–514.
26. Akkerman, Q. A., & Manna, L. What defines a halide perovskite? *ACS Energy Lett.*, 2020, 5(2), 604–610.
27. Weber, D. $\text{CH}_3\text{NH}_3\text{PbX}_3$, ein Pb(II)-System mit kubischer Perowskitstruktur / $\text{CH}_3\text{NH}_3\text{PbX}_3$, a Pb(II)-System with Cubic Perovskite Structure. *Zeitschrift Für Naturforschung B*, 1978, 33(12), 1443–1445.
28. Helmut K., Stuart P. Handbook of magnetism and advanced magnetic materials (first edition 2007). Wiley-Interscience.
29. Mitzi, D. B. Synthesis, structure, and properties of organic-inorganic perovskites and related materials. *Prog. Inorg. Chem.* 1999, 48, 1–121.
30. Baikie, T., Barrow, N. S., Fang, Y., Keenan, P. J., Slater, P. R., Piltz, R. O., Gutmann, M., Mhaisalkar, S. G., & White, T. J. A combined single crystal neutron/X-ray diffraction and solid-state nuclear magnetic resonance study of the hybrid perovskites $\text{CH}_3\text{NH}_3\text{PbX}_3$ (X = I, Br and Cl). *J. Mater. Chem. A*, 2015, 3(17), 9298–9307.
31. Lee, J. H., Bristowe, N. C., Bristowe, P. D., & Cheetham, A. K. (2015). Role of hydrogen bonding and its interplay with octahedral tilting in $\text{CH}_3\text{NH}_3\text{PbI}_3$. *Chem Commun*, 2015, 51(29), 6434–6437.

Chapter 1

32. Ong, K. P., Goh, T. W., Xu, Q., & Huan, A. Mechanical origin of the structural phase transition in methylammonium lead iodide $\text{CH}_3\text{NH}_3\text{PbI}_3$. *J. Phys. Chem. Lett.*, 2015, 6(4), 681–685.
33. Brenner, T. M., Egger, D. A., Kronik, L., Hodes, G., & Cahen, D. Hybrid organic-inorganic perovskites: low-cost semiconductors with intriguing charge-transport properties. *Nat. Rev. Mater.*, 2016, 1(1).
34. Filip, M. R., Eperon, G. E., Snaith, H. J., & Giustino, F. Steric engineering of metal-halide perovskites with tunable optical band gaps. *Nat. Commun.*, 2014, 5(1).
35. Chen, Y., Yi, H. T., Wu, X., Haroldson, R., Gartstein, Y. N., Rodionov, Y. I., Tikhonov, K. S., Zakhidov, A., Zhu, X. Y., & Podzorov, V. Extended carrier lifetimes and diffusion in hybrid perovskites revealed by Hall effect and photoconductivity measurements. *Nat. Commun.*, 2016, 7(1).
36. W. Rehman, R.L. Milot, G.E. Eperon, C. Wehrenfennig, J.L. Boland, H.J. Snaith, M.B. Johnston, L.M. Herz Charge-carrier dynamics and mobilities in formamidinium lead mixed-halide perovskites. *Adv. Mater.*, 2015, 27, 7938-7944.
37. Kojima, A., Teshima, K., Shirai, Y., & Miyasaka, T. Organometal halide perovskites as visible-light sensitizers for photovoltaic cells. *J. Am. Chem. Soc.*, 2009, 131(17), 6050–6051.
38. Best research-cell efficiency chart. Photovoltaic research | NREL (Retrieved: September 2022).
39. Webb, T., Sweeney, S. J., & Zhang, W. Device architecture engineering: progress toward next generation perovskite solar cells. *Adv. Funct. Mater.*, 2021, 31(35), 2103121.
40. Li, Z., Klein, T. R., Kim, D. H., Yang, M., Berry, J. J., van Hest, M. F. A. M., & Zhu, K. Scalable fabrication of perovskite solar cells. *Nat. Rev. Mater.*, 2018, 3(4).
41. Soto-Montero, T., Soltanpoor, W., & Morales-Masis, M. Pressing challenges of halide perovskite thin film growth. *APL Mater.*, 2020, 8(11), 110903.
42. Bai, S., Wu, Z., Wu, X., Jin, Y., Zhao, N., Chen, Z., Mei, Q., Wang, X., Ye, Z., Song, T., Liu, R., Lee, S. T., & Sun, B. High-performance planar heterojunction perovskite solar cells: Preserving long charge carrier diffusion lengths and interfacial engineering. *Nano Res.*, 2014, 7(12), 1749–1758.
43. Lee, M. M., Teuscher, J., Miyasaka, T., Murakami, T. N., & Snaith, H. J., Efficient hybrid solar cells based on meso-superstructured organometal halide perovskites. *Science*, 2012, 338, 643-647.

Chapter 1

44. Xiao, M., Huang, F., Huang, W., Dkhissi, Y., Zhu, Y., Etheridge, J., Weale, A. G., Bach, U., Cheng, Y. B., Spiccia, L. A fast deposition-crystallization procedure for highly efficient lead iodide perovskite thin-film solar cells. *Angew Chem Int Ed Engl.*, 2014, 53, 9898–9903.
45. Lee, J. W., & Park, N. G. Two-step deposition method for high-efficiency perovskite solar cells. *MRS Bull.*, 2015, 40(8), 654–659.
46. Burschka, J., Pellet, N., Moon, S. J., Humphry-Baker, R., Gao, P., Nazeeruddin, M. K., & Grätzel, M. Sequential deposition as a route to high-performance perovskite-sensitized solar cells. *Nature*, 2013, 499(7458), 316–319.
47. Hu, W., Yang, S., & Yang, S. Surface Modification of TiO₂ for Perovskite Solar Cells. *Trends Chem.*, 2020, 2(2), 148–162.
48. Wu, P., Wang, S., Li, X., & Zhang, F. Advances in SnO₂-based perovskite solar cells: from preparation to photovoltaic applications. *J. Mater. Chem. A*, 2021, 9(35), 19554–19588.
49. Zhou, H., Chen, Q., Li, G., Luo, S., Song, T. B., Duan, H. S., Hong, Z., You, J., Liu, Y., & Yang, Y. Interface engineering of highly efficient perovskite solar cells. *Science*, 2014, 345(6196), 542–546.
50. Giordano, F., Abate, A., Correa Baena, J. P., Saliba, M., Matsui, T., Im, S. H., Zakeeruddin, S. M., Nazeeruddin, M. K., Hagfeldt, A., & Graetzel, M. Enhanced electronic properties in mesoporous TiO₂ via lithium doping for high-efficiency perovskite solar cells. *Nat. Commun.*, 2016, 7(1).
51. Pan, H., Zhao, X., Gong, X., Li, H., Ladi, N. H., Zhang, X. L., Huang, W., Ahmad, S., Ding, L., Shen, Y., Wang, M., & Fu, Y. Advances in design engineering and merits of electron transporting layers in perovskite solar cells. *Mater. Horiz.*, 2020, 7(9), 2276–2291.
52. Cho, A. N., Jang, I. H., Seo, J. Y., & Park, N. G. Dependence of hysteresis on the perovskite film thickness: inverse behavior between TiO₂ and PCBM in a normal planar structure. *J. Mater. Chem. A*, 2018, 6(37), 18206–18215.
53. Ke, W., Zhao, D., Xiao, C., Wang, C., Cimaroli, A. J., Grice, C. R., Yang, M., Li, Z., Jiang, C. S., Al-Jassim, M., Zhu, K., Kanatzidis, M. G., Fang, G., & Yan, Y. Cooperative tin oxide fullerene electron selective layers for high-performance planar perovskite solar cells. *J. Mater. Chem. A*, 2016, 4(37), 14276–14283.
54. Yu, Z., Yang, Z., Ni, Z., Shao, Y., Chen, B., Lin, Y., Wei, H., Yu, Z. J., Holman, Z., & Huang, J. Simplified interconnection structure based on C₆₀/SnO_{2-x} for all-perovskite tandem solar cells. *Nat. Energy*, 2020, 5(9), 657–665.

Chapter 1

55. Rombach, F. M., Haque, S. A., & Macdonald, T. J. Lessons learned from Spiro-OMeTAD and PTAA in perovskite solar cells. *Energy Environ. Sci.*, 2021, 14(10), 5161–5190.
56. Yaghoobi Nia, N., Lamanna, E., Zendejdel, M., Palma, A. L., Zurlo, F., Castriotta, L. A., & Di Carlo, A. Doping strategy for efficient and stable triple cation hybrid perovskite solar cells and module based on poly(3-hexylthiophene) hole transport layer. *Small*, 2019, 15(49), 1904399.
57. Jung, E. H., Jeon, N. J., Park, E. Y., Moon, C. S., Shin, T. J., Yang, T. Y., Noh, J. H., & Seo, J. Efficient, stable and scalable perovskite solar cells using poly(3-hexylthiophene). *Nature*, 2019, 567(7749), 511–515.
58. Xia, Y., & Dai, S. Review on applications of PEDOTs and PEDOT:PSS in perovskite solar cells. *J. Mater. Sci. Mater.*, 2020, 32(10), 12746–12757.
59. Han, W., Ren, G., Liu, J., Li, Z., Bao, H., Liu, C., & Guo, W. Recent progress of inverted perovskite solar cells with a modified PEDOT:PSS hole transport layer. *ACS Appl. Mater. Interfaces*, 2020, 12(44), 49297–49322.
60. Yu, Z., & Sun, L. Inorganic hole-transporting materials for perovskite solar cells. *Small Methods*, 2017, 2(2), 1700280.
61. Arul, N. S., & Nithya, V. D. Two-dimensional transition metal dichalcogenides: synthesis, properties, and applications. Springer Publishing, 2019.
62. Shao, H., Ladi, N. H., Pan, H., Zhang, X. L., Shen, Y., & Wang, M. 2D materials as electron transport layer for low-temperature solution-processed perovskite solar cells. *Solar RRL*, 2020, 5(3), 2000566.
63. You, P., Tang, G., & Yan, F. Two-dimensional materials in perovskite solar cells. *Mater.*, 2019, 11, 128–158.
64. Chen, T., Tong, G., Xu, E., Li, H., Li, P., Zhu, Z., Tang, J., Qi, Y., & Jiang, Y. Accelerating hole extraction by inserting 2D $\text{Ti}_3\text{C}_2\text{-MXene}$ interlayer to all inorganic perovskite solar cells with long-term stability. *J. Mater. Chem. A*, 2019, 7(36), 20597–20603.
65. Yang, L., Dall’Agnese, C., Dall’Agnese, Y., Chen, G., Gao, Y., Sanehira, Y., Jena, A. K., Wang, X., Gogotsi, Y., & Miyasaka, T. Surface-modified metallic $\text{Ti}_3\text{C}_2\text{T}_x$ MXene as electron transport layer for planar heterojunction perovskite solar cells. *Adv. Funct. Mater.*, 2019, 29(46), 1905694.
66. Yang, L., Kan, D., Dall’Agnese, C., Dall’Agnese, Y., Wang, B., Jena, A. K., Wei, Y., Chen, G., Wang, X. F., Gogotsi, Y., & Miyasaka, T. Performance improvement of MXene-based perovskite solar cells upon property transition from metallic to semiconductive by oxidation of $\text{Ti}_3\text{C}_2\text{T}_x$ in air. *J. Mater. Chem. A*, 2021, 9(8), 5016–5025.

Chapter 1

67. Shi, J., Li, Y., Li, Y., Li, D., Luo, Y., Wu, H., & Meng, Q. From ultrafast to ultraslow: charge-carrier dynamics of perovskite solar cells. *Joule*, 2018, 2(5), 879–901.
68. A. Marchioro, D. Friedrich, J. Moser, J. Teuscher, M. Kunst, M. Grätzel, R.V.D. Krol, T. Moehl, Unravelling the mechanism of photoinduced charge transfer processes in lead iodide perovskite solar cells, *Nat. Photonics*, 2014, 8, 250-255.
69. Hubbard, S. Photovoltaic solar energy: from fundamentals to applications, (first edition 2017, edited by Reinders, A., Verlinden, P., Sark, W., & Freundlich, A.). © 2017, John Wiley & Sons, Ltd.
70. Luo, D., Su, R., Zhang, W., Gong, Q., & Zhu, R. Minimizing non-radiative recombination losses in perovskite solar cells. *Nat. Rev. Mater.*, 2019, 5(1), 44–60.
71. Ball, J. M. & Petrozza, A. Defects in perovskite- halides and their effects in solar cells. *Nat. Energy*, 2016, 1, 16149.
72. Zhang, X., Shen, J., & Van de Walle, C. G. First-principles simulation of carrier recombination mechanisms in halide perovskites. *Adv. Energy Mater.*, 2019, 10(13), 1902830.
73. Sherkar, T. S., Momblona, C., Gil-Escrig, L., Ávila, J., Sessolo, M., Bolink, H. J., & Koster, L. J. A. Recombination in perovskite solar cells: significance of grain boundaries, interface traps, and defect ions. *ACS Energy Lett.*, 2017, 2(5), 1214–1222.
74. Wright, A. D., Verdi, C., Milot, R. L., Eperon, G. E., Pérez-Osorio, M. A., Snaith, H. J., Giustino, F., Johnston, M. B., & Herz, L. M. Electron–phonon coupling in hybrid lead halide perovskites. *Nat. Commun.*, 2016, 7(1).
75. Huang, J., Yuan, Y., Shao, Y. & Yan, Y. Understanding the physical properties of hybrid perovskites for photovoltaic applications. *Nat. Rev. Mater.*, 2017, 2, 17042.
76. Byrnavand, M. M., & Saliba, M. Defect passivation of perovskite films for highly efficient and stable solar cells. *Solar RRL*, 2021, 5(8), 2100295.
77. Zhang, D., Li, D., Hu, Y., Mei, A., & Han, H. Degradation pathways in perovskite solar cells and how to meet international standards. *Commun. Mater.*, 2022, 3(1).
78. Frost, J. M., Butler, K. T., Brivio, F., Hendon, C. H., van Schilfgaarde, M., & Walsh, A. Atomistic origins of high-performance in hybrid halide perovskite solar cells. *Nano Lett.*, 2014, 14(5), 2584–2590.
79. Bastos, J. P., Paetzold, U. W., Gehlhaar, R., Qiu, W., Cheyng, D., Surana, S., Spampinato, V., Aernouts, T., & Poortmans, J. Light-induced degradation of perovskite solar cells: the influence of 4-tert-butyl pyridine and gold. *Adv. Energy Mater.*, 2018, 8(23), 1800554.

Chapter 1

80. Yang, J., Liu, X., Zhang, Y., Zheng, X., He, X., Wang, H., Yue, F., Braun, S., Chen, J., Xu, J., Li, Y., Jin, Y., Tang, J., Duan, C., Fahlman, M., & Bao, Q. Comprehensive understanding of heat-induced degradation of triple-cation mixed halide perovskite for a robust solar cell. *Nano Energy*, 2018, 54, 218–226.
81. J. M. Azpiroz, E. Mosconi, J. Bisquert, and F. De Angelis, Defect migration in methylammonium lead iodide and its role in perovskite solar cell operation, *Energy Environ. Sci.*, 2015, 8(7), 2118–2127.
82. Rajagopal, A., Yao, K., & Jen, A. K. Toward perovskite solar cell commercialization: a perspective and research roadmap based on interfacial engineering. *Adv. Mater.*, 2018, 30(32), 1800455.
83. Shao, Y., Fang, Y., Li, T., Wang, Q., Dong, Q., Deng, Y., Yuan, Y., Wei, H., Wang, M., Gruverman, A., Shield, J., & Huang, J. Grain boundary dominated ion migration in polycrystalline organic–inorganic halide perovskite films. *Energy Environ. Sci.*, 2016, 9(5), 1752–1759.
84. Shao, S., & Loi, M. A. The role of the interfaces in perovskite solar cells. *Adv. Mater. Interfaces*, 2019, 7(1), 1901469.
85. Yang, Z., Babu, B. H., Wu, S., Liu, T., Fang, S., Xiong, Z., Han, L., & Chen, W. Review on practical interface engineering of perovskite solar cells: from efficiency to stability. *Solar RRL*, 2019, 4(2), 1900257.
86. Boyd, C. C., Checharoen, R., Leijtens, T., & McGehee, M. D. Understanding degradation mechanisms and improving stability of perovskite photovoltaics. *Chem. Rev.*, 2018, 119(5), 3418–3451.
87. Xiang, W., Liu, S. F., & Tress, W. Interfaces and interfacial layers in inorganic perovskite solar Cells. *Angew. Chem. Int. Ed.*, 2021, 60(51), 26440–26453.
88. Agresti, A., Pazniak, A., Pescetelli, S., Di Vito, A., Rossi, D., Pecchia, A., Auf der Maur, M., Liedl, A., Larciprete, R., Kuznetsov, D. V., Saranin, D., & Di Carlo, A. Titanium-carbide MXenes for work function and interface engineering in perovskite solar cells. *Nat. Mater.*, 2019, 18(11), 1228–1234.
89. Weiss, N. O., Zhou, H., Liao, L., Liu, Y., Jiang, S., Huang, Y., & Duan, X. Graphene: an emerging electronic material. *Adv. Mater.*, 2012, 24(43), 5782–5825.
90. Novoselov, K. S., Geim, A. K., Morozov, S. V., Jiang, D., Zhang, Y., Dubonos, S. V., Grigorieva, I. V., & Firsov, A. A. Electric field effect in atomically thin carbon films. *Science*, 2004, 306(5696), 666–669.

Chapter 1

91. Aoki, H., & Dresselhaus, S. M. Physics of graphene, Nano science and technology, 2014 edition, Springer.
92. Katsnelson, M. I., & Katsnel'son, M. I. The physics of graphene. Cambridge University Press, 2019.
93. Acik, M., & Darling, S. B. Graphene in perovskite solar cells: device design, characterization and implementation. *J. Mater. Chem. A*, 2016, 4(17), 6185–6235.
94. Mahmoudi, T., Wang, Y., & Hahn, Y. B. Graphene and its derivatives for solar cells application. *Nano Energy*, 2018, 47, 51–65.
95. Chhowalla, M., Shin, H. S., Eda, G., Li, L. J., Loh, K. P., & Zhang, H. The chemistry of two-dimensional layered transition metal dichalcogenide nanosheets. *Nat. Chem.*, 2013, 5(4), 263–275.
96. Chhowalla, M., Voiry, D., Yang, J., Shin, H. S., & Loh, K. P. Phase-engineered transition-metal dichalcogenides for energy and electronics. *MRS Bull.*, 2015, 40(7), 585–591.
97. Regan, E. C., Wang, D., Paik, E. Y., Zeng, Y., Zhang, L., Zhu, J., MacDonald, A. H., Deng, H., & Wang, F. Emerging exciton physics in transition metal dichalcogenide heterobilayers. *Nat. Rev. Mater.*, 2022.
98. Voiry, D., Mohite, A., & Chhowalla, M. Phase engineering of transition metal dichalcogenides. *Chem. Soc. Rev.*, 2015, 44(9), 2702–2712.
99. Zhang, C., Gong, C., Nie, Y., Min, K. A., Liang, C., Oh, Y. J., Zhang, H., Wang, W., Hong, S., Colombo, L., Wallace, R. M., & Cho, K. Systematic study of electronic structure and band alignment of monolayer transition metal dichalcogenides in Van der Waals heterostructures. *2d Mater.*, 2016, 4(1), 015026.
100. Manzeli, S., Ovchinnikov, D., Pasquier, D., Yazyev, O. V., & Kis, A. 2D transition metal dichalcogenides. *Nat. Rev. Mater.*, 2017, 2(8).
101. Sokolikova, M. S., & Mattevi, C. Direct synthesis of metastable phases of 2D transition metal dichalcogenides. *Chem. Soc. Rev.*, 2020, 49(12), 3952–3980.
102. Starnberg, H. I. Recent developments in alkali metal intercalation of layered transition metal dichalcogenides. *Mod. Phys. Lett. B*, 2000, 14(13), 455–471.
103. Fan, S., Zou, X., Du, H., Gan, L., Xu, C., Lv, W., He, Y. B., Yang, Q. H., Kang, F., & Li, J. Theoretical investigation of the intercalation chemistry of lithium/sodium ions in transition metal dichalcogenides. *J. Phys. Chem. C*, 2017, 121(25), 13599–13605.
104. Heising, J., & Kanatzidis, M. G. Structure of restacked MoS₂ and WS₂ elucidated by electron crystallography, *J. Am. Chem. Soc.*, 1999, 121, 638–643.

Chapter 1

105. Ganal, P., Olberding, W. & Butz, T. Soft chemistry induced host metal coordination change from octahedral to trigonal prismatic 1T-TaS₂. *Solid State Ion.*, 1993, 59, 313–319.
106. Jiang, F., Choy, W. C. H., Li, X., Zhang, D., & Cheng, J. Post-treatment-free solution-processed non-stoichiometric NiO_x nanoparticles for efficient hole-transport layers of organic optoelectronic devices. *Adv. Mater.*, 2015, 27(18), 2930–2937.
107. Chen, W., Zhou, Y., Wang, L., Wu, Y., Tu, B., Yu, B., Liu, F., Tam, H. W., Wang, G., Djurišić, A. B., Huang, L., & He, Z. Molecule-Doped Nickel Oxide: Verified Charge Transfer and Planar Inverted Mixed Cation Perovskite Solar Cell. *Adv. Mater.*, 2018, 30(20), 1800515.

CHAPTER 2

METHODS

The present section contains the experimental setup of synthesizing low-dimensional materials, experimental methodology for device fabrications, thin film characterization, and device characterizations.

2.1 Low-Dimensional Materials Synthesis

2.1.1 Graphene Oxide (GO)

GO was prepared using a modification of Hummers' method. At first 0.225 g of graphite powder was mixed with 30 mL of H₂SO₄/H₃PO₄ (27:3 V/V %) under vigorous stirring. The obtained dark green solution was placed in an ice bath and 1.35 g of KMnO₄ was added slowly while stirring (Figure 2.1 b). Once mixed, the temperature was elevated to 35 °C and the stirring was continued overnight, turning the color of the solution from dark green to dark brown. 30 mL of deionized (DI) water was added, followed by the controlled addition of 2 mL of 30% H₂O₂. The obtained yellowish warm solution (Figure 2.1 c) was centrifuged to remove the excess acid followed by washing with DI water through ultracentrifugation several times until the pH reached 6. The resultant sediment was redispersed in DI water using mild sonication to obtain exfoliated GO or was dried overnight in an oven to obtain GO powder..

2.1.2 Reduced Graphene Oxide (rGO)

The reduction of GO was performed using L-ascorbic acid (C₆H₈O₆). 250 mg of L-ascorbic acid was added to a GO dispersion (50 mg of GO in 250 mL of DI water) followed by vigorous stirring at 60 °C for 1h. The black sediment was collected and centrifuged at 5000 rpm for 15 min. The supernatant was discarded and the sediment was washed another three times with DI water. The resultant sediment was vacuum dried at 80 °C in an oven overnight to obtain rGO. Alternatively, the reduction of GO powder was done under vacuum annealing at 200 °C.

2.1.3 2D-Transition Metal Dichalcogenides (2D-TMDs)

2.1.3.1 Liquid Phase Exfoliation: 100 mg of bulk TMD was dissolved in 30 mL of isopropanol/ethanol (70:30 V/V %) or NMP (N-Methyl-2-pyrrolidone) and the resultant solution was ultrasonicated for 8 h at 15 °C controlled by a chiller. The resultant solution was centrifuged for 30 min at 3000 rpm, to separate unexfoliated flakes from exfoliated flakes and

Chapter 2

the supernatant was collected. The centrifugation was repeated for the supernatant obtained in each step 3 times. The final supernatant was centrifuged at 8000 rpm for 30 min and the residual was collected. The residual was dispersed in isopropanol to obtain the desired concentration.

2.1.3.2 Alkali Metal Intercalation: The intercalation of bulk TMDs was performed using a butyl lithium/hexane (BuLi) solution. For instance, 5 mL of BuLi was added to 200 mg bulk MoS₂ followed by magnetically stirring for 24 h and then ultra-sonication for 2 h. The resultant solution was left to stabilize and the upper solution was discarded. Excess BuLi was washed out by dilution with hexane. The residual was dispersed in 10 mL of isopropanol (IPA) and was ultrasonicated for 2 h. The resultant solution was centrifuged at 8000 rpm for 15 min to remove excess lithium ions by discarding the supernatant. The aforementioned ultrasonication/centrifugation process was repeated two times and the obtained residual was dispersed in isopropanol. The solution was further centrifuged at 2000 rpm for 20 min and 80% of the upper supernatant was collected. The concentration of the final solution was adjusted to about 0.3 mg/ml by evaporation at room temperature.

2.1.4 NiO_x Nanocrystals (NCs)

25 mmol Ni(NO₃)₂·6H₂O was dissolved in 50 mL of deionized (DI) water to obtain a dark green solution. The basic pH was maintained with a dropwise addition of NaOH (10 mol L⁻¹) while being stirred for 30 min. The obtained colloidal precipitation was thoroughly washed with DI water several times via ultracentrifugation followed by drying at 90 °C overnight under vacuum conditions. The obtained green powder was calcined for 2 h at 275 °C to obtain a dark-black powder. 15 mg mL⁻¹ NiO_x nanocrystal ink was prepared by dispersing the as-synthesized NiO_x NCs in DI water. The obtained solution was ultrasonicated at 45 °C for 1 h and filtered using a 0.22 μm nylon filter.

2.2 Perovskite Precursor Synthesis

The different perovskite films were achieved through a two-step spinning program using the following precursor solutions. In the case of MAPbI₃ film, the program was set with 1000 and 4000 rpm for 10 and 30 s, respectively. In all other cases, the program was maintained at 1000 and 6000 rpm for 10 and 30 s, respectively. 112 μL of CB (chlorobenzene, 99%) was dripped on the rotating substrates in the last 10 s before ending the program followed by annealing at 100 °C for 1 h.

Chapter 2

2.2.1 MAPbI₃

Equimolar amounts (1.2 M) of MAI and PbI₂ were dissolved in 1 mL of anhydrous DMSO (dimethyl sulfoxide 99.8%) solvent at 60 °C for overnight to obtain a MAPbI₃ precursor.

2.2.2 (FAPbI₃)_{0.85}(MAPbBr₃)_{0.15}

FAI (1 M), PbI₂ (1.2 M), MABr (0.2 M), and PbBr₂ (0.2 M) were dissolved in 1 mL anhydrous DMF (N, N-dimethylformamide, 99.8%):DMSO 4:1 (v/v) at 60 °C for overnight.

2.2.3 Cs_{0.1}(FA_{0.9}MA_{0.1})_{0.9}Pb(I_{0.9}Br_{0.1})₃

A triple-cation perovskite precursor (CsFAMA) was prepared by mixing CsI (0.1 M), FAI (1.05 M), PbI₂ (1.24 M), MABr (0.12 M), and PbBr₂ (0.12 M) in an anhydrous solvent mixture of DMF and DMSO with a 4:1 (v/v) at 60 °C for overnight.

2.2.4 Rb_{0.05}[(FA_{0.83}MA_{0.17})]_{0.95}Pb(I_{0.83}Br_{0.17})₃

The quadruple-cation perovskite (RbCsFAMA) precursor was prepared using FAI (1 M), PbI₂ (1.1 M), MABr (0.2 M), and PbBr₂ (0.22 M) in 1 mL of an anhydrous solvent mixture of DMF and DMSO with 4:1 (v/v) at 60 °C for overnight. 42 μL of 1.5M CsI in DMF/DMSO (4:1 v/v) and 42 μL of 1.5M RbI in DMF:DMSO (4:1 v/v) were added to the above solution and stirred for 1 h.

2.3 Device Fabrication

Device fabrication was started with the cleaning process of substrates. TCO-coated glass substrates (laser-etched FTO-TEC15, FTO-NSG10, or ITO) were sequentially cleaned by sonication using Hellmanex II (2 vol%) solution, deionized water, ethanol, acetone, and isopropanol for 20 min each followed by air drying using compressed airflow. The substrates were further treated with UV–ozone for 30 min before use.

2.3.1 *n-i-p* planar PSCs

TiO₂ compact layer was deposited on pre-cleaned substrates by spray pyrolysis at 500 °C using 1mL of titanium diisopropoxide bis(acetylacetonate) precursor solution (75 % in 2-propanol) in 19 mL of pure ethanol employing oxygen as carrier gas followed by continuous annealing at 500 °C for another 30 min to acquire anatase phase. Once the films acquired room temperature, they were treated with UV-ozone for another 30 min. SnO₂ quantum dot (QD)

Chapter 2

solution was spin-coated on the TiO₂ compact layer at 500 rpm for 5 s and 5000 rpm for 35 s followed by annealing at 200 °C for 1 h under atmospheric conditions. UV-ozone treatment was conducted for the ETL deposited substrates at room temperature for 30 min [3:1 mass ratio of SnCl₂·2H₂O and CH₄N₂S were dissolved in 30 ml of deionized water under vigorous stirring for 48 h at room temperature to obtain a clear yellow color solution. The obtained SnO₂ QD solution was filtered 3 times using 0.45 μm PTFE filters before use]. The samples were transferred to the Argon-filled glovebox under moisture and oxygen-controlled conditions (H₂O level: <1 ppm and O₂ level: <10 ppm). The perovskite precursor solution was spin-coated on the as-prepared ETL in a two-step spin-coating program as described in the 2.2 section. The films were annealed at 100 °C for 1 h for perovskite crystallization. The HTL was spin-coated using, i.e. i. pristine PTAA (10 mg in toluene) at 3000 rpm for 35 s or ii. Spiro-OMeTAD [70mM, dissolving the desired amount of material in 1mL CB together with 38.4 μL of 4-tert-butylpyridine and 21.1 μL of bis(trifluoromethylsulfonyl)imide lithium salt (520 mg in 1 mL acetonitrile)] at 4000 rpm for 20 s. The devices were completed by evaporating Au (80 nm, <1 Å/s) in an evaporator with vacuum conditions below 2×10⁻⁶ Torr.

In Chapter 3, the interface modification was adapted with 2D-MoS₂ in between triple-cation (CsFAMA) perovskite and pristine PTAA (a detailed description is available in Chapter 3). In Chapter 4, the interface modification was adapted with 2D-WS₂ in between CsFAMA perovskite and pristine PTAA (a detailed description is available in Chapter 4).

2.3.2 *n-i-p* mesoporous PSCs

TiO₂ compact layer was deposited as described in section 2.3.1. Once the substrates were cooled down to room temperature, they were treated with UV-ozone. TiO₂ mesoporous layer (1:8 w/v in ethanol) was spin-coated at 4000 rpm (2000 rpm/s acceleration) for 30 s, followed by progressive heating steps until 500 °C for 30 min. After cooling down the samples were treated with UV-ozone for 30 min. The samples were transferred to the Argon-filled glovebox under moisture and oxygen-controlled conditions (H₂O level: <1 ppm and O₂ level: <10 ppm). The perovskite precursor solution was spin-coated on the mesoporous TiO₂ in a two-step spin-coating program as described in the 2.2 section. HTL was deposited on the perovskite film at room temperature as mentioned in section 2.3.2. In the case of doped PTAA, 10 mg of PTAA in 1mL toluene together with 4 μL of 4-tert-butylpyridine and 10 μL of bis(trifluoromethylsulfonyl)imide lithium salt (170 mg in 1 mL acetonitrile) was dissolved. A

Chapter 2

similar condition could be applicable to the P3HT-based HTL. 80 nm of Au layer was thermally evaporated under a pressure of 2×10^{-6} Torr.

2.3.3 *p-i-n* planar PSCs

The HTL was deposited on the pre-cleaned substrates via spin coating. In the case of PTAA and P3HT, 2 mg was used in 1 mL toluene in its pristine form. Regarding PEDOT:PSS, the spin coating was done at 5000 rpm for 30 s followed by annealing at 140 °C for 30 min. If the HTM is NiO_x, NiO_x nanocrystal solution (15-20 mg in 1mL DI water) was deposited atop FTO substrates by spin coating at 4000 rpm for 35 s with 2000 rpm/s acceleration, followed by annealing at 150 °C for 30 min. The perovskite film was grown according to sections 2.2, 2.3.1, and 2.3.2. The electron transport layer was fabricated by spin-coating a 15 mg/ml PCBM in CB at room temperature atop the perovskite film at 1000 rpm (500 rpm/s) for 20 s followed by annealing for 5 min at 60 °C. A thin layer of BCP (bathocuproine, 0.5mg/ml in IPA) was deposited atop PCBM by spin-coating at 5000 rpm for 40 s. The solar cell fabrication was finished by evaporating Ag (100 nm, $<1 \text{ \AA/s}$) under low vacuum conditions (10^{-6} Torr).

In Chapter 5, interface layers were introduced in the interface between NiO_x and CsFAMA, which has been described in Chapter 5. Interface modification was conducted using PCBM blended with 2D-TiS₂ in an inverted PSC in Chapter 6 and the complete device fabrication process is available in the corresponding chapters.

2.4 Device Characterization

Current density-voltage (*J-V*) curves were performed using air-mass (AM) simulated 1.5G sunlight at 100 mWcm^{-2} (Newport, AAA Oriel solar simulator calibrated using silicon reference cell). The generated photocurrent was recorded using Keithley 2400 source meter with a scan rate of 100 mV/s (pre-sweep delay: 10s). Active area of the device was adjusted to 0.09 cm^2 using a laser-cut black metal mask over the active area of the device. A 150 W xenon lamp attached to a Bentham PVE300 motorized 1/4m monochromator was used to record the incident photon-to-current efficiency (IPCE) measurements (the system was calibrated with the standard silicon reference spectrum before the measurements). Temperature-dependent capacitance-frequency measurements were performed with LCR meter model No. E4980A along with a Linkam (LTS420) sample heating control system filled with nitrogen in a closed environment. BioLogic SP-300 impedance analyzer conducted the electrochemical impedance spectroscopy and the data were fitted with EC-Lab software. Impedance spectroscopy was

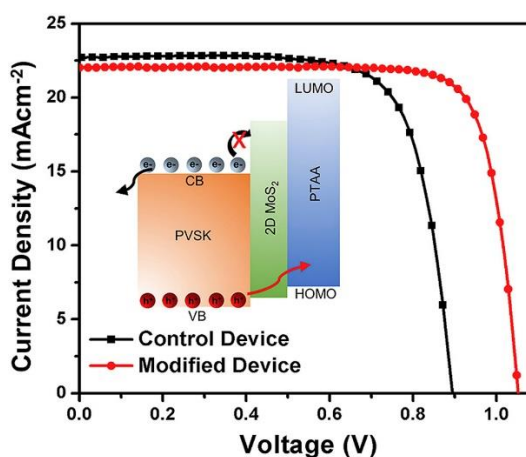
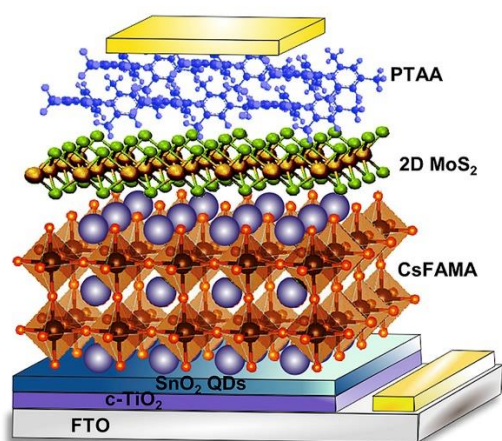
Chapter 2

performed using Biologic SP300 potentiostat in the frequency range of 2 MHz–1 Hz under the perturbation of a 20 mV ac (white LED to provide illumination conditions) in a faradaic chamber. Temperature-dependent capacitance–frequency (admittance spectroscopy) measurements were performed with an LCR meter model No. E4980A along with a Linkam (LTS420) sample heating control system attached to liquid nitrogen in a closed environment together with the temperature-controllable LabVIEW (NI) program. The J - V characteristics under dark conditions were performed using a Keithley 2400 source meter adjusted to a 100 mV/s scan rate.

Materials and thin film characterization techniques could be found in the relevant chapters accordingly.

CHAPTER 3

MITIGATION OF TRAP DENSITY AND INTERFACIAL LOSSES BY INTRODUCING A TWO-DIMENSIONAL MOLYBDENUM DISULFIDE INTERFACE LAYER IN PEROVSKITE SOLAR CELLS



This chapter has been published in *Nano Energy* entitled:

Reduced trap density and mitigating the interfacial losses by placing 2D dichalcogenide material at perovskite/HTM interface in a dopant free perovskite solar cells

Naveen Harindu Hemasiri, Samrana Kazim, Shahzada Ahmad

N.H. Hemasiri et. al., *Nano Energy*, **2020**, 77, 105292.

doi.org/10.1016/j.nanoen.2020.105292

Chapter 3

3.1 Abstract

Solution-processed photovoltaics employing perovskite as a light harvester is the next-generation future energy source owing to its low manufacturing cost and potential to achieve high power conversion efficiency. Significant emphasis has been laid on performance-related investigations, however, the long-term instability under operational conditions and device reproducibility obstruct its potential commercial endeavor. By inserting a thin layer of two-dimensional (2D) MoS₂, which is predominantly in 1T phase, energy level alignment between the pristine poly(triarylamine)-based hole transport layer, and perovskite is realized, thus resulting in suppressed interfacial charge accumulation, fast charge extraction, and subsequently improved photovoltaic performances. A power conversion efficiency of 18.54% with significantly upgraded open-circuit voltage (V_{oc}) and fill factor (FF) was achieved. The stability measurement shows that the resulting 2D-MoS₂ supported dopant-free hole transport layer exhibit notable moisture stability under ambient conditions. Our study put forward the profound experimental understanding of 1T-phase predominant 2D-MoS₂ as an agent for engineering the interface, enlightening the power conversion efficiency and a lifetime of the perovskite solar cells.

3.2 Introduction

In thin film photovoltaics (PV), halide perovskite solar cells (PSCs) have shown astonishing development with an unprecedented rise in power conversion efficiency (PCE) from 3.8% to 25.2% within a decade, signaling as cost-effective renewable PV technology.^{1,2} Despite the tremendous progress in the PCE of PSCs, the issue of intrinsic device stability, mainly induced by light irradiation, ionic migration, moisture corrosion, and oxygen infiltration under prolonged operational conditions hinders their potential commercialization.³ Further, hysteresis in the current density-voltage (J - V) curve in devices due to charge traps of the active layer needs to be rationally addressed for the unification of device performance.^{3,4} The open circuit voltage (V_{oc}) of the devices can easily diminish with a lack of charge-density build-up and pulling down the quasi-Fermi level splitting due to non-radiative carrier recombination centers that arise from electronic trap states through crystallographic defects and higher-dimensional defects such as grain boundaries.^{5,6} Furthermore, these defect sites facilitate nucleating sites for degradation, which annihilate the operation lifetime of the solar cells.^{5,7} Even though numerous endeavors have been directed towards the development of materials to passivate specific defects, most of the additives militate against PCE enhancement.^{6,8} On the

Chapter 3

other hand, photo-generated carriers should be extracted efficiently to avoid the generation of new defects as the active layer i.e. perovskite associated with the low defect formation energy.⁶ The extrinsic environmental condition, i.e., light intensity, electric field, and temperature during device operation can promote the natal local defects towards the degradation of the active layer, thus it is paramount to extract the untrapped and detrapped carriers promptly to militate charge accumulation and recombination.^{6,9,10} The apparent *J-V* hysteresis and poor stability originate not only from the defective active layer and disordered charge transport, but also from perovskite/charge transport layer (CTL) interfaces, and charge extracting materials.^{4,11,12} The interface between the hole transport material (HTM) and the perovskite remains the vulnerable part of the device for stability as trapped charges at the interface between perovskite and the charge extraction layer are responsible for the irreversible degradation caused by moisture.^{11,12} In particular, commonly used organic HTMs, for example, poly(3,4-ethylenedioxythiophene), 2, 2', 7,7' -tetrakis(N,N-di-4-methoxyphenylamine)-9,9' -spirobifluorene (Spiro-OMeTAD), or poly(triarylamine) (PTAA), shows insufficient charge carrier mobility in their pristine form. Doping is a prerequisite and hygroscopic materials are mostly used as a dopant to obtain excellent PV properties.^{3,13,14} The usage of such dopants further accelerates the degradation of the HTM layer and subsequently the perovskite layer.^{3,13,14} To overcome such challenges, strategies have been pointed to improve the stability of the PSCs including rational designing of the transport layer, interface modifications, and eliminating the moisture infiltration into the active layer by the coating of polymers, hydrophobic materials and carbon-based materials, most of these approaches is a trade-off with device PV performance.

Two-dimensional (2D) transition metal dichalcogenides (TMDs), especially MoS₂, owing to its unique optoelectronic properties including fast transport of the charges in the vertical direction and chemical inertness with high electron mobility and fewer traps make it a potential candidate to replace conventional CTLs.¹⁵ Kim et al. first introduced chemical vapour deposition grown MoS₂ in inverted PSCs followed by Huang et al. report on solution-processed MoS₂ to substitute PEDOT:PSS and measured 14% PCE.¹⁶ Further, Li et al. noted that the percentage of metallic octahedral 1T phase decreases with the post-heating due to phase transformation from 1T to 2H, and the reduction of the 1T phase in 2D-MoS₂ influences the PV performances to a large extent. The authors reported enhanced PCE with 1T-rich 2D-MoS₂ as compared to the 1T-poor 2D-MoS₂ as HTL in *p-i-n* type PSCs from 7.64 to 13.62%.¹⁶ Recently, Singh et al. demonstrated 2D-MoS₂ as ETL in PSCs and reported 13% PCE,

Chapter 3

indicating the bottleneck of employing 2D-MoS₂ as individual CTL is not competitive in terms of PCE due to interfacial energy loss via deep ionization levels associated with the 2D-TMDs, despite the excellent stability.^{17,18} Interface engineering utilizing 2D materials has demonstrated promising results in the terms of stability and PCE enhancement. Kakavelakis and co-workers employed solution-based MoS₂ as a hole extraction interlayer with PTAA in inverted PSCs with improved stability and PCE.¹³ However, the elucidation of the functioning and operating mechanisms of the 2D-MoS₂ as an interfacial layer in PSCs are limited and obscure. In the present work, we demonstrate the use of intercalated Li⁺ based solution-processable 2D-MoS₂ flakes as hole extraction interlayer in *n-i-p* type PSCs using triple-cation perovskite [Cs_{0.1}(FA_{0.9}MA_{0.1})_{0.9}Pb(I_{0.9}Br_{0.1})₃] and dopant-free PTAA to improve optoelectronic properties and operation stability. The fabricated device gave an improved PCE of 18.54% and a lifetime as compared to the controlled device without MoS₂ interlayer (15.05% PCE). The improvement is ascribed to the efficient hole extraction with the stabilization of the perovskite/HTM interface, band alignment, and mitigating the degradation in the active layer.

3.3 Results and Discussion

3.3.1 2D-MoS₂ Characterization

The stable 2D-MoS₂ sheets consist of a mixture of two distinct phases; prismatic 2H and octahedral 1T in isopropanol (IPA) were achieved from bulk MoS₂ by Li⁺ intercalation assisted liquid-phase exfoliation (LPE). This enables to exfoliate TMDs into a few layers or in some cases, a monolayer. The buried van der Waals forces in between MoS₂ are attributed to the hydrodynamic shear-force associated with the ultrasonication steps in the LPE process. Figure 3.1a depicts the UV-Vis absorption spectra of the spin-coated 2D-MoS₂ on a quartz substrate. The two shoulder peaks, located at c.a 675 and 625 nm show direct excitonic transitions between the split valance band and the minima of the conduction band at the K-point of the Brillouin zone of layered MoS₂ structure due to the formation of 1T-phase.^{5,13,19,20} Similar absorption features were noted from the 2D-MoS₂ solution in isopropanol (Figure A3.1a, Appendix A). The photoluminescence (PL) peaks at about 680 and 630 nm correspond to the upper (A, 1.82 eV) and lower (B, 1.96 eV) direct-gap optical transitions respectively (inset of Figure 3.1a).²¹⁻²³ The thickness of the MoS₂ flakes was calculated by atomic force microscopy (AFM) imaging (Figure 3.1b). The inset represents the thickness profile and the thickness of the flakes was 5 nm. Transmission electron microscopy (TEM) experiments were carried out

Chapter 3

to further investigate the as-prepared 2D-MoS₂, which confirmed the existence of a 2D layered structure of the exfoliated MoS₂ having an average flake size of 300 nm (Figure A3.1b). The large scan area of the AFM topography image further suggests the thickness of 2D-MoS₂ (Figure A3.2).

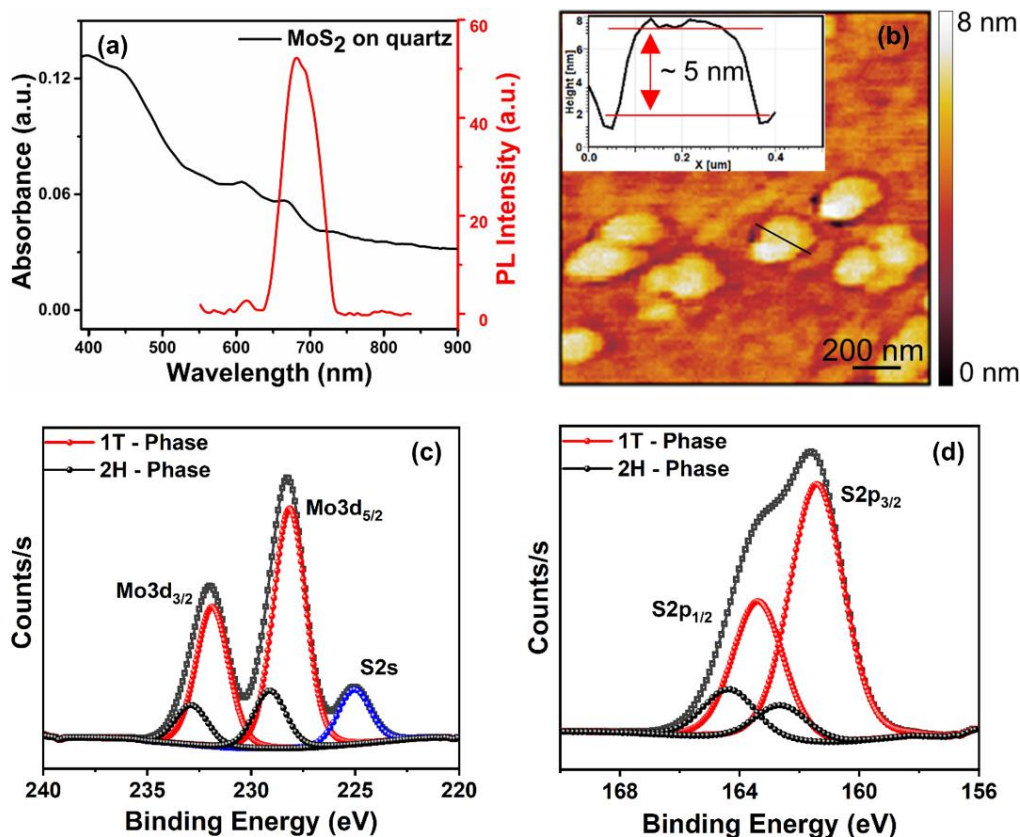


Figure 3. 1 (a) UV–Vis absorbance and photoluminescence spectra of spin coated 2D-MoS₂ on quartz substrate. (b) AFM topography of drop casted MoS₂ thin film on Si substrate, inset shows the thickness profile. XPS narrow spectrum of (c) Mo3d and (d) S2p of spin coated MoS₂ thin film.

We found that the as-prepared 2D-MoS₂ is predominantly in the metallic 1T phase, achieving 78.3%, which was quantitatively investigated from the X-ray photoelectron spectroscopy (XPS) measurements (Figure 3.1c and d). Two identical deconvoluted peaks that appeared at 231.85 and 228.15 eV are assigned to the Mo3d_{3/2} and Mo3d_{5/2} of 1T phase respectively. The Mo3d_{3/2} and Mo3d_{5/2} two peaks relevant to the 1T phase show 1.05 and 0.95 eV differences towards the lower binding energy concerning its 2H phase respectively. The absence of peaks at 236 and 233 eV suggests the synthesized 2D-MoS₂ is free of Mo oxidized phases derived through Li⁺ assisted liquid phase exfoliation process.²⁴ The associated 1T phase corresponding to the binding energy of S2p_{1/2} and S2p_{3/2} reached 163.41 and 161.41 eV respectively (Figure

Chapter 3

3.1d). To evaluate the PV performance upon different phases of 2D-MoS₂ on the PV, 2H-predominant 2D-MoS₂ was synthesized through liquid exfoliation with the absence of alkali metal intercalation.²⁵ The contribution of the 2H phase in synthesized 2D-MoS₂ via the aforementioned method was 81.69% and we noted 232.08 and 229.28 eV binding energies corresponding to Mo3d_{3/2} and Mo3d_{5/2} of the 2H phase respectively (Figure A3.3). A thermodynamically unstable 1T-MoS₂ where Mo atoms arranged in an octahedral manner, consisting of better conduction properties than its counterpart (2H-MoS₂) can undergo phase transformation back to the initial 2H phase under moderate temperature, thus, we managed to avoid the post-heating process of the MoS₂ layer during device fabrication.^{16,18,26,27} Li et al. investigated the charge carrier extraction using PL spectroscopy, 1T rich MoS₂ shows excellent charge carrier extraction from perovskite due to high conductivity associated with 1T phase as compared to the 2H phase, and resulted in improved PV properties.¹⁶

3.3.2 SnO₂ QDs ETL

For the electron selective layer, stable water-soluble colloidal SnO₂-QDs (quantum dots, Figure A3.4a) were synthesized and used as n-type selective contact atop of compact thin blocking layer to improve the hole-blocking properties associated with SnO₂.^{28,29} The scanning electron microscopy (SEM) images of SnO₂-QD layer on compact TiO₂ (Figure 3.2a and b) reveals the formation of uniform, continuous and pinholes free SnO₂ layer. The smooth layer facilitates effective electron transportation and builds a favorable interface for high-quality perovskite deposition. Figure 3.2c depicts the perovskite film grown on SnO₂-QDs exhibiting an average grain size of 315 nm.

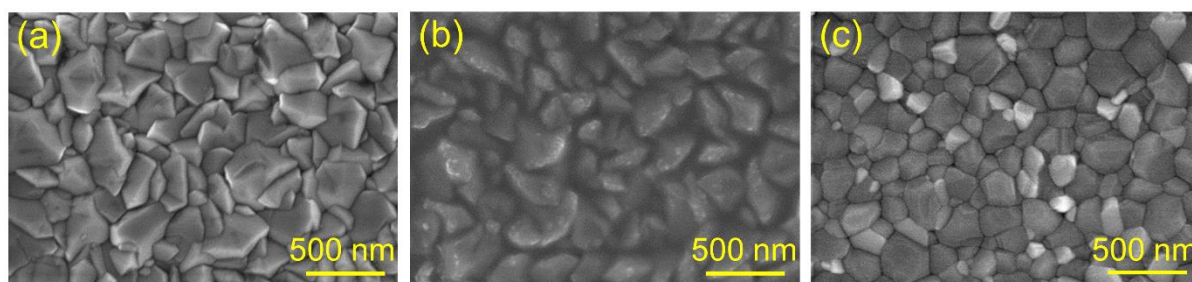


Figure 3. 2 SEM images of (a) FTO substrate, (b) SnO₂-QD layer on c-TiO₂/FTO and (c) the triple cation perovskite grown on SnO₂-QD/c-TiO₂/FTO.

Chapter 3

3.3.3 Device and Photovoltaic Characterization

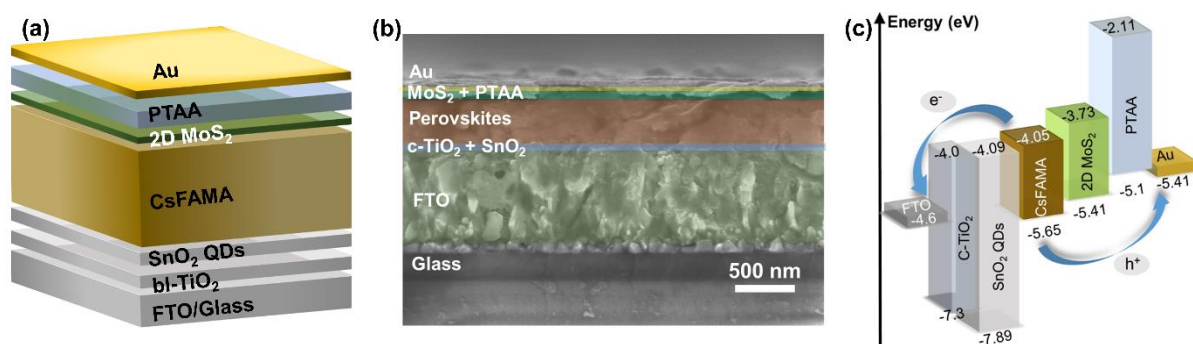


Figure 3. 3 (a) Architecture used for the device fabrication [FTO/c-TiO₂/SnO₂ QD/Cs_{0.1}(FA_{0.9}MA_{0.1})_{0.9}Pb(I_{0.9}Br_{0.1})₃/ MoS₂/PTAA/Au], (b) cross-sectional SEM image of the device with 2D-MoS₂ as interfacial layer and (c) energy level diagram of the fabricated PSCs.

The synthesized layered 2D-MoS₂ was placed as an interfacial layer in a device architecture of FTO/c-TiO₂/SnO₂ QD/Cs_{0.1}(FA_{0.9}MA_{0.1})_{0.9}Pb(I_{0.9}Br_{0.1})₃/ MoS₂/PTAA/Au (Figure 3.3a) and a typical cross-sectional SEM image is illustrated in Figure 3.3b. For ease of terminology hereafter, the triple cation perovskite will be termed CsFAMA. SnO₂-based electron selective layer together with c-TiO₂ provides enhanced hole-blocking ability than only SnO₂. This was used to avoid any direct contact with the bottom charge collector and eliminate possible recombination paths, which in turn will improve the PCE. The energy level alignment of the materials used for the PSC fabrication, with the 2D-MoS₂, is represented in Figure 3.3c, where the valence energy level (E_v) of 2D-MoS₂ minimizes the energetic mismatch between the CsFAMA and pristine PTAA. Figure 3.4a depicts the J - V characteristics under AM 1.5G illumination (100 mW/cm²) of control and MoS₂ based devices, and the PV parameters are represented in Table 1. The control devices yielded an average PCE of 15.05% with a short-circuit current density (J_{sc}) of 22.70 mAcm⁻², an open-circuit voltage (V_{oc}) of 887.7 mV and a fill factor (FF) of 74.64%. Notably, the devices fabricated by placing MoS₂ as an interfacial layer showed significant improvement and gave an average PCE >18%, mainly due to the increased of ~164 mV in V_{oc} and ~ 5% in FF. The increment in V_{oc} was obtained by stabilizing the HOMO level to minimize the mismatch between the absorber and HTM layer to just 0.31 eV and increase carrier concentration, which increases the FF. The device incorporated with 2D-MoS₂ interface layer gave 18.54% PCE, which is a significant increment of 23.2% as compared to the control device, which measured 15.05% PCE under similar conditions. To note the accuracy of the obtained J_{sc} from J - V measurements, we performed the incident

Chapter 3

photon-to-current efficiency (IPCE) measurements (Figure 3.4b). The integrated current density (J_{int}) values from the IPCE spectra are 22.27 and 21.72 mAcm^{-2} for the control and modified device respectively, and the values are in well agreement with J_{sc} obtained from J - V measurements.

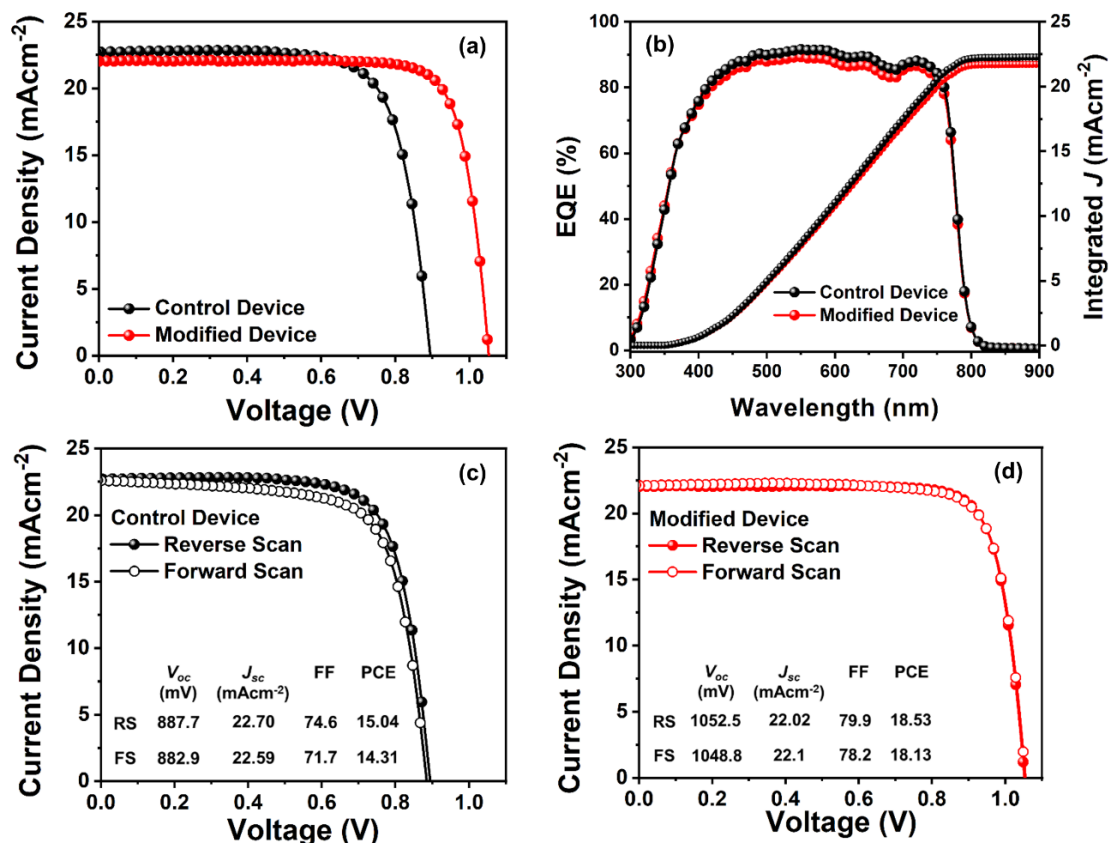


Figure 3.4 (a) J - V curves of the CsFAMA devices (control and modified with 1T-predominant 2D-MoS₂) under simulated AM 1.5G illumination, (b) corresponding IPCE and integrated current density of devices. J - V hysteresis curve of forward and reverse scans of (c) control and (d) of modified device with 1T-predominant 2D-MoS₂ interfacial layer.

The enhanced V_{oc} of the modified device can be explained by the valence band maximum (VBM) of 2D-MoS₂ (-5.4 eV), which reduced the wide energy barrier and mismatching between the valence band energy level ($E_{\text{v}} = -5.65$ eV) of CsFAMA and the HOMO level of pristine PTAA (-5.1 eV), facilitating smooth hole extraction from perovskite to the HTL.^{12,24} In particular, the two-dimensional nature of MoS₂ opens the wide optical bandgap compared to its bulk form from 1.2-1.8 eV, raising the conduction band of MoS₂ atop of the conduction band minimum (CBM) of CsFAMA, subsequently providing electron-blocking properties at perovskite/HTL interface (Figure A3.4b).^{24,30-32} As depicted in Table 1, the control device showed higher series resistance (R_{s}) of 3.21 Ωcm^{-2} , whereas the MoS₂ interlayer based device

Chapter 3

gave notably reduced R_s of $2.85 \Omega \text{ cm}^{-2}$, and subsequently improved FF was obtained. Apart from R_s , shunt resistance (R_{sh}) also affects the FF.³³ The presence of 2D-MoS₂ with effective electron blocking properties is responsible for the high R_{sh} associated with the modified device ($7.09 \text{ k}\Omega \text{ cm}^{-2}$ for RS) compared to the control device ($3.85 \text{ k}\Omega \text{ cm}^{-2}$ for RS). The excellent hole extraction behavior in conjugation with electron-blocking properties of 2D-MoS₂ synergistically suppresses the interfacial recombination losses, providing effective surface passivation to the active layer. Arguably, we can conclude that introducing 2D-MoS₂ as an interfacial layer in between perovskite/HTL, the PV parameters have been noteworthy improved.

Table 3. 1 PV parameters of the fabricated PSCs with and without 1T-predominant 2D-MoS₂ interfacial layer.

Device	Direction	V_{oc} (mV)	J_{sc} (mAcm ⁻²)	FF (%)	PCE (%)	R_s ($\Omega \text{ cm}^{-2}$)	R_{sh} ($\text{k}\Omega \text{ cm}^{-2}$)
Control	RS	887.7	22.70	74.64	15.04	3.21	3.85
	FS	882.9	22.59	71.75	14.31	3.91	0.99
	Statistics	886.1 ± 15.5	22.49 ± 0.18	73.28 ± 0.8	14.65 ± 0.16		
1T- predominant 2D-MoS ₂	RS	1052.5	22.02	79.96	18.54	2.85	7.09
	FS	1048.9	22.10	78.21	18.13	3.11	5.63
	Statistics	1040.4 ± 18.9	22.07 ± 0.11	79.13 ± 0.9	18.17 ± 0.18		

* R_s and R_{sh} of PSCs were estimated by the slope of the J - V curves near V_{oc} and J_{sc} , respectively.

The hysteresis behavior was measured by scanning J - V curves in reverse and forward direction (Figure 3.4c and d), where the hysteresis index (HI) is acquired to quantify the degree of hysteresis using the following equation;^{4,34}

$$HI = \frac{J_{RS(0.8V_{oc})} - J_{FS(0.8V_{oc})}}{J_{RS(0.8V_{oc})}} \quad (3.1)$$

where $J_{RS(0.8V_{oc})}$ and $J_{FS(0.8V_{oc})}$ represent the J_{sc} at 80% of V_{oc} of the reverse and forward scan respectively. The calculated HI of the device with 1T-predominant 2D-MoS₂ interfacial layer shows alleviated photocurrent hysteresis (0.001) compared to the control device (0.05).

Chapter 3

The PSCs with 2H-predominant 2D-MoS₂ as an interfacial layer also gave improved PV performance than of control device (without any interfacial layer), the device yielded a PCE of 17.34% with a (J_{sc}) of 22.22 mAcm⁻², V_{oc} of 1018.9 mV and FF of 76.61% under AM 1.5G illumination (100 mWcm⁻²). The J - V hysteresis curve and corresponding IPCE are presented in Figures 3.5a and b, respectively. However, we noted limited improvement in device performance as compared to the PSCs with 1T-predominant 2D-MoS₂ (Table A3.1). We ascribed this to the higher conductivity value (107 times higher) associated with 1T-MoS₂ as compared to 2H-MoS₂, which influences PV performances when used as an interfacial layer in PSCs.^{16,35}

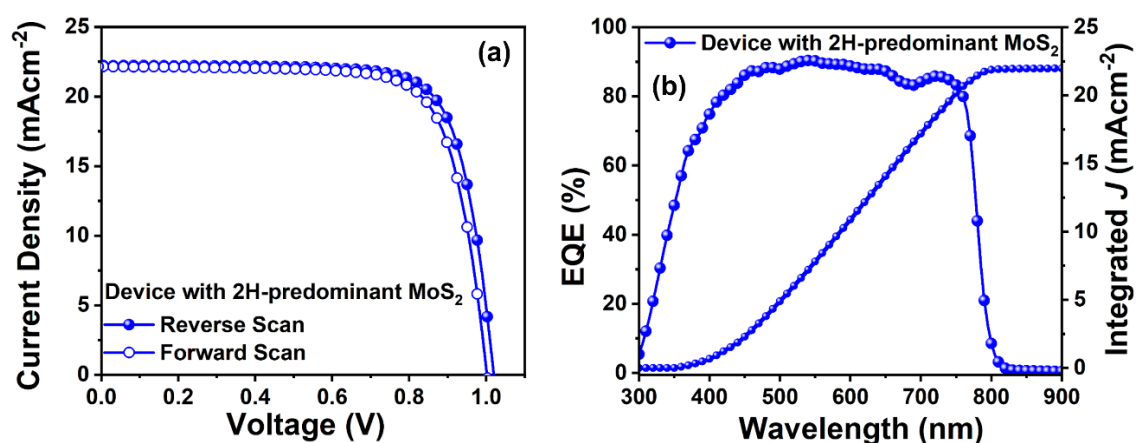


Figure 3. 5 (a) J - V hysteresis curve and (b) corresponding IPCE and integrated current for the device with 2H-predominant 2D-MoS₂ as an interfacial layer.

3.3.4 Device Stability

2D-MoS₂ based PSCs gave superior PV properties, to ascertain the interfacial engineering might compromise the operational stability of devices, we conducted maximum power point tracking (MPPT) of the un-encapsulated devices under constant 1 sun illumination and 45–50% humidity at room temperature (Figure 3.6a). The control device drastically lost 20% of its initial photocurrent value after 22 h of continuous testing, while the modified device with 2D-MoS₂ maintained 80% of its initial photocurrent for around 45 h of continuous operation. Further, the modified device showed 75% of its initial photocurrent after 100 h continuous operation conditions. The stabilized power output of the devices under constant 1 sun illumination at ambient atmosphere for the initial 1000s was shown in Figure 3.6b. We probed the long-term stability of PSCs in storage conditions where the un-encapsulated PSCs were

Chapter 3

stored in a dry box with relative humidity maintained at 45–50% at room temperature (Figure 3.6c). The modified devices maintained 96% of their initial PCE for 2952 h while the control devices showed 89% of their initial PCE during this time.

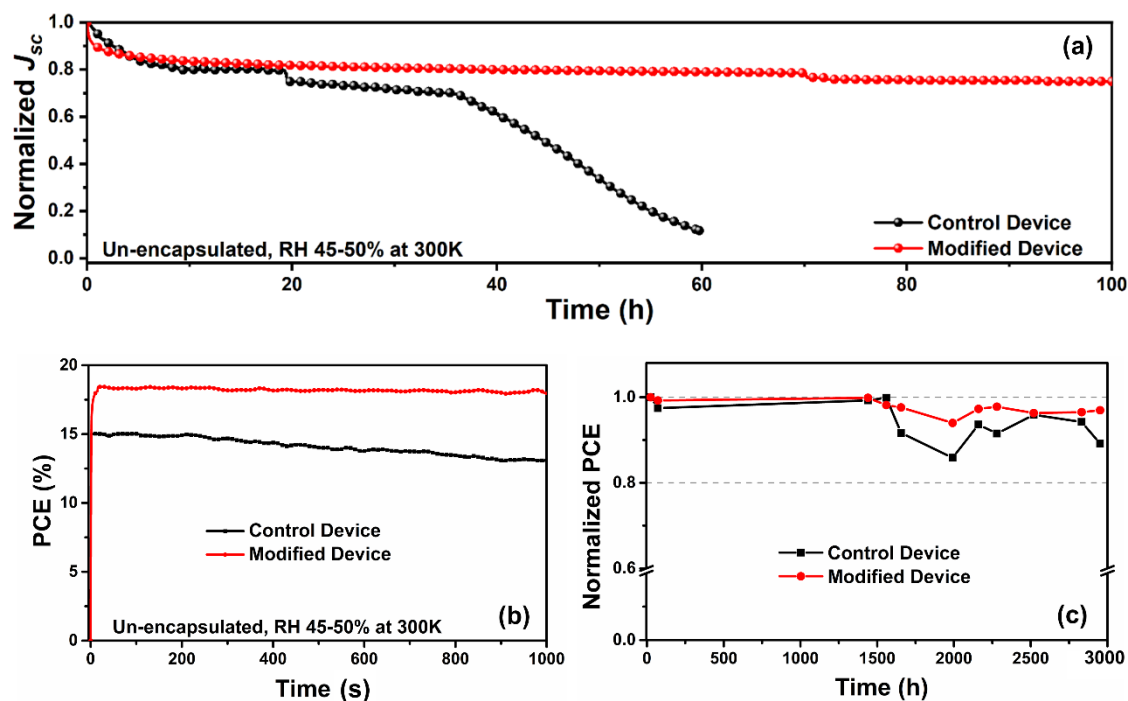


Figure 3. 6 (a) Continuous MPP tracking of the control and modified devices under constant 1 sun illumination at ambient atmosphere, (b) the stabilized power output of the devices under constant 1 sun illumination at ambient atmosphere, (c) normalized PCE with the storage time of control and modified devices.

The plausible reason for this was improved surface properties obtained by the placement of MoS_2 , which will act as a barrier for moisture diffusion inside the perovskite layer. Surface topography images revealed that the RMS roughness of films was reduced from 15.39 to 12.33 nm by the placement of 2D- MoS_2 (Figure A3.5). Arguably, this induced surface smoothness on the perovskite layer facilitates uniform distribution of the PTAA atop it, and we noted, the RMS roughness of the PTAA layer was reduced from 4.14 to 1.61 nm with the placement of the interfacial layer. The humid environment negatively influences the stability of the perovskite active layers and form perovskite hydrates easily, this initiates the decomposition and device degradation.⁴³ The hindering of moisture penetration to the active layer mitigates the degradation process and will subsequently extend the lifetime of the devices. The hydrophobic nature associated with 2D- MoS_2 put forward a strong affinity for water repulsion

Chapter 3

and moisture protection to the active layer.⁴⁴⁻⁴⁹ The water contact angle value is higher for the samples with PTAA deposited on perovskite with the presence of MoS₂ as interfacial layers, as compared to the reference device (Figure A3.6a-c). Pointing towards the attained hydrophobicity associated with the modified devices that can mitigate the water penetration into the active perovskite layer.

3.3.5 Admittance Spectroscopy and Mitigation of Trap Density

Both electronic and ionic type charge carriers in perovskite play determining role in the overall performance, however under an electric field ionic defects can drift and accumulate at the interface due to poor extraction and mobility of charge transporting carriers, resulting in capacitance build-up in the device.⁵⁰⁻⁵² To identify the factors accountable for the increment in PCE of fabricated PSCs, we studied the charge accumulation behavior of the devices with and without the 2D-MoS₂ interfacial layer through capacitance-frequency measurement at variable temperatures under dark conditions. Figure 3.7a and b enumerate the variation of capacitance (C) as a function of frequency (f) of devices at different temperatures. Three identical features were observed according to the three distinct regions of frequency: low (LF, 20 Hz - 1 kHz), intermediate (IF, 1-100 kHz), and high (HF, 100 kHz - 2 MHz) in both graphs. At the IF region, a constant capacitance is identified and assigned to dielectric relaxation in the active layer, which is mainly determined by the geometrical capacitance per unit area (C_g). This varies with the dielectric constant (ϵ), the geometrical layer thickness (L) of the perovskite layer, and vacuum permittivity (ϵ_0), [$C_g = \epsilon\epsilon_0/L$].^{52,53} The constant value of capacitance at IF with an increase in temperature of both devices suggests, the stable geometrical capacitance associated with the perovskite layer. Toward low frequencies, thermally-activated capacitance improvement was deducted which was ascribed to the charge accumulation at the interface and interfacial properties rather than bulk.⁵⁴⁻⁵⁶ However, the control device showed much higher capacitance than the device with 2D-MoS₂ interface layer in the LF region, suggesting that the charge carrier build-up at the interface is higher for the control device. Owing to the presence of 2D-MoS₂, the trapped-carriers located at the interface gain sufficient thermal energy to depart from the interface and migrate towards the bulk perovskite, consequently, the drop of the thermal-activated capacitance increment at the LF of the modified device occurs.^{54,56,57} Arguably, the presence of 2D-MoS₂ as an interfacial layer avoid charge accumulation at the perovskite/HTL interface and capacitance build-up in the PSCs under DC bias voltage. The

Chapter 3

capacitance drop at the HF region correlates to the effect of the series resistance caused by the conductive contact layer.⁵⁶

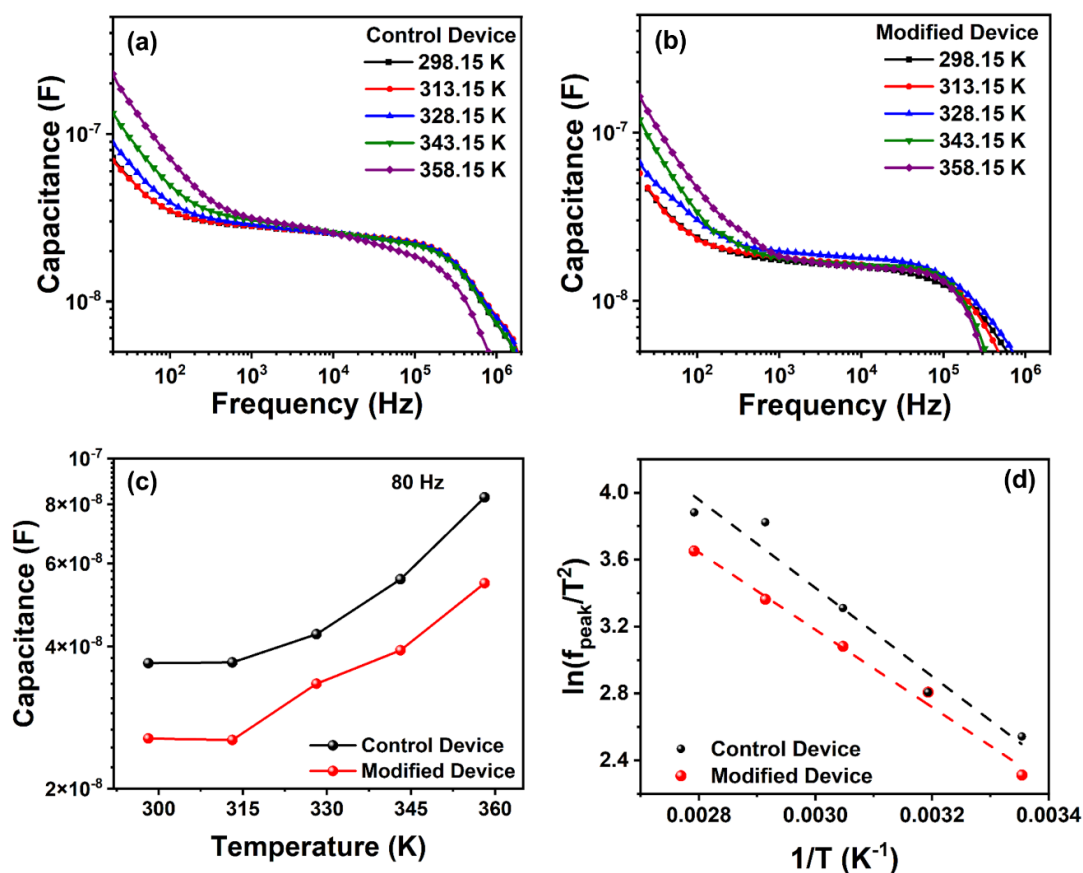


Figure 3. 7 Capacitance-frequency-temperature spectra obtained from (a) control device and (b) with 2D-MoS₂ interface layer. (c) Temperature-dependence low-frequency capacitance of control and modified devices and (d) Arrhenius plot of $\ln(f_{\text{peak}}/T^2)$ versus $1/T$ for control and modified devices, extracted from $-fdC/df$ versus f spectra.

Figure 3.7c depicts the capacitance measured at around 80 Hz as a function of the temperature, slight increment in thermally activated capacitance in both devices can be deducted, while comparatively higher capacitance values were identified for the control device at variable temperature range due to high charge accumulation at the perovskite/PTAA interface through poor carrier extraction and migration. Further, the unbalance charge extraction and transport associated with the pristine PTAA allows the capacitance build-up at perovskite/HTL interface.⁵⁷ To elucidate the role of the interfacial layer on the distribution of trap density in the CsFAMA layer, we determined the frequency of peak (f_{peak}) emission rate of electrons from a trap state located below E_T to E_C (conduction band edge) and activation energy for the

Chapter 3

devices. The f_{peak} was extracted from the derivative of capacitance spectra in the form of $-\text{d}C/\text{d}f$ as a function of f (Figure A3.7a and b). The activation energy E_a was calculated from the Arrhenius plot (Figure 3.7d), $\ln f_{\text{peak}}/T^2$ vs. $1/T$ and the following equation,⁵⁷⁻⁵⁹

$$\ln \frac{e_n}{T^2} = \ln \frac{v_0}{T^2} - \frac{E_a}{K_B T} \quad (3.2)$$

where e_n is the emission rate of electrons from a trap state, v_0 is attempt-to-escape frequency (ATEF), E_a is the activation energy, K_B is the Boltzmann constant, and T is the temperature. The trap energy for control and MoS₂ based devices are 227 and 199 meV respectively, indicating that charge transportation is hindered in the control device.^{58,60,61} The intercepts of the Arrhenius plot yield corresponding ATEF (v_0) of 7.58×10^9 Hz for the control device which is much higher than of the modified device showing v_0 of 2.22×10^9 Hz and Table 3.2 summarizes the extracted parameter.

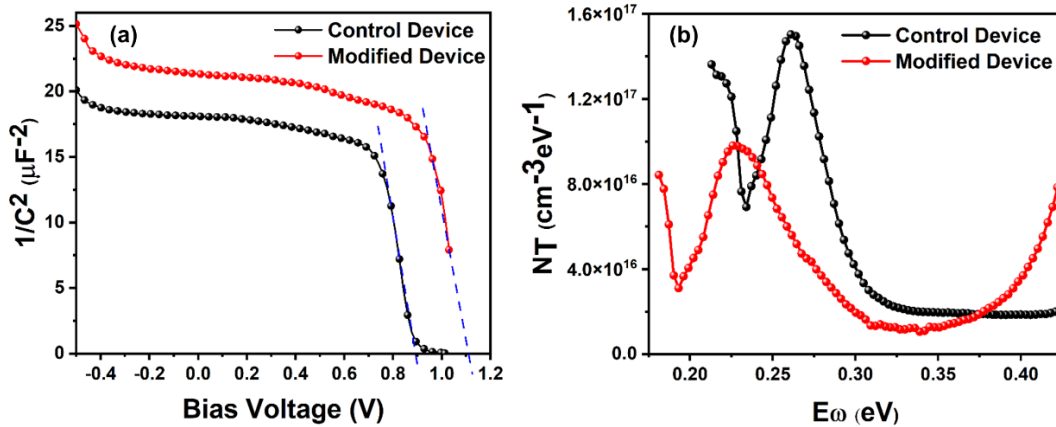


Figure 3. 8 (a) Mott-Schottky analysis at 10 kHz and (b) trap density (N_T) of control and modified devices measured at 300 K.

The trap density distribution (N_T), built-in-potential (v_{bi}), and depletion layer width (W) at perovskite/HTL interface were determined by using Mott-Schottky analysis along with thermal admittance spectroscopy (TAS). Figure 3.8a depicts the Mott-Schottky plot of devices at 10 kHz, the plot yields a straight region from which v_{bi} was extracted from the intercept on the bias axis and the doping density of immobile ions (N) at the depletion region was determined from the slope. The aforementioned parameters are related to the capacitance (C) as follows;⁶²⁻

64

$$\frac{1}{C^2} = \frac{2}{\epsilon \epsilon_0 A^2 q N} \left[V - v_{bi} - \frac{K_B T}{q} \right] \quad (3.3)$$

Chapter 3

where ε is the relative dielectric constant of perovskite (taken as the value of 32 from a previous report), ε_0 is the permittivity of free space and A is the active interfacial area.⁶⁵ Here K_B , T , and q represent Boltzmann's constant, the absolute temperature, and elementary charge, respectively. The built-in-potential for the modified device with 2D-MoS₂ interfacial layer was found to be increased to 1137.6 mV from 895.5 mV for the control device without the interface layer. Consequently, the depletion width ($W = \sqrt{\frac{2\varepsilon\varepsilon_0 v_{bi}}{qN}}$) of the active layer was increased from 131.69 nm for the control device to 134.43 nm for the device with 2D-MoS₂ interface layer. The enhanced depletion region assists in the proper charge separation and annihilates the recombination, and thus contributes to the increases in the PCE. The energetic profile of trap density of state (t_{DOS}) was calculated from the following equations,^{66,67}

$$N_T(E_f) = -\frac{v_{bi}}{qWK_B T} \left[f \frac{dc}{df} \right] \quad (3.4)$$

$$E_f = K_B T \ln \left[\frac{v_0}{f} \right] \quad (3.5)$$

Table 3.2. Electrical parameters calculated for control and modified devices from thermal admittance spectroscopy and Mott-Schottky plot at 300 K.

Parameters	Control	With 2D-MoS ₂
Activation energy E_a (meV)	227	199
ATEF v_0 (Hz)	7.58×10^9	2.22×10^9
Built-in-potential V_{bi} (V)	0.8955	1.1376
Depletion layer thickness (nm)	131.69	134.43
Trap density at Peak, t_{DOS} (eVcm ³) ⁻¹	1.50×10^{17}	9.8×10^{16}
energy at peak (E_ω) t_{DOS} (eV)	0.261	0.226

The trap density (N_T) profile as shown in Figure 3.8b indicates that the incorporation of 2D-MoS₂ as an interfacial layer significantly reduced the overall trap density of state in the perovskite. The distribution of trap density of state (t_{DOS}) in the control device exhibit a peak value of 1.5×10^{17} cm⁻³ eV⁻¹ situated at 0.26 eV which shifts to the lower energy at 0.226 eV with reduce the value of 9.8×10^{16} cm⁻³ eV⁻¹ in case of MoS₂ based device. The remarkable decrease of the t_{DOS} was consistent with the decreased photocurrent hysteresis, indicating the effective passivation of charge traps in CsFAMA by 2D-MoS₂. The suppressed trap density in

Chapter 3

the band gap of the perovskite in combination with 2D-MoS₂ efficiently extracts the photo-generated carriers to mitigate the interfacial charge recombination. We speculate this reduced trap density as a result of a possible electron blocking effect from 2D-MoS₂, suggesting the reduced or eventually eliminating the PV hysteresis in the devices.

3.4 Conclusions

To summarize, we have presented the role of 2D-MoS₂ as an interfacial layer in perovskite solar cells, in improving the opto-electrical properties by minimizing energetic mismatch and suppressing trap density in the perovskite layers. In a triple cation (CsFAMA) based perovskite environment, we noted 2D-MoS₂ interfacial layer reduces the energy required for detrapping the trapped-charges, by providing prompt extraction of photo-generated charges while mitigating the interfacial charge recombination. Our strategy based on interface engineering enables us to demonstrate dopant-free *n-i-p* structured devices with 18.54% power conversion efficiency along with enhanced long-term operational stability. The present work put forward the placement of 2D-interlayer in conjugation with dopant free hole transport layer to amplify the device photovoltaic performance and stability, which is paramount for the success of perovskite solar cells.

3.5 Experimental Section

3.5.1 Materials

Molybdenum (iv) sulfide (MoS₂, 99% metal basis, -325 mesh powder), tin (ii) chloride dehydrate (SnCl₂·2H₂O, 98%), and thiourea (CH₄N₂S, 99%) were procured from Alfa Aesar while butyl lithium (1.6 M, hexane) from Sigma-Aldrich. The chemicals for perovskite were purchased from Dyesol except PbI₂ and CsI₂, which were obtained from Tokyo Chemical Industry (TCI) and were employed as such. PTAA (M_n = 5000-15000 by GPC) was procured from Xi'an Polymer Light Technology Corp.

3.5.2 Device fabrication

Device fabrication was conducted as described in Chapter 2 section 2.3.1. Interfacial layer was introduced between CsFAMA and pristine PTAA film. Once the perovskite layer cooled down to room temperature, 0.3 mg/ml MoS₂ in isopropanol solution was spin coated at 2000 rpm for

Chapter 3

30 s (process was repeated 3-4 times). For control devices, PTAA was directly deposited on the perovskite active layer.

3.5.3 Materials characterization

X-ray photoelectron spectroscopy (XPS) experiments were carried out on a SPECS system (Berlin, Germany) equipped with Phoibos 150 1D-DLD analyzer with monochromated Al K_{α} radiation (1486.7 eV). The wide scan was performed with the step energy of 1 eV (dwell time: 0.1 s, pass energy: 80 eV), and detailed analysis of the elements was performed using 0.08 eV step energy (dwell time: 0.1 s, pass energy: 30 eV) with an electron exit angle of 90°. The spectra was adjusted using CasaXPS 2.3.16 software, which models Gauss-Lorentzian contributions. Atomic Force Microscopy (AFM) images were acquired with CSI Nano observer AFM and data were analyzed using Gwyddion software. (The dispersion of 2D-MoS₂ was diluted 1:10 in IPA for AFM, 25 μ l of the dilution was drop-cast onto SiO₂ wafer and dried at room temperature). The absorption spectra and PL steady-state measurements were acquired with the help of UV–vis–IR spectrophotometer (Varian Cary 50 UV/Vis Spectrophotometer) and a fluorescence spectrophotometer (PerkinElmer Instrument LS55) respectively. Cross and top-view microstructure were acquired by a Hitachi S–4800 scanning electron microscope.

Additional data is available in Appendix A

3.6 Bibliography

1. A. Kojima, K. Teshima, Y. Shirai, T. Miyasaka, Organometal halide perovskites as visible-Light sensitizers for photovoltaic cells. *J. Am. Chem. Soc.*, 131 (2009) 6050–6051.
2. “NREL Efficiency Chart. http://www.nrel.gov/ncpv/images/efficiency_chart.jpg,” (n.d).
3. L.-L. Jiang, Z.-K. Wang, M. Li, C.-H. Li, P.-F. Fang, L.-S. Liao, Flower-like MoS₂ nanocrystals: a powerful sorbent of Li⁺ in the spiro-OMeTAD layer for highly efficient and stable perovskite solar cells. *J. Mater. Chem. A*, 7 (2019) 3655–3663.

Chapter 3

4. J. Luo, J. Xia, H. Yang, L. Chen, Z. Wan, F. Han, H.A. Malik, X. Zhu, C. Jia, Toward high-efficiency, hysteresis-less, stable perovskite solar cells: unusual doping of a hole-transporting material using a fluorine-containing hydrophobic Lewis acid. *Energy Environ. Sci.*, 11 (2018) 2035–2045.
5. X. Zheng, Y. Hou, C. Bao, J. Yin, F. Yuan, Z. Huang, K. Song, J. Liu, J. Troughton, N. Gasparini, C. Zhou, Y. Lin, D.-J. Xue, B. Chen, A.K. Johnston, N. Wei, M. N. Hedhili, M. Wei, A.Y. Alsalloum, P. Maity, B. Turedi, C. Yang, D. Baran, T. D. Anthopoulos, Y. Han, Z.-H. Lu, O.F. Mohammed, F. Gao, E.H. Sargent, O. M. Bakr, Managing grains and interfaces via ligand anchoring enables 22.3%-efficiency inverted perovskite solar cells. *Nat. Energy*, 5 (2020) 131–140.
6. X. Liu, Y. Cheng, B. Tang, Z.G. Yu, M. Li, F. Lin, S. Zhang, Y.-W. Zhang, J. Ouyang, H. Gong, Shallow defects levels and extract detrapped charges to stabilize highly efficient and hysteresis-free perovskite photovoltaic devices. *Nano Energy*, 71 (2020) 104556.
7. M. Chen, M.-G. Ju, H.F. Garces, A.D. Carl, L.K. Ono, Z. Hawash, Y. Zhang, T. Shen, Y. Qi, R.L. Grimm, D. Pacifici, X.C. Zeng, Y. Zhou, N.P. Padture, Highly stable and efficient all-inorganic lead-free perovskite solar cells with native-oxide passivation. *Nat. Commun.*, 16 (2019).
8. Y. Liu, Z. Liu, E.-C. Lee, High-performance inverted perovskite solar cells using doped poly(triarylamine) as the hole transport layer. *ACS Appl. Energy Mater.*, 2 (2019) 1932–1942.
9. Q. Wang, N. Phung, D.D. Girolamo, P. Vivo, A. Abate, Enhancement in lifespan of halide perovskite solar cells. *Energy Environ. Sci.*, 12 (2018) 865–886.
10. X. Liu, T.J. Huang, L. Zhang, B. Tang, N. Zhang, D. Shi, H. Gong, Highly stable, new, organic-inorganic perovskite (CH₃NH₃)₂PdBr₄: synthesis, structure, and physical properties. *Chem. Eur.*, 24 (2018) 4991–4998.
11. N. Arora, M.I. Dar, A. Hinderhofer, N. Pellet, F. Schreiber, S.M. Zakeeruddin, M. Grätzel, Perovskite solar cells with CuSCN hole extraction layers yield stabilized efficiencies greater than 20%. *Science*, 358 (2017) 768–771.
12. N. Ahn, K. Kwak, M.S. Jang, H. Yoon, B.Y. Lee, J.-K. Lee, P.V. Pikhitsa, J. Byun, M. Choi, Trapped charge-driven degradation of perovskite solar cells. *Nat. Commun.*, 7 (2016).
13. G. Kakavelakis, I. Paradisanos, B. Paci, A. Generosi, M. Papachatzakis, T. Maksudov, L. Najafi, A.E.D.R. Castillo, G. Kioseoglou, E. Stratakis, F. Bonaccorso, E. Kymakis,

Chapter 3

- Extending the continuous operating lifetime of perovskite solar cells with a molybdenum disulfide hole extraction interlayer *Adv. Energy Mater.*, 8 (2018) 1702287.
14. S. Tsarev, I.K. Yakushchenko, S.Y. Luchkin, P.M. Kuznetsov, R.S. Timerbulatov, N. N. Dremova, L.A. Frolova, K.J. Stevenson, P.A. Troshin, A new polytriarylamine derivative for dopant-free high-efficiency perovskite solar cells. *Sustain. Energy Fuels*, 3 (2019) 2627–2632.
 15. R. Singh, A. Giri, M. Pal, K. Thiyagarajan, J. Kwak, J.-J. Lee, U. Jeong, K. Cho, Perovskite solar cells with an MoS₂ electron transport layer. *J. Mater. Chem. A*, 7 (2019) 7151–7158.
 16. P. Huang, Z. Wang, Y. Liu, K. Zhang, L. Yuan, Y. Zhou, B. Song, Y. Li, Water-soluble 2D transition metal dichalcogenides as the hole-transport layer for highly efficient and stable *p-i-n* perovskite solar cells. *ACS Appl. Mater. Interfaces*, 9 (2017) 25323–25331.
 17. D.H. Shin, J.S. Ko, S.K. Kang, S.-H. Choi, Enhanced flexibility and stability in perovskite photodiode-solar cell nanosystem using MoS₂ electron-transport layer. *ACS Appl. Mater. Interfaces*, 12 (2020) 4586–4593.
 18. X. Yang, W. Fu, W. Liu, J. Hong, Y. Cai, C. Jin, M. Xu, H. Wang, D. Yang, H. Chen, Au nanoparticles on ultrathin MoS₂ sheets for plasmonic organic solar cells. *J. Mater. Chem. A*, 2 (2014) 14798–14806.
 19. J. Kopaczek, M.P. Polak, P. Scharoch, K. Wu, B. Chen, S. Tongay, R. Kudrawiec, Direct optical transitions at K- and H-point of Brillouin zone in bulk MoS₂, MoSe₂, WS₂, and WSe₂. *J. Appl. Phys.*, 119 (2016), 235705.
 20. E. Singh, K.S. Kim, G.Y. Yeom, H.S. Nalwa, Atomically thin-layered molybdenum disulfide (MoS₂) for bulk-heterojunction solar cells. *ACS Appl. Mater. Interfaces*, 9 (2017) 3223–3245.
 21. B. Zheng, Y. Chen, Controllable growth of monolayer MoS₂ and MoSe₂ crystals using three-temperature-zone furnace *IOP Conf. Ser. Mater. Sci. Eng.*, 274 (2017), 012085.
 22. A.M.V.D. Zande, P.Y. Huang, D.A. Chenet, T.C. Berkelbach, Y. You, G.-H. Lee, T. F. Heinz, D.R. Reichman, D.A. Muller, J.C. Hone, Grains and grain boundaries in highly crystalline monolayer molybdenum disulphide. *Nat. Mater.*, 12 (2013) 554–561.
 23. K.F. Mak, C. Lee, J. Hone, J. Shan, T.F. Heinz, Atomically thin MoS₂: a new direct-gap semiconductor. *PRL* 105 (2010), 136805.

Chapter 3

24. L. Najafi, B. Taheri, B. Martín-García, S. Bellani, D.D. Girolamo, A. Agresti, R. Oropesa-Nuñez, S. Pescetelli, L. Vesce, E. Calabrò, M. Prato, A.E.D.R. Castillo, A. D. Carlo, F. Bonaccorso, MoS₂ quantum dot/graphene hybrids for advanced interface engineering of a CH₃NH₃PbI₃ perovskite solar cell with an efficiency of over 20%. *ACS Nano*, 12 (2018) 10736–10754.
25. C. Backes, N.C. Berner, X. Chen, P. Lafargue, P. LaPlace, M. Freeley, G.S. Duesberg, J.N. Coleman, A.R. McDonald, Functionalization of liquid-exfoliated two-dimensional 2H-MoS₂. *Angew Chem. Int. Ed. Engl.*, 23 (2015) 2638–2642.
26. Y. Cai, X. Yang, T. Liang, L. Dai, L. Ma, G. Huang, W. Chen, H. Chen, H. Su, M. Xu, Easy incorporation of single-walled carbon nanotubes into two-dimensional MoS₂ for high-performance hydrogen evolution, *Nanotechnology*, 25 (2014) 465401.
27. G. Eda, H. Yamaguchi, D. Voiry, T. Fujita, M. Chen, M. Chhowalla, Photoluminescence from chemically exfoliated MoS₂. *Nano Lett.*, 12 (2011) 5111–5116.
28. M. Abuhelaiqa, S. Paek, Y. Lee, K.T. Cho, S. Heo, E. Oveisi, A.J. Huckaba, H. Kanda, H. Kim, Y. Zhang, R.H. Baker, S. Kinge, A.M. Asiri, M.K. Nazeeruddin, Stable perovskite solar cells using tin acetylacetonate based electron transporting layers. *Energy Environ. Sci.*, 12 (2019) 1910–1917.
29. H. Guo, H. Zhang, J. Yang, H. Chen, Y. Li, L. Wang, X. Niu, TiO₂/SnO₂ nanocomposites as electron transporting layer for efficiency enhancement in planar CH₃NH₃PbI₃-based perovskite solar cells. *ACS Appl. Energy Mater.*, 1 (2018) 6936–6944.
30. J.K. Ellis, M.J. Lucero, G.E. Scuseria, The indirect to direct band gap transition in multilayered MoS₂ as predicted by screened hybrid density functional theory. *Appl. Phys. Lett.*, 99 (2011), 261908.
31. W.S. Yun, S.W. Han, S.C. Hong, I.G. Kim, J.D. Lee, Thickness and strain effects on electronic structures of transition metal dichalcogenides: 2H-MX₂ semiconductors (M = Mo, W; X = S, Se, Te) *Phys. Rev. B*, 85 (2012), 033305.
32. C.H. Ng, T.S. Ripolles, K. Hamada, S.H. Teo, H.N. Lim, J. Bisquert, S. Hayase, Tunable open circuit voltage by engineering inorganic cesium lead bromide/iodide perovskite solar cells *Sci. Rep.*, 8 (2018) 2482.
33. N.J. Jeon, H.G. Lee, Y.C. Kim, J. Seo, J.H. Noh, J. Lee, S.I. Seok, o-Methoxy substituents in Spiro-OMeTAD for efficient inorganic–organic hybrid perovskite solar cells *J. Am. Chem. Soc.*, 136 (2014) 7837–7840.

Chapter 3

34. H.S. Kim, N.G. Park, Parameters affecting I - V hysteresis of $\text{CH}_3\text{NH}_3\text{PbI}_3$ perovskite solar cells: effects of perovskite crystal size and mesoporous TiO_2 layer. *J. Phys. Chem. Lett.*, 5 (2014) 2927–2934.
35. W. Wei, K. Sun, Y.H. Hu, An efficient counter electrode material for dye-sensitized solar cells-flower-structured 1T metallic phase MoS_2 . *J. Mater. Chem. A*, 4 (2016) 12398–12401.
36. F. Zhang, H. Lu, J. Tong, J.J. Berry, M.C. Beard, K. Zhu, Advances in two-dimensional organic–inorganic hybrid perovskites. *Energy Environ. Sci.*, 13 (2020) 1154–1186.
37. G. Wu, X. Li, J. Zhou, J. Zhang, X. Zhang, X. Leng, P. Wang, M. Chen, D. Zhang, K. Zhao, S. Liu, H. Zhou, Y. Zhang, Fine multi-phase alignments in 2D perovskite solar cells with efficiency over 17% via slow post-annealing. *Adv. Mater.*, 31 (2019), 1903889.
38. F. Zhang, K. Zhu, Additive engineering for efficient and stable perovskite solar cells. *Adv. Energy Mater.*, 10 (2020) 1902579–1902605.
39. L. Meng, C. Sun, R. Wang, W. Huang, Z. Zhao, P. Sun, T. Huang, J. Xue, J.W. Lee, C. Zhu, Y. Huang, Y. Li, Y. Yang, Tailored phase conversion under conjugated polymer enables thermally stable perovskite solar cells with efficiency exceeding 21%. *J. Am. Chem. Soc.*, 140 (2018) 17255–17262.
40. J. Yang, S. Xiong, T. qu, Y. Zhang, X. He, X. Guo, Q. Zhao, S. Braun, J. Chen, J. Xu, Y. Li, X. Liu, C. Duan, J. Tang, M. Fahlman, Q. Bao, Extremely low-cost and green cellulose passivating perovskites for stable and high-performance solar cells. *ACS Appl. Mater. Interfaces*, 11 (2019) 13491–13498.
41. Z. Liu, K. Liu, F. Zhang, S.M. Jain, T. He, Y. Jiang, P. Liu, J. Yang, H. Liu, M. Yuan, $\text{CH}_3\text{NH}_3\text{PbI}_3:\text{MoS}_2$ heterostructure for stable and efficient inverted perovskite solar cell. *Sol. Energy*, 195 (2020) 436–445.
42. A. Agresti, S. Pescetelli, A.L. Palma, B.M. Garcia, L. Najafi, S. Bellani, I. Moreels, M. Prato, F. Bonaccorso, A.D. Carlo, Two-dimensional material interface engineering for efficient perovskite large-area modules. *ACS Energy Lett.*, 4 (2019) 1862–1871.
43. B. Zhang, Y. Zhou, Q. Xue, J. Tian, Q. Yao, Y. Zang, L. Wang, W. Yang, H.L. Yip, Y. Cao, The energy-alignment engineering in polytriphenylamines-based hole transport polymers realizes low energy loss and high efficiency for all-inorganic perovskite solar cells. *Solar RRL*, 3 (2019), 1900265.

Chapter 3

44. J. Lee, P. Dak, Y. Lee, H. Park, W. Choi, M.A. Alam, S. Kim, Two-dimensional Layered MoS₂ biosensors enable highly sensitive detection of biomolecules. *Sci. Rep.*, 4 (2014), 07352.
45. J.H. Kim, T.J. Ko, E. Okogbue, S.S. Han, M.S. Shawkat, M.G. Kaium, K.H. Oh, H. S. Chung, Y. Jung, Centimeter-scale green integration of layer-by-layer 2D TMD vdW heterostructures on arbitrary substrates by water-assisted layer transfer. *Sci. Rep.*, 9 (2019) 1641.
46. S. Kelebek, Critical surface tension of wetting and of floatability of molybdenite and sulphur. *J. Colloid Interface Sci.*, 124 (1988) 504–514.
47. S. Zhang, X. Zeng, Z. Tang, M. Tan, Exploring the antisticking properties of solid lubricant thin films in transfer molding. *Int. J. Mod. Phys. B*, 16 (2002) 1080–1085.
48. Q.H. Wang, K.K. Zadeh, A. Kis, J.N. Coleman, M.S. Strano, Electronics and optoelectronics of two-dimensional transition metal dichalcogenides. *Nat. Nanotechnol.*, 7 (2012) 699–712.
49. A.P. Gaur, S. Sahoo, M. Ahmadi, S.P. Dash, M.J. Guinel, R.S. Katiyar, Surface energy engineering for tunable wettability through controlled synthesis of MoS₂. *Nano Lett.*, 14 (2014) 4314–4321.
50. I. Zarazua, J. Bisquert, G. Garcia-Belmonte, Light-induced space-charge accumulation zone as photovoltaic mechanism in perovskite solar cells. *J. Phys. Chem. Lett.*, 7 (2016) 525–528.
51. G.G. Belmonte, J. Bisquert, Distinction between capacitive and noncapacitive hysteretic currents in operation and degradation of perovskite solar cells. *ACS Energy Lett.*, 1 (2016) 683–688.
52. O. Almora, C. Aranda, G. Garcia-Belmonte, Do capacitance measurements reveal light-induced bulk dielectric changes in photovoltaic perovskites? *J. Phys. Chem. C*, 122 (2017) 13450–13454.
53. O. Almora, A. Guerrero, G. Garcia-Belmonte, Ionic charging by local imbalance at interfaces in hybrid lead halide perovskites. *Appl. Phys. Lett.*, 108 (2016), 043903.
54. R.A. Awni, Z. Song, C. Chen, C. Li, C. Wang, M.A. Razooqi, L. Chen, X. Wang, R. J. Ellingson, J.V. Li, Y. Yan, *Joule*, 4 (2020) 644–657.
55. H. Zang, Y.C. Hsiao, B. Hu, *Phys. Chem. Chem. Phys.*, 16 (2014) 4971–4976.
56. O. Almora, I. Zarazua, E. Mas-Marza, I. Mora-Sero, J. Bisquert, G. Garcia-Belmonte, Capacitive dark currents, hysteresis, and electrode polarization in lead halide perovskite solar cells. *J. Phys. Chem. Lett.*, 6 (2015) 1645–1652.

Chapter 3

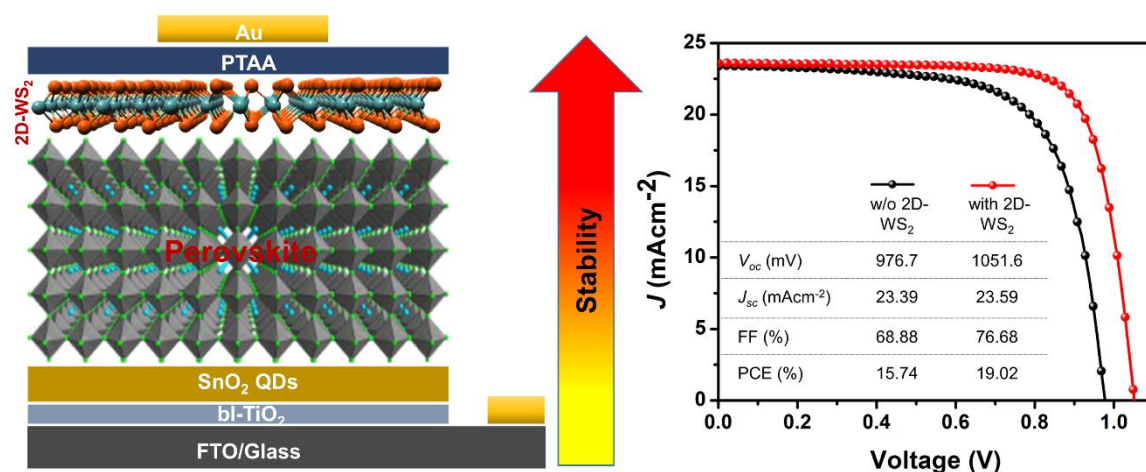
57. M.T. Khan, A.R.D. Almohammed, S. Kazim, S. Ahmad, Electrical methods to elucidate charge transport in hybrid perovskites thin films and devices. *Chem. Rec.*, 20 (2020) 452–465.
58. M. Samiee, S. Konduri, B. Ganapathy, R. Kottokkaran, H.A. Abbas, A. Kitahara, P. Joshi, L. Zhang, M. Noack, V. Dalal, Defect density and dielectric constant in perovskite solar cells. *Appl. Phys. Lett.*, 105 (2014), 153502.
59. J.A. Carr, M. Elshobaki, S. Chaudhary, Deep defects and the attempt to escape frequency in organic photovoltaic materials. *Appl. Phys. Lett.*, 107 (2015), 203302.
60. H. Jin, E. Debroye, M. Keshavarz, I.G. Scheblykin, M.B.J. Roeffaers, J. Hofkens, J. A. Steele, It's a trap! On the nature of localised states and charge trapping in lead halide perovskites. *Mater. Horiz.*, 7 (2020) 397–410.
61. N.H. Hemasiri, S. Kazim, L. Calio, S. Paek, M. Salado, G. Pozzi, L. Lezama, M. K. Nazeeruddin, S. Ahmad, Elucidating the doping mechanism in fluorene–dithiophene-based hole selective layer employing ultrahydrophobic ionic liquid dopant. *ACS Appl. Mater. Interfaces*, 12 (2020) 9395–9403.
62. K. Gelderman, L. Lee, S.W. Donne, Flat-band potential of a semiconductor: using the Mott–Schottky equation. *J. Chem. Educ.*, 84 (2007) 685–688.
63. A. Guerrero, E.J. Juarez-Perez, J. Bisquert, I. Mora-Sero, G. Garcia-Belmonte, Electrical field profile and doping in planar lead halide perovskite solar cells. *Appl. Phys. Lett.*, 105 (2014), 133902.
64. S. Aharon, S. Gamliel, B.E. Cohen, L. Etgar, Depletion region effect of highly efficient hole conductor free $\text{CH}_3\text{NH}_3\text{PbI}_3$ perovskite solar cells. *Phys. Chem. Chem. Phys.*, 16 (2014) 10512–10518.
65. T. Bu, X. Liu, Y. Zhor, J. Yi, X. Huang, L. Luo, J. Xiao, Z. Ku, Y. Peng, F. Huang, Y. B. Cheng, J. Zhong, A novel quadruple-cation absorber for universal hysteresis elimination for high efficiency and stable perovskite solar cells. *Energy Environ. Sci.*, 10 (2017) 2509–2515.
66. Y. Shao, Z. Xiao, C. Bi, Y. Yuan, J. Huang, Origin and elimination of photocurrent hysteresis by fullerene passivation in $\text{CH}_3\text{NH}_3\text{PbI}_3$ planar heterojunction solar cells. *Nat. Commun.*, 5 (2014) 5784.
67. J.A. Carr, S. Chaudhary, The identification, characterization and mitigation of defect states in organic photovoltaic devices: a review and outlook. *Energy Environ. Sci.*, 6 (2013) 3414–3438.

Chapter 3

68. G. Yang, C. Chen, F. Yao, Z. Chen, Q. Zhang, X. Zheng, J. Ma, H. Lei, P. Qin, L. Xiong, W. Ke, G. Li, Y. Yan, G. Fang, Effective carrier-concentration tuning of SnO₂ quantum dot electron-selective layers for high-performance planar perovskite solar cells. *Adv. Mater.*, 30 (2018), 1706023.

CHAPTER 4

PHOTO-INDUCED CHARGE TRANSFER DYNAMICS IN DOPANT-FREE PEROVSKITE SOLAR CELLS UPON 1T-RICH WS₂ INTERFACIAL LAYER



This chapter has been published in *Journal of Materials Chemistry C* with the front cover of the volume 9, 2021 entitled:

1T-Rich 2D-WS₂ as an interfacial agent to escalate photo-induced charge transfer dynamics in dopant-free perovskite solar cells

Naveen Harindu Hemasiri, Samrana Kazim, Shahzada Ahmad
 N.H. Hemasiri et. al., *J. Mater. Chem. C*, **2021**, 9, 9865-9873.
doi.org/10.1016/j.nanoen.2020.105292

Chapter 4

4.1 Abstract

Excellent charge extractability and device performance are promoted by controlling the charge build-up and recombination at interfaces, which has become one of the effective techniques in this area. Motivated by the previous findings from Chapter 3, here, we introduce a few-atom thick 1T-rich 2D-WS₂ as an interfacial layer on an active perovskite film to minimize the energy barrier and charge accumulation at the interface to intensify the extraction of detrapped charges and charge transfer dynamics in PSCs. By combining the interfacial layer in a dopant-free device architecture, we achieved a stabilized efficiency of over 19% with a significantly enhanced open-circuit voltage and fill factor. We discovered a 25% drop in trap density upon 1T-rich WS₂ interface layer where photocurrent saturation was seen at a rather low effective voltage (0.3 V). Our work put forward the deep experimental understanding of 2D materials as an interfacial agent toward their stabilized performances.

4.2 Introduction

Despite the astonishing compositional engineering that has been studied by many groups, challenges remain for achieving long-term stability that is further complicated by ionic migration, light irradiation, and moisture corrosion of the PSCs.^{1,2} Beyond the active material, the energy band alignment of the perovskite layer at the interfaces with the charge selective layers is a prerequisite in governing the device performance and stability.^{3,4} Perovskites are sandwiched between charge selective layers with possibly associated energy and chemical incompatibilities with the contacting layers making the interfaces a crucial zone with a high potential to instigate the device failure.^{1,5,6} Arguably, photo-generated charge separation and transfer to the corresponding interfaces from the light-absorbing layer could occur with the absence of energy losses without recombination at the interfaces. Moreover, the ideal electron/hole selective layers should allow their corresponding charges only, while having no recombination and transport losses at the interfaces.^{5,7,8} However, due to imbalanced charge separation and transfer, inferior interface band alignment, and defects associated with the interfaces under real conditions can deteriorate the PV performances of PSCs.^{7,9-11} At the device level, stress due to extrinsic environmental conditions such as varying temperatures, electric fields, atmospheres, and light intensities intensively propagate the degradation mechanism.^{12,13} Furthermore, unbalanced charge injection, trapped charges, and capacitive current promote the charge accumulation at the interfaces between the perovskite and charge selective layers, and ultimately the trapped charged driven degradation may take place in

Chapter 4

addition to the photo-generated hysteresis.¹⁴⁻¹⁶ Several approaches have been devoted toward long-term PV performance including the introduction of the interface energy alignment layer, tuning the work function of the perovskite layer, doping mechanism into charge transport layers, and self-assembled derivatives to overcome photo-generated carrier traps, improving the quality of the interfacial coupling, and defect passivation.^{3,4} However, the hygroscopic nature associated with doping or interfacial materials can further accelerate the degradation of the perovskite layer.¹⁷⁻¹⁹

The accession of the interfacial layer gave promising results in terms of PV performance and stability as discussed in the previous chapter.²⁰⁻²⁴ Among different 2D materials, 2D transition metal dichalcogenides (TMDs) are recognized as a promising class of semiconductors for PV applications including PSCs owing to their outstanding chemical, physical and electronic properties which can be further tuned by their synthesis route.^{2,24,25} The scalable synthesis of 2D-TMD materials with high purity and specific functionalities remains a key to advanced PV applications. Among the different synthetic protocols, Li⁺ intercalated liquid-phase exfoliation of layered materials is a promising approach that offers high yield, simplistic method, up-scalability, and cost-effectiveness. Reports dealing with 2D-TMDs such as MoS₂ and WS₂ in PSCs as an HTM or ETL showed moderate PCE values.^{26,27,28} However, the PCE associated with 2D-TMDs as an individual HTM or ETM is not comparable towards commercialization, stipulating the limitation of 2D-TMDs as individual charge transport layers. In contrast, the utilization of 2D-TMDs as an interfacial layer between the active and charge transport layers led to significantly improved PV performance with an extended lifetime.^{2,18,29-31} The non-covalent interactions and the dangling bond-free nature of 2D-TMDs could aid in further stabilizing the active layer from hygroscopic additives in charge transport materials.^{24,30} Li⁺ intercalation of VI group transition metal-based TMDs promote metastable 1T phase, which has high conductivity when compared with their counterpart 2H phase. We have shown in Chapter 1 that Li⁺ intercalated VI group MoS₂ with predominantly 1T phase as an interfacial layer in dopant-free *n-i-p* PSCs, achieving an upgraded PCE. For further understanding, herein, we report our findings on the successful implementation of Li⁺ intercalated liquid-phase exfoliated 2D-WS₂ as an interfacial layer on a triple cation Cs_{0.1}(FA_{0.9}MA_{0.1})_{0.9}Pb(I_{0.9}Br_{0.1})₃ perovskite, leading to a significantly enhanced PCE and an extended lifetime. A prompt photo-generated charge collection and exciton dissociation is a paramount feature in PV solar cells, which has been investigated in PSCs upon the 2D-WS₂ interface layer. We show that the incorporation of the interface layer effect in enlarging the maximum exciton generation rate

Chapter 4

and saturation of photocurrent at a relatively low effective voltage, resulting in feasible photo-charge dynamics in the device. Subsequently, boosted PCE from 15.7% to 19.02% owing to the upgraded open-circuit voltage (V_{oc}) and fill factor (FF).

4.3 Results and Discussion

4.3.1 2D-WS₂ Characterization

We derived a few layers of 1T predominant WS₂ nanosheets in isopropanol (IPA) from bulk WS₂ powder using rapid Li⁺ intercalation in combination with ultra-sonication and a series of ultracentrifugation steps. During the Li⁺ intercalation process into WS₂, the lithiation intermediate (Li_xWS₂) was thoroughly reacted with H₂O to separate the van der Waals bonded layers and form few- or single-layer WS₂ sheets. The microstructure of the synthesized 2D-WS₂ nanosheets was analyzed under a transmission electron microscope (TEM) and an atomic force microscope (AFM). Figure 4.1a illustrates a representative TEM image of 2D-WS₂ with a lateral size of ca. 120 nm. The topographic AFM image (Figure 4.2b) together with the inset thickness profile suggests the thickness of the 2D-WS₂ in the 5-6 nm range, affirming the existence of few-layer nanosheets. Figure 4.3c shows the statistical distribution with the maximum population peaks at 5.15 nm.

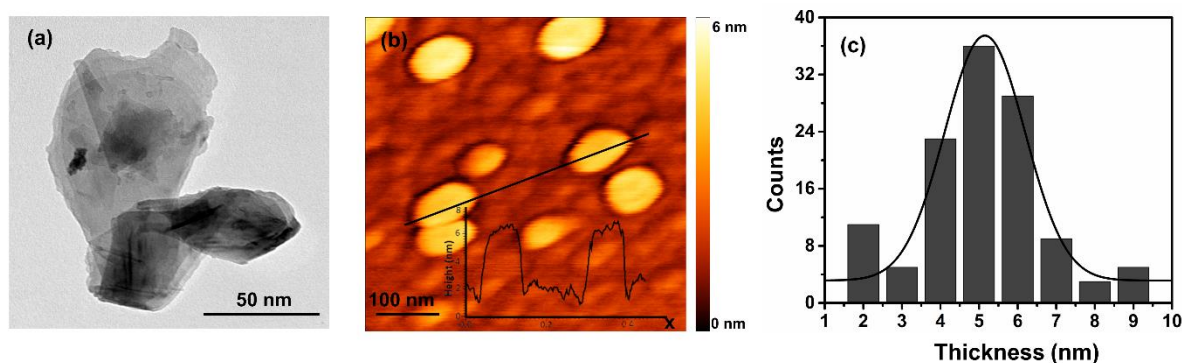


Figure 4. 1 Characterization of the synthesized 2D-WS₂. (a) TEM image of WS₂ flakes, (b) AFM image of selected WS₂ flakes. Inset represents the thickness profile of the selected flakes, (c) Statistical distribution of WS₂ flake thickness.

The X-ray diffraction (XRD) pattern of 2D-WS₂ shows a high intense single diffraction peak at 2θ of 14.521, corresponding to the (002) crystal plane of hexagonal WS₂, and the absence of additional peaks related to the bulk WS₂, confirming the highly oriented phase crystallinity of the synthesized 2D-WS₂ nanosheets (Figure 4.2a).³² The UV-Vis absorption of 2D-WS₂

Chapter 4

nanosheets dispersed in IPA solution (Figure 4.2b) leads to the weak shoulder peaks located at 637 and 528 nm corresponding to the A and B excitonic transitions, confirming the formation of 1T rich 2D-WS₂ nanosheets.³³ The optical bandgap estimated from the Tauc plot is about 1.76 eV (inset of Figure 4.2b).

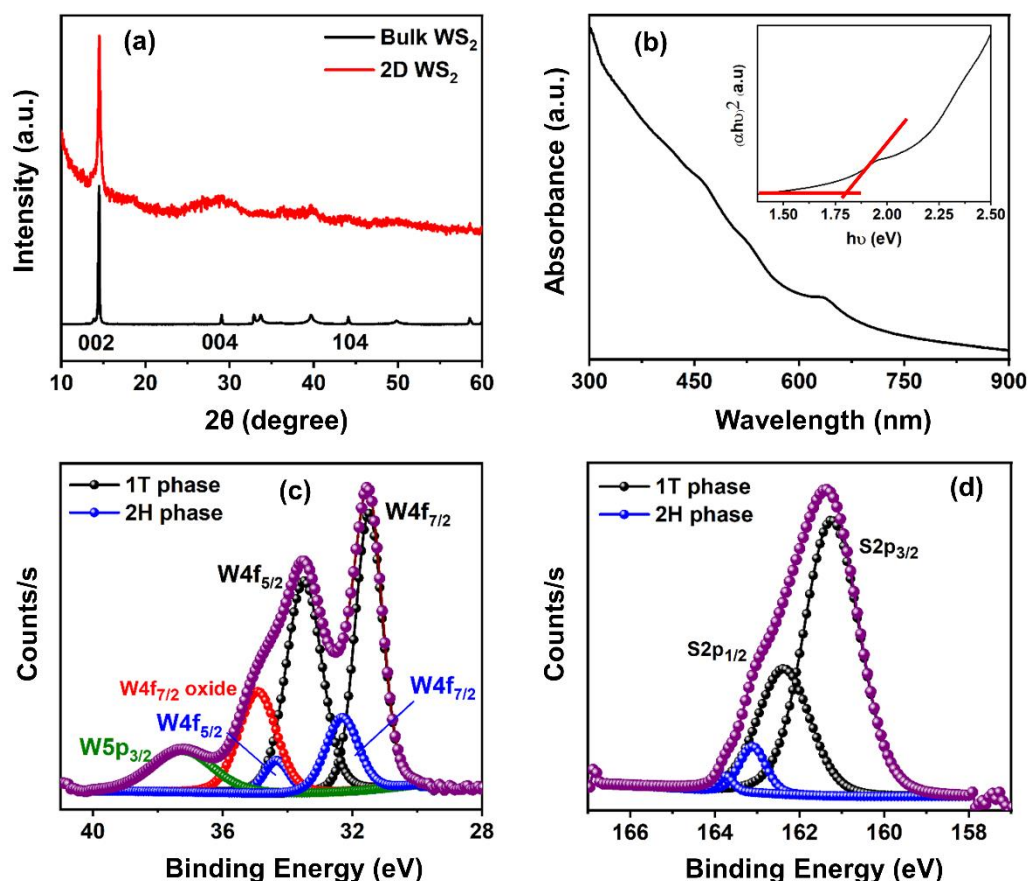


Figure 4. 2 (a) XRD patterns of bulk and 2D-WS₂. (b) Optical absorption spectrum; inset shows the calculated optical band gap of WS₂ flakes from the Tauc plot. High-resolution XPS spectra of W4f (c) and S2p (d).

The positions of core-level peaks corresponding to W4f_{7/2} and W4f_{5/2} originated from X-ray photoelectron spectroscopy (XPS) is an effective way to specify the phase and chemical state of the elements composing the 2D-WS₂ nanosheets. We ascribed the emerged doublet (Figure 4.2c) at 31.49 and 33.48 eV to the W4f_{7/2} and W4f_{5/2} core levels of the metallic 1T-phase, respectively, attributing the presence of the predominant contribution of the 1T phase with 82.25% in the as-prepared 2D-WS₂. However, the less intense additional peaks at 32.31 and 34.33 eV were also observed, showing the simultaneous existence of the partial semiconducting 2H phase in WS₂ nanosheets.³³ A similar phase contribution can be deduced

Chapter 4

from the high-resolution XPS spectra of S2p (Figure 4.2d), in which two identical peaks relevant to S2p_{3/2} and S2p_{1/2} for the 1T phase emerged at 161.24 and 162.37 eV, respectively.

4.3.2 Thin-Film Characterization

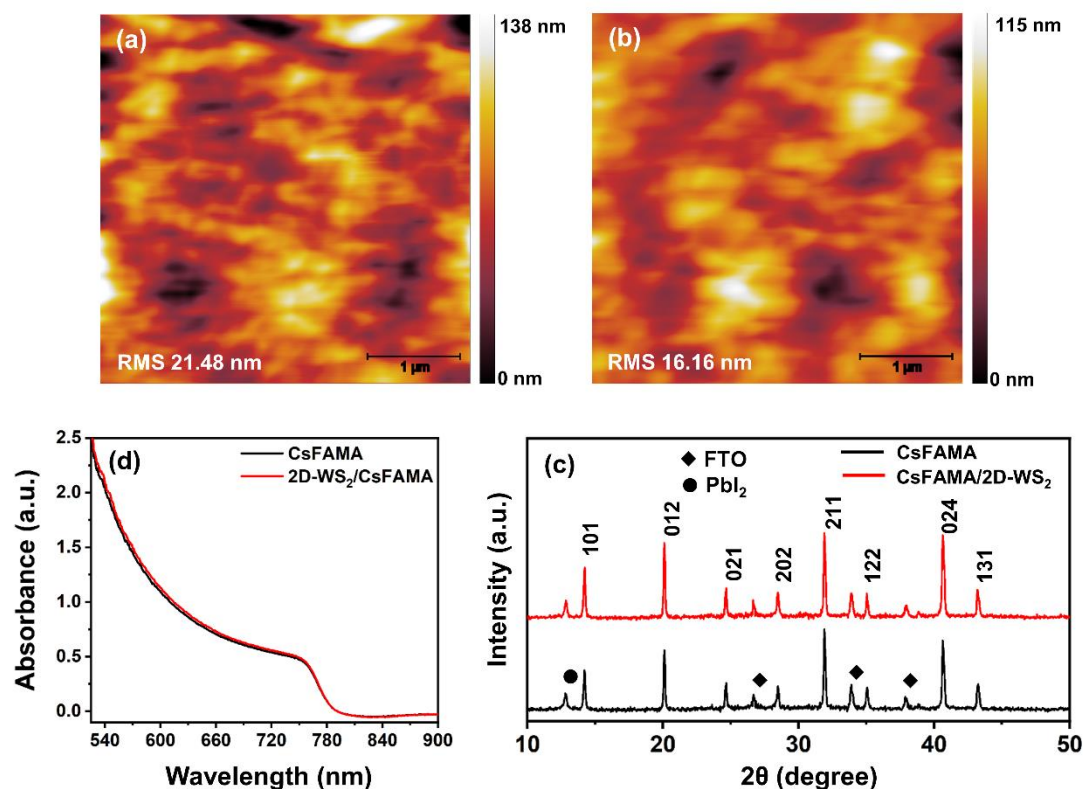


Figure 4. 3 AFM topography images of (a) CsFAMA film and (b) 2D-WS₂/CsFAMA film. (c) XRD patterns of CsFAMA and 2D-WS₂/CsFAMA films. (d) UV-Vis absorption spectrum of perovskite and 2D-WS₂/perovskite.

We examined the microstructure of the CsFAMA perovskite layer grown on the SnO₂ QD layer using SEM and AFM analyses (Figure A4.1, Appendix B, Figure 4.3a and b). Notably from AFM analysis, we deduce that the perovskite roughness decreases from 21.48 nm to 16.16 nm after the deposition of 2D-WS₂ nanosheets on the perovskite. However, full coverage of the 2D-WS₂ layer on the perovskite can only be achieved through multiple depositions of the solution of 2D-WS₂ as previously reported, and in this report, we deposited 2D-WS₂ nanosheets three times. The XRD analysis (Figure 4.3c) indicating the presence of 2D-WS₂ does not influence the crystallinity of the perovskite. No visible changes were noted in the UV-visible spectra of the perovskite with/without the 2D WS₂ interface layer (Figure 4.3d). The interaction between 2D-WS₂ nanosheets and the perovskite layer at the interface was further investigated

Chapter 4

using XPS characterization. As shown in Figure 4.4a the Pb4f_{5/2} and Pb4f_{7/2} peaks of the bare perovskite layers are located at 142.98 and 138.1 eV, respectively, and these peaks show an apparent binding energy shift of 0.11 eV towards the higher binding region with the presence of 2D-WS₂ layers. A similar binding energy shift can be deduced in I3d peaks when the perovskite layer is placed with 2D-WS₂ in which the shift is around 0.15 eV (Figure 4.4b), corroborating a possible strong interaction of S–Pb, S–I, and the modified chemical environment of the [PbI₆]⁴⁻ octahedral.^{29,34,35}

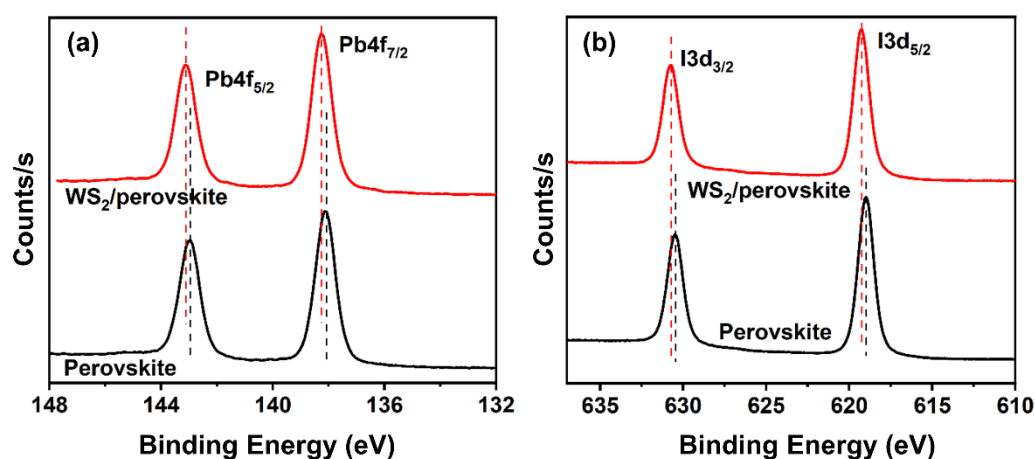


Figure 4. 4 High-resolution XPS spectra of (e) Pb4f and (f) I3d for perovskite and perovskite/2D-WS₂ layers.

4.3.3 Device and Photovoltaic Characterization

PSCs were fabricated based on the planar *n-i-p* configuration with stacked layers of FTO/bl-TiO₂/SnO₂-QDs/ Cs_{0.1}(FA_{0.9}MA_{0.1})_{0.9}Pb(I_{0.9}Br_{0.1})₃ /2D-WS₂/PTAA/Au (Figure 4.5a and b) to evaluate the PV performances by the placement of 2D-WS₂ as an interfacial layer. The energy levels of the materials used in the device architecture including the as-prepared 2D-WS₂ (Figure 4.5c) suggest the compatibility of the valence band energy of the interface layer at the HTM/perovskite interface which overcomes the energy barrier for effective free hole extraction.^{1,36-39}

The photocurrent-density-voltage (*J-V*) characteristics of PSCs with and without the interface layer are illustrated (Figure 4.6a), and the corresponding PV parameters are summarized in Table 4.1 (Table A4.1 and Table A4.2, Appendix B). A significant increase was measured from the PSCs incorporating 2D-WS₂ as an interlayer, with a value of 19.02% PCE along with an open-circuit voltage (*V*_{oc}) of 1051 mV, a short-circuit current density (*J*_{sc}) of 23.59 mA cm⁻²,

Chapter 4

and a fill factor (FF) of 76.68%. Under similar conditions, the control devices showed a PCE of 15.74% with V_{oc} , J_{sc} , and FF being 976.7 mV, 23.39 mA cm⁻², and 68.88%, respectively. Notably, the PSCs with an interface layer show an average improvement of PCE by 23.5%

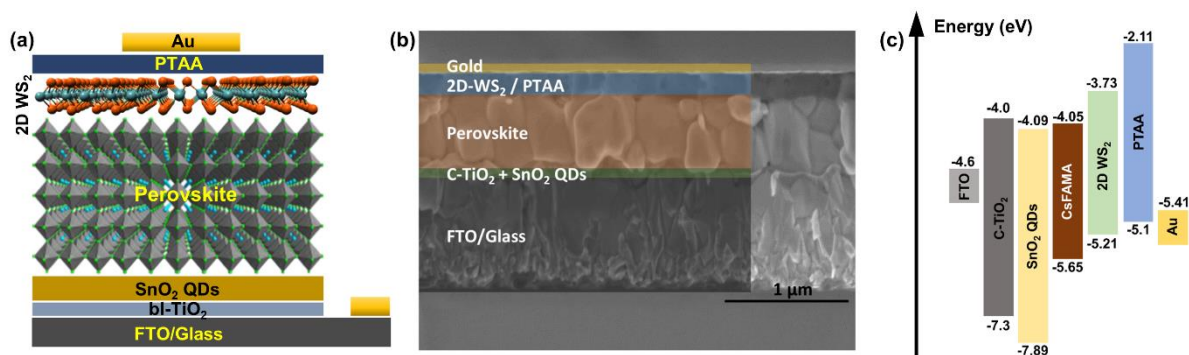


Figure 4. 5 (a) Device structure of planar perovskite solar cells incorporating the 2D-WS₂ interface layer, (b) cross-sectional SEM image of the PSC with 2D-WS₂ interface layer, and (c) energy band alignment of the corresponding layers.

from the control PSC owing to an improvement in the V_{oc} and FF. The integrated J_{sc} values extracted from the external quantum efficiency (EQE) measurement are 22.97 and 22.28 mA cm⁻² for the PSC with and without the interface layer, in agreement with the J_{sc} obtained from J - V curves (Figure 4.6b). The corresponding integrated currents of the two PSCs show a slight reduction compared to the J_{sc} obtained from the J - V curve possibly due to the difference in the light source used, which is much lower in intensity than of the solar simulator system.²⁴

Notably, we noted a significant reduction in the device hysteresis (HI index from 0.05 to 0.02) after introducing the interface layer (Figure 4.6c). We attribute the enhanced V_{oc} to the reduction of the high energy barrier between the valence band energy level of the perovskite ($E_V = 5.65$ eV) and the HOMO level of PTAA (-5.1 eV) by placing the interface layer, and this facilitates a facial photo-generated charge transfer between the perovskite and PTAA layer.^{2,18} Moreover, the PSC fabricated with the 2D-WS₂ interfacial layer shows a decreased interfacial series resistance (R_s) and a higher shunt resistance (R_{sh}), which suppress the interfacial charge losses through decreased charge recombination, to enlarge the FF.

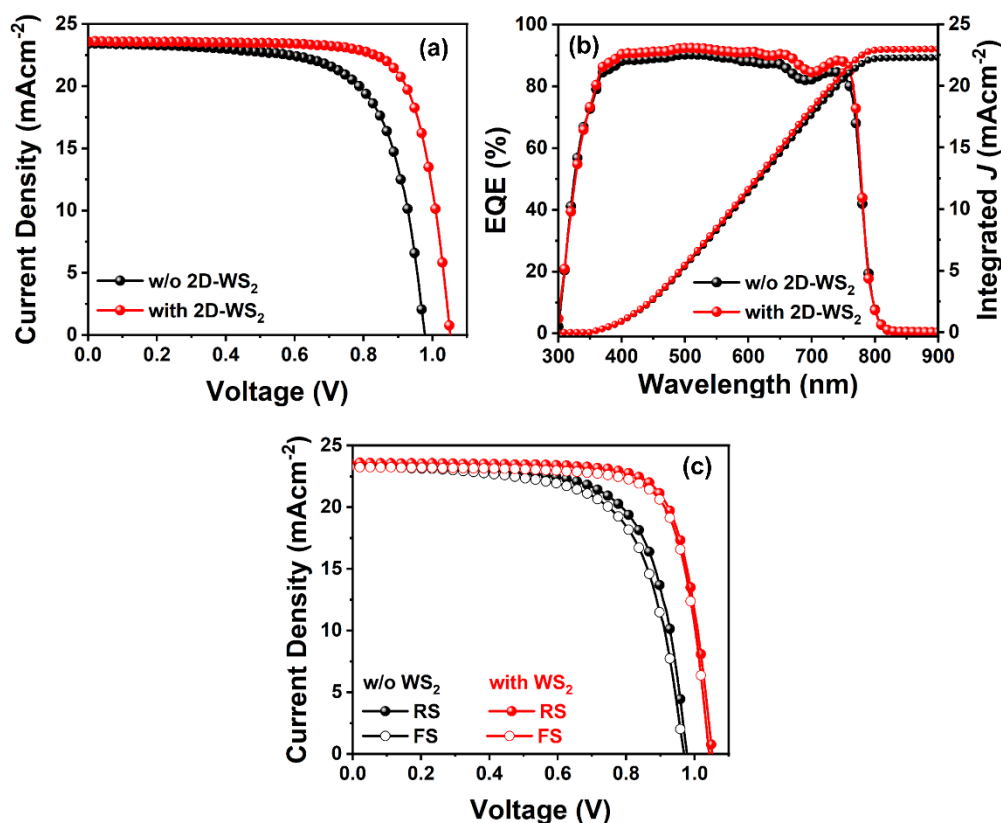


Figure 4. 6 (a) J - V curves of the champion PSCs with and without the interface layer, and (b) the corresponding EQE and integrated current. (c) J - V hysteresis curve of forward and reverse scans of the champion PSCs.

Table 4. 1 PV parameters of the champion devices with or without the 2D-WS₂ interfacial layer.

Device	Direction	V_{oc} (mV)	J_{sc} (mAcm ⁻²)	FF (%)	PCE (%)	R_s (Ω)	R_{sh} (k Ω)
Without WS ₂	RS	976.7	23.39	68.88	15.74	46.75	19.52
	FS	967.6	23.29	66.47	14.98	52.33	14.38
	Statistics	970.90 \pm 9.89	22.66 \pm 0.86	70.01 \pm 2.41	15.38 \pm 0.36		
With WS ₂	RS	1051.6	23.59	76.68	19.02	36.54	61.12
	FS	1041.6	23.24	76.93	18.62	38.77	45.27
	Statistics	1043.12 \pm 10.15	23.31 \pm 0.39	76.86 \pm 0.68	18.69 \pm 0.31		

4.3.4 Photo-Induced Charge Transfer Dynamics

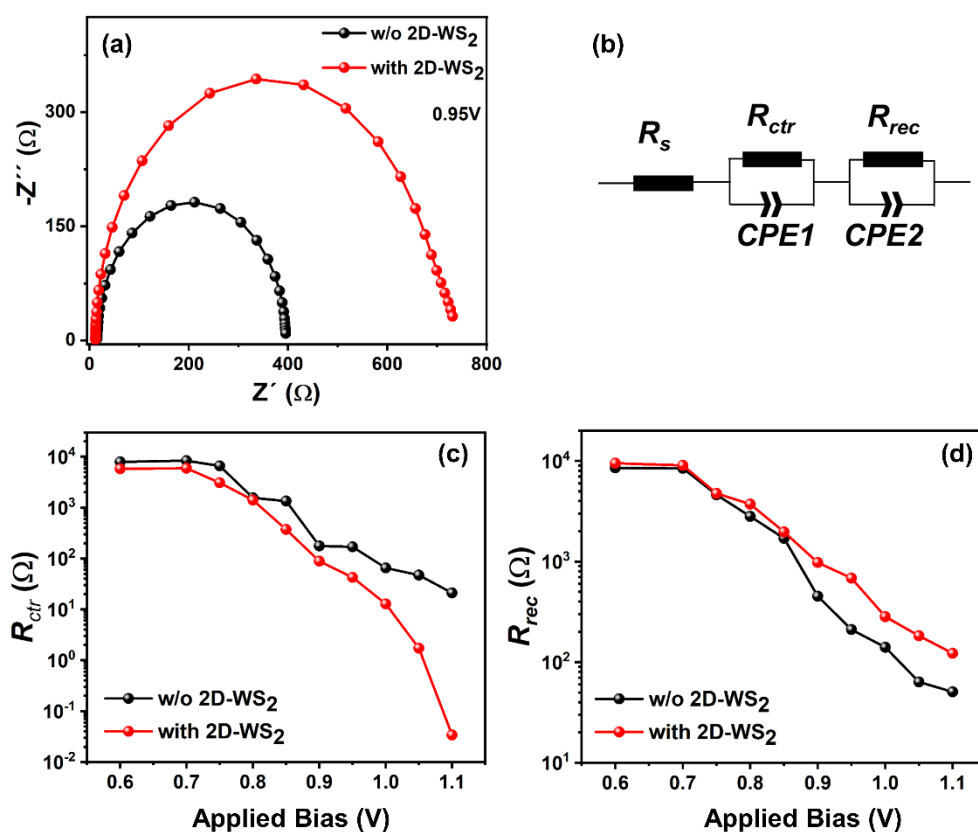


Figure 4. 7 (a) Electrochemical impedance spectra of PSCs recorded with an applied voltage of 0.95 V and under dark conditions. (b) The equivalent circuit used for the fitting of the impedance spectra. The potential bias-dependent (b) charge transport resistance and (c) interfacial charge recombination resistance.

The influence of the 2D-WS₂ interface layer on charge dynamics in the PSCs was analyzed using electrochemical impedance spectroscopy (EIS) under dark conditions. The Nyquist plot is shown with the equivalent circuit model (Figure 4.7a, and Table 4.2) that comprises single series resistance (R_s), charge transfer resistance (R_{ctr}), and charge recombination resistance (R_{rec}) at the interface between the perovskite/HTL (Figure 4.7b), and two constant phase elements related to carrier diffusion in the perovskite and selective layers (CPE1 and CPE2). We noted that at a given potential bias, the R_{ctr} in the PSC with a 2D-WS₂ interfacial layer is much lower than that of the control device, inferring that the interfacial layer plays a critical role in promoting the charge transfer dynamics at the perovskite/HTM interface (Figure 4.7c). The relative trend of R_{ctr} is in agreement with that of the R_s obtained from the J - V curves. This reduced R_s correlated with the lower R_{ctr} further confers the enhanced FF of the device with the

Chapter 4

2D-WS₂ interfacial layer⁴⁰. Furthermore, at a similar potential bias, the PSC with the interfacial layer features a higher R_{rec} than the control device, which reflects the higher resistance for charge annihilating at the interface (Figure 4.6d). The carrier recombination behavior was further assessed using the semi-logarithmic J - V curve recorded in the dark (Figure 4.8a). By fitting the exponential region of the curve with the Shockley equation, we obtain^{41,42}

$$J_{\text{dark}} = J_0 \left[\exp \left(\frac{qV}{n_{\text{id}} K_B T} \right) - 1 \right] \quad (4.1)$$

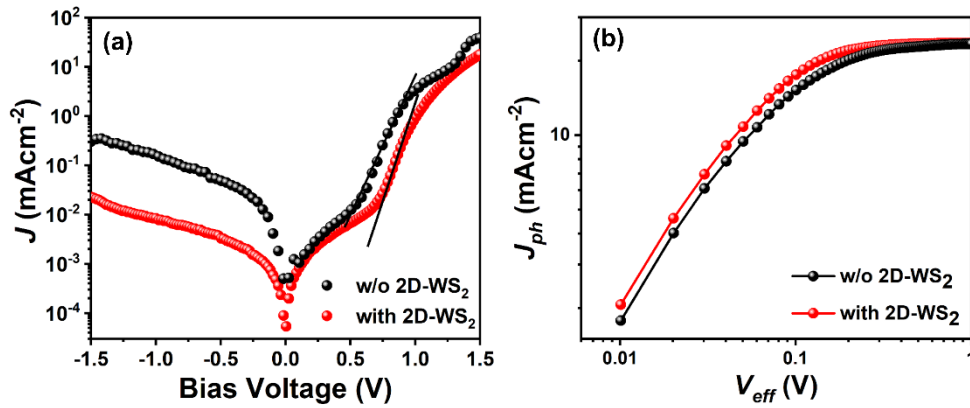


Figure 4. 8 (a) The dark J - V curve of the PSCs and (b) photo-generated current density, J_{ph} vs. effective voltage (V_{eff}).

in which J_{dark} is the dark current density, J_0 is the saturation current density, V is the applied voltage, q is the electron charge, K_B is the Boltzmann constant, T is the temperature, and n_{id} is the ideality factor. We estimated the J_0 and n_{id} for the control PSC to be 4.834×10^{-6} mAcm⁻² and 2.69, respectively, and those for the device with the 2D-WS₂ interface layer are 2.109×10^{-7} mAcm⁻² and 2.47, respectively. Such low J_0 and n_{id} values associated with the use of the 2D-WS₂ interface layer indicate a low leakage current density and significantly hindered carrier recombination, enhancing the charge transfer dynamics in the PSC. This escalates the FF, V_{oc} , and subsequently the PCE of the PSC with the use of an interfacial layer.^{25,43} The dark current results are consistent with the R_{rec} obtained from the EIS measurements. To identify the charge collection and exciton dissociation in the presence of the 2D-WS₂ interlayer, we measured (Figure 4.8b) the photocurrent density (J_{ph}) as a function of effective voltage (V_{eff}). The J_{ph} is defined as the difference between the current density under illumination (J_L) and in the dark (J_D); ($J_{\text{ph}} = J_L - J_D$). The term V_{eff} follows the formula of $V_{\text{eff}} = V_0 - V$, where V_0 is the compensation voltage defined as $J_{\text{ph}} = 0$, and V is the applied voltage.⁴³⁻⁴⁵ Remarkably, the

Chapter 4

device with the 2D-WS₂ interface layer displays a saturation of photocurrent at a relatively low V_{eff} (0.3 V) compared to that of the control PSC (0.58 V), suggesting an effective charge extraction behavior in the PSC with a 2D-WS₂ interfacial layer. Ideally, the efficiency of charge dissociation and collection depends on the maximum exciton generation rate (G_{max}), which follows the relationship of $J_{\text{sat}} = eLG_{\text{max}}$, where J_{sat} , e , and L are the saturated J_{ph} , elementary charge, and the thickness of the perovskite layer, respectively.⁴⁵ As tabulated in Table 4.3), we calculated the G_{max} to be $3.68 \times 10^{21} \text{ s}^{-1}$ for the 2D-WS₂ interface-layer-based PSC, which is slightly higher than $3.65 \times 10^{21} \text{ s}^{-1}$ for the control PSC. This enhanced G_{max} suggests that the introduction of a 2D-WS₂ layer at the PTAA/perovskite interface promotes the interfacial charge transfer dynamics in the PSCs.

Table 4. 2 Data extracted from the electrochemical impedance spectroscopy at an applied voltage of 0.95 V in dark conditions.

Device parameter	Without 2D-WS ₂	With 2D-WS ₂
R_s (Ω)	15.58	12.33
R_{ctr} (Ω)	169.1	42.39
R_{rec} (Ω)	210.6	682.5
CPE1 (F)	94.9×10^{-9}	15.15×10^{-6}
CPE2 (F)	0.1389×10^{-6}	64.88×10^{-9}

Table 4. 3 Photoelectrical parameters of the devices.

Device parameter	Without 2D-WS ₂	With 2D-WS ₂
Ideality factor, n_{id}	2.69	2.47
Saturation current density, J_0 (mAcm ⁻²)	4.834×10^{-6}	2.109×10^{-7}
Effective voltage, V_{eff} (V)	0.3	0.58
Saturation photocurrent density, J_{sat} (mA)	23.39	23.60
Maximum excitation generation rate, G_{max} (S ⁻¹)	3.65×10^{21}	3.68×10^{21}

Chapter 4

4.3.5 Low-Temperature Admittance Spectroscopy

Arguably, the photo-generated charge carriers can easily drift under an operational electric field and accumulate at the interfaces due to the poor band alignment and/or poor mobility of the charge transport layers or poor charge extraction, which promotes the charge build-up at the interface and consequently deficit the V_{oc} .⁴⁶⁻⁴⁸ Additionally, the trap density plays the foremost role in governing the overall performance of the PSC in which the trapped charges at the interface show restriction to their mobility. The increase in trap density can further diminish the trapped charge carriers through nonradiative recombination, thereby limiting the PCE.⁴⁷ To gain further insight into the charge accumulation behavior at the perovskite/HTL interface with and without the 2D-WS₂ interface layer, we performed the temperature-dependent capacitance-frequency (*c-f*) measurement.

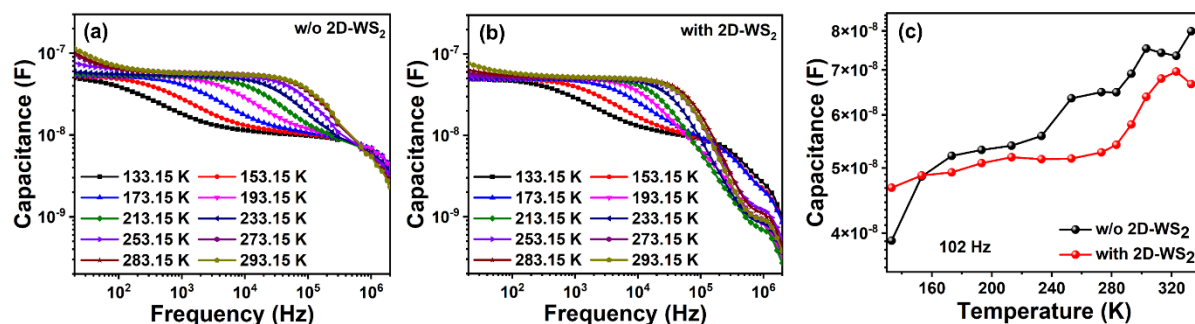


Figure 4. 9 Temperature-dependent capacitance–frequency (*c-f*) measurements of the PSCs without (a) and with (b) the 2D-WS₂ interfacial layer. (c) Temperature-dependent low-frequency capacitance variation of the devices with and without 2D-WS₂.

Figure 4.9a and b show the *c-f* data for PSCs as a function of temperature from 133.15–293.15 K under short circuit dark conditions. We noted that below 213.15 K, the geometrical capacitance, as determined from the constant capacitance plateau at the intermediate frequency region, freezes out in both devices. Deeper traps participate in the capacitance as the frequency decreases resulting in a capacitance build-up at the low-frequency region.⁴⁹ In the low-frequency region, the control device shows limited capacitance build-up from low temperatures until 233.15 K, and later, thermally activated capacitance shows a significant increment that can be ascribed to the charge accumulation and build-up at the interfaces.^{49,50} In particular, the PSC with the additional interfacial layer displays a nearly constant capacitance until 253.15 K from low temperatures throughout the low-frequency region, and then it increases slightly,

Chapter 4

beyond this temperature. However, the capacitance build-up is high in the PSCs without the interfacial layer as compared to the PSC with the 2D-WS₂ layer, confirming that the 2D-WS₂ layer can hinder the charge accumulation at the perovskite/PTAA interface. Figure 4.9c further illustrates the temperature-dependent capacitance variation in the PSC at low frequency (102 Hz). We investigated the trap profile associated with the PSCs by identifying the characteristic trap emission parameter, known as an attempt-to-escape frequency (ν_0), which represents the dynamics of trap emission and defines the maximum rate of detrapping the trapped charges. Figure 4.10a and b illustrate the variation of $-fdC/df$ as a function of frequency and the peak emission rates (f_{peak}) were extracted. The f_{peak} increases gradually with temperature from 133.15 K until room temperature and then plateau on a further increment of temperature (Figure 4.8 c and d). According to the Arrhenius relationship, the emission rate (e_n) of the trapped charge in a defect shows the following correlation with the associated trap activation energy E_T ,⁵⁰

$$\ln\left(\frac{e_n}{T^2}\right) = \ln\left(\frac{\nu_0}{T^2}\right) - \frac{E_T}{K_B T} \quad (4.2)$$

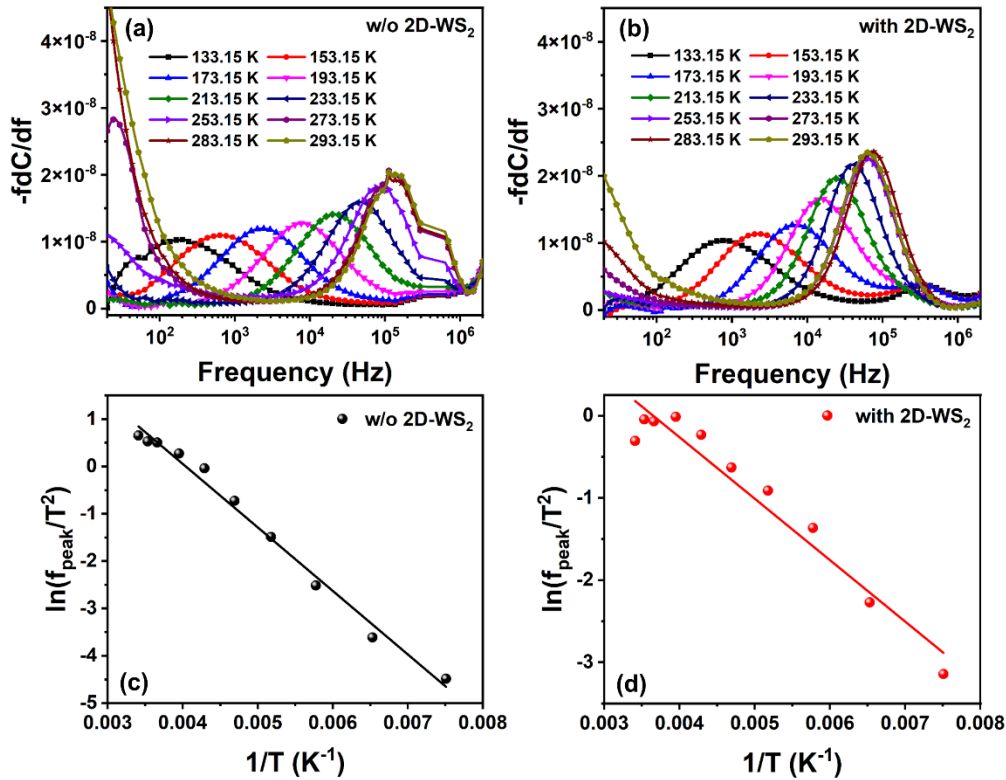


Figure 4. 10 $-fdC/df$ vs. frequency variation at low temperature for the devices without (a) and with (b) 2D-WS₂ interface layer. Arrhenius plot of the PSCs without (c) and with (d) the 2D-WS₂ interfacial layer.

Chapter 4

where e_n is the measurement frequency at peak (f_{peak}), K_B is the Boltzmann constant, and T is the temperature. The calculated trap energy for the PSC with and without 2D-WS₂ is 115.63 and 64.38 meV respectively from the trap energy plot (Figure 4.10c and d). The corresponding ν_0 of the control PSC is 2.04×10^7 Hz, which is much higher than that of the PSC with the interface layer (1.38×10^6 Hz).

We identified the trap-state distributions and energies affected by the 2D-WS₂ interface layer, by the trap state profile using thermal admittance spectra along with the Mott-Schottky spectra (Figure 4.11a). At room temperature, the built-in-potential (v_{bi}) and the depletion layer thickness (W) obtained for the control PSC are 991.80 mV and 140.17 nm, respectively. Expectedly, the PSC with the 2D-WS₂ interface layer shows improved results achieving a v_{bi} of 1073.85 mV and a w of 236.10 nm. The increased v_{bi} and W values escalate the charge separation and transfer at the perovskite/PTAA interface. In the trap density profiles shown in Figure 4.11b, at room temperature (303.15 K), for control PSCs, a peak trap density of $3.45 \times 10^{17} \text{ cm}^{-3} \text{ eV}^{-1}$ at 0.134 eV appears, while the PSC with 2D-WS₂ displays a smaller peak intensity of $2.58 \times 10^{17} \text{ cm}^{-3} \text{ eV}^{-1}$ at a shallow energy level of 0.77 eV. Furthermore, the control PSC shows an intense trap density across the higher energy region from 0.3-0.36 eV. Based on these results, we can conclude that the 2D-WS₂ interface layer can passivate charge traps at the perovskite interface. This highlights the critical role of the interface layer in controlling the interface charge separation and recombination in the device, leading to a significant improvement in V_{oc} and PCE.

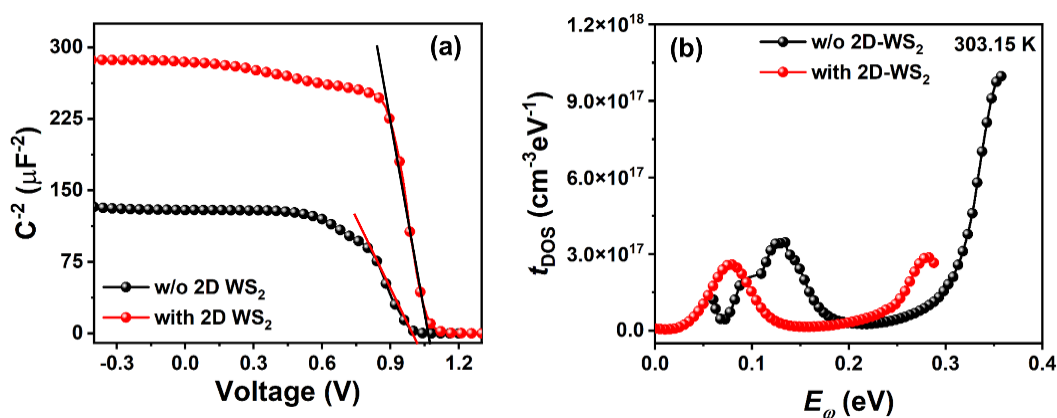


Figure 4. 11 (a) Mott–Schottky analysis at 10 kHz and (b) trap density of states deduced from temperature-dependent C – f spectroscopy for the PSCs without and with 2D-WS₂.

4.3.6 Long-Term Device Stability

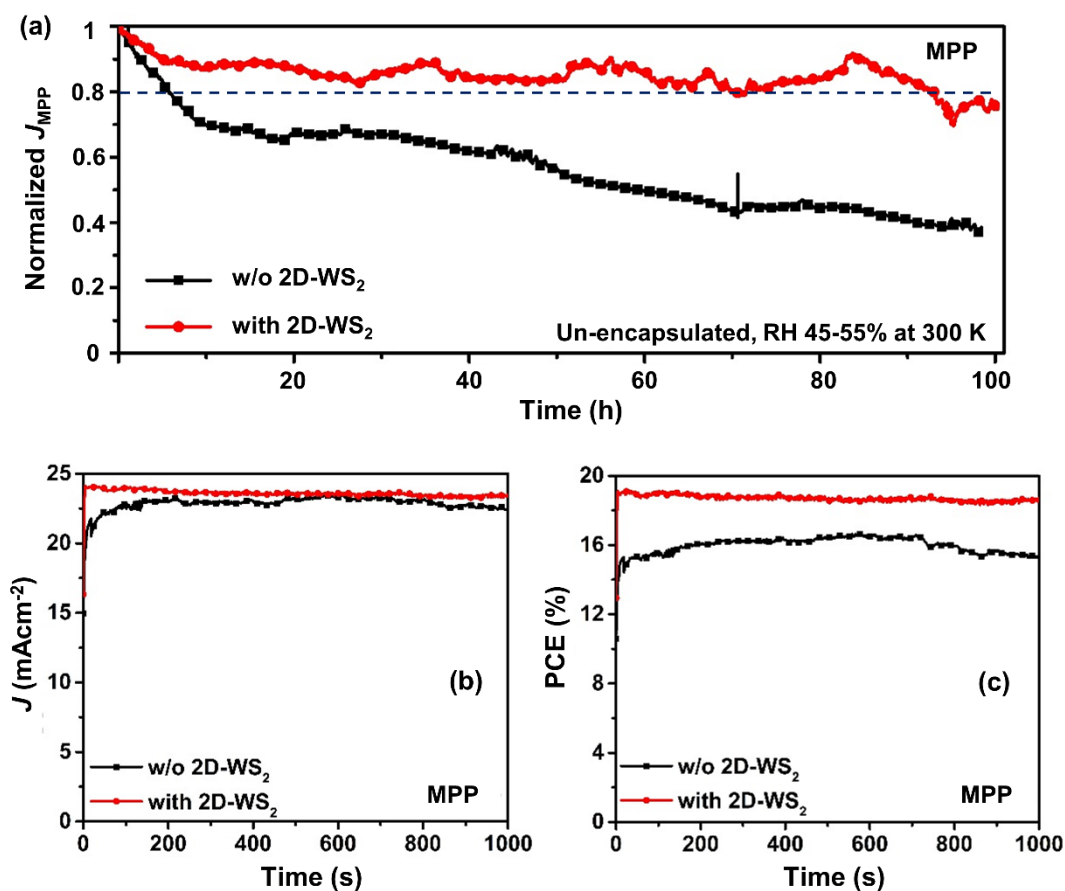


Figure 4. 12 (a) Normalized J_{sc} for 100 h of continuous MPP tracking for un-encapsulated PSCs under an ambient atmosphere. Initial 1000 s MPP tracking of (b) J and (c) PCE.

The beneficial role played by the incorporation of the 2D-WS₂ layer in charge transfer dynamics while promoting PV performances led us to study its impact on the long-term operational stability; MPP tracking⁵¹ of un-encapsulated PSCs was conducted under 1 sun illumination at room temperature with 50-60% humidity (Figure 4.12). The control PSCs reached 80% of their initial photocurrent after 8 h of continuous illumination and the photocurrent reduces continuously under ambient conditions, while, under similar conditions, the PSCs with the 2D-WS₂ interface layer retained 80% of their initial photocurrent for 100 h. Moreover, the PSC with a 2D-WS₂ interfacial layer showed more stabilized J_{sc} and V_{oc} (Figure 4.10 b and c). 2D-WS₂ deposited on the perovskite layer yielded a higher contact angle of $87 \pm 1^\circ$ compared to that of the bare perovskite ($81 \pm 1^\circ$) suggesting the hydrophobic nature

Chapter 4

associated with the 2D-WS₂ that can mitigate the water penetration into the active perovskite layer in the PSC (Figure A4.2, Appendix B).

4.4 Conclusions

In summary, we demonstrated the role of 1T-rich 2D-WS₂ nanosheets, particularly synthesized via Li⁺ intercalated liquid-phase exfoliation, in enhancing the optoelectronic properties via stimulating the photo-induced charge transfer dynamics and suppressing the surface trap density. We found that the trap density reduction in the target device was about 25% with a saturation of photocurrent at a relatively low V_{eff} (0.3 V) due to the 2D-WS₂ interfacial layer. The presented protocol based on the introduction of 2D-WS₂ between the un-doped PTAA and the perovskite absorber enabled the demonstration of *n-i-p* PSCs with a stabilized efficiency of over 19%, paving the way toward reliability enhancement in PSCs for commercial viability.

4.5 Supporting Information

4.5.1 Materials

Lead iodide (99.9%) was purchased from Tokyo Chemical Industry (TCI) and employed as such. Methylammonium iodide (MAI) and formamidinium iodide (FAI) were purchased from Dyesol. Solvents including DMF, DMSO, ethyl acetate, ethanol, and chlorobenzene were purchased from Acros Chemicals and used as such.

4.5.2 Device fabrication

Device fabrication was conducted as described in Chapter 2 section 2.3.1. Interfacial layer was introduced between CsFAMA and pristine PTAA film. Once the perovskite layer cooled down to room temperature, 0.3 mg/ml WS₂ in isopropanol solution was spin-coated at 2000 rpm for 30 s (the process was repeated 3-4 times). For control devices, PTAA was directly deposited on the perovskite active layer.

4.5.3 Trap density measurements.

Temperature-dependent capacitance–frequency measurements were performed with an LCR meter, model no. E4980A, along with a Linkam (LTS420) sample heating control system filled with nitrogen in a closed environment. The energetic profile of trap density of state (t_{DOS}) was calculated with the following equations:⁵²

Chapter 4

$$N_T(E_\omega) = -\frac{v_{bi}}{qw} \frac{dC}{d\omega} \frac{\omega}{K_B T} \quad (4.3)$$

$$E_\omega = K_B T \ln\left(\frac{v_0}{\omega}\right) \quad (4.4)$$

$$\frac{1}{c^2} = \frac{2}{\varepsilon \varepsilon_0 A^2 q N} \left[v - v_{bi} - \frac{K_B T}{q} \right] \quad (4.5)$$

where v_{bi} is the built-in-potential, w is the depletion layer thickness, C is the capacitance measured at an angular frequency ω , T is the temperature, K_B is the Boltzmann constant, q is the elementary charge, ε is the relative dielectric constant of the perovskite (ε is 13 from a previous report)⁴⁹, ε_0 is the permittivity of free space, and A is the active interfacial area.

4.5.4 Materials and thin-film characterization

X-Ray photoelectron spectroscopy (XPS) experiments were carried out on a SPECS system (Berlin, Germany) equipped with a Phoibos 150 1D-DLD analyzer with monochromated Al K_α radiation (1486.7 eV). The wide scan was performed with step energy of 1 eV (dwell time: 0.1 s, pass energy: 80 eV), and a detailed analysis of the elements was performed using 0.08 eV step energy (dwell time: 0.1 s, pass energy: 30 eV) with an electron exit angle of 90°. The spectra were adjusted using CasaXPS 2.3.16 software, which models Gauss–Lorentzian contributions. X-ray diffractograms were recorded using a D8 Advance diffractometer from Bruker (Bragg–Brentano geometry, with an X-ray tube Cu K_α , $\lambda = 1.5406 \text{ \AA}$). For obtaining surface topologies and phase images, atomic force microscopy (CSI Nano observer AFM) was used and the data were analyzed using Gwyddion software. We recorded the absorption spectra with the help of a UV-vis-IR spectrophotometer (Varian Cary 50 UV/Vis Spectrophotometer). The cross-sectional and top-views of the microstructure were acquired with the help of a Hitachi S-4800 scanning electron microscope.

Additional data is available in Appendix B

4.6 Bibliography

1. X. Liu, Y. Cheng, B. Tang, Z. G. Yu, M. Li, F. Lin, S. Zhang, Y.-W. Zhang, J. Ouyang and H. Gong, Shallow defects levels and extract detrapped charges to stabilize highly efficient and hysteresis-free perovskite photovoltaic devices. *Nano Energy*, 2020, 71, 104556.
2. K.-G. Lim, S. Ahn and T.-W. Lee, Energy level alignment of dipolar interface layer in organic and hybrid perovskite solar cells. *J. Mater. Chem. C*, 2018, 6, 2915–2924.
3. A. Agresti, A. Pazniak, S. Pescetelli, A. Di Vito, D. Rossi, A. Pecchia, M. A. der Maur, A. Liedl, R. Larciprete, D. V. Kuznetsov, D. Saranin and A. Di Carlo, Titanium-carbide MXenes for work function and interface engineering in perovskite solar cells. *Nat. Mater.*, 2019, 18, 1264.
4. A. Rajagopal, K. Yao and A. K.-Y. Jen, Toward perovskite solar cell commercialization: A perspective and research roadmap based on interfacial engineering. *Adv. Mater.*, 2018, 30, 1800455.
5. T. Wang, Z. Cheng, Y. Zhou, H. Liu and W. Shen, Highly efficient and stable perovskite solar cells via bilateral passivation layers. *J. Mater. Chem. A*, 2019, 7, 21730–21739.
6. L. Calio', S. Kazim, M. Gra'tzel and S. Ahmad, Hole-transport materials for perovskite solar cells. *Angew. Chem., Int. Ed.*, 2016, 55, 14522–14545.
7. N. E. Courtier, J. M. Cave, J. M. Foster, A. B. Walker and G. Richardson, How transport layer properties affect perovskite solar cell performance: insights from a coupled charge transport/ion migration model. *Energy Environ. Sci.*, 2019, 12, 396–409.
8. S. Wang, T. Sakurai, W. Wen and Y. Qi, Energy level alignment at interfaces in metal halide perovskite solar cells. *Adv. Mater. Interfaces*, 2018, 5, 1800260.
9. M. I. Saidaminov, J. Kim, A. Jain, R. Quintero-Bermudez, H. Tan, G. Long, F. Tan, A. Johnston, Y. Zhao, O. Voznyy and E. H. Sargent, Suppression of atomic vacancies via incorporation of isovalent small ions to increase the stability of halide perovskite solar cells in ambient air. *Nat. Energy*, 2018, 3, 648–654.
10. I. Lee, J. H. Yun, H. J. Son and T.-S. Kim, Accelerated degradation due to weakened adhesion from Li-TFSI additives in perovskite solar cells. *ACS Appl. Mater. Interfaces*, 2017, 9, 7029–7035.

Chapter 4

11. K. Domanski, E. A. Alharbi, A. Hagfeldt, M. Graetzel and W. Tress, Systematic investigation of the impact of operation conditions on the degradation behaviour of perovskite solar cells. *Nat. Energy*, 2018, 3, 61–67.
12. A. R. Bowring, L. Bertoluzzi, B. C. O'Regan and M. D. McGehee, Reverse bias behavior of halide perovskite solar cells. *Adv. Energy Mater.*, 2017, 8, 1702365.
13. N. Ahn, K. Kwak, M. S. Jang, H. Yoon, B. Y. Lee, J.-K. Lee, P. V. Pikhitsa, J. Byun and M. Choi, Trapped charge-driven degradation of perovskite solar cells. *Nat. Commun.*, 2016, 7, 13422.
14. B. Chen, M. Yang, S. Priya and K. Zhu, Origin of J - V hysteresis in perovskite solar cells. *J. Phys. Chem. Lett.*, 2016, 7, 905–917.
15. W. Tress, N. Marinova, T. Moehl, S. M. Zakeeruddin, M. K. Nazeeruddin and M. Graetzel, Understanding the rate-dependent J - V hysteresis, slow time component, and aging in $\text{CH}_3\text{NH}_3\text{PbI}_3$ perovskite solar cells: the role of a compensated electric field. *Energy Environ. Sci.*, 2015, 8, 995–1004.
16. L.-L. Jiang, Z.-K. Wang, M. Li, C.-H. Li, P.-F. Fang and L.-S. Liao, Flower-like MoS_2 nanocrystals: a powerful sorbent of Li^+ in the Spiro-OMeTAD layer for highly efficient and stable perovskite solar cells *J. Mater. Chem. A*, 2019, 7, 3655–3663.
17. G. Kakavelakis, I. Paradisanos, B. Paci, A. Generosi, M. Papachatzakis, T. Maksudov, L. Najafi, A. E. Del Rio Castillo, G. Kioseoglou, E. Stratakis, F. Bonaccorso and E. Kymakis, Extending the continuous operating lifetime of perovskite solar cells with a molybdenum disulfide hole extraction interlayer. *Adv. Energy Mater.*, 2018, 8, 1702287.
18. S. Tsarev, I. K. Yakushchenko, S. Y. Luchkin, P. M. Kuznetsov, R. S. Timerbulatov, N. N. Dremova, L. A. Frolova, K. J. Stevenson and P. A. A. Troshin, A new polytriarylamine derivative for dopant-free high-efficiency perovskite solar cells. *Energy Fuels*, 2019, 3, 2627–2632.
19. G. S. Han, Y. H. Song, Y. U. Jin, J.-W. Lee, N.-G. Park, B. K. Kang, J.-K. Lee, I. S. Cho, D. H. Yoon and H. S. Jung, Reduced graphene oxide/mesoporous TiO_2 nanocomposite based perovskite solar cells. *ACS Appl. Mater. Interfaces*, 2015, 7, 23521–23526.
20. A. Agresti, S. Pescetelli, L. Cina, D. Konios, G. Kakavelakis, E. Kymakis and A. D. Carlo, Efficiency and stability enhancement in perovskite solar cells by inserting lithium-neutralized graphene oxide as electron transporting layer. *Adv. Funct. Mater.*, 2016, 26, 2686–2694.

Chapter 4

21. W. Li, H. Dong, X. Guo, N. Li, J. Li, G. Niu and L. Wang, Graphene oxide as dual functional interface modifier for improving wettability and retarding recombination in hybrid perovskite solar cells. *J. Mater. Chem. A*, 2014, 2, 20105–20111.
22. M. Hadadian, J.-P. Correa-Baena, E. K. Goharshadi, A. Ummadisingu, I.-J. Seo, J. Luo, S. Gholipour, S. M. Zakeeruddin, M. Saliba, A. Abate, M. Graetzel and A. Hagfeldt, Enhancing efficiency of perovskite solar cells via N-doped graphene: crystal modification and surface passivation. *Adv. Mater.*, 2016, 28, 8681–8686.
23. G. Kakavelakis, E. Kymakis and K. Petridis, 2D materials beyond graphene for metal halide perovskite solar cells. *Adv. Mater. Interfaces*, 2018, 5, 1800339.
24. N. Alias, A. A. Umar, N. A. A. Malek, K. Liu, X. Li, N. A. Abdullah, M. M. Rosli, M. Y. Abd Rahman, Z. Shi, X. Zhang, H. Zhang, F. Liu, J. Wang and Y. Zhan, Photoelectrical dynamics uplift in perovskite solar cells by atoms thick 2D TiS₂ layer passivation of TiO₂ nanograss electron transport layer. *ACS Appl. Mater. Interfaces*, 2021, 13, 3051–3061.
25. P. Huang, Z. Wang, Y. Liu, K. Zhang, L. Yuan, Y. Zhou, B. Song and Y. Li, Water-soluble 2D transition metal dichalcogenides as the hole-transport layer for highly efficient and stable *p-i-n* perovskite solar cells. *ACS Appl. Mater. Interfaces*, 2017, 9, 25323–25331.
26. D. H. Shin, J. S. Ko, S. K. Kang and S.-H. Choi, Enhanced flexibility and stability in perovskite photodiode–solar cell nanosystem using MoS₂ electron-transport layer. *ACS Appl. Mater. Interfaces*, 2020, 12, 4586–4593.
27. K. Sobayel, M. Akhtaruzzaman, K. S. Rahman, M. T. Ferdaous, Z. A. A. Mutairi, H. F. Alharbi, N. H. Alharthi, M. R. Karim, S. Hasmady and N. Amin, A comprehensive defect study of tungsten disulfide (WS₂) as electron transport layer in perovskite solar cells by numerical simulation. *Results Phys.*, 2019, 12, 1097–1103.
28. R. Singh, A. Giri, M. Pal, K. Thiyagarajan, J. Kwak, J. J. Lee, U. Jeong and K. Cho, Perovskite solar cells with an MoS₂ electron transport layer. *J. Mater. Chem. A*, 2019, 7, 7151–7158.
29. G. Tang, P. You, Q. Tai, A. Yang, J. Cao, F. Zheng, Z. Zhou, J. Zhao, P. K. L. Chan and F. Yan, Solution-phase epitaxial growth of perovskite films on 2D material flakes for high-performance solar cells. *Adv. Mater.*, 2019, 1807689.
30. A. Capasso, F. Matteocci, L. Najafi, M. Prato, J. Buha, L. Cina, V. Pellegrini, A. D. Carlo and F. Bonaccorso, Few-layer MoS₂ flakes as active buffer layer for stable perovskite solar cells. *Adv. Energy Mater.*, 2016, 6, 1600920.

Chapter 4

31. Z. Liu, N. Li, C. Su, H. Zhao, L. Xu, Z. Yin, J. Li and Y. Du, Colloidal synthesis of 1T' phase dominated WS₂ towards durable electrocatalysis. *Nano Energy*, 2018, 50, 176–181.
32. N. A. A. Malek, N. Alias, A. A. Umar, X. Zhang, X. Li, S. K. M. Saad, N. A. Abdullah, H. Zhang, Z. Weng, Z. Shi, C. Li, M. M. Rosli and Y. Zhan, Enhanced charge transfer in atom-thick 2H–WS₂ nanosheets' electron transport layers of perovskite solar cells. *Sol. RRL*, 2020, 4, 2000260.
33. M. H. Li, T. G. Sun, J. Y. Shao, Y. D. Wang, J. S. Hu and Y. W. Zhong, A sulfur-rich small molecule as a bifunctional interfacial layer for stable perovskite solar cells with efficiencies exceeding 22%. *Nano Energy*, 2021, 79, 105462.
34. Y. Zhou, C. Liu, F. Meng, C. Zhang, G. Wei, L. Gao and T. Ma, Recent progress in perovskite solar cells modified by sulfur compounds. *Sol. RRL*, 2021, 2000713.
35. J. Wang, H. Shi, N. Xu, J. Zhang, Y. Yuan, M. Lei, L. Wang and P. Wang, Aza[5]helicene rivals N-annulated perylene as π -linker of D– π –D typed hole-transporters for perovskite solar cells. *Adv. Funct. Mater.*, 2020, 30, 2002114.
36. H. Liu, X. Fu, W. Fu, B. Zong, L. Huang, H. Bala, S. Wang, Z. Guo, G. Sun, J. Cao and Z. Zhang, An effective TiO₂ blocking layer for hole-conductor-free perovskite solar cells based on carbon counter electrode. *Org. Electron.*, 2018, 59, 253–259.
37. G. Yang, C. Chen, F. Yao, Z. Chen, Q. Zhang, X. Zheng, J. Ma, H. Lei, P. Qin, L. Xiong, W. Ke, G. Li, Y. Yan and G. Fang, Effective carrier-concentration tuning of SnO₂ quantum dot electron-selective layers for high-performance planar perovskite solar cells. *Adv. Mater.*, 2018, 30, 1706023.
38. N. E. Courtier, J. M. Cave, J. M. Foster, A. B. Walker and G. Richardson, How transport layer properties affect perovskite solar cell performance: insights from a coupled charge transport/ion migration model. *Energy Environ. Sci.*, 2019, 12, 1718.
39. Y. Liu, Z. Liu and E. C. Lee, High-performance inverted perovskite solar cells using doped poly(triarylamine) as the hole transport layer. *ACS Appl. Energy Mater.*, 2019, 2, 1932–1942.
40. G. A. H. Wetzelaer, M. Kuik, M. Lenes and P. W. M. Blom, Origin of the dark-current ideality factor in polymer: fullerene bulk heterojunction solar cells. *Appl. Phys. Lett.*, 2011, 99, 153506.
41. A. Mahapatra, N. Parikh, P. Kumar, M. Kumar, D. Prochowicz, A. Kalam, M. M. Tavakoli and P. Yadav, Changes in the electrical characteristics of perovskite solar cells with aging time. *Molecules*, 2020, 25, 2299.

Chapter 4

42. N. E. Courtier, Interpreting ideality factors for planar perovskite solar cells: ectypal diode theory for steady-state operation. *Phys. Rev. Appl.*, 2020, 14, 024031–024052.
43. Z. Luo, G. Li, W. Gao, K. Wu, Z. G. Zhang, B. Qiu, H. Bin, L. Xue, F. Liu, Y. Li and C. Yang, A universal nonfullerene electron acceptor matching with different band-gap polymer donors for high-performance polymer solar cells. *J. Mater. Chem. A*, 2018, 6, 6874–6881.
44. J. Troughton, N. Gasparini and D. Baran, $\text{Cs}_{0.15}\text{FA}_{0.85}\text{PbI}_3$ perovskite solar cells for concentrator photovoltaic applications. *J. Mater. Chem. A*, 2018, 6, 21913–21917.
45. L. Xiao, T. Liang, K. Gao, T. Lai, X. Chen, F. Liu, T. P. Russell, F. Huang, X. Peng and Y. Cao, Ternary solar cells based on two small molecule donors with same conjugated backbone: The role of good miscibility and hole relay process. *ACS Appl. Mater. Interfaces*, 2017, 9, 29917–29923.
46. H. Jin, E. Debroye, M. Keshavarz, I. G. Scheblykin, M. B. J. Roeffaers, J. Hofkens and J. A. Steele, It's a trap! On the nature of localised states and charge trapping in lead halide perovskites. *Mater. Horiz.*, 2020, 7, 397–410.
47. I. Zarazua, J. Bisquert and G. G. Belmonte, Light-induced space-charge accumulation zone as photovoltaic mechanism in perovskite solar cells. *J. Phys. Chem. Lett.*, 2016, 7, 525–528.
48. M. Samiee, S. Konduri, B. Ganapathy, R. Kottokkaran, H. A. Abbas, A. Kitahara, P. Joshi, L. Zhang, M. Noack and V. Dalal, Defect density and dielectric constant in perovskite solar cells. *Appl. Phys. Lett.*, 2014, 105, 153502.
49. J. A. Carr, M. Elshobaki and S. Chaudhary, Deep defects and the attempt to escape frequency in organic photovoltaic materials. *Appl. Phys. Lett.*, 2015, 107, 203302.
50. N. H. Hemasiri, S. Kazim and S. Ahmad, Reduced trap density and mitigating the interfacial losses by placing 2D dichalcogenide material at perovskite/HTM interface in a dopant free perovskite solar cells. *Nano Energy*, 2020, 77, 105292.
51. M. V. Khenkin, E. A. Katz, A. Abate, G. Bardizza, J. J. Berry, C. Brabec, F. Brunetti, V. Bulovic, Q. Burlingame, A. D. Carlo, R. Cheacharoen, Y. B. Cheng, A. Colmann, S. Croa, K. Domanski, M. Dusza, C. J. Fell, S. R. Forrest, Y. Galagan, D. D. Girolamo, M. Gratzel, A. Hagfeldt, E. V. Hauff, H. Hoppe, J. Kettle, H. Kobler, M. S. Leite, S. Liu, Y. L. Loo, J. M. Luther, C. Q. Ma, M. Madsen, M. Manceau, M. Matheron, M. McGehee, R. Meitzner, M. K. Nazeeruddin, A. F. Nogueira, C. Odabasi, A. Osherov, N. G. Park, M. O. Reese, F. D. Rossi, M. Saliba, U. S. Schubert, H. J. Snaith, S. D. Stranks, W. Tress, P. A. Troshin, V. Turkovic, S. Veenstra, I. V. Fisher, A. Walsh, T.

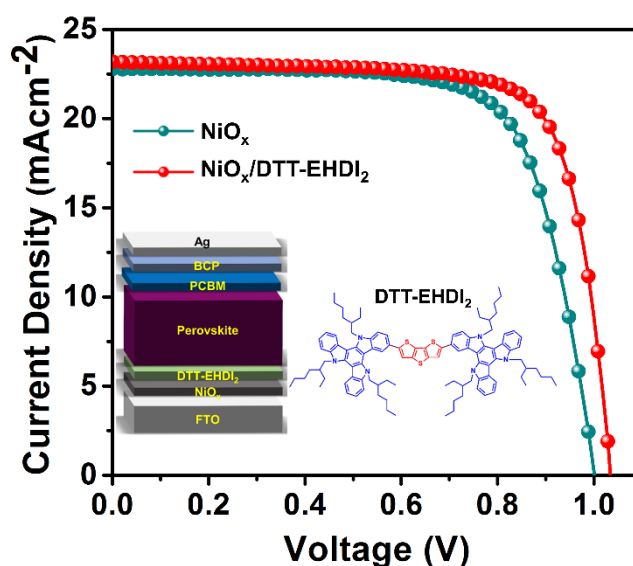
Chapter 4

Watson, H. Xie, R. Yildirim, S. M. Zakeeruddin, K. Zhu and M. L. Cantu, Consensus statement for stability assessment and reporting for perovskite photovoltaics based on ISOS procedures. *Nat. Energy*, 2020, 5, 35–49.

52. J. N. Wilson, J. M. Frost, S. K. Wallace and A. Walsh, Dielectric and ferroic properties of metal halide perovskites. *APL Mater.*, 2019, 7, 010901.

CHAPTER 5

NiO_x NANOCRYSTAL ASSISTED INTERFACE MODULATION FOR THE PERFORMANCE BOOSTING OF INVERTED PEROVSKITE SOLAR CELLS



Data presented in this chapter are based on the following publication:

Molecular interface engineering via triazatruxene-based moieties/NiO_x as hole-selective bilayers in perovskite solar cells for reliability.

Naveen Harindu Hemasiri, Laura Calì, Meenakshi Pegu, Samrana Kazim, Shahzada Ahmad
Solar RRL, 2022, 6, 2100793.
doi.org/10.1002/solr.202100793

Chapter 5

5.1 Abstract

Inverted perovskite solar cells are among the most exciting photovoltaic systems as they combine low fabrication cost, time, ease of fabrication, and high spectral tenability upon perovskite grain growth. Many promising fabrication techniques are widely available for devices fabricating, but the drawback of the perovskite solar cell is the lack of device stability. Engineering the interface at hole transport layers and perovskite not only eliminates the defective charge build-up at the interface, accelerating the charge transfer process of the device but also enhances the stability by avoiding the possible degradation mechanisms of perovskite originating from the hole transport layer. Herein, we demonstrate the application of an interface modulation of NiO_x nanocrystal assisted low-temperature processed inverted perovskite solar cells using an organic semiconductor (DTT-EHDI₂), which is composed of dithienothiophene (DTT) as the core and a planar triazatruxene incorporating an alkyl chain as the side group. Our strategy, therefore, provides an effective direction of the cost-effective thiophene derivative as an interfacial agent together with an inorganic nanocrystal layer to escalate the optoelectronic performances in photovoltaics.

5.2 Introduction

Most of the highly efficient PSCs are categorized in the regular architecture (*n-i-p*), in which the high-temperature sintered mesoporous TiO₂ is a prerequisite.¹ On the other hand; planar inverted (*p-i-n*) configuration can be adapted to low-temperature fabrication techniques with potentially high manufacturing processability, giving rise to intense research interest for the flexible PSCs and large area modules. However, the PCE of inverted PSCs still lags behind that of their structural counterpart (*n-i-p*) devices.^{2,3}

The hole transport layer (HTL) is rationally selected by taking into consideration the charge mobility, energy-level alignment, and compatibility with the perovskite absorber.^{4,5} The bottom layers have a significant impact on the development and crystallinity of the perovskite film with a minimum defective structure and surface, which is grown on the HTL in the case of *p-i-n* devices. Further, incompatibility between HTL and perovskite promotes the hysteresis and the degradation of electrical performances in PSCs, and such issues can be addressed by the interface engineering of PSCs.⁶⁻⁹ The frequently used HTLs in planar *p-i-n* PSCs are poly(3,4-ethylenedioxythiophene)-poly(styrenesulfonate)-{PEDOT:PSS} and poly[bis(4-

Chapter 5

phenyl)(2,4,6-trimethylphenyl)amine] {PTAA}.^{10,11,12} However, the hygroscopic nature and highly acidic property associated with PEDOT:PSS accelerate the degradation of the perovskite layer and compromise the long-term PSCs stability.^{13,14} Further, perovskite shows appalling film coverage on severe nonwetting HTL such as pristine PTAA, which renders PSCs with poor short-circuit current density (J_{sc}) and fill factor (FF).¹⁵

PSCs using NiO_x nanocrystals (NCs) as HTL exhibited excellent stability under prolonged operational conditions.¹⁶ Even though, the intrinsic NiO_x is a wide-bandgap (>3.5 eV) *p*-type semiconductor with high hole mobility, it suffers from weak built-in-field strength and large energy level offset at the interface of NiO_x/perovskite due to limited hole concentration and the wide gap between Fermi level and its valence band maximum (VBM).^{2,17,18} The large energy level offset at the interface can result in the hole accumulation at the HTL/perovskite interface, thus with the possibility of photo-induced charge recombination at the interface.¹⁹ To minimize this, considerable efforts have been laid to improve the energy band alignment, which in turn can enhance photo-induced charge transfer dynamics at the NiO_x/perovskite interface through the incorporation of an interfacial layer.

In this chapter, we systematically investigate the performance enhancement of *p-i-n* PSCs based on simple yet effective interface modulation on NiO_x NC film using an organic molecules labeled as DTT-EHDI₂, with dithieno[3,2-b:2',3'-d]thiophene (DTT) as the core and 5,10,15-tris(2-ethylhexyl)-10,15-dihydro-5H-diindolo[3,2-a:3',2'-c]carbazole (EHDI) as substituents. Thiophene-based derivatives as HTM have been extensively utilized since the electron-rich sulfur atoms in thiophene render a strong electron donor character, that facilitates efficient charge transport.²⁰⁻²² In addition, the high polarizability of sulfur atoms and lower stabilization energy in thiophene rings allows the stabilization of the conjugated chain and reduces the energy level, and subsequently enhance the charge transport properties, accelerating the extraction of holes from the surface of the perovskite.^{20,21} Planar nitrogen-containing triazatruxene (TAT) came out as a promising donor core unit or side group for organic molecules owing to the tunable electro-optical properties.²³⁻²⁸ TAT is a synthetically versatile constituent with three indole units fused to a benzene ring in a π -conjugated structure that provides a route to high hole mobility as a consequence of electron-donating properties and strong π - π intermolecular interaction.²⁵ Moreover, the three indole cores in the TAT building block can be easily modified to increase stability and solubility.²³ However, hitherto, the behavior of thiophene and TAT-based molecules has not been thoroughly studied as an

Chapter 5

interfacial layer in inverted PSCs. We found that a thin layer of DTT-EHDI₂ tuned the wettability of the NiO_x NC film, which tends to lessen the number of nucleation sites in the perovskite. The π -bridge between the thiophene core and the donor groups renders high performance in PSCs indicating 18.15% PCE and exhibiting a significant performance increment to that of the reference PSCs (16.66%).

5.3 Results and Discussion

5.3.1 Materials and Thin-Film Characterization

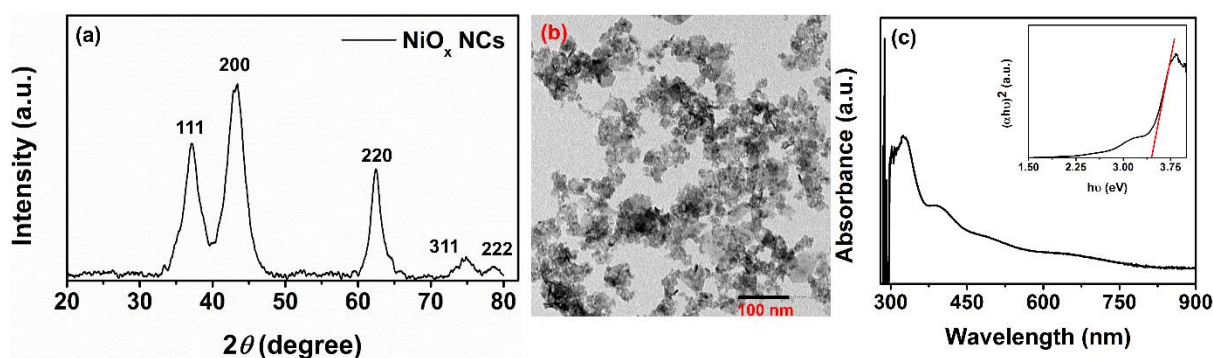


Figure 5. 1 (a) UV–vis absorption spectra, (b) Transition electron microscopy (TEM) of drop-casted NiO_x NC aqueous solution, and (c) X-ray diffraction (XRD) pattern of the NiO_x film.

The X-ray diffraction (XRD) pattern of as-synthesized NiO_x NCs exhibit a cubic crystal structure with the characteristic diffraction peaks at 37.18° , 43.28° , and 62.42° corresponding to the (111), (200), and (220) planes (Figure 5.1a).^{16,29} Figure 5.1b shows the good uniformity of NiO_x NCs with similar particle sizes from transition electron microscopy (TEM). The estimated optical bandgap derived from the UV-vis of the NiO_x film was 3.45 eV (Figure 5.1c). Owing to the high absorption and higher thermal stability, triple-cation perovskite (FA, MA, and Cs) was used as a light harvester to fabricate PSCs.¹⁸ The microstructures of the NiO_x NC film and DTT-EHDI₂ deposited on FTO were investigated by scanning electron microscopy (SEM), as illustrated in Figures 5.2a and b, respectively. The contact angles of the perovskite precursor on NiO_x and DTT-EHDI₂/NiO_x were measured to be $33 \pm 1^\circ$ and $58 \pm 1^\circ$ (Figure 5.2c and d), suggesting the role of the DTT-EHDI₂ layer in the surface property. Notably, we observed that the grain size of perovskite grown on DTT-EHDI₂/NiO_x is slightly larger and uniform than that on the NiO_x film (Figure 5.3e and f). The enhanced grain growth could be attributed to the lower wettability of DTT-EHDI₂ compared with NiO_x that tends to shrink the

Chapter 5

number of nucleation sites in the perovskite and provides extra space for larger grain growth during annealing, resulting in diminishing the trap states and possible recombination pathways.^{30,31}

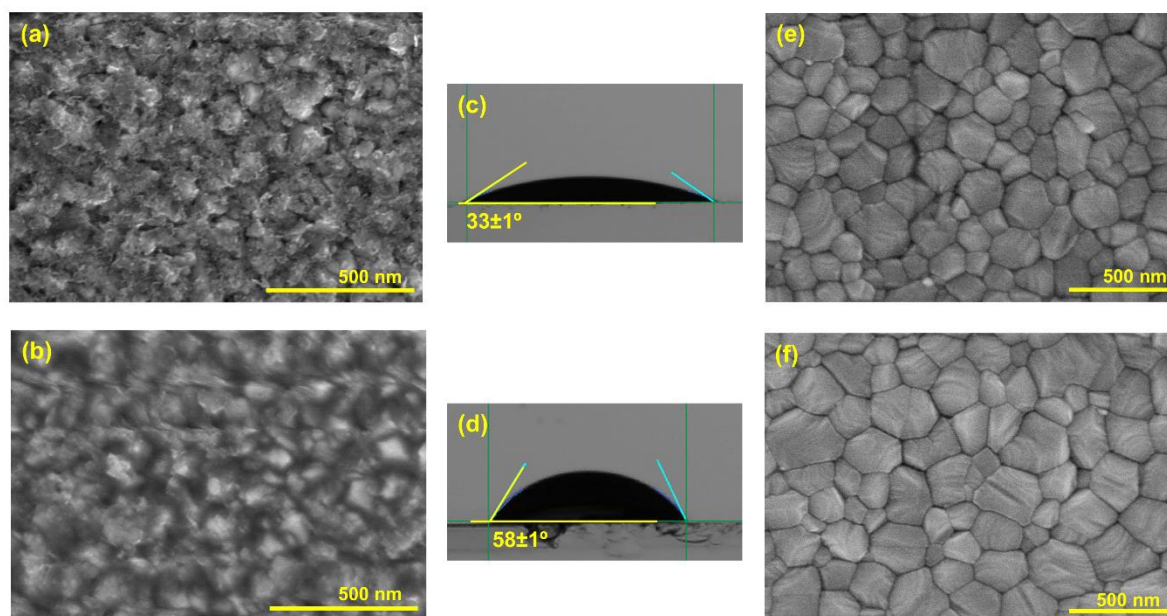


Figure 5. 2 Surface SEM images of (a) NiO_x NC film, (b) DTT-EHDI₂ deposited on NiO_x NC film. Contact angle of perovskite on (a) NiO_x, and (b) DTT-EHDI₂/NiO_x NC films. Surface SEM images of CsFAMA grown on (e) NiO_x film and (f) DTT-EHDI₂/NiO_x NC film. To note here, images (a) and (b) are in 90 K magnification, while (e) and (f) are in 60 K magnification.

We probed the surface with scanning probe microscopy (SPM) to evaluate the surface microstructure and roughness of NiO_x and DTT-EHDI₂/NiO_x. We noted that root-mean square (RMS) roughness of the NiO_x and DTT-EHDI₂/NiO_x films are 35.77 and 24.59 nm, respectively (Figure A5.1, Appendix C), crediting surface smoothness upon DTT-EHDI₂ deposition, where the interfacial properties impact the charge transport properties of the device. The surface topography and phase images (Figure 5.3) of the perovskite deposited on different surfaces, where the perovskite displays uniform and significantly reduced RMS roughness (31.77 nm) on DTT-EHDI₂/NiO_x, as compared with that of the perovskite on NiO_x (40.44 nm). The DTT-EHDI₂ assisted in perovskite crystallization, which is favorable for effective charge extraction. Diffractograms were recorded to decipher the crystal structure of the perovskite (Figure 5.3a), in which the predominant peak appears at 14.1° in both situations corresponding to the (101) crystal plane of CsFAMA; this indicates the suitable crystallinity of the perovskite.

Chapter 5

In the UV-vis absorption spectra (Figure 5.3b), the absorption edge of the films largely remains unchanged upon interface engineering with DTT-EHDI₂.

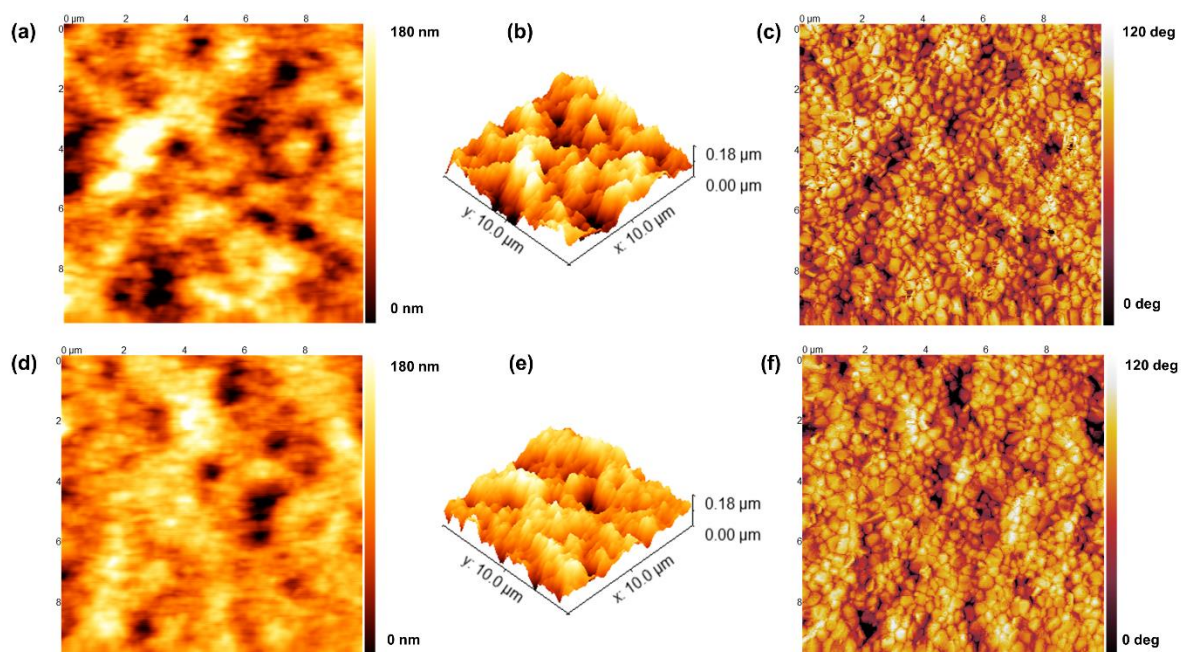


Figure 5. 3 Topography, 3D height, and phase images of the perovskite deposited on NiO_x (a, b, and c) and on DTT-EHDI₂/NiO_x (d, e, and f), respectively.

The influence of the thin film of DTT-EHDI₂ on the charge transport properties of NiO_x as HTLs was probed by measuring their thin-film *I-V* profile, in FTO/NiO_x/Au and FTO/NiO_x/DTT-EHDI₂/Au configurations in the dark (Figure 5.4c). The conductivity of NiO_x/DTT-EHDI₂ was $37.59 \times 10^{-6} \text{ S cm}^{-1}$, similar to NiO_x ($28.24 \times 10^{-6} \text{ S cm}^{-1}$). The hole mobility of NiO_x with and without DTT-EHDI₂ interfacial layer was 2.78×10^{-5} and $6.91 \times 10^{-5} \text{ cm}^2 \text{ V}^{-1} \text{ s}^{-1}$, respectively, derived from semilogarithmic $J^{0.5}$ -*V* curves of the hole-only devices in the dark (Figure 5.4d) via the classical Mott–Gurney space–charge-limited-current (SCLC) law;

$$J = 9\varepsilon\varepsilon_0\mu V_{app}^2/8L^3 \quad (5.1)$$

Here, ε_0 , ε , and *L* represent the dielectric constant of free space, the relative dielectric constant, and the thickness of the charge transport layer, respectively.³² The dielectric constant for NiO_x was taken as 4.8.³³ We estimated the hole mobility of DTT-EHDI₂ and noted it to be $1.12 \times 10^{-6} \text{ cm}^2 \text{ V}^{-1} \text{ s}^{-1}$ (Figure A5.2, Appendix C).

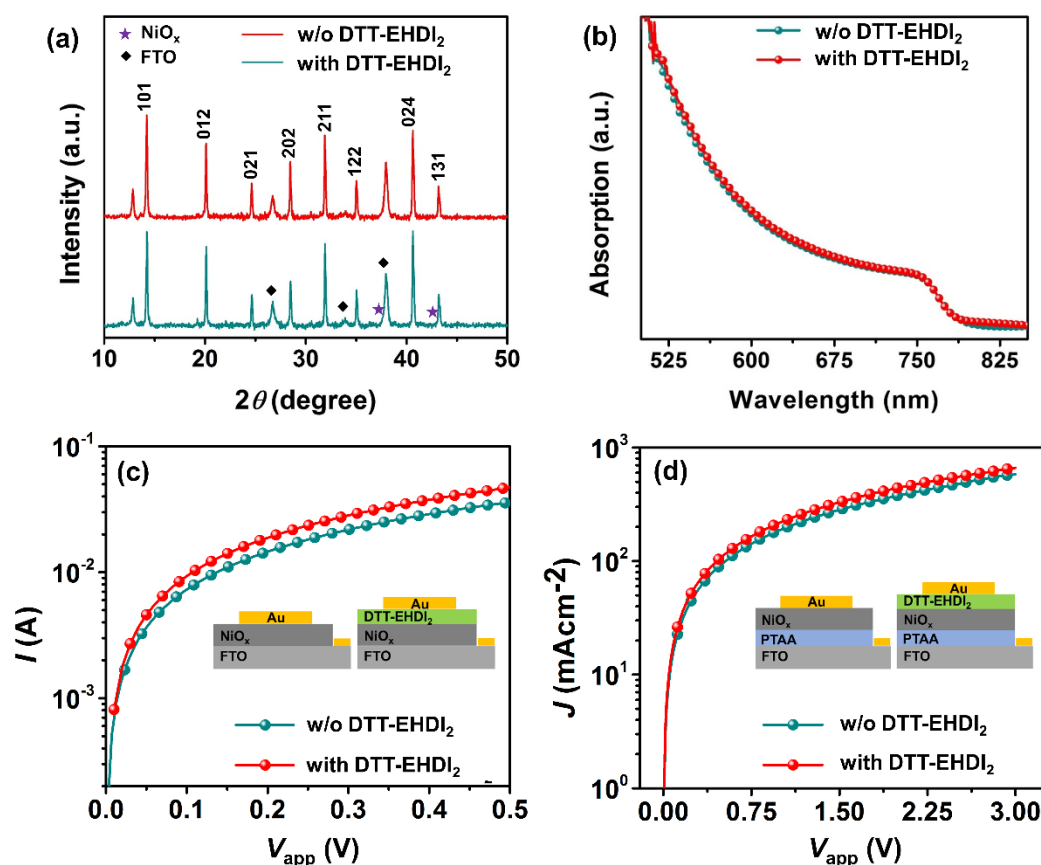


Figure 5. 4 XRD patterns of CsFAMA perovskite deposited on NiO_x film and DTT-EHDI₂/NiO_x film. (b) UV-Vis spectra of NiO_x/CsFAMA with and without DTT-EHDI₂ interface layer (c) I - V curves for conductivity measurements in the configuration of FTO/NiO_x/Au and FTO/NiO_x/DTT-EHDI₂ in the dark. (d) J - V curves for hole-mobility measurements with the hole-only device with the configurations of FTO/PTAA/NiO_x/Au and FTO/PTAA/NiO_x/DTT-EHDI₂/Au in the dark.

5.3.2 Device and Photovoltaic Characterization

The chemical structure of the DTT-EHDI₂ is shown in Figure 5.5a. The calculated HOMO level for DTT-EHDI₂ (-5.34 eV) is suitable with the valence band of Cs_{0.1}(FA_{0.9}MA_{0.1})_{0.9}Pb(I_{0.9}Br_{0.1})₃, which is assumed as -5.80 eV, as reported by Wu et al. for triple-cation perovskites.³⁴ The LUMO level was found to be -2.81 eV, which is beneficial to overcome the undesirable electron transfer from perovskite to the HTL. The energy bandgap between the HOMO and LUMO of DTT-EHDI₂ was measured to be 2.53 eV. The valence band maximum of NiO_x NC film is -5.21 eV, which is about 0.13 eV higher compared with the HOMO level of DTT-EHDI₂, indicating a narrow energy barrier for hole transfer between

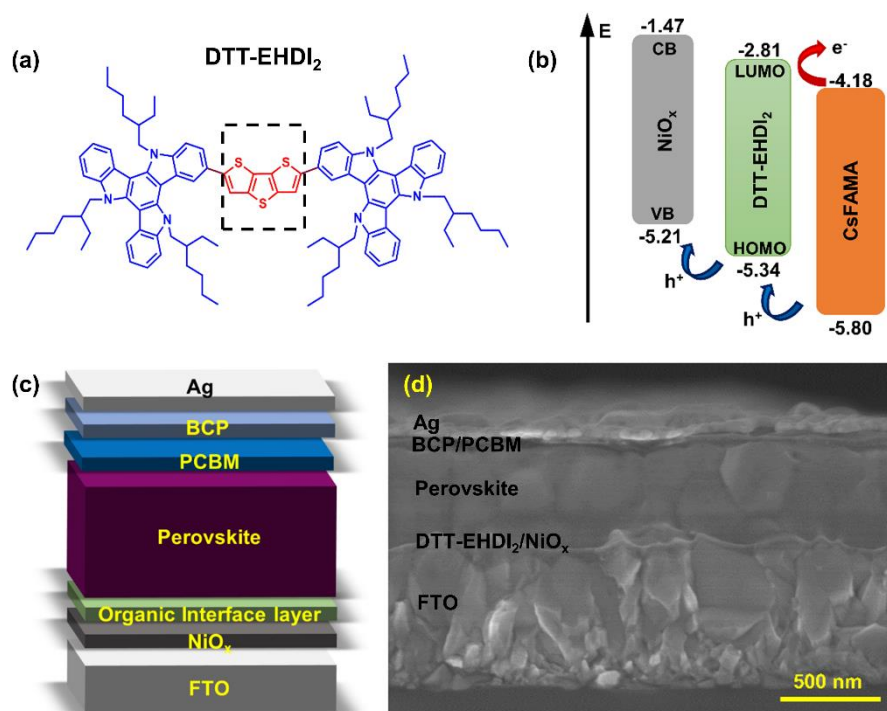


Figure 5. 5 (a) Chemical structure of DTT-EHDI₂ (2,6-bis(5,10,15-tris(2-ethylhexyl)-10,15-dihydro-5H-diindolo[3,2-a:3',2'-c]carbazol-3-yl)dithieno[3,2-b:2',3'-d]thiophene). (b) Energy band alignment at the NiO_x/CsFAMA interface. (c) p-i-n device structure and (d) cross-sectional SEM image of the fabricated PSC.

perovskite/NiO_x (Figure 5.5b), and will form a beneficial spike structure.¹⁸ We assessed the organic interface layer in planar PSCs with a device architecture, FTO/NiO_x/interface layer/Cs_{0.1}(FA_{0.9}MA_{0.1})_{0.9}Pb(I_{0.9}Br_{0.1})₃/PC₆₀BM/BCP/Ag (Figure 5.5c). The cross-sectional SEM image of PSCs with the interfacial layer (Figure 5.5d) reveals an interconnected and sandwiched structure of NiO_x (~70 nm) and the interface layer (~20 nm), together with a ~400 nm-thick perovskite layer. The typical current-voltage (*J-V*) curves of the PSCs with and without the interfacial layer are shown (Figure 5.6a) and the corresponding PV parameters are represented in Table 5.1. It can be deduced from the reverse scan *J-V* curves that the interface layer on NiO_x enabled the *V*_{oc}, *J*_{sc}, and FF of the PSCs to increase from 1000.13 mV, 22.79 mA cm⁻², and 72.96% to 1034.09 mV, 23.18 mA cm⁻², and 75.71%, respectively. Subsequently, the interface modulated PSCs yielded an overall PCE of 18.15% with an average PCE of 17.93%, while the control PSCs showed a maximum PCE of 16.66%. Furthermore, the incident photon-to-current efficiency (IPCE) spectrum and the achieved integrated current densities (*J*_{int}) of 21.42 and 21.79 mA cm⁻² for devices with and without the interface layer, respectively, exhibit a consistent trend with the characteristic *J-V* curve (Figure 5.6b). We evaluated the

Chapter 5

hysteresis index (HI) following the equation $HI = [J_{RS}(0.8V_{oc}) - J_{FS}(0.8V_{oc})]/J_{RS}(0.8V_{oc})$, where $J_{RS}(0.8V_{oc})$ and $J_{FS}(0.8V_{oc})$ represent the J_{sc} at 80% of V_{oc} from reverse and forward J - V scans, respectively (Figure 5.6c).³⁵ The molecularly engineered interface-based PSCs exhibit negligible hysteresis effect with 0.02, which is considerably lower than that of the control PSCs (0.05), suggesting the upgraded photoinduced charge transfer dynamic induced by the interfacial layer. Moreover, the PSC with the interface layer showed stabilized J_{sc} (Figure 5.6d) at maximum power point (MPP) tracking under ambient conditions (~ 40 – 60% RH at 28°C). The statistical PV parameters of PSCs w/o and with DTT-EHDI₂ interface layer were summarized in Figure A5.3 (Appendix C).

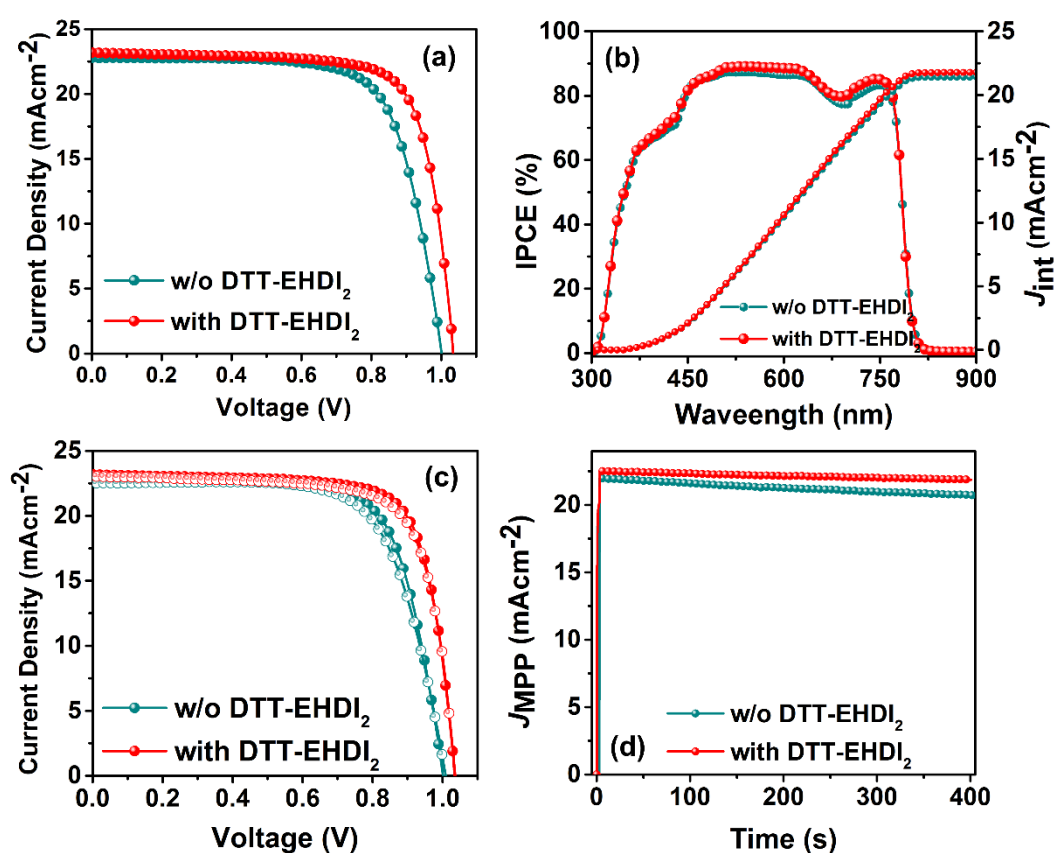


Figure 5. 6 (a) J - V curve of the champion device without and with DTT-EHDI₂ interface layer in reverse scan under simulated AM 1.5G illumination. (b) The corresponding IPCE and integrated current density. (c) J - V hysteresis curve of forward and reverse scans of the champion PSCs. (d) Stabilized initial 400 s MPP tracking of J_{sc} under ambient conditions.

We further analyzed the series resistance (R_s) and shunt resistance (R_{sh}) by estimating the slope of the J - V curves near V_{oc} and J_{sc} , respectively (Table 1). The control PSC showed higher R_s of $42.99\ \Omega$ and lower R_{sh} of $32.88\ \text{k}\Omega$, whereas the interlayer-based PSC gave notably reduced R_s

Chapter 5

of 36.05 Ω and higher R_{sh} of 65.96 k Ω values. We attribute the significantly enhanced FF for the PSC with the interface layer to the relatively reduced R_s and higher R_{sh} .³⁵ The presence of a interface layer with effective electron-blocking properties and synergistically suppressed interfacial recombination losses is responsible for the observed high R_{sh} .

Table 5. 1 PV parameters of the champion devices with and without the organic interfacial layer.

Device	Direction	V_{oc} (mV)	J_{sc} (mAcm ⁻²)	FF (%)	PCE (%)	* R_s (Ω)	* R_{sh} (k Ω)
Without WS ₂	RS	1001.38	22.80	72.96	16.66	42.99	32.88
	FS	1008.96	22.52	70.34	15.98	45.38	28.20
	Statistics	997.35 \pm 9.8	22.58 \pm 0.29	72.34 \pm 0.85	16.29 \pm 0.42		
With WS ₂	RS	1034.09	23.18	75.71	18.15	36.05	65.96
	FS	1036.07	23.04	74.21	17.72	37.73	57.94
	Statistics	1031.17 \pm 3.9	23.06 \pm 0.13	75.36 \pm 0.47	17.92 \pm 0.13		

* R_s and R_{sh} of PSCs were estimated by the slope of the J - V curves near V_{oc} and J_{sc} , respectively.

5.3.3 Recombination and Charge-Transfer Kinetics

We investigated the charge transfer kinetics and recombination mechanism in PSCs with and without the interfacial layer using electrochemical impedance spectroscopy (EIS) techniques under dark conditions. Figure 5.7a shows the Nyquist plot at 950mV applied bias voltage in the dark which is fitted with the equivalent circuit model of $R_s + R_{ctr}/CPE1 + R_{rec}/CPE2$, where R_s , R_{ctr} , and R_{rec} represent single-series resistance, charge transfer resistance, and charge recombination resistance at the interface between perovskite/HTL, respectively.^{36,37} R_{ctr} was extracted from the high-frequency region, while R_{rec} was determined in the low-frequency region (Table 5.2). Two constant phase elements related to carrier diffusion in perovskite and selective layers were assigned as CPE1 and CPE2. The interface modulated PSC featured a higher R_{rec} at the entire bias range (Figure 5.7b), leading to lower charge recombination and mitigated charge annihilation at the interface. The introduction of the interface layer reduces the energy barrier at the perovskite/HTM interface, which facilitates efficient charge extraction

Chapter 5

without charge build-up at the interface impacting V_{oc} enhancement. Moreover, at a given potential bias, the PSC incorporating the interface layer shows a much lower R_{ctr} than that of the control PSC (Figure 5.7c). Generally, the EIS analysis is consistent with the R_s and R_{sh} obtained from the J - V curve, inferring that the interfacial layer promotes the photoinduced charge transfer kinetics at the perovskite/HTM interface.

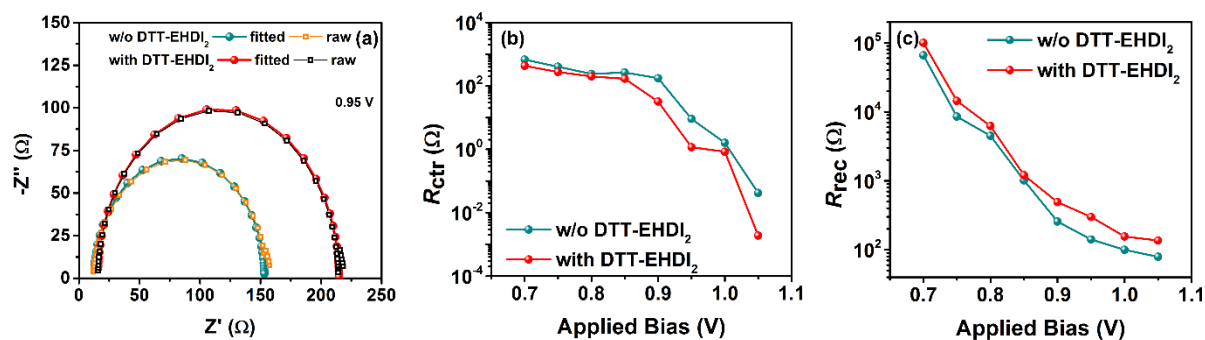


Figure 5. 7 (a) Electrochemical impedance spectra of PSCs measured at an applied voltage of 950 mV in the dark (raw and fitted data). The potential bias-dependent (b) charge transport resistance, (c) interfacial charge recombination resistance extracted from Nyquist plots in the dark.

Bode EIS spectra were conducted at 0.95 V in the dark (Figure 5.8a) to elucidate the impact of the interface layer on charge lifetime (τ), followed by $\tau = 1/(2\pi f_p)$. Here, f_p denotes the peak frequency corresponding to the electrochemical reaction of the charge transfer process at the perovskite/ NiO_x interface.³⁸ The PSC based on the interfacial layer showed a longer charge lifetime (0.73 μ s) compared with that in the PSC without the interfacial layer (0.57 μ s). The enhanced electron lifetime can be credited to the reduced charge recombination, resulting in rapid charge carrier transport and enhanced electron density at NiO_x /perovskite interface. Further, τ of the modified PSC is higher than that of the control PSC at various bias voltages (Figure 5.8b). The J - V profile in the dark was conducted to further understand the leakage current and carrier recombination behavior of the PSCs (Figure 5.8c). The leakage current represented by the semilogarithmic curve at the negative bias potential of the interface layer-based PSCs is much lower than that of the control PSC, signaling that the higher J_{sc} obtained is through suppressing recombination. By fitting the linear part of the curve with the Shockley equation as explained in Chapter 4, we extracted the ideality factor (n_{id}) of the PSCs. The estimated J_0 and n_{id} for the PSCs without the interface layer were 9.35×10^{-6} mA cm^{-2} and 3.17, respectively, whereas those for the PSCs with the interface layer were 5.07×10^{-7} mA cm^{-2} and 2.58, respectively. Such low J_0 and n_{id} values of the interface layer- incorporated PSCs indicate

Chapter 5

the efficient recombination suppression along with lower leakage current outside the depletion region upon the interfacial layer, resulting in enhanced V_{oc} , FF, and charge transfer dynamics in the fabricated PSCs.

Table 5. 2 Extracted electrochemical parameters of the PSCs with and without the interface layer at 950 mV bias voltage under dark conditions.

Device	R_{ctr} (Ω)	R_{rec} (Ω)	f_p (μs)	τ (μs)
w/o interface layer	9.02	140.70	3.58	0.57
with interface layer	1.16	299.10	4.57	0.73

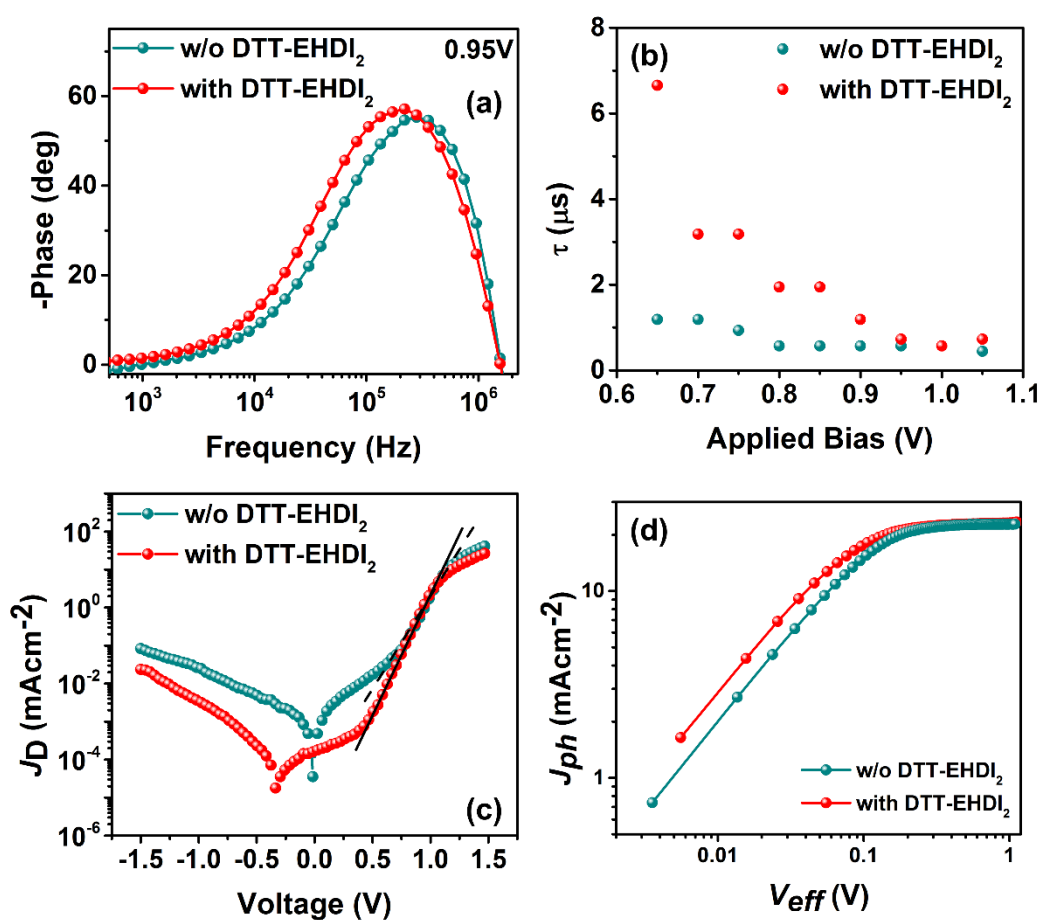


Figure 5. 8 (a) Bode spectra of PSCs measured at an applied voltage of 950 mV in the dark, (b) applied bias-dependent charge lifetime in the dark, and (c) dark J - V curves for the PSCs with and without the interfacial layer. (d) Photogenerated current density (J_{ph}) versus effective voltage (V_{eff}).

Chapter 5

To provide mechanistic insights into the interface layer impact on the photoinduced charge transfer dynamics in PSCs, we investigated the effective voltage (V_{eff})-dependent photocurrent density (J_{ph}) (Figure 5.8d). J_{ph} and V_{eff} follow the relationships of $J_{\text{ph}} = J_{\text{L}} - J_{\text{D}}$ and $V_{\text{eff}} = V_0 - V$, respectively, where J_{L} is current density under illumination, J_{D} is current density in the dark, V_0 is the compensation voltage defined at $J_{\text{ph}} = 0$, and V is the external bias voltage.³⁶ Notably, the PSC based on the interface layer displays a rapid saturation of photocurrent at a relatively low V_{eff} of 0.207 V when compared with that of the control device (0.376 V), which we attribute to the effective charge separation and extraction behavior in the PSC on interfacial layer placement. The maximum exciton generation rate (G_{max}) is a crucial factor in PSCs, which governs the charge dissociation and collection and thus the saturation current density (J_{sat}), following the relation of $J_{\text{sat}} = eLG_{\text{max}}$ (where, e and L are elementary charges and the thickness of the perovskite layer, respectively).³⁹ G_{max} of the interface layer-based PSC was calculated to be $3.62 \times 10^{21} \text{ cm}^{-3}\text{s}^{-1}$, which is slightly higher than that of the control device with $3.55 \times 10^{21} \text{ cm}^{-3}\text{s}^{-1}$. The enhancement in G_{max} indicates the promoted photoinduced charge generation and efficient charge transfer dynamics of the PSC on the interface layer placement.

5.4. Conclusions

We demonstrated a facile yet effective interface reform at NiO_x /perovskite in inverted PSCs by introducing an ultrathin layer of dopant-free organic small molecule, composed of planar triazatruxene branches with thiophene core-based semiconductor, DTT-EHDI₂. We noted that the placement of a thin interfacial layer improves the hole extraction ability and conductivity of NiO_x through the intermolecular charge transfer effect. DTTEHDI₂ also helps in reducing the energy barrier at the interface, diminishing the possible nonradiative recombination, while promoting the photoinduced charge transfer dynamics. Interface engineering with the DTT-EHDI₂ boosted the device V_{oc} and FF, with an overall efficiency of up to 18.15%. Our findings offer a promising molecular interface engineering approach to fabricate dopant-free-inverted planar PSCs, which can potentially be exploited for other combinations of use of inorganic semiconductors in PVs.

Chapter 5

5.5 Supporting Information

5.5.1 Materials

Chlorobenzene (CB, 99%), isopropanol (IPA, 99.9%), anhydrous dimethyl sulfoxide (DMSO, 99.8%), and N, N-dimethylformamide (DMF, 99.8%) were purchased from Acros Organics. Starting materials for perovskite were purchased from Dyesol except for PbI₂ and CsI that were procured from Tokyo Chemical Industry (TCI). PC₆₀BM (> 99.5%) and Bathocuproine (BCP) were purchased from Solenne BV and TCI, respectively. Nickel (II) nitrate hexahydrate (Ni(NO₃)₂·6H₂O, 99.999%) and NaOH were obtained from Sigma-Aldrich. All the chemicals were purchased commercially and used without further purification.

5.5.2 NiO_x nanocrystals (NCs) synthesis

NiO_x NCs were prepared based on reported procedures elsewhere¹⁸, with modifications noted in Chapter 2, section 2.1.4.

5.5.3 Device fabrication

Inverted solar cell: Device fabrication was conducted as described in Chapter 2, section 2.3.3. After substrates cleaning, NiO_x film was formed atop FTO substrates by spin coating at 4000 rpm for 35 s, followed by annealing at 150 °C for 30 min. The samples were transferred immediately at 100 °C (to avoid moisture absorption to the samples) to the argon-filled glovebox under controlled moisture and oxygen conditions. A thin layer of DTT-EHDI₂ (~20 nm) was achieved through spin coating DTT-EHDI₂ in chlorobenzene (3 mg mL⁻¹) at 2000 rpm for 20 s atop NiO_x. The rest of the steps have been described in Chapter 2, section 2.3.3.

5.5.4. Device and thin-film characterization

Current density-voltage (*J-V*) curves were performed using an Oriel AAA solar simulator (Newport) producing 1 sun AM1.5G (100mWcm²) simulating sunlight and were recorded by applying an external potential bias to the devices. The generated photocurrent was recorded at a scan rate of 100 mV s⁻¹ (pre-sweep delay: 10 s) with the help of a Keithley 2400 source meter and 0.09 cm² black metal mask as the active area. IPCE measurements were carried out using a 150W xenon lamp attached to a Bentham PVE300-motorized 1/4m monochromator as the light source.

Chapter 5

X-ray diffractograms were acquired using a D8 Advance diffractometer from Bruker (Bragg–Brentano geometry, with an X-ray tube Cu K α , $\lambda = 1.5406 \text{ \AA}$). For surface topography and phase, the images were recorded with the help of scanning probe microscopy (CSI Nano observer) and an NSG10 cantilever (NTMDT) was used; data were processed through Gwyddion software. Absorption spectra were registered with the help of a UV–vis–IR spectrophotometer (Varian Cary 50 UV/Vis Spectrophotometer), and a Hitachi S-4800 scanning electron microscope was used to image the surface microstructure. BioLogic SP-300 impedance analyzer was used to record the electrochemical impedance response.

Additional data is available in Appendix C

5.6 Bibliography

1. J. Jeong, M. Kim, J. Seo, H. Lu, P. Ahlawat, A. Mishra, Y. Yang, M. A. Hope, F. T. Eickemeyer, M. Kim, Y. J. Yoon, I. W. Choi, B. P. Darwich, S. J. Choi, Y. Jo, J. H. Lee, B. Walker, S. M. Zakeeruddin, L. Emsley, U. Rothlisberger, A. Hagfeldt, D. S. Kim, M. Grätzel, J. Y. Kim, Pseudo-halide anion engineering for α -FAPbI₃ perovskite solar cells, *Nature*, 2021, 592, 381.
2. D. Saranin, T. Komaricheva, L. Luchnikov, D. S. Muratov, T. S. Le, Y. Karpov, P. Gostishchev, S. Yurchuk, D. Kuznetsov, S. Didenko, A. di Carlo, Hysteresis-free perovskite solar cells with compact and nanoparticle NiO for indoor application, *Sol. Energy Mater. Sol. Cells*, 2021, 227, 111095.
3. Q. Cao, Y. Li, H. Zhang, J. Yang, J. Han, T. Xu, S. Wang, Z. Wang, B. Gao, J. Zhao, X. Li, X. Ma, S. M. Zakeeruddin, W. E. I. Sha, X. Li, M. Grätzel, Efficient and stable inverted perovskite solar cells with very high fill factors via incorporation of star-shaped polymer, *Sci. Adv.*, 2021, 7, eabg0633.
4. N. E. Courtier, J. M. Cave, J. M. Foster, A. B. Walker, G. Richardson, How transport layer properties affect perovskite solar cell performance: insights from a coupled charge transport/ion migration model, *Energy Environ. Sci.*, 2019, 12, 396.
5. Z. K. Wang, L. S. Liao, Doped charge-transporting layers in planar perovskite solar cells, *Adv. Opt. Mater.*, 2018, 6, 1800276.

Chapter 5

6. S. Shao, M. A. Loi, The role of the interfaces in perovskite solar cells, *Adv. Mater. Interfaces*, 2019, 7, 1901469.
7. A. Fakharuddin, L. Schmidt-Mende, G. Garcia-Belmonte, R. Jose, I. Mora-Sero, Effect of electron-transport material on light-induced degradation of inverted planar junction perovskite solar cells, *Adv. Electron. Mater.*, 2017, 7, 1.
8. S. Wang, T. Sakurai, W. Wen, Y. Qi, Energy level alignment at interfaces in metal halide perovskite solar cells, *Adv. Mater. Interfaces*, 2018, 5, 1.
9. J. Chen, N. G. Park, Materials and methods for interface engineering toward stable and efficient perovskite solar cells, *ACS Energy Lett.*, 2020, 5, 2742.
10. D. Saranin, S. Pescetelli, A. Pazniak, D. Rossi, A. Liedl, A. Yakusheva, L. Luchnikov, D. Podgorny, P. Gostischev, S. Didenko, A. Tameev, D. Lizzit, M. Angelucci, R. Cimino, R. Larciprete, A. Agresti, A. di Carlo, Transition metal carbides (MXenes) for efficient NiO-based inverted perovskite solar cells, *Nano Energy*, 2021, 82, 105771.
11. M. Bidikoudi, E. Kymakis, Novel approaches and scalability prospects of copper based hole transporting materials for planar perovskite solar cells, *J. Mater. Chem. C*, 2019, 7, 13680.
12. L. Calì, S. Kazim, M. Graetzel, S. Ahmad, Hole-transport materials for perovskite solar cells, *Angew. Chem., Int. Ed.* 2016, 55, 14522.
13. J. Cameron, P. J. Skabara, The damaging effects of the acidity in PEDOT:PSS on semiconductor device performance and solutions based on non-acidic alternatives, *Mater. Horiz.*, 2020, 7, 1759.
14. K. M. Reza, A. Gurung, B. Bahrami, S. Mabrouk, H. Elbohy, R. Pathak, K. Chen, A. H. Chowdhury, M. T. Rahman, S. Letourneau, H. C. Yang, G. Saianand, J. W. Elam, S. B. Darling, Q. Qiao, Tailored PEDOT: PSS hole transport layer for higher performance in perovskite solar cells: enhancement of electrical and optical properties with improved morphology, *J. Energy Chem.*, 2020, 44, 41.
15. X. Xu, C. Ma, Y. Cheng, Y. M. Xie, X. Yi, B. Gautam, S. Chen, H. W. Li, C. S. Lee, F. So, S. W. Tsang, Ultraviolet-ozone surface modification for non-wetting hole transport materials based inverted planar perovskite solar cells with efficiency exceeding 18%, *J. Power Sources*, 2017, 360, 157.
16. M. B. Islam, M. Yanagida, Y. Shirai, Y. Nabetani, K. Miyano, NiO_x hole transport layer for perovskite solar cells with improved stability and reproducibility, *ACS Omega*, 2017, 2, 2291.

Chapter 5

17. A. Liu, G. Liu, H. Zhu, B. Shin, E. Fortunato, R. Martins, F. Shan, Hole mobility modulation of solution-processed nickel oxide thin-film transistor based on high-k dielectric, *Appl. Phys. Lett.*, 2016, 108, 233506.
18. W. Chen, Y. Zhou, L. Wang, Y. Wu, B. Tu, B. Yu, F. Liu, H. W. Tam, G. Wang, A. B. Djurišić, L. Huang, Z. He, Molecule-doped nickel oxide: verified charge transfer and planar inverted mixed cation perovskite solar cell, *Adv. Mater.*, 2018, 30, 1800515.
19. W. Chen, F. Z. Liu, X. Y. Feng, A. B. Djurišić, W. K. Chan, Z. B. He, Cesium doped NiO_x as an efficient hole extraction layer for inverted planar perovskite solar cells, *Adv. Energy Mater.*, 2017, 7, 1700722.
20. M. Saliba, S. Orlandi, T. Matsui, S. Aghazada, M. Cavazzini, J. P. Correa-Baena, P. Gao, R. Scopelliti, E. Mosconi, K. H. Dahmen, F. De Angelis, A. Abate, A. Hagfeldt, G. Pozzi, M. Graetzel, M. K. Nazeeruddin, A molecularly engineered hole-transporting material for efficient perovskite solar cells, *Nat. Energy*, 2016, 1, 15017.
21. H. Li, K. Fu, P. P. Boix, L. H. Wong, A. Hagfeldt, M. Grätzel, S. G. Mhaisalkar, A. C. Grimsdale, Hole-transporting small molecules based on thiophene cores for high efficiency perovskite solar cells, *ChemSusChem*, 2014, 7, 3420.
22. L. Calìò, S. Kazim, M. Salado, I. Zimmermann, M. K. Nazeeruddin, S. Ahmad, Design of cyclopentadithiophene-based small organic molecules as hole selective layers for perovskite solar cells, *Sustain. Energy Fuels*, 2018, 2, 2179.
23. C. Igci, S. Paek, K. Rakstys, H. Kanda, N. Shibayama, V. Jankauskas, C. Roldán-Carmona, H. Kim, A. M. Asiri, M. K. Nazeeruddin, D- π -A-Type triazatruxene-based dopant-free hole transporting materials for efficient and stable perovskite solar cells, *Sol. RRL*, 2020, 4, 2000173.
24. L. Calìó, C. Momblona, L. Gil-Escrig, S. Kazim, M. Sessolo, N. Sastre-Santos, H. J. Bolink, S. Ahmad, Vacuum deposited perovskite solar cells employing dopant-free triazatruxene as the hole transport material, *Sol. Energy Mater. Sol. Cells*, 2017, 163, 237.
25. A. Connell, Z. Wang, Y. H. Lin, P. C. Greenwood, A. A. Wiles, E. W. Jones, L. Furnell, R. Anthony, C. P. Kershaw, G. Cooke, H. J. Snaith, P. J. Holliman, Low cost triazatruxene hole transporting material for >20% efficiency perovskite solar cells, *J. Mater. Chem. C*, 2019, 7, 5235.
26. F. J. Ramos, K. Rakstys, S. Kazim, M. Grätzel, M. K. Nazeeruddin, S. Ahmad, Rational design of triazatruxene-based hole conductors for perovskite solar cells, *RSC Adv.*, 2015, 5, 53426.

Chapter 5

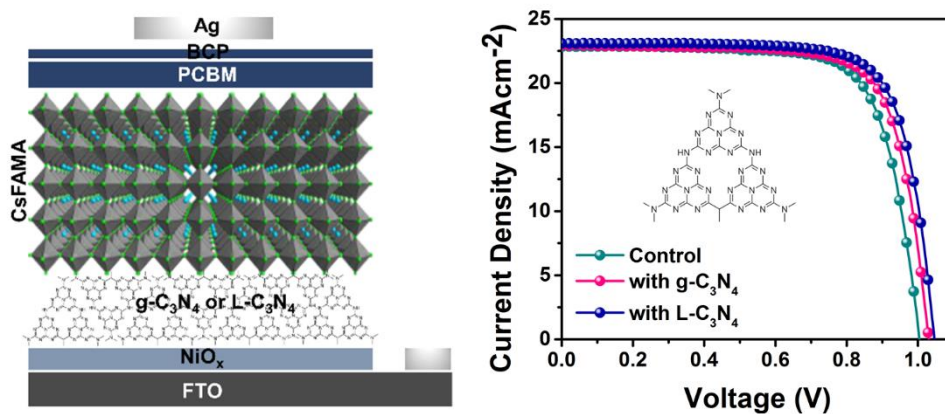
27. K. Rakstys, A. Abate, M. I. Dar, P. Gao, V. Jankauskas, G. Jacopin, E. Kamarauskas, S. Kazim, S. Ahmad, M. Grätzel, M. K. Nazeeruddin, Triazatruxene-based hole transporting materials for highly efficient perovskite solar cells, *J. Am. Chem. Soc.*, 2015, 137, 16172.
28. P. Y. Su, L. B. Huang, J. M. Liu, Y. F. Chen, L. M. Xiao, D. B. Kuang, M. Mayor, C. Y. Su, A multifunctional poly-N-vinylcarbazole interlayer in perovskite solar cells for high stability and efficiency: a test with new triazatruxene-based hole transporting materials, *J. Mater. Chem. A*, 2017, 5, 1913.
29. R. Li, P. Wang, B. Chen, X. Cui, Y. Ding, Y. Li, D. Zhang, Y. Zhao, X. Zhang, NiO_x/Spiro hole transport bilayers for stable perovskite solar cells with efficiency exceeding 21%, *ACS Energy Lett.*, 2019, 5, 79.
30. Q. Zhao, R. Wu, Z. Zhang, J. Xiong, Z. He, B. Fan, Z. Dai, B. Yang, X. Xue, P. Cai, S. Zhan, X. Zhang, J. Zhang, Achieving efficient inverted planar perovskite solar cells with nondoped PTAA as a hole transport layer, *Org. Electron.*, 2019, 71, 106.
31. Y. Yang, Q. Yuan, H. Li, Y. Niu, D. Han, Q. Yang, Y. Yang, S. Yi, D. Y. Zhou, L. Feng, Dopant free mixture of Spiro-OMeTAD and PTAA with tunable wettability as hole transport layer enhancing performance of inverted CsPbI₂Br perovskite solar cells, *Org. Electron.*, 2020, 86, 105873.
32. H. Y. Park, D. Lim, K. D. Kim, S. Y. Jang, Performance optimization of low-temperature-annealed solution-processable ZnO buffer layers for inverted polymer solar cells, *J. Mater. Chem. A*, 2013, 1, 6327.
33. M. Tyagi, M. Tomar, V. Gupta, Postdeposition annealing of NiO_x thin films: A transition from n-type to p-type conductivity for short wave length optoelectronic devices, *J. Mater. Res.*, 2013, 28, 723.
34. S. Wu, Z. Li, J. Zhang, T. Liu, Z. Zhu, A. K. Y. Jen, Efficient large guanidinium mixed perovskite solar cells with enhanced photovoltage and low energy losses, *ChemComm.*, 2019, 55, 4315.
35. N. H. Hemasiri, S. Kazim, S. Ahmad, Reduced trap density and mitigating the interfacial losses by placing 2D dichalcogenide material at perovskite/HTM interface in a dopant free perovskite solar cells, *Nano Energy*, 2020, 77, 105292.
36. N. Harindu Hemasiri, S. Kazim, S. Ahmad, 1T-Rich 2D-WS₂ as an interfacial agent to escalate photo-induced charge transfer dynamics in dopant-free perovskite solar cells, *J. Mater. Chem. C*, 2021, 9, 9865.

Chapter 5

37. J. Lee, S. Baik, Enhanced crystallinity of $\text{CH}_3\text{NH}_3\text{PbI}_3$ by the pre-coordination of PbI_2 -DMSO powders for highly reproducible and efficient planar heterojunction perovskite solar cells, *RSC Adv.*, 2018, 8, 1005.
38. J. Li, T. Jiu, C. Duan, Y. Wang, H. Zhang, H. Jian, Y. Zhao, N. Wang, C. Huang, Y. Li, Improved electron transport in MAPbI_3 perovskite solar cells based on dual doping graphdiyne, *Nano Energy*, 2018, 46, 331.
39. L. Xiao, T. Liang, K. Gao, T. Lai, X. Chen, F. Liu, T. P. Russell, F. Huang, X. Peng, Y. Cao, Ternary solar cells based on two small molecule donors with same conjugated backbone: The role of good miscibility and hole relay process, *ACS Appl. Mater. Interfaces*, 2017, 9, 29917.

CHAPTER 6

INTERFACE TWEAKING OF PEROVSKITE SOLAR CELLS WITH CARBON NITRIDE-BASED 2D MATERIALS



Data presented in this chapter are currently under revision submission on *Nano Energy* entitled:

Interface Tweaking of Perovskite Solar Cells with Carbon Nitride-based 2D Materials.

Naveen Harindu Hemasiri¹, Muhammad Ashraf, Samrana Kazim¹, Robert Graf, Rüdiger Berger, Nisar Ullah, Muhammad Nawaz Tahir, and Shahzada Ahmad

Chapter 6

6.1 Abstract

Strong Coulomb interactions are present in two-dimensional van der Waals layered materials, and these interactions lead to high exciton binding energies. Tuning the interface is the basis of devices including optoelectrical, and their delineation is of paramount importance. 2D-carbon nitrides, so-called C_3N_4 display graphene-like atomic structure, and their use in engineering the interface at hole transport layers and perovskite, can eliminate defective charge build-up and suppress the charge carrier recombination in PSCs. The fabricated solar cells with L- C_3N_4 or g- C_3N_4 interface layers gave an improved performance with boosted open-circuit voltage and fill factor, delivering the PCE above 19%. Our interface layers avoid the direct contact of NiO_x with perovskite, overcoming the possible instability of the active layer via iodide oxidation and deprotonation of cationic amines. The carbon nitride-based 2D materials will serve as an effective interfacial layer for long-term reliability in photovoltaics.

6.2 Introduction

The third pillar for commercial relevance after efficiency and manufacturing cost is the operational stability of any PV system. Interface engineering overcomes the degradation of perovskite through moisture infiltration, boosting the long-term reliability of PSCs. Organic materials are reported to passivate specific defects of perovskite bulk while improving the quality of the interfacial coupling and eventually enhancing the PV performance.^{1,2-5} In most cases, however, the used organic materials are hygroscopic and can accelerate the degradation mechanism of the perovskite.^{5,6} A rational choice of interfacial materials can influence the electrical, physical, and chemical compatibility of each layer. Moreover, the engineering of interfaces is a straightforward but effective methodology to align the energy band-level at interfaces, to influence the perovskite crystallization and microstructure, defect passivation, and to control ion migration.^{7,8-10}

Recently, two-dimensional (2D) materials are being explored as interlayers in PSCs, owing to their ease of electronic structure tailoring through functionalization and synthesis route.¹¹⁻¹⁴ Metal-free carbon nitride (CN) are nontoxic, earth-abundant, polymeric 2D type crystalline semiconductor materials, which display continuous porosity and high surface free energy along with appealing optoelectronic properties.¹⁵⁻¹⁷ Graphitic carbon nitride (g- C_3N_4) is regarded as the most studied and highly stable architecture among the five phases of C_3N_4 , composed of tri-*s*-triazine (*s*-heptazine), rich in amino ($-NH_2$) and nitrogen, establishing the π -conjugated

Chapter 6

electronic structure.^{16,17} It displays a moderate bandgap of 2.7 eV with conduction (E_{CB}) and valence (E_{VB}) band edge positions of -1.1 and +1.6 eV, respectively, attributing to the continuous repetition of the heptazine motif.¹⁷ The chemical structure of 2D-carbon nitride can be altered by the addition of extra nitrogen-rich moieties, resulting in an extended π -conjugated system of heptazine motif, which leads to a robust and band edge tuned CN framework.¹⁷ g-C₃N₄ has been reported as an additive in perovskite to control the nucleation process thus enhancing the grains and microstructure quality of the perovskite, and measured lower defect density.^{16,18-20} This strategy was further extended and g-C₃N₄ was also noted to enhance the charge transfer dynamics and this mitigates the charge recombination via heterogeneously concentrated carbon nitride additives around perovskite grain boundaries.²¹ The functionalization of chemically modified CN materials in PSCs boosted the PV performances, through the control of the undesirable charge dynamics at perovskite/CTL interfaces.^{15,22} The use of NiO_x as CTL creates a direct connection to perovskites and prompts iodide oxidation and deprotonate cationic amines (MA⁺) which compromise the perovskite stability.

Here, we study the potential of g-C₃N₄ (based on solid-state) and L-C₃N₄ (based on solvothermal) as an interface layer with an inorganic hole selective layer (NiO_x) in inverted planar triple-cation based PSCs. We investigated their interaction with [CS_{0.1}(FA_{0.9}MA_{0.1})_{0.9}Pb(I_{0.9}Br_{0.1})₃] at the interface of the layers, and deduced coordination of FA-amine and MA-ammonia groups provides a favorable interaction at the interface between C₃N₄ and perovskite, promoting the stability of perovskite in the device. The enhanced photo-induced charge transfer dynamics and attenuated charge recombination behavior upon 2D-carbon nitrides led to improved PV performances in the PSCs. Subsequently, the low bandgap L-C₃N₄-modified interlayer-based PSCs gave 19.33%, whereas with high bandgap g-C₃N₄ delivered a PCE of 18.58%, surpassing the control PSCs performance and reliability.

6.3 Results and Discussion

6.3.1. g-C₃N₄ and L-C₃N₄ Characterization

The 2D graphitic-carbon nitride framework is composed of tri-s-triazine connected through planar tertiary amines (Figure 6.1a). The powder X-ray diffraction (XRD) pattern shows two distinct reflections at 2θ values of 27.3° and 12.8° corresponding to the (002) and (100) crystalline planes (Figure 6.2b) for g-C₃N₄. The strongest (002) reflection with ~0.33 nm interplanar d spacing is characteristic of the stacking of the conjugated aromatic system, while

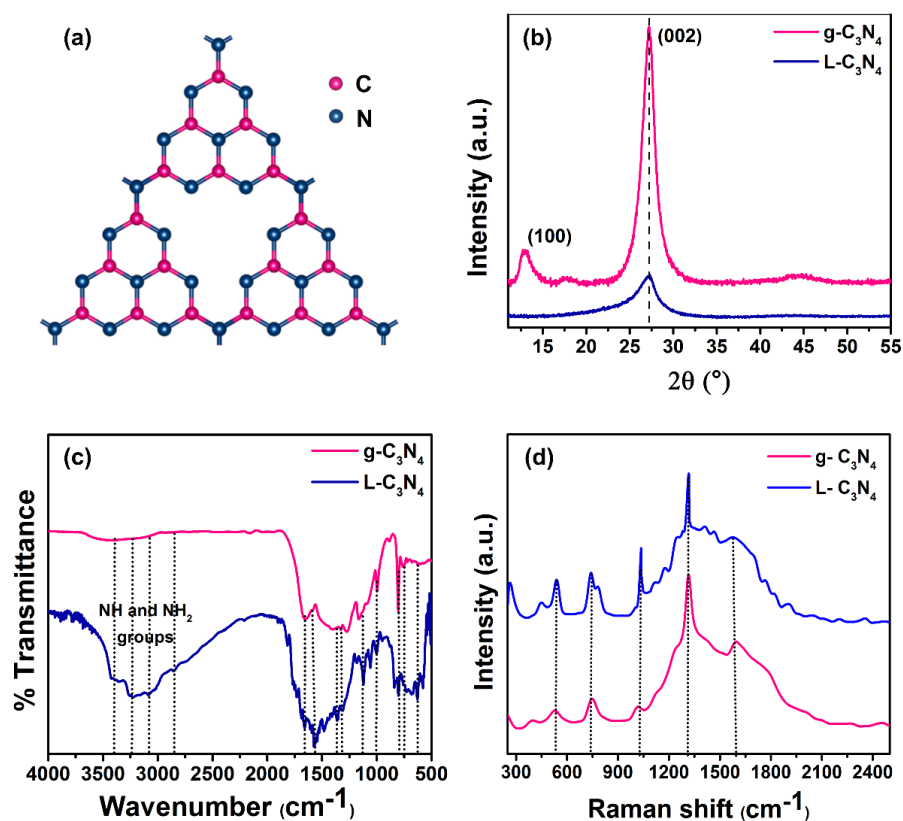


Figure 6. 1 (a) Chemical structure of tri-s-triazine-based graphitic- C_3N_4 . XRD pattern (b), FTIR spectra (c), and Raman spectra (d) for g- C_3N_4 and L- C_3N_4 .

the low intense reflection is related to the (100) plane (~ 0.69 nm d spacing) that is correlated to in-planar structural tri-s-triazine morphology of g- C_3N_4 .^{18,23} The g- C_3N_4 is synthesized at 550 °C using solid-state synthesis method where the stacking of 2D-layers is expected to be highly regular (thermodynamic control) than that of L- C_3N_4 which was synthesized at 140 °C in solution (kinetic control). However, the reflection indexed to the in-plane structural packing of heptazine units is absent in the case of L- C_3N_4 , attributing to the possible distortion in the carbon nitride framework.¹⁶ We registered the variation in the functional groups and the physical state of the materials by Fourier transform infrared (FTIR) spectroscopy (Figure 6.1c). A series of IR bands are observed corresponding to C-N stretching of tri-s-triazine aromatic nucleus from 1700 to 1000 cm^{-1} in both materials.^{24,25} The combinational symmetric and asymmetric N-H stretches of terminal amino groups induce intense broadband at 2900-3500 cm^{-1} in L- C_3N_4 .^{16,25} A significantly weak characteristic N-H band arises in g- C_3N_4 owing to the residual $-NH_2$ present in the carbon nitride framework. The peak observed at around 800 cm^{-1} is assigned to the bending vibration of triazine rings, and is prominent in the case of g- C_3N_4 .^{16,24} A subsidiary peak is noted around 2200 cm^{-1} , suggesting the presence of a negligible amount of cyano groups ($C\equiv N$), that is favorable for the continuous formation of CN

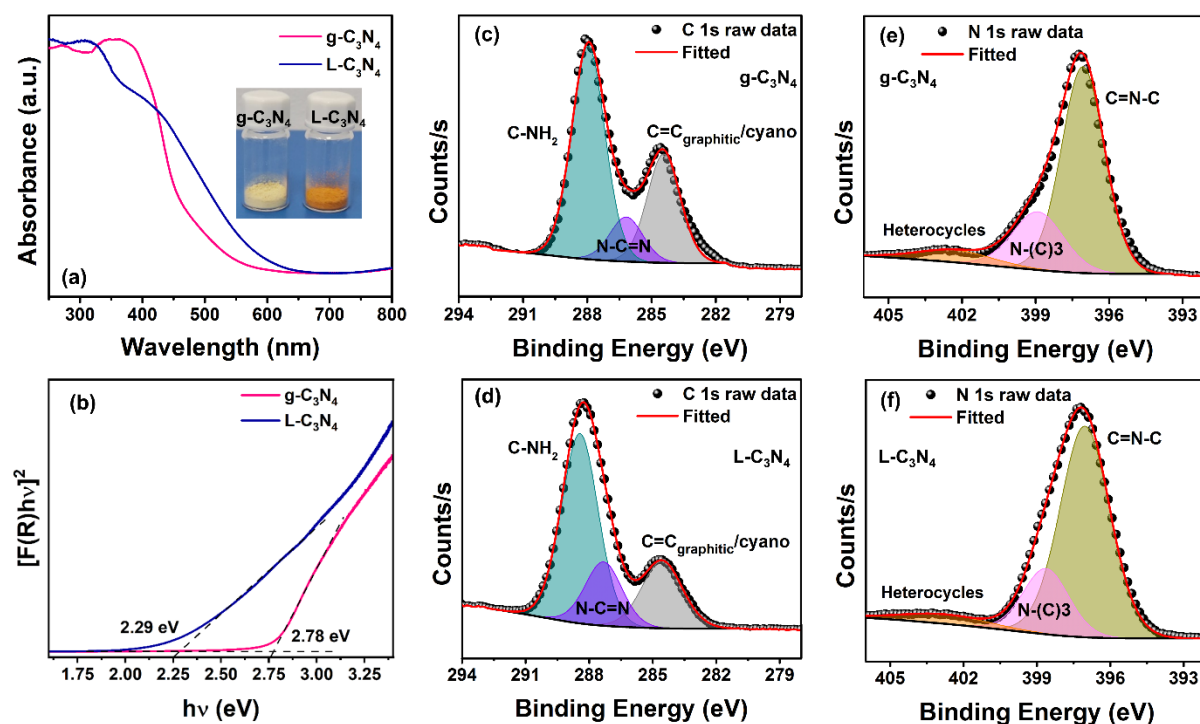


Figure 6. 2 DR-UV-Vis spectra (a) Inset: obtained powders of CN materials, and $[F(R)hv]^2$ vs. $h\nu$ plot (b) for $g\text{-C}_3\text{N}_4$ and $L\text{-C}_3\text{N}_4$. High-resolution X-ray photoelectron spectroscopy (XPS) of C1s of (c) $g\text{-C}_3\text{N}_4$ and (d) $L\text{-C}_3\text{N}_4$, N1s of (e) $g\text{-C}_3\text{N}_4$ and (f) $L\text{-C}_3\text{N}_4$.

network.²⁶⁻²⁸ Raman spectra represent (Figure 6.1d) characteristic peaks at 530, 750, and 1025 cm^{-1} core positions related to the breathing mode of the in-plane heptazine rings available in both $g\text{-C}_3\text{N}_4$ and $L\text{-C}_3\text{N}_4$.²⁵ Further, there are two fingerprint bands at 1320 and 1596 cm^{-1} owing to the disordered D band and graphitic G band, respectively. The broad hump $\sim 1000 - 1800 \text{ cm}^{-1}$ observed in both materials can be attributed to the bending of residual $-\text{NH}_2$ and multilayer stacking of carbon nitride layers.²⁴ We recorded the UV-Vis diffuse reflectance spectra (DRS) and $g\text{-C}_3\text{N}_4$ shows two absorption peaks at around 280 and 375 nm relevant to $\pi\text{-}\pi^*$ transition in the conjugated polymeric network and $n\text{-}\pi^*$ transition between nonbonding orbitals of nitrogen and aromatic ring, respectively (Figure 6.2a).²⁹ Notably, $L\text{-C}_3\text{N}_4$ shows a strong absorption shoulder with a red-shifted absorption edge at $\sim 650 \text{ nm}$ compared to $g\text{-C}_3\text{N}_4$ (absorption edge at $\sim 575 \text{ nm}$). This resulted in an upshifted valance band together with $\pi\text{-}\pi^*$ transition at low energy and thus the extended absorption in the visible range, exhibiting the orange color of $L\text{-C}_3\text{N}_4$.¹⁶ From the UV-Vis DRS along with the Kubelka-Munk relationship (Figure 6.2b), we deduced a reduced optical bandgap from 2.78 eV to 2.29 eV for the $L\text{-C}_3\text{N}_4$ compared to $g\text{-C}_3\text{N}_4$ which can be correlated to the J-type aggregation of inter-planar tri-s-triazine rings.²⁸ Moreover, we calculated the optical band gap of the exfoliated C_3N_4 in iso-

Chapter 6

propanol/ethanol solution using UV-Vis together with Tauc plot (Figure A6.1, Appendix D) and the optical bandgap was calculated to be 3.3 and 2.5 eV for g-C₃N₄ and L-C₃N₄, respectively.

We performed scanning electron microscopy (SEM) and transmission electron microscopy (TEM) studies of synthesized and exfoliated C₃N₄ materials (Figure A6.2, Appendix D). The bulk g-C₃N₄ reveals a highly porous, heterogeneously distributed, and agglomerated structure (Figure A6.2a, Appendix D) while L-C₃N₄ shows anisotropic wires type morphology (Figure A6.2b, Appendix D). In the TEM image, the liquid phase assisted (LPA) exfoliated 2D g-C₃N₄ shows the irregular layered structure (Figure A6.2c, Appendix D), consisting of light and dark areas, attributing to the thin nanosheets and overlap or multilayer nanosheets, respectively. Moreover, L-C₃N₄ maintains its random arrangement of anisotropic nanostructure even after the exfoliation (Figure A6.2d, Appendix D). We analyzed the chemical state and composition of the CN materials using X-ray photoelectron spectroscopy (XPS) (Figure 6.2c-f and Figure A6.3, Appendix D). The high-resolution C1s XPS spectrum of g-C₃N₄ (Figure 6.2c) shows three peak components, which can be assigned to sp² C in aromatic structure (N-C=N) at 286.18 eV, sp² aromatic C attached to NH₂ group at 287.95 eV, and sp³ C-C at 284.43 eV.²⁷ The sp³ carbon peak stems from graphitic or/and cyano group carbon in the C₃N₄ network.^{25,26} Aforementioned three peaks originated at 287.33, 288.44, and 284.56 eV, respectively, in the case of L-C₃N₄. The core level N1s of the g-C₃N₄ show three peaks after deconvolution where the predominant peak at ca. 397.07 eV is assigned to sp² N percent in triazine rings as C=N-C, while the medium peak at 398.9 eV corresponding to bridging N atoms in N-(C)₃.²² The positive charge localization or charging effects of heterocycles can further lead to the appearance of a minor peak at around 402.29 eV.^{15,26,27} The above peaks at 397.04, 398.63, and 402.75 eV, respectively were observed in the case of L-C₃N₄. Additionally, two peak components were recognized in Cl2p from L-C₃N₄ at a binding energy of 198.69 and 195.29 eV, attributing to Cl2p_{1/2} and Cl2p_{3/2}, respectively (Figure A6.4, Appendix D)

6.3.2. Thin-Film Characterization

We deduced uniform layers of L-C₃N₄ over NiO_x as compared to g-C₃N₄ on NiO_x (Figure 6.3a-d). SEM images of perovskite (i.e., triple cation perovskite will be termed as CsFAMA) layers directly deposited on g-C₃N₄ and L-C₃N₄ show a slightly enhanced grain size to that on NiO_x film (Figure 6.3e-g). The corresponding histogram of the grain size distribution is shown in Figure 6e'-g' with the average grain size (length) of 202.396, 208.013, and 209.088 nm for the

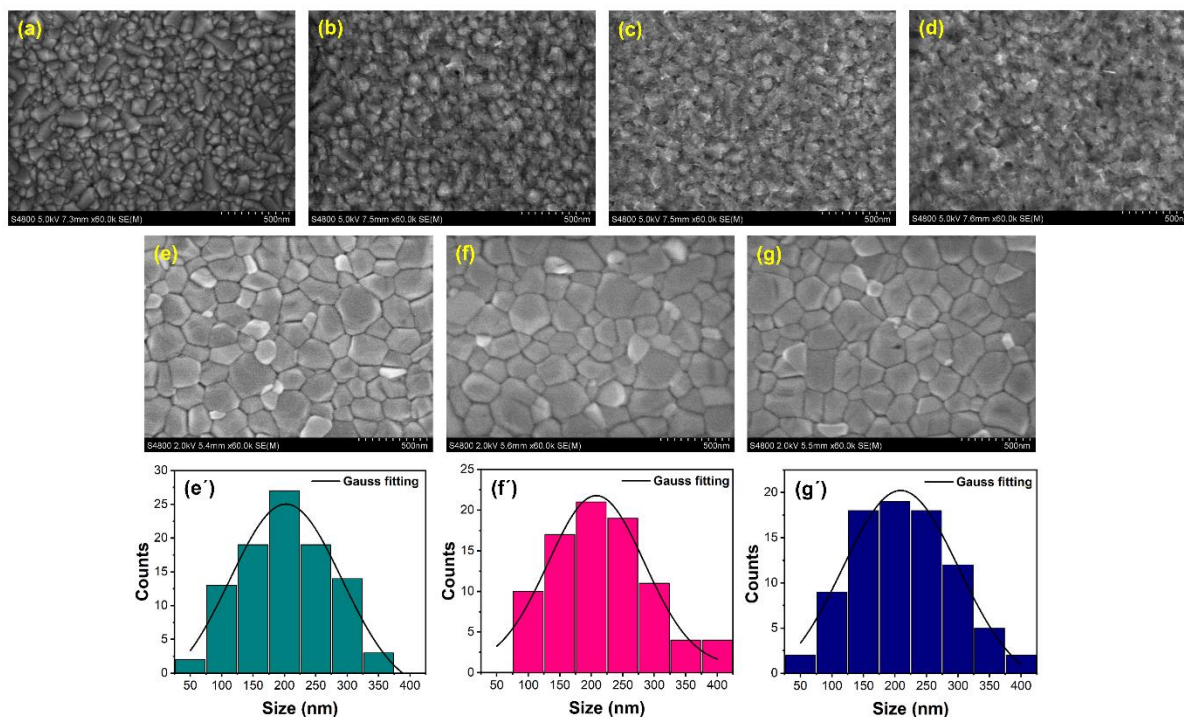


Figure 6. 3 SEM image of (a) FTO, (b) NiO_x/FTO, (c) g-C₃N₄/NiO_x/FTO, and (d) L-C₃N₄/NiO_x/FTO films. SEM image and the corresponding histogram of grain size (length) distribution of CsFAMA perovskite deposited on (e and e') NiO_x/FTO, (f and f') g-C₃N₄/NiO_x/FTO, and (g and g') L-C₃N₄/NiO_x/FTO, respectively.

perovskite grown on NiO_x, g-C₃N₄/NiO_x, and L-C₃N₄/NiO_x, respectively. Moreover, a solidly compacted grain morphology was observed upon g-C₃N₄ and L-C₃N₄. The powder XRD (Figure 6.4a) patterns of the perovskite deposited on CN under layer display a notably increased ratio of the (101) plane to (012), (021), (211), and (122) crystal planes without a shift in the reflection, attributing faster growth and preferential orientation of (101) grains with the absence

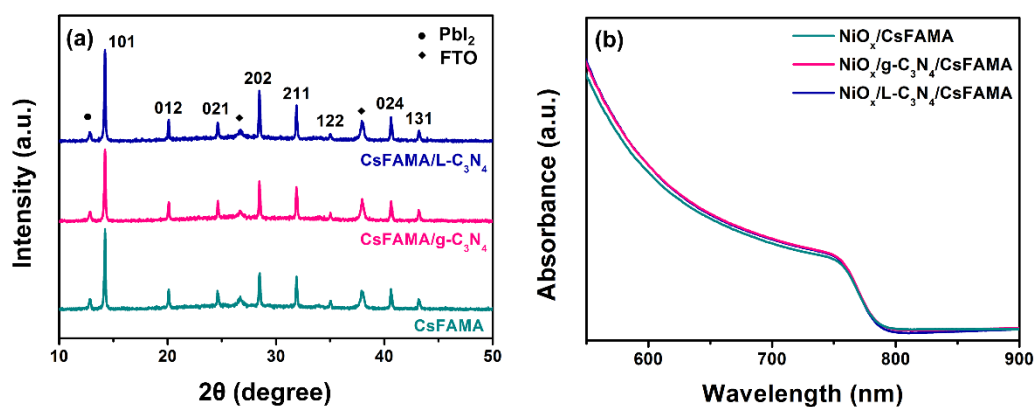


Figure 6. 4 (a) XRD patterns of CsFAMA deposited on NiO_x, g-C₃N₄/NiO_x, and L-C₃N₄/NiO_x. (b) UV-Vis spectra of CsFAMA perovskite deposited on different bottom layers.

of influence from the down layer. The absorption of the CsFAMA layer is unchanged by the CN under layer as depicted in UV-Vis absorption spectra (Figure 6.4b).

6.3.3 Interaction between C_3N_4 and CsFAMA Perovskite

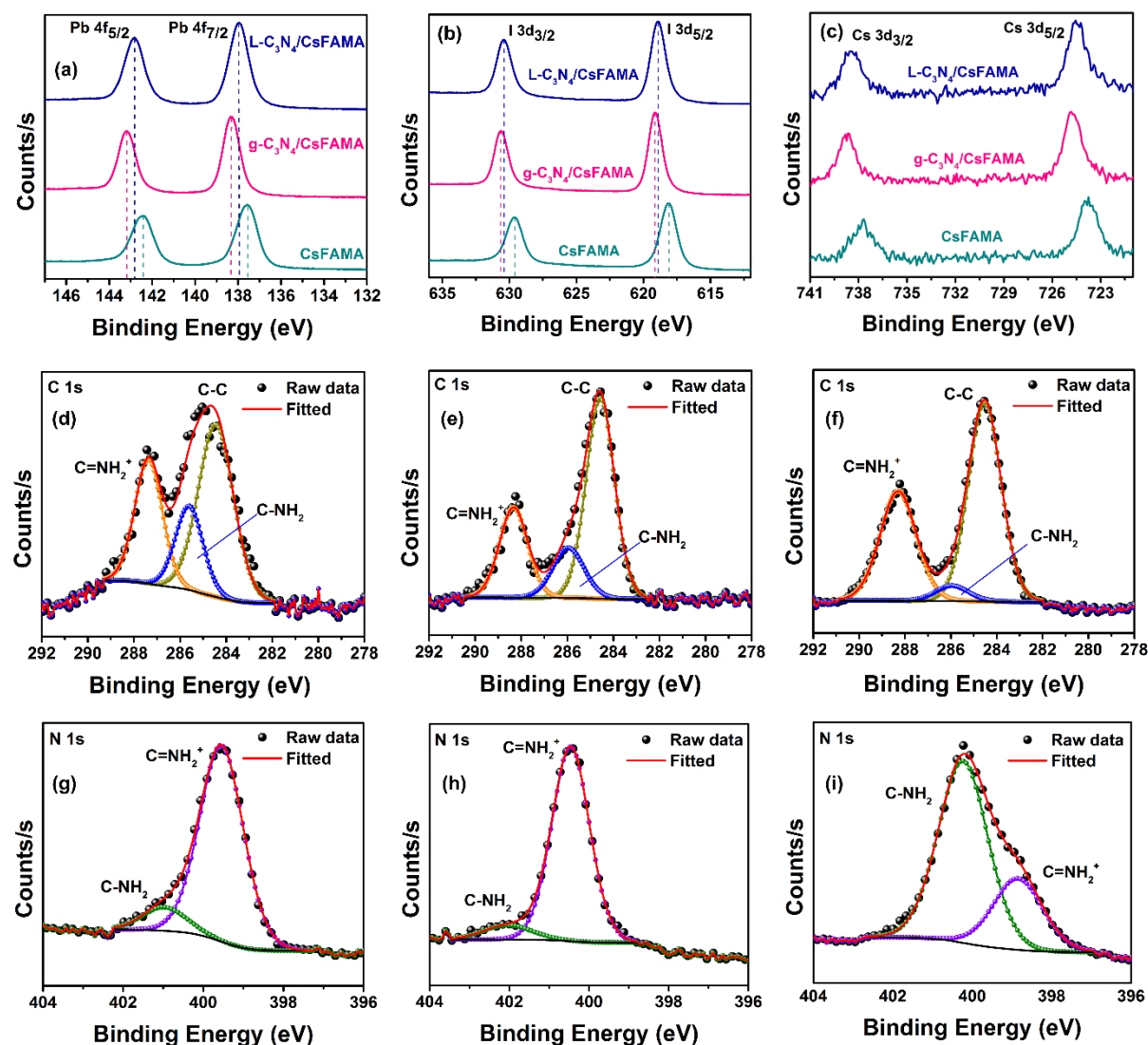


Figure 6. 5 High-resolution XPS of (a) Pb4f and (b) I3d, and (c) Cs3d detected from CsFAMA, CsFAMA/g- C_3N_4 , and CsFAMA/L- C_3N_4 . . High-resolution XPS of C1s (d, e, and f) and N1s (g, h, and i) found from CsFAMA, CsFAMA/g- C_3N_4 , and CsFAMA/L- C_3N_4 , respectively [here CsFAMA denotes $Cs_{0.1}(FA_{0.9}MA_{0.1})_{0.9}Pb(I_{0.9}Br_{0.1})_3$].

We further performed XPS measurements to unravel the potential interactions of the underlayer C_3N_4 materials with perovskite. For this, CsFAMA powder was collected after spin-coated onto the g- C_3N_4 and L- C_3N_4 separately. Compared with control CsFAMA, g- C_3N_4 and L- C_3N_4

Chapter 6

incorporated CsFAMA showed core-level peaks of Pb 4f and I 3d (Figure 6.5a and b) that were shifted towards higher binding energies. This phenomenon indicates that the CN materials impact the chemical environment of the $[\text{PbI}_6]^{4-}$ octahedron.^{2,30,31} Additionally, the core-level peaks of Cs 3d (Figure 6.5c), C 1s, and N 1s are shown (Figure 6.5d-i) and the individual peak positions were tabulated (Table A6.1, Appendix D). A visible peak was observed at around 800 cm^{-1} from the FTIR of the C_3N_4 -modified CsFAMA, which can be assigned to the bending vibration of triazine rings, showing evidence of the existence of C_3N_4 materials (Figure 6.6).

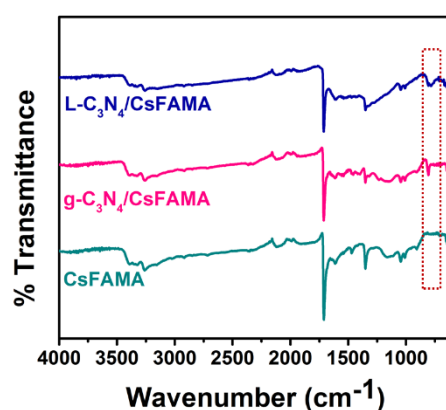


Figure 6. 6 FTIR spectrum of CsFAMA, CsFAMA/g- C_3N_4 , and CsFAMA/L- C_3N_4 .

We undertook solid-state NMR studies to deduce possible changes in the atomistic environment of the MA and FA cations at the interface of the C_3N_4 - and perovskite. From NMR studies by Kubicki et al., it is known that FA and MA cations of the mixed-perovskites exhibit at ambient conditions fast in place reorientation dynamics with 10 ps and 100 ps correlation time, respectively, with only minor variations depending on the FA/MA mixing ratio.³² These fast molecular motions facilitate the acquisition of highly resolved ^1H MAS spectra of CsFAMA at moderate MAS spinning frequencies of 25 kHz (Figure 6.7a). Upon mixing the perovskite with C_3N_4 , broad background signals appear between 3 – 14 ppm together with residual solvent signals around 1 ppm (Figure 6.7b). The broadened FA and MA signals can be visibly deduced when the signals of pure bulk perovskite, i.e. signals of perovskite sites that are not in direct contact with the C_3N_4 surface and therefore are unaffected by the blending and are subtracted from the spectrum. The deducted spectrum (Figure 6.7c) shows residual FA signals, indicating that the MA cations have stronger coordination with the C_3N_4 .

In the NMR spectrum, the methyl signal of the coordinating MA ions stays at the same chemical shift as in the bulk perovskite, whereas the amine and ammonia signals of FA and MA shift to higher ppm values. This shift towards higher ppm values indicates an electronic

Chapter 6

deshielding of the ^1H sites, which is often indicative of a hydrogen bonding. Here, positively charged hydrogen sites may coordinate with unbound nitrogen electron pairs at the edges of the triangular inner voids of the two-dimensional C_3N_4 . This coordination stops the almost isotropic local dynamics of the cations at the interface of the perovskite and leads to broad ^1H MAS signals with significantly shorter T_1 relaxation time ($\sim 3\text{s}$). In the ^{13}C CP-MAS NMR spectra of perovskite samples with and without C_3N_4 (Figure 6.7e, and 6.7d respectively) acquired at ambient conditions, the FA-CH site is noted as the sharp signal at 155 ppm, similar to low-temperature measurements.³² The MA-CH₃ signals around 30 ppm, however, show a significantly bigger splitting, and a substantial broadening is observed in our spectra compared to the published low-temperature CP-MAS spectra which may originate from additional processing steps. By subtracting the CP-MAS NMR spectrum of the pure perovskite (Figure 6.7d) from the spectrum of the perovskite- C_3N_4 (Figure 6.7e) the ^{13}C CP-MAS spectrum of the C_3N_4 (Figure 6.7f) with two broad signals at 165 ppm and 157 ppm can be obtained.

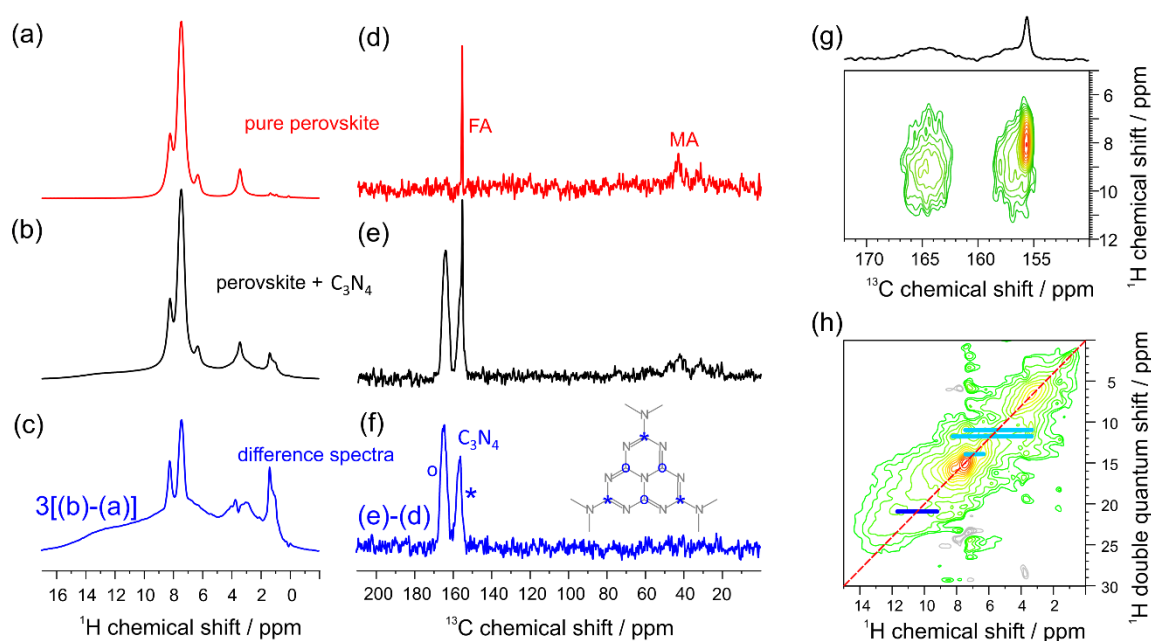


Figure 6. 7 Solid-state NMR results of CsFAMA perovskite samples with and without C_3N_4 addition: (a,b) ^1H MAS and (d,e) ^{13}C CP-MAS NMR spectrum of CsFAMA perovskite, pure and blended with C_3N_4 material, respectively, and the resulting ^1H (c) and ^{13}C (f) difference spectra. (g) ^1H - ^{13}C CP-MAS correlation spectrum of the perovskite + C_3N_4 material acquired with 5ms CP-contact and (h) the ^1H DQ correlation spectrum of the same material with 1 rotor period BABA-xy16 DQ excitation at 25 kHz MAS.

Chapter 6

The two signals, which have equal intensity for CP-MAS acquisition with longer CP contact times, are assigned to the two chemically inequivalent carbon sites in the C_3N_4 structure. The 1H - ^{13}C CP-MAS correlation spectrum (Figure 6.7g) demonstrates that the ^{13}C nuclei of the C_3N_4 are primarily polarized via immobilized hydrogen nuclei bound to a nitrogen atom. Polarization transfer from strongly hydrogen-bonded protons around 12 ppm as well as from MA-methyl or FA-CH protons to the C_3N_4 , ^{13}C sites is not observed. The 1H double-quantum (DQ) correlation spectrum (Figure 6.7h), recorded with 40 μs DQ excitation time, confirms the homogeneous distribution of MA cations in the material, e.g. the intermolecular correlation between MA ammonia sites and FA amine sites compared to intramolecular ammonia correlations (Figure 6.7h), light blue correlation.³³ The correlation highlighted in dark blue, however, indicates the spatial proximity between NH-protons strongly hydrogen-bonded to the C_3N_4 and their neighboring hydrogen sites within the FA-amine and MA-ammonia groups. Simple MM2-MD simulations of the behavior of FA and MA molecules at the C_3N_4 surface support this behavior and suggest significantly stronger coordination of the ammonia groups due to competing pi-electron interaction in the case of FA. The deduced coordination of FA-amine and MA-ammonia groups suggests an attractive interaction at the interface between C_3N_4 and perovskite, which stems from the stabilization of the FA and MA cations at the interface as a passivation layer for the perovskite.

6.3.4 Device and Photovoltaic Characterization

We fabricated the PSCs based on inverted architecture using g- C_3N_4 and L- C_3N_4 as interface layers in-between NiO_x and perovskite absorber layers (Figure 6.8a). We employed triple-cation perovskite as the photoactive layer (thickness of ~ 420 nm, Figure 6.8b) deposited on NiO_x or interface layer (C_3N_4) by an antisolvent-assisted spin-coating technique. The concentration of the interfacial layer was optimized to 1.25 mg/ml (Figure A6.5, Table A6.2, Appendix D). The thickness of the C_3N_4 layer was about 12 nm, which was measured using atomic force microscopy (AFM) as shown in Figure A6.6 Appendix D). The current density-voltage (J - V) curves of the PSCs were registered under standard solar illumination (AM 1.5G, 100 $mWcm^{-2}$) (Figure 6.8c) and summarized in Table 6.1. Devices gave 16.85, 17.67, and 18.21% performances from control, g- C_3N_4 -based, and L- C_3N_4 -based, respectively. We further deposited PEAI at the perovskites/ ETM layer and the maximum PCE of 17.48% with an open-circuit voltage (V_{oc}) of 1020.93 mV, a short-circuit current density (J_{sc}) of 22.86 $mAcm^{-2}$, and a fill-factor (FF) of 74.88% under reverse scan was measured for the control device. L- C_3N_4

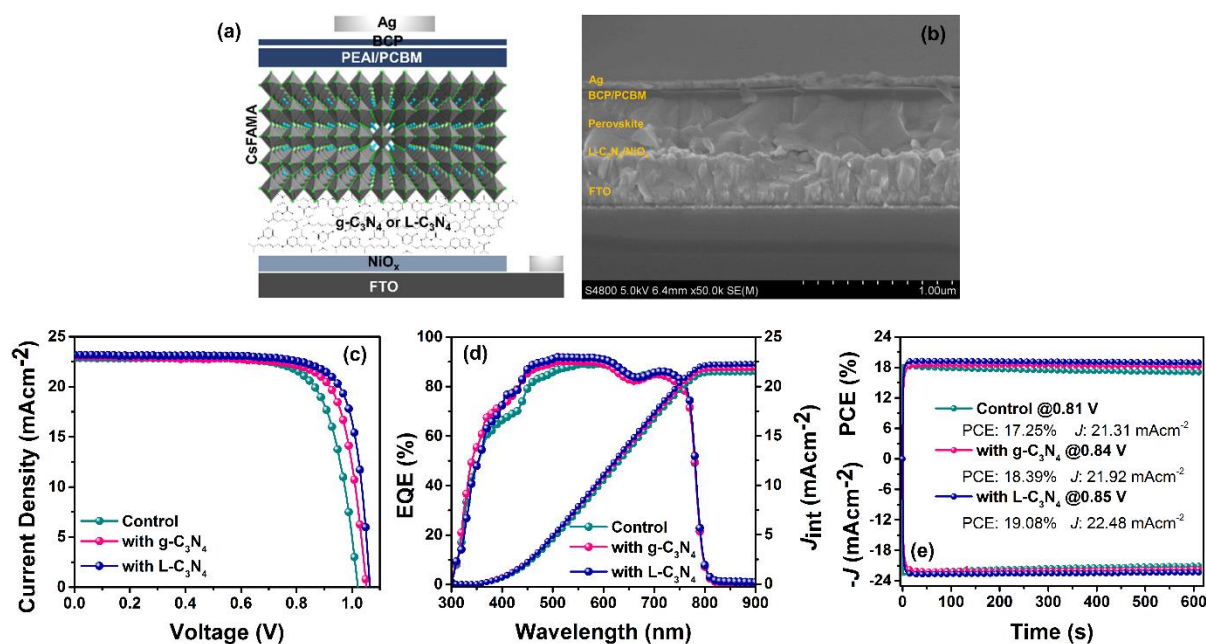


Figure 6. 8 (a) Device configuration and (b) corresponding cross-section SEM image of the PSC incorporating L-C₃N₄ interface layer. (c) J - V curve of the champion devices without and with g-C₃N₄ or L-C₃N₄ interface layer measured in reverse scan under simulated AM 1.5G illumination, (d) IPCE and integrated current density of the corresponding devices, (e) steady-state power output of PSCs.

interface layer effectively yielded an improved PCE of 19.33% with a significant enhancement in V_{oc} (1064.37 mV) and FF (78.35). In particular, the PSCs with g-C₃N₄ interlayer also showed us a visible development in PCE, and an optimized PSC provided 18.58% PCE with V_{oc} of 1051.50 mV, J_{sc} of 23.05 mA, and FF of 76.64%.

The voltage deficit was minimized and the significant reduction in V_{oc} loss with the L-C₃N₄-based interfacial layer can be attributed to the constructively annihilated recombination losses at NiO_x/perovskite interface. Notably, a high fill factor is noted with C₃N₄ interfacial layer in PSCs due to improved charge dynamics arising from the improved crystallization in the perovskite active layer and better charge collection to NiO_x as HTL at the interface developed here with minimum parasitic losses from shunt (R_{sh}) and series (R_s) resistances (Table A6.3, Appendix D).^{3,34} The R_{sh} and R_s were detected from the slope of the J - V curves near J_{sc} and V_{oc} , respectively. High R_{sh} in combination with low R_s detected represents the suppressed nonradiative charge recombination and interfacial charge losses in the PSCs with modified interfaces.^{3,11,35}

Chapter 6

Table 6. 1 Summary of the PSC performances using with and without different C₃N₄ interlayers.

Devices	Scan	V _{oc} (mV)	J _{sc} (mAcm ⁻²)	FF (%)	PCE (%)
NiO _x	Reverse	1020.93	22.86	74.88	17.48
	Forward	1021.90	22.85	73.90	17.26
	Average	1007.8±8.7	22.77±0.14	72.69±1.18	16.68±0.43
NiO _x /g-C ₃ N ₄	Reverse	1051.50	23.05	76.64	18.58
	Forward	1053.12	23.03	75.78	18.38
	Average	1032.36±15.8	22.98±0.07	74.76±0.96	17.74±0.48
NiO _x /L-C ₃ N ₄	Reverse	1064.37	23.18	78.35	19.33
	Forward	1063.97	23.11	77.97	19.11
	Average	1049.77±9.2	23.05±0.12	75.60±1.33	18.30±0.52

We calculated the hysteresis index using the equation; $HI = [J_{RS}(0.8V_{oc}) - J_{FS}(0.8V_{oc})] / J_{RS}(0.8V_{oc})$, where $J_{RS}(0.8V_{oc})$ and $J_{FS}(0.8V_{oc})$ denote the J_{sc} at 80% of V_{oc} from reverse and forward scan, respectively. Remarkably, both C₃N₄-based PSCs showed negligible hysteresis index in the J - V scans of reverse and forward bias (Table A6.3 and Figure A6.7, Appendix D). The integrated photocurrent densities collected from the external quantum efficiency spectra (Figure 6.8d) were 21.44, 21.86, and 22.28 mAcm⁻² for NiO_x, NiO_x/g-C₃N₄, and NiO_x/L-C₃N₄, respectively, are in agreement with those obtained from the J - V curves. The enhancement of EQE observed in the region of 400-500 nm in the devices with L-C₃N₄ and g-C₃N₄ could be attributed to the slight improvement of perovskite grains, leading to a better absorption due to a greater absorption coefficient of the perovskite at shorter wavelength.³⁶ The steady-state power output (SPO, Figure 6.8e) stabilized at 19.08% of PCE (with 22.48 mAcm⁻² at 0.85V) upon L-C₃N₄ whereas for g-C₃N₄, those were at approximately 18.39% and 21.92 mAcm⁻² at 0.84V under ambient conditions (~40-60 % RH at 28 °C). Figure 6.9a-d shows the statistical distribution of PV parameters of the devices (54 devices in total) from different batches, which indicates the excellent reproducibility of the PSCs with C₃N₄-based interface engineering.

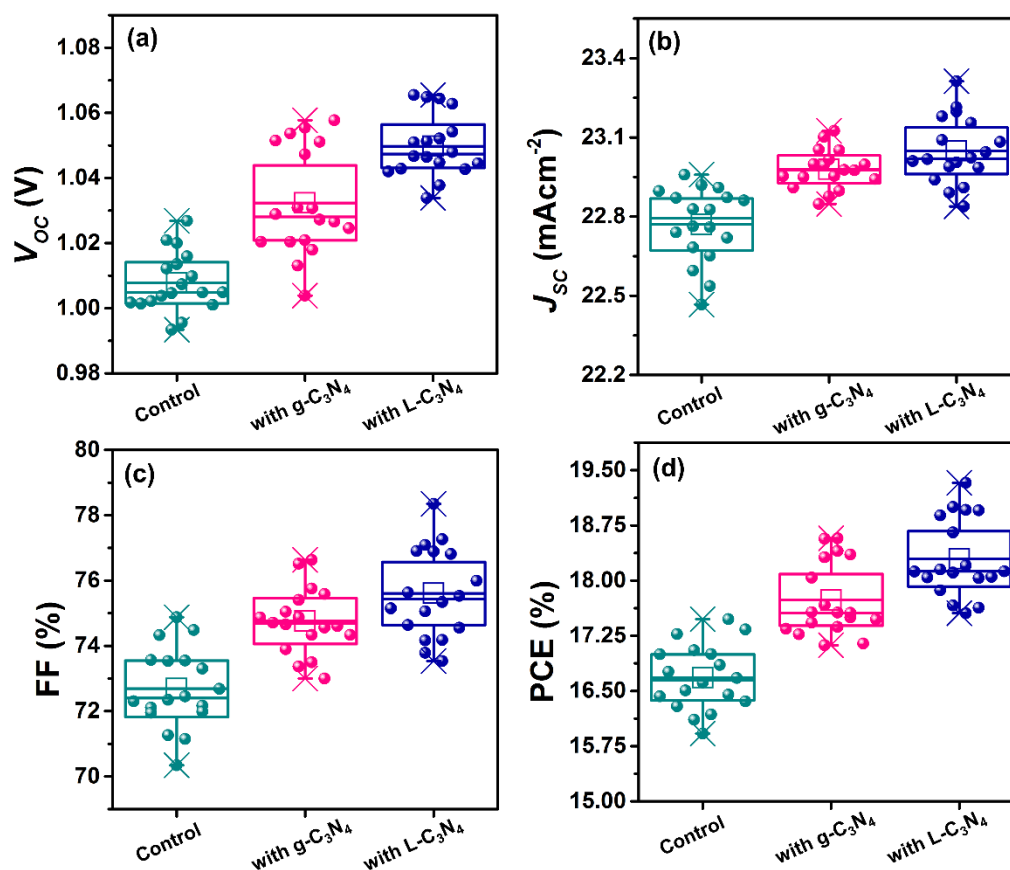


Figure 6. 9 Statistical distribution of PV parameters extracted from J - V curves of the PSCs form different batches.

6.3.5 Trap-Density Reduction & Charge Kinetics

To quantify the improvement in FF, we measured resistance losses and leakage current behavior from the J - V profile under dark conditions (Figure 6.10a). The reverse saturation currents of the L-C₃N₄ and g-C₃N₄-PSCs are reduced as compared to the control PSC. The ideality factor n_{id} was quantized from the Shockley liner part of the semi-logarithmic dark J - V profile based on; $J_D = J_0 \left[\exp\left(\frac{qV}{n_{id}K_B T}\right) - 1 \right]$, where J_D is the dark current density, J_0 is the saturation current density, q is the electron charge, V is the applied bias, K_B is the Boltzmann constant, and T is the temperature.^{11,37} The shifting of the dark current (J_D) minimum point and the exponential area in PSCs are significantly influenced by changes in the electric field, scanning rate, and temperature.^{38,39} Since the external factors such as scanning rate and the temperature were constant during the experiment in each case, the slight shifting of the J_D minimum point upon C₃N₄ interface layers with respect to that of the control device could be

Chapter 6

attributed to the modification of an internal built-in electric field of the devices. The calculated J_0 and n_{id} for the PSC with L- C_3N_4 were 4.346×10^{-8} mAcm $^{-2}$ and 2.29, respectively, whereas for the PSC with g- C_3N_4 were 4.918×10^{-7} mAcm $^{-2}$ and 2.55, respectively, which are significantly lower than that of the control device (2.564×10^{-5} mAcm $^{-2}$, 3.36). Such low J_0 and n_{id} observed in the PSCs with C_3N_4 interfacial layers indicate a low leakage current density and notably inhibited photo-charge recombination, thus resulting in upgraded FF.³⁷ The lowest J_0 and n_{id} detected from the L- C_3N_4 -based PSCs further describe the enhanced photo-induced charge transfer dynamics in the PSCs, which is beneficial towards V_{OC} improvement, and subsequently boosts the PCE.

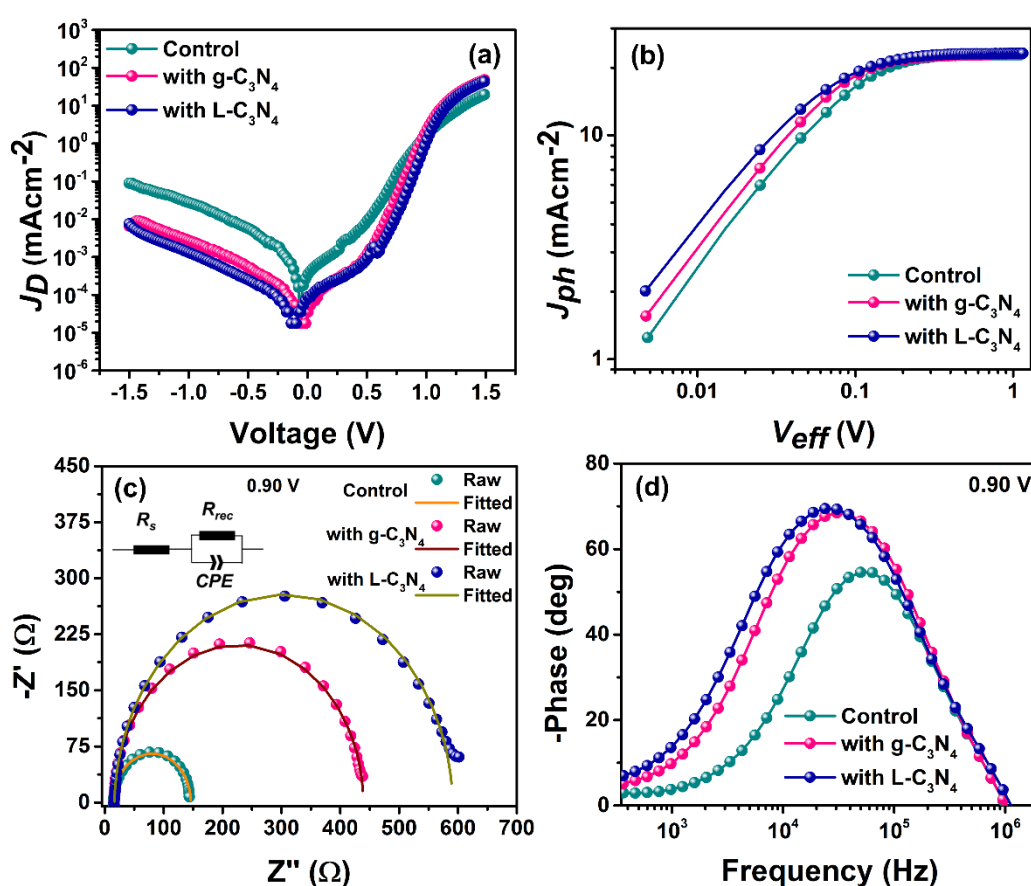


Figure 6. 10 (a) Dark $J-V$ curves and (b) photo-generated current density vs. effective voltage of PSCs. (c) Electrochemical impedance spectra of PSCs measured at an applied voltage of 900 mV under dark conditions (raw and fitted data). Inset: the equivalent circuit diagram used for EIS data fitting. (d) Bode spectra of PSCs measured at an applied voltage of 900 mV under dark conditions.

Chapter 6

To decipher, the effect of the C_3N_4 network as an interfacial layer on the photo-induced charge transfer dynamics in PSC, charge generation, and dissociation were particularly identified, by following the effective voltage (V_{eff}) dependent photocurrent density (J_{ph}) (Figure 6.10b). Herein, V_{eff} and J_{ph} are defined by $V_{eff} = V_0 - V_{app}$ and $J_{ph} = J_L - J_D$ respectively, where V_0 is the compensation voltage obtained at $J_{ph}=0$, V_{app} is the applied bias voltage, J_L is the current density under illumination, and J_D is the current density under dark conditions.^{40,41} The saturation of photocurrent (J_{sat}) for L- C_3N_4 and g- C_3N_4 based PSCs were detected at a relatively low V_{eff} of 0.287 and 0.368 V, respectively, when compared with that of the control device (0.428 V), which we attribute to the constructive charge dissociation and separation in the PSCs upon interface engineering with C_3N_4 .⁴¹ Furthermore, the efficiency of charge dissociation from photogenerated excitons and free charge collection ultimately depends on the maximum exciton generation rate (G_{max}), following $J_{sat} = qLG_{max}$, where L is the perovskite layer thickness.¹⁶ It has been calculated that the G_{max} is slightly higher upon L- C_3N_4 , reaching $3.447 \times 10^{21} \text{ S}^{-1}\text{cm}^{-3}$ when compared with g- C_3N_4 -based PSC ($3.426 \times 10^{21} \text{ S}^{-1}\text{cm}^{-3}$) and control PSC ($3.398 \times 10^{21} \text{ S}^{-1}\text{cm}^{-3}$). The enrichment of the carrier charge generation and the exciton generation rate further explain the slightly advanced EQE upon C_3N_4 interlayers.⁴²

Electrochemical impedance spectroscopy (EIS) under dark conditions was carried out to gain insight into photo-induced charge carrier recombination behavior at HTL/perovskite interface in PSCs with interfacial engineering. The resulting Nyquist plot at 0.9 V bias voltage was fitted (Figure 6.10c) with the equivalent circuit model of R_s+R_{rec}/CPE (Insert Figure 6.10c), where R_s is series resistance, R_{rec} is recombination resistance at the perovskite/ NiO_x interface, and CPE is a carrier diffusion-based constant phase element. The obtained R_{rec} of the L- C_3N_4 -based PSC after fitting the Nyquist plot at 0.9V applied bias features a higher value followed by the g- C_3N_4 -based and control PSC (Table A6.4, Appendix D). Owing to the inverse proportionality, the interfacial charge recombination was remarkably subdued upon the L- C_3N_4 interface layer, followed by the g- C_3N_4 interface layer, and thus significant improvements in V_{oc} in L- C_3N_4 and g- C_3N_4 PSCs, when compared with the control PSC.^{11,43} Furthermore, the trend of R_{rec} is consistent with the trend of R_{sh} detected from the J - V profile. The influence of different interfacial layers on the charge lifetime (τ) of the PSCs was further identified by bode EIS spectra under the dark condition at 0.9 V applied bias (Figure 6.10d) with the relationship of $\tau = 1/(2\pi f_p)$, where f_p denotes the peak frequency corresponding to the charge-transfer process at the perovskite/ NiO_x interface.^{44,45} The charge lifetime of the PSCs with L- C_3N_4 and g- C_3N_4 were 6.65 and 5.20 μs , respectively, which are significantly longer than that of the

Chapter 6

control device (2.49 μs). The extended charge lifetime upon L-C₃N₄ and g-C₃N₄ can be concluded to the annihilated charge build-up and mitigated charge recombination at the interface, thus resulting in proper charge transfer dynamics towards the upgraded PV performances in PSCs.⁴⁵

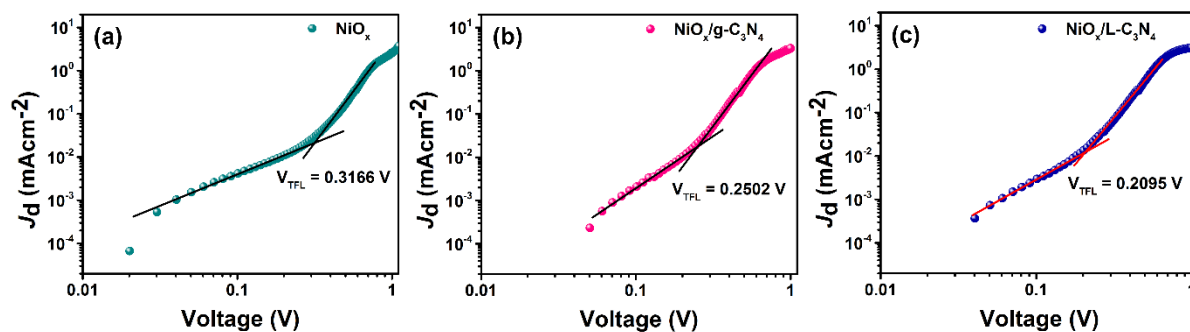


Figure 6. 11 Space-charge-limited current (SCLC) vs voltage of hole only devices with the structure of (a) FTO/NiO_x/perovskite/PTAA/Au, (b) FTO/NiO_x/g-C₃N₄/perovskite/PTAA/Au, and (c) FTO/NiO_x/L-C₃N₄/perovskite/PTAA/Au.

Reduced trap-assisted recombination was further identified by measuring the space-charge-limited current-voltage (J - V) curves of the hole-only device with the structure of FTO/NiO_x/C₃N₄(with or without)/perovskite/PTAA/Au. As shown in Figure 6.11a-c, the limit voltage of the trap-filled (V_{TFL}) is determined to be 0.317, 0.250, and 0.209 V for the control, g-C₃N₄, and L-C₃N₄ based devices, respectively. The defect density; N_{trap} [which is followed by the equation $N_{\text{trap}} = (2\epsilon\epsilon_0 V_{TFL})/(qL^2)$, where, ϵ is the relative permittivity, ϵ_0 is the vacuum permittivity, q is the elementary charge, and L is the perovskite thickness]² was calculated to be 5.77×10^{15} and 6.89×10^{15} cm⁻³ upon g-C₃N₄ and L-C₃N₄, respectively, those are much lower than that of the control device with 8.72×10^{15} cm⁻³.

6.3.6 Long-Term Device Stability

Despite the excellent intrinsic stability observed in inorganic NiO_x, a possible redox reaction at NiO_x/perovskite initiates and promotes the degradation of the active layer and subsequently the instability of the devices.^{46,47} Dual behavior (proton acceptor and Lewis electron acceptor) of Ni^{i≥3+} in NiO_x is responsible for the oxidizing iodide and deprotonating cationic amines (MA⁺) when in contact with perovskite, resulting in perovskite lattice deformation and producing PbI_{2-x}Br_x based hole extraction barriers at the interface. To unravel the influence of the L-C₃N₄ interface layer to overcome the possible degradation of perovskite and defect pathways from NiO_x, long-term operational stability of the un-encapsulated PSCs with and

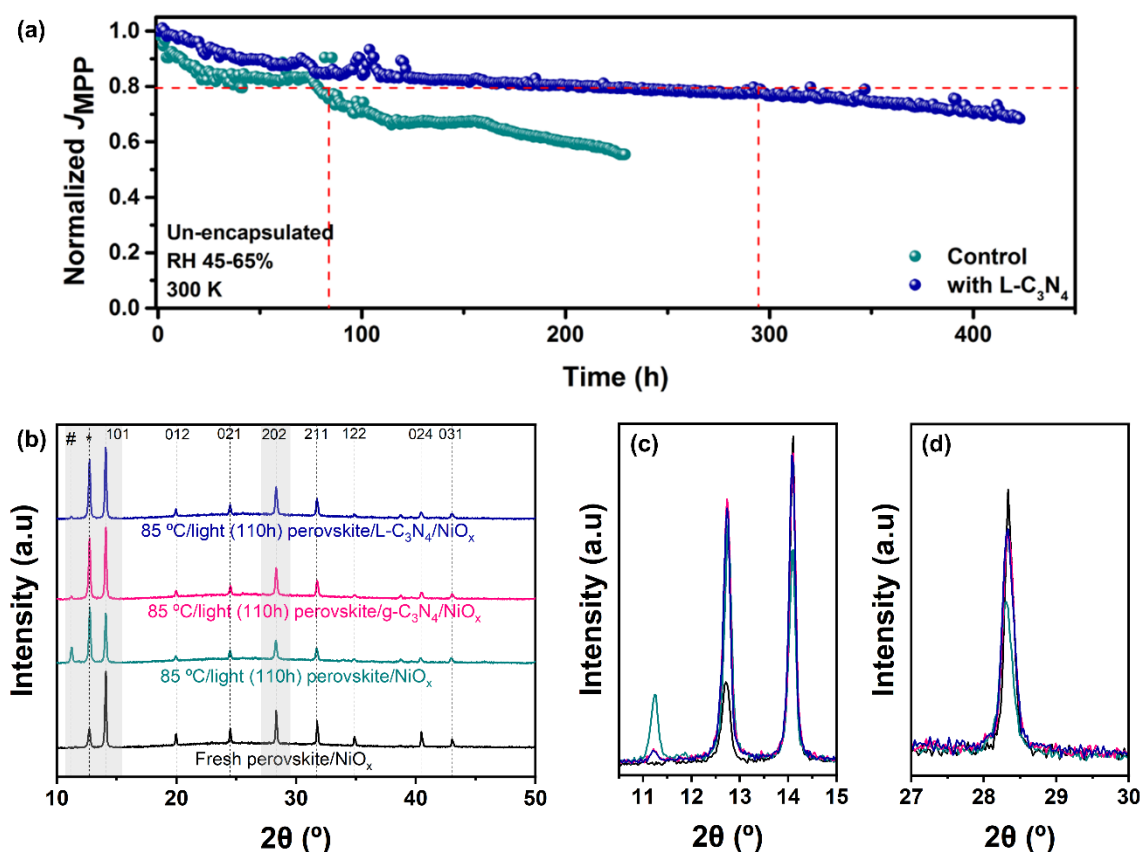


Figure 6.12 (a) The normalized current density of continuous MPP tracking for un-encapsulated PSCs under atmospheric conditions (RH 45-65 %, 300 K). (b) XRD of fresh perovskite on NiO_x and thermal/light stressed perovskite films deposited on NiO_x , $g-C_3N_4/NiO_x$, and $L-C_3N_4/NiO_x$. (c) Zoom in view of XRD patterns of around $2\theta=10.5^\circ$ - 15° and (d) Zoom in view of XRD patterns of (202) peak around $2\theta=28.5^\circ$. # and * represent the δ -phase of $FAPbI_3$ and the cubic PbI_2 , respectively.

without the $L-C_3N_4$ interface layer was investigated through maximum power point (MPP) tracking under 45-65 % ambient RH conditions. The prolonged stability of the device (Figure 6.12a), by the placement of the $L-C_3N_4$ interface layer, was exhibited when compared with the control device. The control device rapidly lost 20% of its initial PCE after 85h of continuous, while the $L-C_3N_4$ incorporated device exhibited 80% of its initial PCE for almost 300h of continuous operation. Further, we have studied the structural stability of the perovskite layer deposited on different down layers under constant thermal and illumination conditions. Samples were heated at 85 $^\circ C$ for about 110h under daylight and RH 55-75% conditions followed by XRD measurements (Figure 6.12b-d). In the fresh samples, two major peaks at 14.10° and 28.33° corresponding to (101) and (202) crystal planes, respectively, which are characteristics of perovskite were identified. After thermal/light exposure, a peak at 12.71°

Chapter 6

corresponding to the cubic PbI_2 was detected as the predominant peak from the perovskite directly deposited on NiO_x with a 1.12:1 intensity ratio of PbI_2 and (101). Even though, perovskites deposited on $\text{g-C}_3\text{N}_4/\text{NiO}_x$ and $\text{L-C}_3\text{N}_4/\text{NiO}_x$ films also feature a significantly intense PbI_2 peak after the thermal/light exposure, their intensity ratios with (101) plane are 0.86:1 and 0.83:1, respectively. A prominent peak observed from the perovskite/ NiO_x after the thermal/light exposure at 11.24° is recognized as the δ -phase of FAPbI_3 , which is the major part in the triple-cation perovskite studied in the current work.^{48,49} This peak is marginal upon C_3N_4 interlayers in between the perovskite and NiO_x , suggesting that the structural distortion and degradation of the perovskite is noticeably lower with the presence of $\text{g-C}_3\text{N}_4$ and $\text{L-C}_3\text{N}_4$ interlayers. Moreover, the absorption features were studied for the aforementioned perovskite films after the thermal/light exposure (Figure 6.13). After thermal/light stress, all of the samples showed a drastically decreased absorption spectrum, but the degradation is particularly pronounced in the perovskite/ NiO_x , which has begun bleaching its original dark color. This suggests that the thermal/light stress has an aggressive impact on the stability of the perovskite that is directly deposited on NiO_x . The perovskite deposited on $\text{g-C}_3\text{N}_4/\text{NiO}_x$ and $\text{L-C}_3\text{N}_4/\text{NiO}_x$, on the other hand, exhibits only slight bleaching and retains the majority of its dark hue, concluding that the underneath C_3N_4 layers influence on the stability of the perovskite. It is important to note here that the aforementioned experiment was done for the un-encapsulated perovskite films, thus the humidity has a major impact on the degradation of perovskite that is assumed as equal in each film.

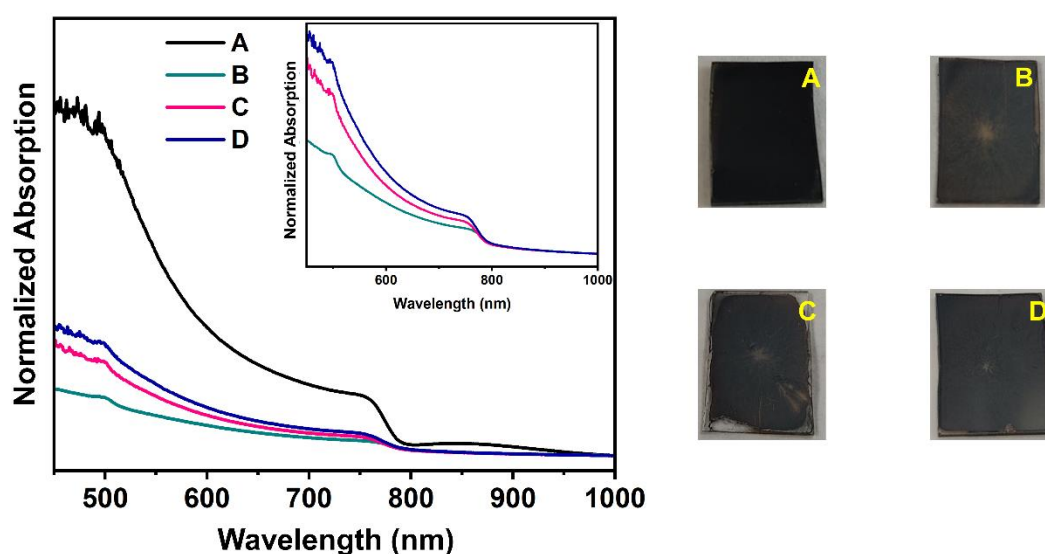


Figure 6. 13 UV-Vis spectra of fresh perovskite on NiO_x (A) and thermal/light stressed perovskite films deposited on NiO_x (B), $\text{g-C}_3\text{N}_4/\text{NiO}_x$ (C), and $\text{L-C}_3\text{N}_4/\text{NiO}_x$ (D). Images of each perovskite film are shown on the right side.

Chapter 6

6.4 Conclusions

To summarize, we demonstrated interface engineering of inverted PSCs using carbon nitride-based 2D materials, in particular g-C₃N₄ and L-C₃N₄. Our work demonstrates the potential of carbon nitride as an interfacial layer to diminish the non-radiative recombination and enhance charge transfer dynamics at HTM/perovskite interface. Through C₃N₄-based engineered interfaces we achieved an improvement in device performance and reliability as compared to the control architecture, measuring a power conversion efficiency of 19.33%, with complete suppression of the device hysteresis using inorganic HTMs. The solid-state NMR experiments suggest a hydrogen bonding of MA⁺ cations with C₃N₄. We noted that the positively charged hydrogen sites can coordinate with unbound nitrogen electron pairs at the edges of the triangular inner voids of the two-dimensional C₃N₄. The deduced coordination of FA-amine and MA-ammonia groups provides a favorable interaction at the interface between C₃N₄ and perovskite. Furthermore, C₃N₄ may overcome the possible instability of the active layer via iodide oxidation and deprotonating of cationic amines when perovskite is in contact directly with NiO_x, leading to improved long-term operational stability of the devices. Our investigation distinctly illustrates the advancement of 2D-based materials as an interface layer to uplift the reliability of the PSCs, which will pave the way for the industrial endeavor.

6.5 Supporting Information

6.5.1 Materials

The chemicals for perovskite were purchased from Dyesol except for PbI₂ and CsI₂ which were procured from Tokyo Chemical Industry (TCI) and were employed without further purification. [60]PCBM >99.5 % and Bathocuproine (BCP) were purchased from Solenne BV and TCI, respectively. Nickel (II) nitrate hexahydrate (Ni(NO₃)₂·6H₂O, 99.999 %) and NaOH were obtained from Sigma-Aldrich. Chlorobenzene (CBZ, 99 %), isopropanol (IPA, 99.9 %), ethanol (EtOH, 99 %), anhydrous dimethyl sulfoxide (DMSO, 99.8 %), and N, N-dimethylformamide (DMF, 99.8 %) were purchased from Acros Organics.

6.5.2 Preparation of C₃N₄-based solutions

To prepare C₃N₄-based solutions, 5 mg of each material was dissolved in 1 mL of isopropanol/absolute ethanol (70/30, V/V) mixture by sonication for 8 h at 45 °C and rest for 30 min. The upper part of the solution was collected and ultra-centrifuged for 15 min at 2000

Chapter 6

rpm. The supernatant was carefully collected and precipitation was discarded. The final concentrations (1, 1.25, and 1.5 mg/mL) were adjusted by adding the mixture of isopropanol/absolute ethanol (70/30, V/V).

6.5.3 Device fabrication

Device fabrication was conducted as described in Chapter 2, section 2.3.3. After substrates cleaning, NiO_x films were formed atop FTO substrates by spin coating a 20 mg/mL aqueous solution of NiO_x NCs at 4000 rpm for 35 s with 2000 rpm/s acceleration, followed by annealing at 150 °C for 30 min. The solutions of g-C₃N₄ and L-C₃N₄ with different concentrations were spin-coated on the NiO_x layer and annealed at 60 °C for 5 min to achieve the desired interfacial layer. To avoid moisture absorption, samples were transferred immediately to the argon-filled glovebox under controlled moisture and oxygen conditions (H₂O level: <1 ppm and O₂ level: <10 ppm) and annealed for another 5 min at 60 °C. The triple-cation-perovskite film was fabricated as described in Chapter 2, section 2.3.3. For PEAIE treatment, the PEAIE solution (20 mg/mL) in IPA was spin-coated onto the perovskite surface at a spin rate of 3000 rpm (2000 rpm/s) for 20s without further processing. The electron transport layer was fabricated by spin-coating a 15 mg/ml PCBM in CBZ at room temperature atop the perovskite film at 1000 rpm (500 rpm/s) for 20 s and then the films were annealed for 5 min at 60 °C. A thin layer of BCP (0.5mg/ml in IPA) was deposited atop PC₆₀BM by spin-coating at 5000 rpm for 40 s. The solar cell fabrication was finished by evaporating Ag (100 nm, <1 Å/s) in a thermal evaporator under low vacuum conditions (10⁻⁶ Torr). The control device was fabricated according to the above procure without the interfacial layer.

6.5.4. Device characterization

Current density-voltage (*J-V*) curves were measured under air-mass (AM) simulated 1.5G sunlight at 100 mWcm⁻² (Newport, AAA solar simulator, calibrated using silicon reference cell) and were recorded by applying an external potential bias to the devices. The measurements were done at room temperature under ambient conditions. The generated photocurrent was recorded at a scan rate of 100 mV/s (pre-sweep delay: 10s) with the help of a Keithley 2400 source meter and laser cut 0.09 cm² black metal mask as the active area. IPCE measurements were carried out using a 150 W xenon lamp attached to a Bentham PVE300 motorized 1/4 m monochromator as the light source and the system was calibrated with the standard silicon

Chapter 6

reference spectrum before the measurements. BioLogic SP-300 impedance analyzer conducted the electrochemical impedance spectroscopy and the data were fitted with EC-Lab software.

6.5.5 Materials and thin film characterization

The absorbance spectra of thin films were performed with a UV–vis spectrophotometer (Varian Cary 50 UV/Vis Spectrophotometer). X-ray diffractograms were recorded using a D8 Advance diffractometer from Bruker (Bragg-Brentano geometry, with an X-ray tube Cu K α , $\lambda = 1.5406$ Å). A scan range of 3°–80° was selected with an acquisition time of 1° per min. A scanning electron microscope (SEM Hitachi S-4800) was used to capture the cross-sectional and top-view microstructure of the samples. X-ray photoelectron spectroscopy (XPS) experiments were carried out on a SPECS system (Berlin, Germany) equipped with Phoibos 150 1D-DLD analyzer with monochromated Al K α radiation (1486.7 eV). The wide scan was performed with the step energy of 1 eV (dwell time, 0.1 s; pass energy, 80 eV), and a high-resolution detailed analysis of the elements was performed using 0.08 eV step energy (dwell time, 0.1 s; pass energy, 30 eV) with an electron exit angle of 90°. The spectra were calibrated with C1s as 284.6 eV and analyzed using CasaXPS 2.3.16 software, which models Gauss–Lorentzian contributions.

6.5.6 Sample preparation for solid-state NMR

The solutions of exfoliated g-C₃N₄ and L-C₃N₄ (1.25 mg/mL) in a mixture of isopropanol/absolute ethanol (70/30, V/V) were spin-coated on pre-cleaned glass substrates and annealed at 60 °C for 5 min. The triple-cation perovskite precursor in DMF/DMSO (4/1, V/V) was spin-coated to fabricate the perovskite films by a single-step method involving the CB-based antisolvent technique. After the complete crystallization of perovskite, the samples were cooled down to room temperature, and powder was collected by scratching the films.

Additional data is available in Appendix D

6.6 Bibliography

1. X. Li, W. Zhang, X. Guo, C. Lu, J. Wei, J. Fang, Constructing heterojunctions by surface sulfidation for efficient inverted perovskite solar cells, *Science*, 375 (2022), 434–437.
2. Q. Sun, B. Zong, X. Meng, B. Shen, X. Li, B. Kang, S. R. P. Silva, Interface regulation by an ultrathin wide-bandgap halide for stable and efficient inverted perovskite solar cells, *ACS Appl. Mater. Interfaces*, 14 (2022), 6702–6713.
3. Q. Cao, Y. Li, H. Zhang, J. Yang, J. Han, T. Xu, S. Wang, Z. Wang, B. Gao, J. Zhao, X. Li, X. Ma, S. M. Zakeeruddin, W. E. I. Sha, X. Li, M. Grätzel, Efficient and stable inverted perovskite solar cells with very high fill factors via incorporation of star-shaped polymer, *Sci. Adv.*, 7 (2021).
4. X. Ding, H. Wang, Y. Miao, C. Chen, M. Zhai, C. Yang, B. Wang, Y. Tian, M. Cheng, Bi(trifluoromethyl) benzoic acid-assisted shallow defect passivation for perovskite solar cells with an efficiency exceeding 21%, *ACS Appl. Mater. Interfaces*, 14 (2022), 3930–3938.
5. N. H. Hemasiri, S. Kazim, L. Calio, S. Paek, M. Salado, G. Pozzi, L. Lezama, M. K. Nazeeruddin, S. Ahmad, Elucidating the doping mechanism in fluorene–dithiophene-based hole selective layer employing ultrahydrophobic ionic liquid dopant, *ACS Appl. Mater. Interfaces*, 12 (2020), 9395–9403.
6. T. Wu, R. Zhuang, R. Zhao, R. Zhao, L. Zhu, G. Liu, R. Wang, K. Zhao, Y. Hua, Understanding the effects of fluorine substitution in lithium salt on photovoltaic properties and stability of perovskite solar cells, *ACS Energy Lett.*, 6 (2021), 2218–2228.
7. P. Schulz, D. Cahen, A. Kahn, Halide perovskites: Is it all about the interfaces?, *Chem. Rev.*, 119 (2019), 3349–3417.
8. M. S. Lee, S. Sarwar, S. Park, U. Asmat, D. T. Thuy, C. H. Han, S. Ahn, I. Jeong, S. Hong, Efficient defect passivation of perovskite solar cells via stitching of an organic bidentate molecule, *Sustain. Energy Fuels*, 4 (2020), 3318–3325.
9. T. Wang, Z. Cheng, Y. Zhou, H. Liu, W. Shen, Highly efficient and stable perovskite solar cells via bilateral passivation layers, *J. Mater. Chem. A*, 7 (2019), 21730–21739.
10. A. Rajagopal, K. Yao, A. K. Jen, Toward perovskite solar cell commercialization: a perspective and research roadmap based on interfacial engineering, *Adv. Mater.*, 30 (2018), 1800455.

Chapter 6

11. N. H. Hemasiri, S. Kazim, S. Ahmad, 1T-rich 2D-WS₂ as an interfacial agent to escalate photo-induced charge transfer dynamics in dopant-free perovskite solar cells, *J. Mater. Chem. C*, 9 (2021), 9865–9873.
12. P. You, G. Tang, J. Cao, D. Shen, T. W. Ng, Z. Hawash, N. Wang, C. K. Liu, W. Lu, Q. Tai, Y. Qi, C. S. Lee, F. Yan, 2D materials for conducting holes from grain boundaries in perovskite solar cells, *Light Sci. Appl.*, 10 (2021).
13. N. H. Hemasiri, S. Kazim, S. Ahmad, Reduced trap density and mitigating the interfacial losses by placing 2D dichalcogenide material at perovskite/HTM interface in a dopant free perovskite solar cells, *Nano Energy*, 77 (2020) 105292.
14. B. W. N. H. Hemasiri, J. K. Kim, J. M. Lee, Synthesis and characterization of graphene/ito nanoparticle hybrid transparent conducting electrode, *Nanomicro Lett.*, 10 (2017).
15. F. Xie, G. Dong, K. Wu, Y. Li, M. Wei, S. Du, In situ synthesis of g-C₃N₄ by glass-assisted annealing route to boost the efficiency of perovskite solar cells, *J. Colloid Interface Sci.*, 591 (2021), 326–333.
16. P. Kumar, E. Vahidzadeh, U. K. Thakur, P. Kar, K. M. Alam, A. Goswami, N. Mahdi, K. Cui, G. M. Bernard, V. K. Michaelis, K. Shankar, C₃N₅: A low bandgap semiconductor containing an azo-linked carbon nitride framework for photocatalytic, photovoltaic and adsorbent applications, *J. Am. Chem. Soc.*, 141 (2019), 5415–5436.
17. X. Yang, L. Zhao, S. Wang, J. Li, B. Chi, Recent progress of g-C₃N₄ applied in solar cells, *J. Materiomics*, 7 (2021), 728–741.
18. L. L. Jiang, Z. K. Wang, M. Li, C. C. Zhang, Q. Q. Ye, K. H. Hu, D. Z. Lu, P. F. Fang, L. S. Liao, Perovskite solar cells: passivated perovskite crystallization via g-C₃N₄ for high-performance solar cells, *Adv. Funct. Mater.*, 28 (2018), 1870047.
19. Z. Li, S. Wu, J. Zhang, Y. Yuan, Z. Wang, Z. Zhu, Improving photovoltaic performance using perovskite/surface-modified graphitic carbon nitride heterojunction, *Sol. RRL*, 4 (2019), 1900413.
20. D. Cruz, J. Garcia Cerrillo, B. Kumru, N. Li, J. Dario Perea, B. V. K. J. Schmidt, I. Lauermaun, C. J. Brabec, M. Antonietti, Influence of thiazole-modified carbon nitride nanosheets with feasible electronic properties on inverted perovskite solar cells, *J. Am. Chem. Soc.*, 141 (2019), 12322–12328.
21. J. F. Liao, W. Q. Wu, J. X. Zhong, Y. Jiang, L. Wang, D. B. Kuang, Enhanced efficacy of defect passivation and charge extraction for efficient perovskite photovoltaics with a small open circuit voltage loss, *J. Mater. Chem. A*, 7 (2019), 9025–9033.

Chapter 6

22. Z. Liu, S. Wu, X. Yang, Y. Zhou, J. Jin, J. Sun, L. Zhao, S. Wang, The dual interfacial modification of 2D g-C₃N₄ for high-efficiency and stable planar perovskite solar cells, *Nanoscale Adv.*, 2 (2020), 5396–5402.
23. X. Wang, K. Maeda, A. Thomas, K. Takanabe, G. Xin, J. M. Carlsson, K. Domen, M. Antonietti, A metal-free polymeric photocatalyst for hydrogen production from water under visible light, *Nat. Mater.*, 8 (2008), 76–80.
24. B. Jürgens, E. Irran, J. Senker, P. Kroll, H. Müller, W. Schnick, Melem (2,5,8-triamino-tri-s-triazine), an important intermediate during condensation of melamine rings to graphitic carbon nitride: synthesis, structure determination by X-ray powder diffractometry, solid-state NMR, and theoretical studies, *J. Am. Chem. Soc.*, 125 (2003), 10288–10300.
25. J. Xu, L. Zhang, R. Shi, Y. Zhu, Chemical exfoliation of graphitic carbon nitride for efficient heterogeneous photocatalysis, *J. Mater. Chem. A*, 1 (2013), 14766.
26. S. Yang, Y. Gong, J. Zhang, L. Zhan, L. Ma, Z. Fang, R. Vajtai, X. Wang, P. M. Ajayan, Exfoliated graphitic carbon nitride nanosheets as efficient catalysts for hydrogen evolution under visible light, *Adv. Mater.*, 25 (2013), 2452–2456.
27. Y. Cui, J. Zhang, G. Zhang, J. Huang, P. Liu, M. Antonietti, X. Wang, Synthesis of bulk and nanoporous carbon nitride polymers from ammonium thiocyanate for photocatalytic hydrogen evolution, *J. Mater. Chem.*, 21 (2011), 13032.
28. Y. Cui, Z. Ding, X. Fu, X. Wang, Construction of conjugated carbon nitride nanoarchitectures in solution at low temperatures for photoredox catalysis, *Angew. Chem. Int. Ed.*, 124 (2012), 11984–11988.
29. S. Tonda, S. Kumar, S. Kandula, V. Shanker, Fe-doped and -mediated graphitic carbon nitride nanosheets for enhanced photocatalytic performance under natural sunlight, *J. Mater. Chem. A*, 2 (2014), 6772.
30. J. Chang, Y. C. Wang, C. Song, L. Zhu, Q. Guo, J. Fang, Carboxylic ester-terminated fulleropyrrolidine as an efficient electron transport material for inverted perovskite solar cells, *J. Mater. Chem. C*, 6 (2018), 6982–6987.
31. M. Liu, G. Zhong, Y. Yin, J. Miao, K. Li, C. Wang, X. Xu, C. Shen, H. Meng, Aluminum-doped cesium lead bromide perovskite nanocrystals with stable blue photoluminescence used for display backlight, *Adv. Sci.*, 4 (2017), 1700335.
32. D. J. Kubicki, D. Prochowicz, A. Hofstetter, P. Péchy, S. M. Zakeeruddin, M. Grätzel, L. Emsley, Cation dynamics in mixed-cation (MA)_x(FA)_{1-x}PbI₃ hybrid perovskites from solid-state NMR, *J. Am. Chem. Soc.*, 139 (2017), 10055–10061.

Chapter 6

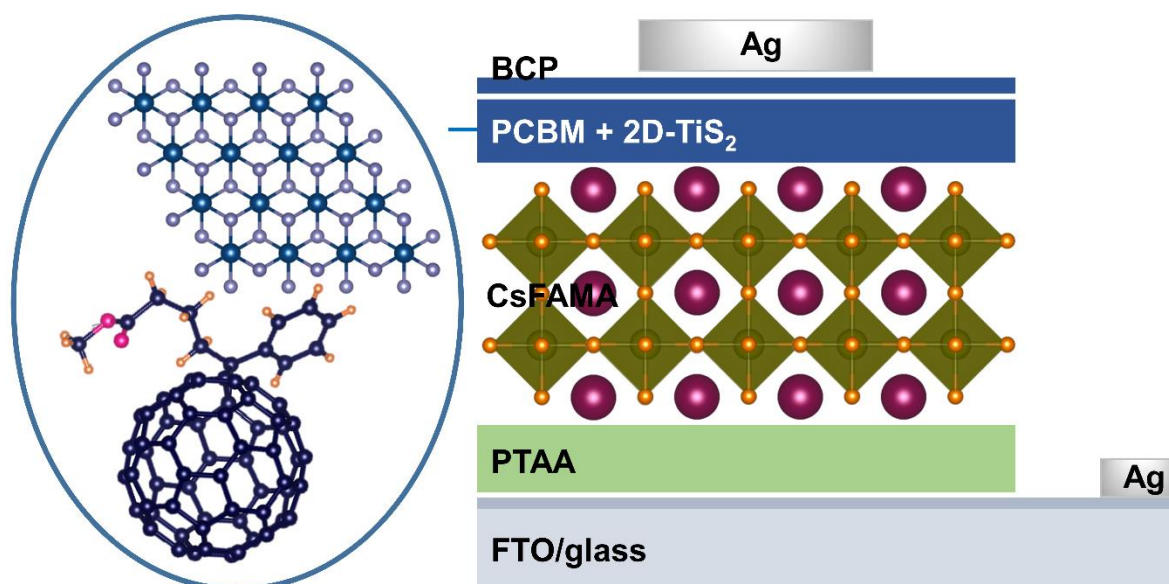
33. K. Saalwächter, F. Lange, K. Matyjaszewski, C. F. Huang, R. Graf, BaBa-xy16: robust and broadband homonuclear DQ recoupling for applications in rigid and soft solids up to the highest MAS frequencies, *J Magn. Reson.*, 212 (2011), 204–215.
34. C. Blaga, G. Christmann, M. Boccard, C. Ballif, S. Nicolay, B. A. Kamino, Palliating the efficiency loss due to shunting in perovskite/silicon tandem solar cells through modifying the resistive properties of the recombination junction, *Sustain. Energy Fuels*, 5 (2021), 2036–2045.
35. M. T. Khan, N. H. Hemasiri, S. Kazim, S. Ahmad, Decoding the charge carrier dynamics in triple cation-based perovskite solar cells, *Sustain. Energy Fuels*, 5 (2021), 6352–6360.
36. N. Klipfel, J. Xia, P. Čulík, S. Orlandi, M. Cavazzini, N. Shibayama, H. Kanda, C. Igci, W. Li, Y. B. Cheng, V. Jankauskas, K. Genevicius, A. M. Asiri, C. Momblona, K. Rakstys, G. Pozzi, M. K. Nazeeruddin, Zn(II) and Cu(II) tetrakis(diarylamine)phthalocyanines as hole-transporting materials for perovskite solar cells, *Mater. Today Energy*, 2022, 29, 101110.
37. C. Li, Z. Song, D. Zhao, C. Xiao, B. Subedi, N. Shrestha, M. M. Junda, C. Wang, C. S. Jiang, M. Al-Jassim, R. J. Ellingson, N. J. Podraza, K. Zhu, Y. Yan, Reducing saturation-current density to realize high-efficiency low-bandgap mixed tin–lead halide perovskite solar cells, *Adv. Energy Mater.*, 9 (2018), 1803135.
38. W. Tress, N. Marinova, T. Moehl, S. M. Zakeeruddin, M. K. Nazeeruddin, M. Grätzel, Understanding the rate-dependent J – V hysteresis, slow time component, and aging in $\text{CH}_3\text{NH}_3\text{PbI}_3$ perovskite solar cells: the role of a compensated electric field, *Energy Environ. Sci.*, 8 (2015), 995–1004.
39. M. S. Alvar, P. W. M. Blom, G. J. A. H. Wetzelaer, Space-charge-limited electron and hole currents in hybrid organic-inorganic perovskites, *Nat. Commun.*, 2020, 11(1).
40. K. Liu, Y. Sun, Q. Li, C. Yang, M. Azam, Z. Wang, S. Qu, Z. Wang, A wrinkled structure with broadband and omnidirectional light-trapping abilities for improving the performance of organic solar cells with low defect density, *Nanoscale*, 11 (2019), 22467–22474.
41. Z. Luo, G. Li, W. Gao, K. Wu, Z. G. Zhang, B. Qiu, H. Bin, L. Xue, F. Liu, Y. Li, C. Yang, A universal nonfullerene electron acceptor matching with different band-gap polymer donors for high-performance polymer solar cells, *J. Mater. Chem. A*, 6 (2018), 6874–6881.

Chapter 6

42. L. Xiao, T. Liang, K. Gao, T. Lai, X. Chen, F. Liu, T. P. Russell, F. Huang, X. Peng, Y. Cao, Ternary solar cells based on two small molecule donors with same conjugated backbone: the role of good miscibility and hole relay process, *ACS Appl. Mater. Interfaces*, 2017, 9(35), 29917–29923.
43. H. Dhifaoui, N. H. Hemasiri, W. Aloui, A. Bouazizi, S. Kazim, S. Ahmad, An approach to quantify the negative capacitance features in a triple-cation based perovskite solar cells, *Adv. Mater. Interfaces*, 8 (2021), 2101002.
44. N. H. Hemasiri, L. Calì, M. Pegu, S. Kazim, S. Ahmad, Molecular interface engineering via triazatruxene-based moieties/ NiO_x as hole-selective bilayers in perovskite solar cells for reliability, *Sol. RRL*, (2022), 2100793.
45. J. Li, T. Jiu, C. Duan, Y. Wang, H. Zhang, H. Jian, Y. Zhao, N. Wang, C. Huang, Y. Li, Improved electron transport in MAPbI_3 perovskite solar cells based on dual doping graphdiyne, *Nano Energy*, 46 (2018), 331–337.
46. C. C. Boyd, R. C. Shallcross, T. Moot, R. Kerner, L. Bertoluzzi, A. Onno, S. Kavadiya, C. Chosy, E. J. Wolf, J. Werner, J. A. Raiford, C. de. Paula, A. F. Palmstrom, Z. J. Yu, J. J. Berry, S. F. Bent, Z. C. Holman, J. M. Luther, E. L. Ratcliff, N. R. Armstrong, M. D. McGehee, Overcoming redox reactions at perovskite-nickel oxide interfaces to boost voltages in perovskite solar cells, *Joule*, 4 (2020), 1759-1775.
47. T. Guo, Z. Fang, Z. Zhang, Z. Deng, R. Zhao, J. Zhang, M. Shang, X. Liu, Z. Hu, Y. Zhu, L. Han, Self-assembled interlayer aiming at the stability of NiO_x based perovskite solar cells, *J. Energy Chem.*, 69 (2022), 211–220.
48. S. H. Turren-Cruz, M. Saliba, M. T. Mayer, H. Juárez-Santiesteban, X. Mathew, L. Nienhaus, W. Tress, M. P. Erodici, M. J. Sher, M. G. Bawendi, M. Grätzel, A. Abate, A. Hagfeldt, J. P. Correa-Baena, Enhanced charge carrier mobility and lifetime suppress hysteresis and improve efficiency in planar perovskite solar cells, *Energy Environ. Sci.*, 2018, 11(1), 78–86.
49. Y. Sun, J. Peng, Y. Chen, Y. Yao, Z. Liang, Triple-cation mixed-halide perovskites: towards efficient, annealing-free and air-stable solar cells enabled by $\text{Pb}(\text{SCN})_2$ additive, *Sci. Rep.*, 2017, 7(1).

CHAPTER 7

CURTAILEMENT OF INTERFACE RECOMBINATION FOR ENHANCED EFFICIENCY IN INVERTED PEROVSKITE SOLAR CELLS VIA 2D-TiS₂-PCBM ELECTRON TRANSPORT LAYER



Chapter 7

7.1 Abstract

The fabrication of effective, low-cost, stable solar cells is one of the scientific milestones of the next couple of years. Among the 2D library of materials, layered 2D-TiS₂ has shown advances in regular perovskite solar cells (PSCs) as interface layers. This chapter highlights the contributions of 2D-TiS₂ toward the construction of efficient and long-lifetime inverted PSCs. It is shown that the non-radiation recombination is mediated by the optimal addition of 15 wt% 2D-TiS₂ into PCBM. The addition of 2D-TiS₂ results in the improvement of both mobility and conductivity while reducing the trap density of the PCBM layer. The target device based on 2D-TiS₂ exhibited an enhanced PCE of 17.95% when compared to the control device owing to the notable build-up in V_{oc} and fill factor. The unencapsulated devices retained 85 % of their initial current density stressed under constant illumination for 60 h at 27 °C in an ambient atmosphere.

7.2 Introduction

Inverted PSCs with a positive-intrinsic-negative (often referred to as the *p-i-n*) architecture are attractive for future commercialization, owing to several factors, including, their low-cost fabrication, diversified material choices, reliable operation with negligible hysteresis, and fewer parasitic absorption losses over regular *n-i-p* configuration, which makes it compatible for tandem solar cells.¹⁻³ However, the power conversion efficiency of *p-i-n* architecture still being behind their structural counterpart *n-i-p*, containing the same active layer. Among two charge transport layers (CTLs); the electron transport layer (ETL) plays a crucial role in improving the PV performances and extended stability in *p-i-n* PSCs.⁴⁻⁶

A fullerene derivative, commonly known as PCBM that is [6,6]-phenyl-C61-isomethyl butyrate is regarded as the highly utilized ETL in *p-i-n* configuration since their first application in PSCs in 2013 by Chen and co-workers.⁷ Their excellent solubility is an advantage for solution-processed device fabrication; however, the existence of exohedral moieties in the C₆₀ cage sacrifice the high electron affinity and original electron mobility found in pristine fullerene leading to inferior efficiency of inverted PSCs.⁸ Further, the quality of the PCBM film is heavily reliant on the surface morphology of the underlying perovskite film, in which surface rough perovskite films may result in a discontinued PCBM layer, leading to an interfacial nonradiative recombination current leakage current.^{9,10} Aggregation under annealing conditions is another possible drawback of PCBM rendering homogeneous film

Chapter 7

formation.¹¹ Typical remedies to overcome such a defaulted ETL on the perovskite such as thermal evaporation of C₆₀ or C₆₀/bathocuproine (BCP) as a capping layer before the PCBM deposition, deposition of C₆₀ on PCBM, or blended C₆₀-PCBM mixture may not only introduce additional cost but also extend the fabrication process.^{8-10,12-14} On the other hand, inexpensive pristine C₆₀ or C₇₀ show low solubility in organic solvents, which results in a high tendency of crystallization during the spin-coating process.⁸

Following the remarkable results achieved by the use of 2D materials in optoelectronics, tunable work function and energy bandgap are the main advantages of layered 2D-TMDs to be exploited in PVs.¹⁵⁻²⁰ As observed in Chapter 1 and Chapter 2, the main impacts of TMDs on PVs are the extended operational stability under various degradation protocols and the enhancement of PV performances, which can be attributed to: i. the dangling bond-free nature, making those materials more resistant to react with foreign species, ii. ballistic carrier charge transportation, and iii. quantum confinement effect leading to enhanced photoluminescence.²¹ Several studies have reported the utilization of 2D-TMDs as HTL or interlayer in between HTL and perovskites since it is observed that most commonly exploited TMDs (MoS₂, MoSe₂, and WS₂) performed better in the *p*-side in both *n-i-p* and *p-i-n* device. Limited reports exist regarding the utilization of 2D-TiS₂ as ETLs or interface layer at ETL/perovskite interface in the regular *n-i-p* configuration.^{22,23} So far, only Kymakis and co-workers have studied the device performance and stability in the inverted configuration upon *n*-type TMDs incorporating metallic 2D-TaS₂ as a buffer layer.²⁴

The challenges of incorporation of 2D-TMDs in PSCs to be tackled are numerous including the optimization of the film formation and low-cost embodiments. This Chapter highlights the contribution of Li⁺ intercalated 2D-TiS₂ toward the construction of efficient and stable inverted PSCs. The 2D-TiS₂ was utilized as either an interface layer between PCBM and perovskite or blended with PCBM and applied as an ETL in the devices. It was found that the effect of 2D-TiS₂ on PV performance is higher when it is mixed with PCBM rather than used as an interface layer. Upon optimal addition of 15 wt% of 2D-TiS₂ into PCBM-based ETL, we succeeded in preparing devices with suppressed non-radiative recombination, leading to V_{oc} as high as 1.057 V, FF to 77.56 %, and ultimately the PCE up to 17.95%. Our findings demonstrate that at the perovskite/PCBM interface, increased charge extraction and a longer electron lifespan are the major factors controlling the improvement of PCE.

7.3 Results and Discussion

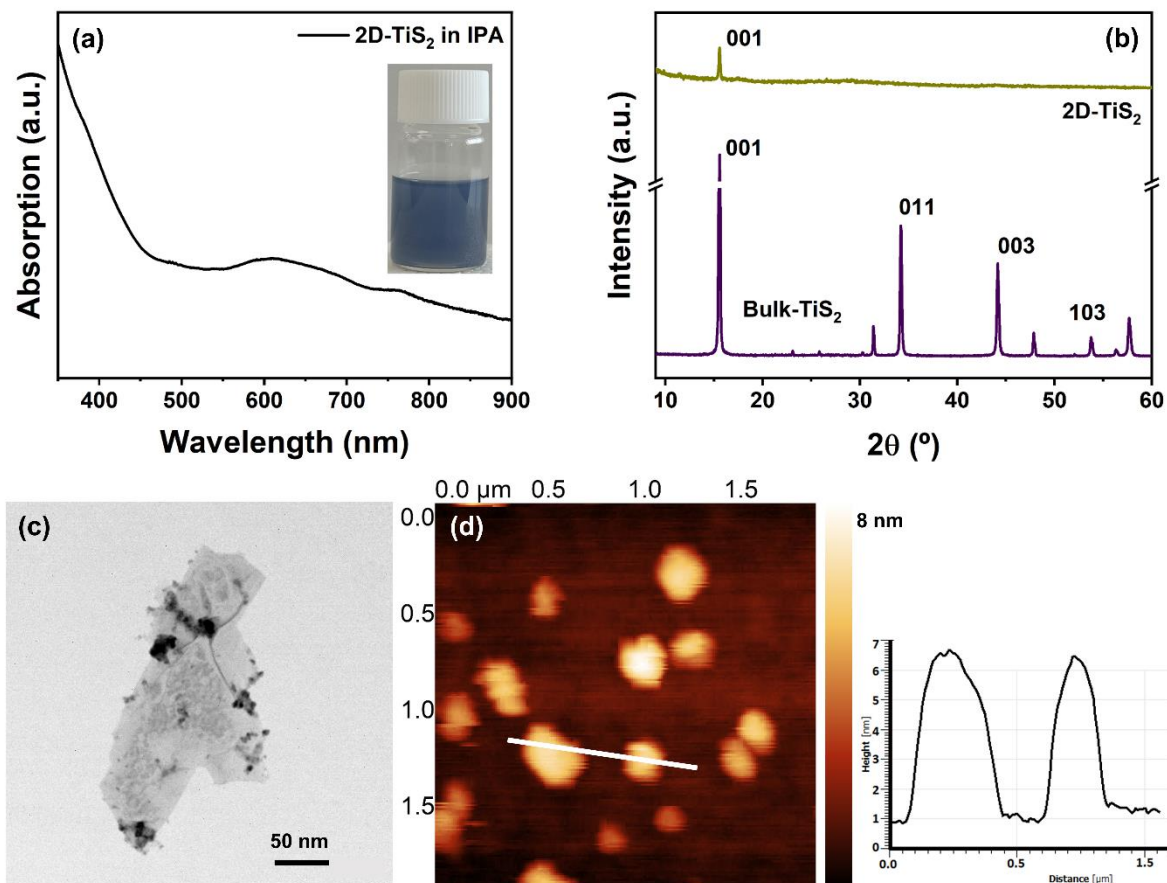
7.3.1 Exfoliated 2D-TiS₂ Characterization

Figure 7.2 (a) UV-Vis absorption spectrum of exfoliated 2D-TiS₂ in isopropanol, insert shows the suspension of 2D-TiS₂ in isopropanol. (b) XRD patterns of bulk and exfoliated TiS₂. TEM (c) and AFM (d) images of exfoliated 2D-TiS₂, insert of (d) shows the thickness profile along the line.

Alkali metal-assisted liquid phase exfoliation of bulk TiS₂ was performed as described in Chapter 2, resulting in a colloidal suspension of highly exfoliated few-layered 2D-TiS₂ in isopropanol (Insert Figure 7.1a). Exciton peaks in the UV-Vis spectra of the exfoliated TiS₂ are not prominent (Figure 7.1a), which is a common feature of group VI TMDs.^{25,26} These exciton peaks are not visible in monolayers due to their semimetallic electronic structure; thus, we can conclude that the as exfoliated TiS₂ consists not only of monolayers but also a few layers.²⁵ The structural characterization of 2D-TiS₂ and the comparison with the bulk TiS₂ were conducted by powder-X-ray diffraction (XRD) measurements (Figure 7.1b). The exfoliated TiS₂ is responsible to produce only an intense peak corresponding to (001), attributing to the

Chapter 7

structural changes from bulk to layered 2D-TiS₂.^{27,28} The lateral size of the exfoliated flakes is in the micron size (~300-500 nm) with ~4-5 nm thickness according to the transmission electron microscopy (TEM, Figure 7.1c) and the atomic force microscopy (AFM, Figure 7.1d), respectively. The narrow scan X-ray photoelectron spectroscopy (XPS) was used to analyze the chemical states in the as-exfoliated TiS₂, where the quadruple peaks (Ti2p) were detected concerning Ti-O and Ti-S at 456.03, 458.46, 461.50, and 464.19 eV corresponding to Ti⁴⁺ 2p_{3/2}, Ti³⁺ 2p_{3/2}, Ti⁴⁺ 2p_{1/2}, and Ti³⁺ 2p_{1/2}, respectively (Figure 7.2a). Typical S 2p narrow XPS spectrum was noted with S²⁻ 2p_{3/2} at 160.38 eV and S²⁻ 2p_{1/2} at 161.53 eV. Additionally, a broad peak was observed centered at 169.08 eV, attributing to the surface adsorbed sulfate.^{27,29,30}

7.3.2 Thin-Film Characterization

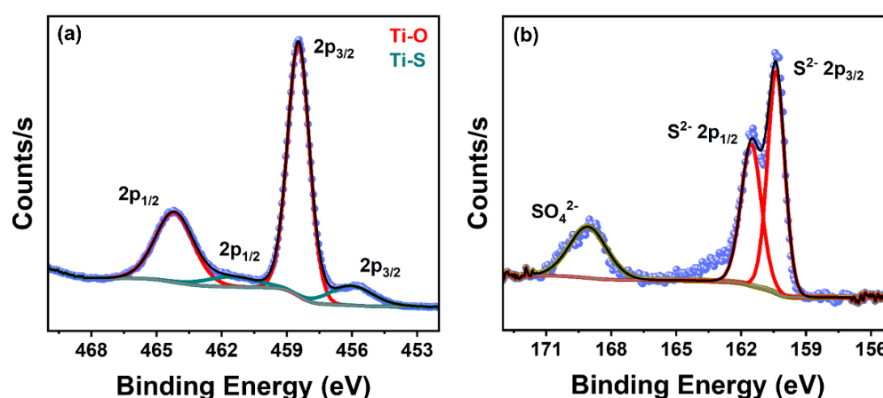


Figure 7. 3 XPS narrow spectrum of Ti 2p (a) and S 2p (b).

The surface morphology of the PCBM and 2D-TiS₂ combined PCBM on triple-cation perovskite film was examined by SEM and AFM (Figure 7.3). From the AFM topography image, we noted that the TiS₂+PCBM film displays a relatively uniform and smooth surface when compared with the pristine PCBM on the perovskite film, with the RMS roughness of 8.94 and 10.02 nm, respectively.

To evaluate the enhancement of the conductivity and mobility upon the addition of 2D-TiS₂ into PCBM, we fabricated electron-only devices with the structures of FTO/ PCBM (with or without 2D-TiS₂)/Ag and FTO/SnO₂/ PCBM (with or without 2D-TiS₂)/Ag, respectively as shown in Figure 7.4a and b. The conductivity (σ) of the pristine PC₆₀BM was extracted from the *I-V* profile (Figure 7.4c) along with the relation: $\sigma = (J/V)d$ (where *d* is the thickness of the film)³¹ and calculated to be 3.18 μ S/cm. Contrary; the addition of as-exfoliated 2D-TiS₂

Chapter 7

into PCBM showed us a noticeable improvement in conductivity (4.25 $\mu\text{S}/\text{cm}$). The addition of 2D-TiS₂ into PCBM was 15 wt%, which is optimized according to the best efficiency of PSCs. The influence of 2D-TiS₂ for the electron mobility was further analyzed (Figure 7.4d) from electron-only devices along with the classical Mott-Gurney space-charge-limited-current (SCLC) relation;^{32,33}

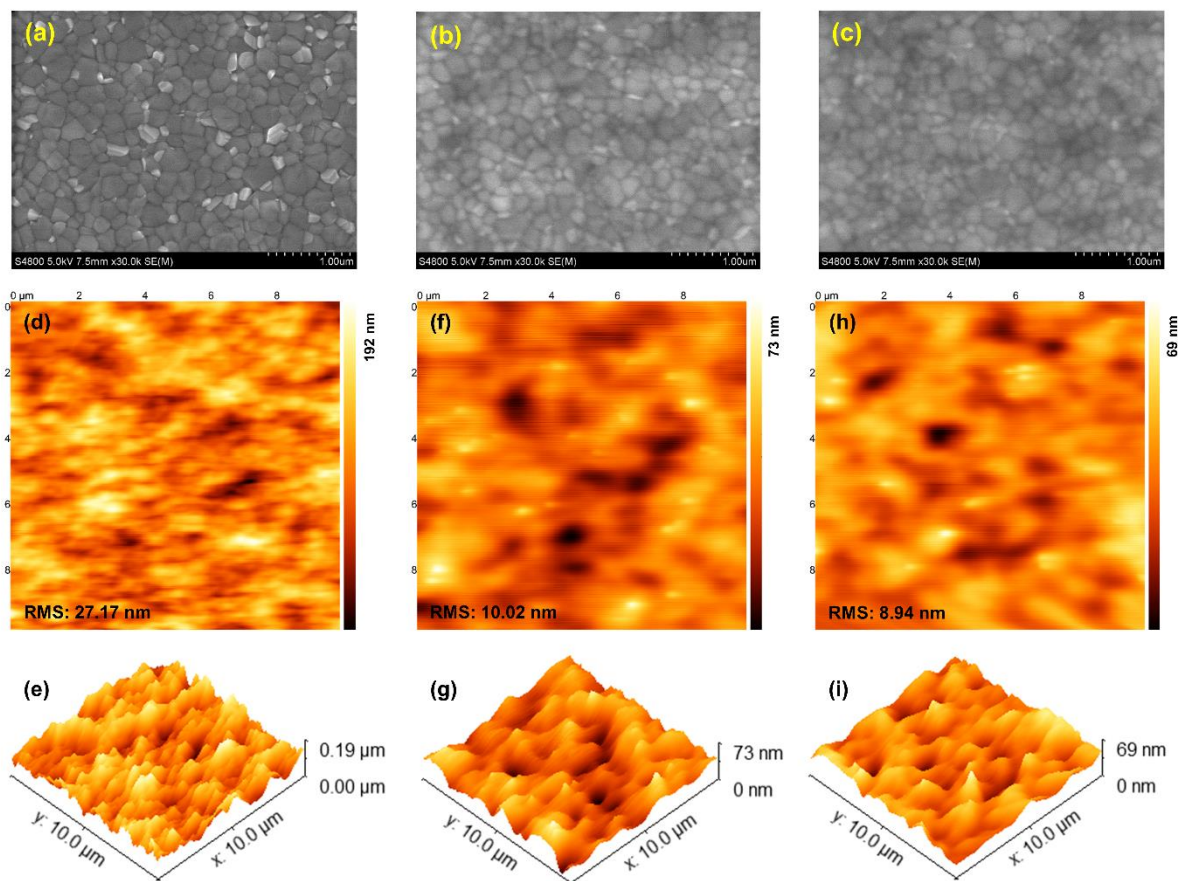


Figure 7. 4 SEM images of (a) CsFAMA perovskite, (b) PCBM on CsFAMA perovskite, and (c) PCBM + 15 wt% 2D-TiS₂ on CsFAMA perovskite. AFM topography and 3D height images of CsFAMA perovskite (d and e), PC_BM on CsFAMA perovskite (f and g), and PCBM + 15 wt% 2D-TiS₂ on CsFAMA perovskite (h and i), respectively.

$$J = 9\varepsilon\varepsilon_0\mu\frac{V_{app}^2}{8L^3} \quad (6.1)$$

where, ε , ε_0 , μ , V_{app} , and L represent the dielectric constant of air, the relative dielectric constant, the thickness of the charge transport layer, charge carrier mobility, and applied potential, respectively. The dielectric constant of the PCBM was taken as 3.¹⁵ The estimated

Chapter 7

electron mobility of each device was tabulated in Table 7.1, indicating that the incorporation of 2D-TiS₂ into PCBM results in 4 times boosting in electron mobility in the ETL. Moreover, the defect density (N_{Defects}) was evaluated (Table 7.1) from the logarithmic J - V plot (Figure 7.4e) and the relation followed by;^{35,36}

$$N_{\text{Defects}} = 2\varepsilon\varepsilon_0 \frac{V_{\text{TFL}}}{eL^2} \quad (6.2)$$

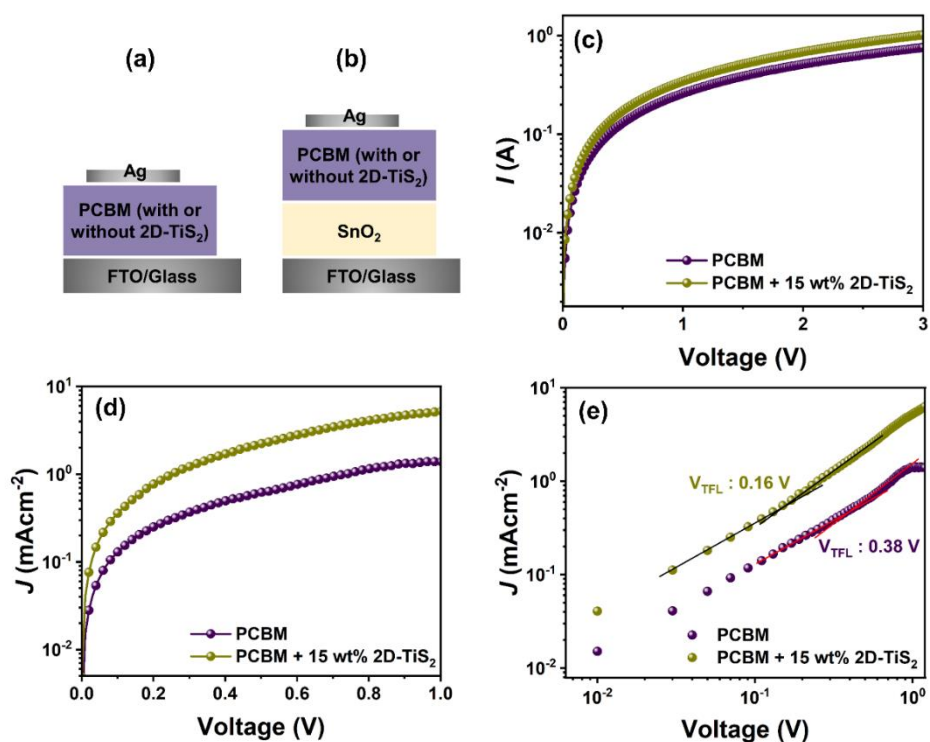


Figure 7.5 (a) Device configuration for the conductivity: FTO/PCBM(with or without 15 wt% 2D-TiS₂)/Ag. (b) Device configuration for the mobility and space-charge-limited current (SCLC): FTO/SnO₂/PCBM(with or without 15 wt% 2D-TiS₂)/Ag. (c) I - V curves for conductivity measurements in the dark. (d) J - V curves for electron-mobility measurements with the electron-only device in the dark. (e) SCLC for devices with electron-only device in the dark.

where V_{TFL} is the intersection point between the Ohmic and trap-filled limited (TFL) region. Upon 15 wt% addition of 2D-TiS₂ into PCBM results in notable suppression of the defect density from $15.64 \times 10^{15} \text{ cm}^{-3}$ to $6.5 \times 10^{15} \text{ cm}^{-3}$ when compared with the pristine form of PCBM.

Chapter 7

Table 7. 1 Electrical parameters of the electron only devices.

Device	σ ($\mu\text{S}/\text{cm}$)	μ (cm^2/Vs)	V_{TFL} (V)	N_{Defects} (cm^{-3})
PCBM	3.18	2.62×10^{-6}	0.38	15.64×10^{15}
PCBM + 15 wt% 2D-TiS ₂	4.25	1.18×10^{-5}	0.16	6.5×10^{15}

7.3.3 Device and Photovoltaic Characterization

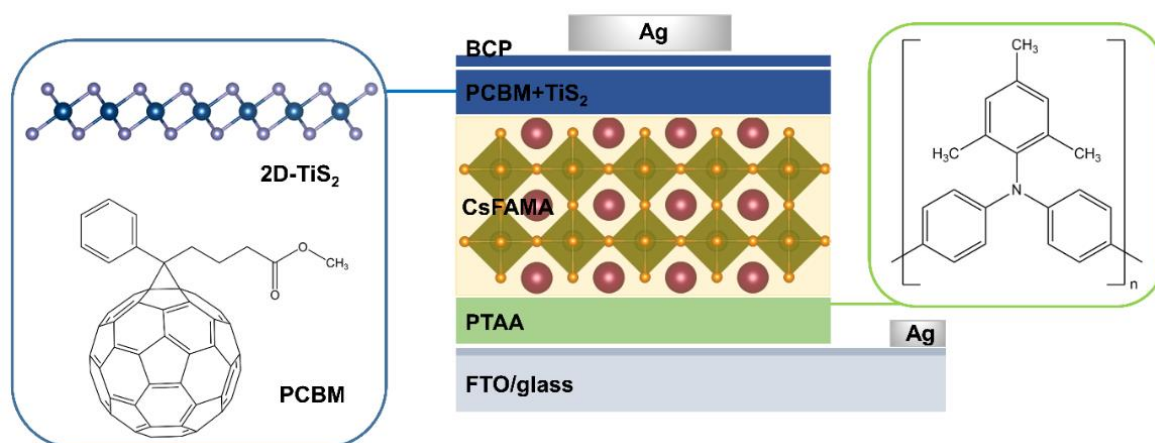


Figure 7. 6 Schematic of the proposed device architecture. FTO: fluorine-doped tin oxide/PTAA: poly(triaryl amine)/CsFAMA: $\text{Cs}_{0.1}(\text{FA}_{0.9}\text{MA}_{0.1})_{0.9}\text{Pb}(\text{I}_{0.9}\text{Br}_{0.1})_3$ /PCBM: [6,6]-phenyl-C₆₁-isomethyl butyrate + 2D-TiS₂/BCP: bathocuproine/Ag.

The device architecture used in this study was based on the *p-i-n* configuration FTO/PTAA/perovskite: $\text{Cs}_{0.1}(\text{FA}_{0.9}\text{MA}_{0.1})_{0.9}\text{Pb}(\text{I}_{0.9}\text{Br}_{0.1})_3$ /PCBM+2D-TiS₂/BCP/Ag, where PTAA [poly(triaryl) amine] is the hole transport layer (HTL), illustrated in Figure 7.5. The perovskite layer was fabricated by an anti-solvent assisted, one-step deposition method as described in Chapter 2. In the control device, PCBM as ETL was used in their pristine form with 20 mg in 1 mL chlorobenzene whereas for the modified devices different weight percentages (5%, 15%, and 20% w/w) of as exfoliated 2D-TiS₂ were added to 20 mg of PC₆₀BM in 1 mL chlorobenzene.

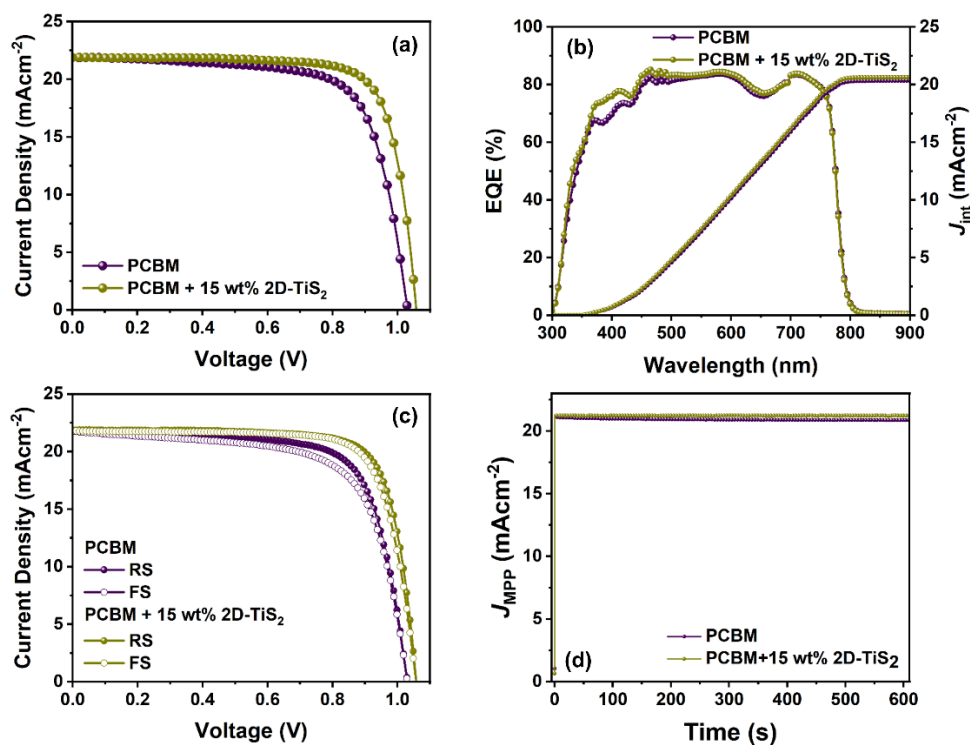


Figure 7.7 $J-V$ curves of the champion devices under simulated AM1.5G light at reverse scan with 100 mV/s scan rate (a) and the corresponding EQE and integrated current (b). (c) Reverse and forward $J-V$ curves of the champion devices. (d) Stabilized initial 600 s MPP tracking of J_{sc} under ambient conditions.

We first evaluated the effect of 2D-TiS₂ addition into PCBM on the PV performances of the devices. The current density-voltage ($J-V$) under AM1.5G illumination at 100 mV/s scan rate (Figure 7.6a). The best improvement was observed with the 15 wt% addition of 2D-TiS₂ into PCBM, in which the PCE increased from 15.89 % to 17.95 %. Noticeable increments of V_{oc} and FF were observed in 15 wt% addition on 2D-TiS₂ while J_{sc} was almost unchanged. Table 6.1 summarizes the photovoltaic parameters V_{oc} , J_{sc} , FF, and PCE for the champion devices with their statistics. The integrated current densities extracted from the external quantum efficiency (EQE) spectra in Figure 7.6b are 20.35 and 20.64 mAcm^{-2} for control and 15 wt% added 2D-TiS₂ devices, respectively, showing an agreement with those obtained from $J-V$ curves. The modified device based on a 15 wt% addition of 2D-TiS₂ into ETL is less prone to hysteresis with 0.008 HI (hysteresis index) when compared with the control device (0.059 of HI). The HI was evaluated from the equation, $HI = [J_{\text{RS}}(0.8V_{\text{oc}}} - J_{\text{FS}}(0.8V_{\text{oc}})]/J_{\text{RS}}(0.8V_{\text{oc}})$, where $J_{\text{RS}}(0.8V_{\text{oc}})$ and $J_{\text{FS}}(0.8V_{\text{oc}})$ represent the J_{sc} at 80% of V_{oc} from reverse and forward $J-V$ scans, respectively.³⁷

Chapter 7

The device performance was further verified with the steady-state power output (SPO) of the PCBM and PCBB + 15 wt% 2D-TiS₂-based devices for initial 600 s operation (Figure 7.6d) at their corresponding MPP (maximum power point). The MPP was determined from the relation following, $V_{MPP} = KV_{oc}$, where K was taken as 0.8.³⁸ The pristine PCBM-based control device yielded a steady-state current density of 20.9 mAcm⁻² at 0.83 V while the optimal addition of 2D-TiS₂-based device showed a steady-state current density of 21.3 mAcm⁻² at 0.85 V. The photocurrent densities and PCEs extracted from both devices based on MPP were consistent with their corresponding J - V curves. Contrary, in the case of 5 wt% and 20 wt% amounts of 2D-TiS₂ addition into PCBM enhance only V_{oc} while J_{sc} and FF were almost unchanged, resulting in a little increment in PCE (Figure 7.7a and b).

Table 7. 2 PV parameters of the champion devices with and without 15 wt% 2D-TiS₂ addition.

Device	Direction	V_{oc} (mV)	J_{sc} (mAcm ⁻²)	FF (%)	PCE (%)	* R_s (Ω)	* R_{sh} (k Ω)
PCBM	RS	1030.52	21.87	70.52	15.89	51.64	11.07
	FS	1030.07	21.74	68.11	15.25	55.08	5.85
	Statistics	1029.89 \pm 1.6	21.88 \pm 0.02	69.17 \pm 1.3	15.59 \pm 0.31		
PCBM + 15 wt% 2D-TiS ₂	RS	1057.20	21.89	77.56	17.95	34.05	49.14
	FS	1057.68	21.79	75.93	17.50	47.56	31.22
	Statistics	1056.37 \pm 3.3	21.96 \pm 0.14	76.93 \pm 0.76	17.84 \pm 0.08		

* R_s and R_{sh} of PSCs were estimated by the slope of the J - V curves near V_{oc} and J_{sc} , respectively.

The series resistance (R_s) and shunt resistance (R_{sh}) were estimated from the slope of the J - V curves near V_{oc} and J_{sc} , respectively (Table 1), showing a higher R_s of 51.63 Ω and lower R_{sh} of 11.07 k Ω associated with the control device. However, the modified device with PCBM + 15 wt% 2D-TiS₂ showed us a notably reduced R_s of 34.05 Ω and higher R_{sh} of 49.13 k Ω values in the reverse scan. The trend of R_s and R_{sh} in the forward scan is also similar to that in the reverse scan. The high R_{sh} is responsible to suppress the interfacial recombination and minimize the photo charge build-up at the perovskite/ETL interface, thus resulting in improved FF as observed in the modified device.³⁹

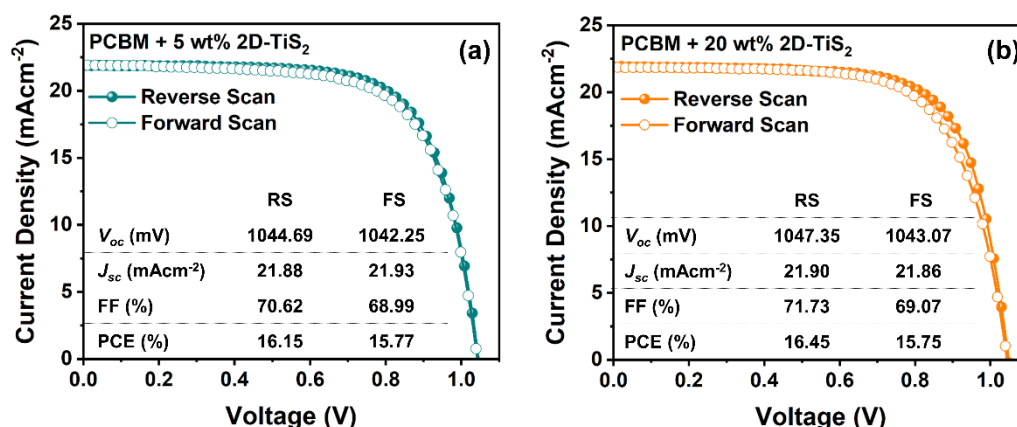


Figure 7.7 Reverse and forward J - V curves of (a) 5 wt% addition of 2D-TiS₂ into PCBM, (b) 20 wt% addition of 2D-TiS₂ into PPCBM.

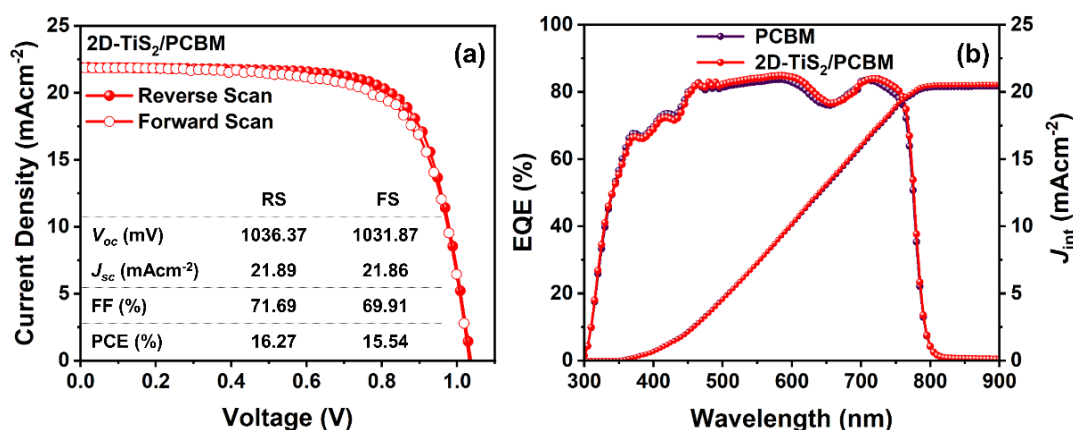


Figure 7.8 Reverse and forward J - V curves of the device with the 2D-TiS₂ as an interface layer in the device structure of FTO/PTAA/CsFAMA/2D-TiS₂/PCBM/BCP/Ag (a) and the corresponding EQE and integrated current density (b).

For further study, we fabricated a p - i - n PSC with the synthesized 2D-TiS₂ as an interface layer at the perovskite/PCBM interface in the architecture follows: FTO/PTAA/CsFAMA/2D-TiS₂/PCBM/Ag. The measured PCE for the interface-modified device was 16.27% with 1036.37 V of V_{oc} , 21.89 mAcm⁻² of J_{sc} , and 71.69 of FF, showing a slight improvement in PCE when compared with the control device. The J - V and accompanying IPCE along with the integrated current density of the champion device with 2D-TiS₂ as an interface layer are shown in Figures 7.8a and b, respectively. The improvement of PCE upon the introduction of 2D-TiS₂ as an interface layer is mainly due to the increase of V_{oc} , which can be attributed to the reduced energy barrier between perovskite and ETL.⁴⁰

Hereafter we only discuss the optimized addition of a 15 wt% 2D-TiS₂-based PSCs.

7.3.4 Exciton Generation and Photocharge Transfer Kinetics

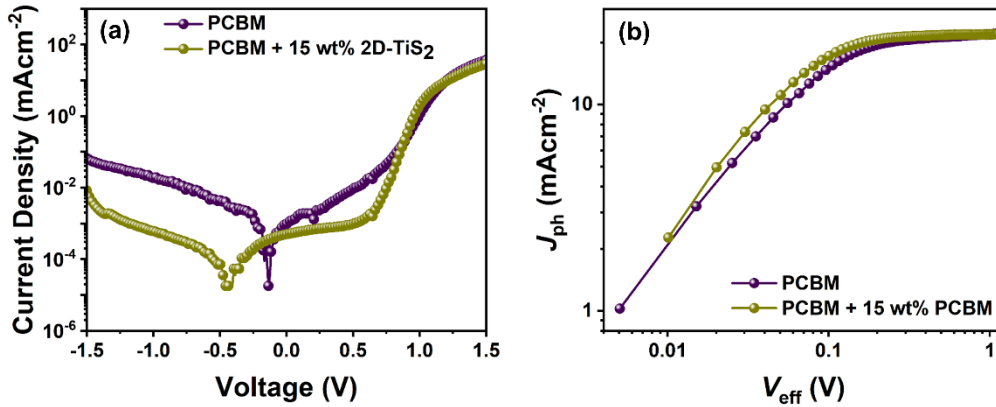


Figure 7. 8 (a) The dark J - V curve of the PSCs with and without 15 wt% 2D-TiS₂ addition. (b) photo-generated current density, J_{ph} vs. effective voltage (V_{eff}) curve.

It is paramount to evaluate the interfacial effect and the internal charge kinetics of the PCBM-based ETL upon 2D-TiS₂ to understand the enhancement of FF and V_{oc} in the devices. In PSCs, the ideality factor (n_{id}) of the dark current is commonly used as an indicator to describe the trap-assisted recombination in the device, which is derived from the semi-logarithmic curve (Figure 6.9a) under dark conditions using the following equation;^{41,42}

$$n_{id} = \frac{K_B T}{q} \left(\frac{d \ln J_D}{dV} \right)^{-1} \quad (6.3)$$

where J_D , V , K_B , T , and q are dark current density, bias voltage, Boltzmann constant, temperature, and charge of the electron, respectively. Further, the linear region of the semi-logarithmic plot is described with the Shockley diode equation to evaluate the reverse saturation current density (J_0) that is related to deprivation of photo-generated charge carriers at the defects due to recombination;⁴²

$$J_D = J_0 \left[\exp \left(\frac{qV}{n_{id} K_B T} \right) - 1 \right] \quad (6.4)$$

Table 7.3 summarizes the calculated n_{id} and J_0 for the devices based on PCBM and PCBM + 15 wt% 2D-TiS₂, in which the pristine PCBM-based device gave us 2.72 and 7.06×10^{-7} for n_{id} and J_0 respectively. Smaller n_{id} and J_0 were detected (1.92 and 3.34×10^{-9} , respectively) upon the addition of 15 wt% 2D-TiS₂ into PCBM attributing to a decreased charge recombination at the interface between perovskite/ETL, thus resulting in improvement of V_{oc} and FF upon addition of 2D-TiS₂. The enhancement of FF can be further described by the effective voltage

Chapter 7

(V_{eff}) dependent photocurrent density (J_{ph}) as shown in Figure 7.9b. V_{eff} is defined by $V_{\text{eff}} = V_0 - V_{\text{app}}$, where V_0 is the voltage at $J_{\text{ph}} = 0$ and V_{app} is the applied bias voltage. J_{ph} is given by $J_{\text{ph}} = J_L - J_D$, where J_L and J_D are the current densities under illumination and dark conditions, respectively.^{31,43} A linear increase of J_{ph} can be detected for the lower V_{eff} region from both devices. However, the device with the PCBM+15 wt% 2D-TiS₂ displays a saturation of photocurrent density (J_{sat}) at a relatively low V_{eff} of 0.235 V compared to that of the control device (0.398 V), which suggest a greater charge extraction ability upon 2D-TiS₂ addition into PCBM, providing another evidence for the high FF observed in the device based on 2D-TiS₂.^{44,45}

Table 7. 3 Photo-charge kinetic parameters extracted from dark current and $J_{\text{ph}}-V_{\text{eff}}$ curves.

Device	n_{id}	J_0 (mAcm ⁻²)	V_{eff}	J_{sat} (mAcm ⁻²)
PCBM	2.7	7.06×10^{-7}	0.235	20.95
PCBM + 15 wt% 2D-TiS ₂	1.9	3.34×10^{-9}	0.398	21.31

To gain insight into photo-induced charge extraction and recombination phenomena upon 2D-TiS₂ addition, the electrochemical impedance spectroscopy (EIS) was conducted at a range of potential bias near the corresponding V_{oc} under dark conditions. Figure 6.10a shows the EIS of the two different devices at 0.95 V bias voltage in the dark. The curves are fitted with the equivalent circuit inserted (Figure 7.10a): $R_s + R_{\text{rec}}/Q1$, where R_s and R_{rec} represent single-series resistance and charge recombination resistance at the interface between perovskite/ETL, respectively. A constant phase element related to carrier diffusion in the device was assigned as Q1. The extracted parameters were tabulated in Table 7.4. It is noted from Figure 7.10b that at a given potential bias, the 2D-TiS₂ incorporated PSC featured a higher R_{rec} than that of pristine PCBM-based PSC, which can be rationalized in terms of aforesaid suppressed photo-charge recombination at the interface of perovskite/ETL upon 2D-TiS₂.^{37,46} The relative trend of R_{rec} is in good accordance with the R_{sh} detected from the $J-V$ curve of the devices under 1 sun illumination.

The influence of 2D-TiS₂ on the electron lifetime was estimated from Bode EIS at 0.95V under dark conditions from 1 Hz to 2 MHz with 20 mV perturbation ac signal (Figure 7.10c and d). The peak frequency (f_p) was extracted from the frequency-dependent $-Z''$ and the electron charge lifetime (τ) was derived from the relation $\tau=1/(2\pi f_p)$.⁴⁷ The pristine PCBM-based device shows an electron lifetime of 13.91 while the 2D-TiS₂ incorporated device featured a longer

Chapter 7

electron lifetime of 37.27 μs , indicating mitigated charge recombination at the perovskite/ETL interface upon 2D-TiS₂ into PCBM.

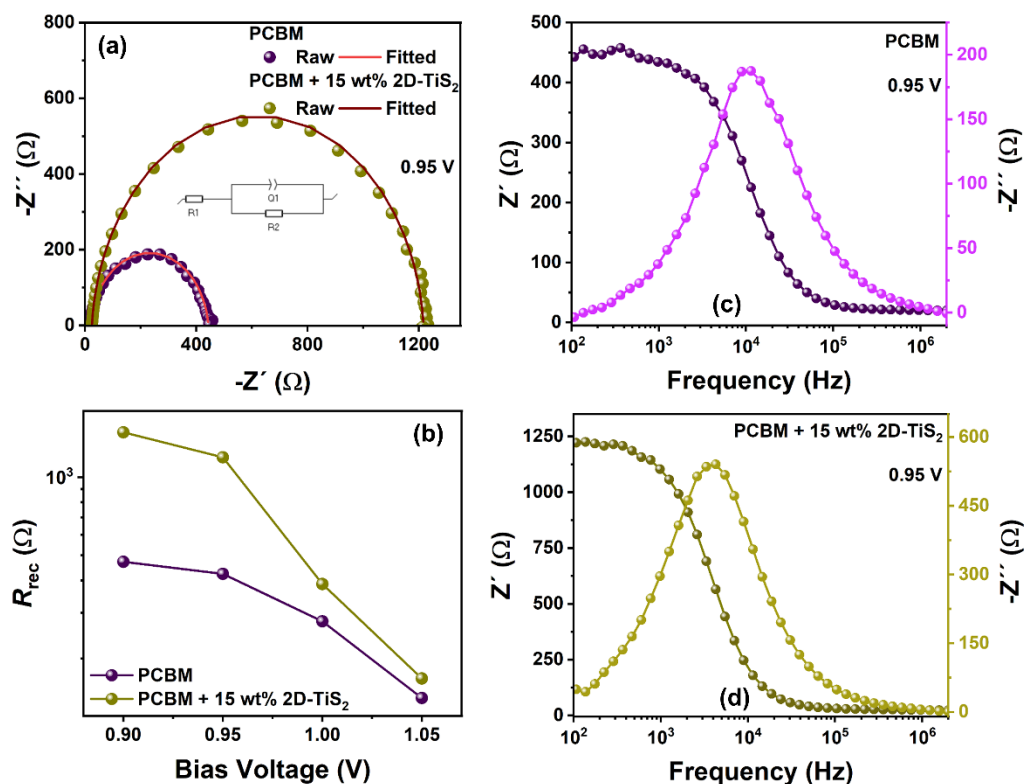


Figure 7. 9 (a) Electrochemical impedance spectra of PSCs recorded with an applied bias voltage of 0.95 V under dark conditions in the frequency range of 1 Hz - 2 MHz with 20 mV perturbation ac signal, and the raw data were fitted with the equivalent circuit inserted in the figure. (b) The potential bias-dependent interfacial charge recombination resistance. The Bode plot of the impedance spectrum of (c) pristine PCBM and (d) PCBM + 15 wt% 2D-TiS₂-based devices.

Figure 7.11 shows the frequency-dependent capacitance variation at 0.95 V bias voltage extracted from the EIS at the corresponding bias under dark conditions. Throughout the selected frequency range, the device based on 2D-TiS₂ promotes lower charge build-up when compared with the pristine PCBM-based device, suggesting that the smooth and fast charge extraction in the device upon 2D-TiS₂ addition.⁴⁸

Chapter 7

Table 7. 4 Electrochemical parameters of the PSCs with and without 2D-TiS₂ at 950 mV applied bias in the dark.

Device	R_{rec} (Ω)	f_p (μs)	τ (μs)
PCBM	423.5	87.41	13.91
PCBM + 15 wt% 2D-TiS ₂	1192	233.84	37.22

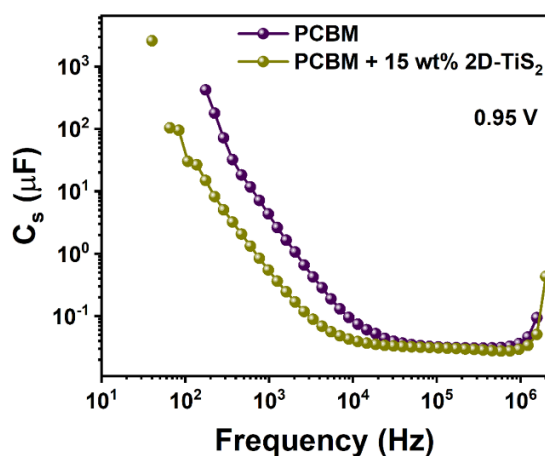


Figure 7. 10 Frequency-dependent series capacitance extracted from the EIS at 0.95 V under dark conditions.

7.3.5 Long-Term Device Stability

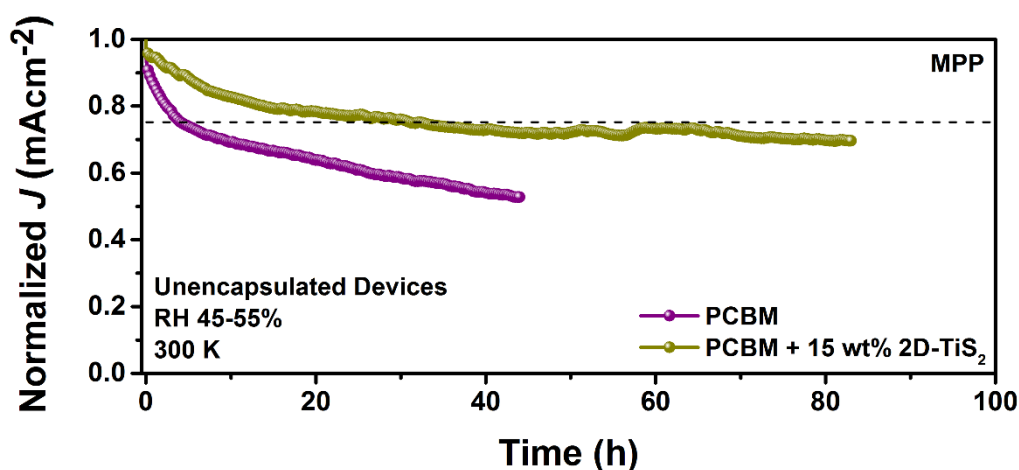


Figure 7. 11 The normalized current density of continuous MPP tracking for un-encapsulated PSCs under atmospheric conditions (RH 45-65 %, 300 K).

Chapter 7

The photostability of the PCBM- and PCBM+15 wt% 2D-TiS₂-based unencapsulated devices was investigated at MPP with continuous illumination under ambient conditions (RH 45-55 % and 300 K). As shown in Figure 7.12, the PCBM+15 wt% 2D-TiS₂-based device demonstrated enhanced operational stability and preserved 75 % of its original photo current density for about 65 h. However, under the same conditions, the PCBM-based devices rapidly dropped to 75 % of their original photo current density within 5 h.

7.4 Conclusions

In summary, we thoroughly investigated the performance and the ambient stability enhancement of inverted perovskite solar cells using Li⁺ intercalated liquid-phase exfoliated layered 2D-TiS₂. The optimal addition of 15 wt% 2D-TiS₂ into PCBM featured a notably enhanced V_{oc} and FF, ultimately resulting in amplified PCE up to 17.95%. We attributed this to significantly improved electron charge mobility of the PCBM+2D-TiS₂ layer and suppressed non-radiative recombination at the interface of perovskite/ETL. We also showed that the saturation of photocurrent density was reached at a relatively lower effective voltage when PCBM incorporated with 15 wt% 2D-TiS₂, which suggested that the modified device has greater electron extraction ability as evident from a strengthened FF. The unencapsulated device with 2D-TiS₂ into PCBM featured inflated operational stability up to 65 h with 75% of their initial current density under constant illumination at ambient conditions. This work suggests an effective scheme to reduce non-radiative recombination and prompt charge extraction for high V_{oc} and FF targeting magnified PCE devices with extended operational stability.

7.5 Experimental Section

7.5.1 Materials

Titanium (IV) sulfide, 99.8% (metals basis, TiS₂) was purchased from Alfa Aesar while lead iodide (99.9%) was purchased from Tokyo Chemical Industry (TCI) and used as such. Methylammonium iodide (MAI) and formamidinium iodide (FAI) were purchased from Dyesol. [60]PCBM > 99.5% and Bathocuproine (BCP) were purchased from Solenne BV and TCI, respectively. All the solvents including DMF, DMSO, ethyl acetate, ethanol, and chlorobenzene were purchased from Acros Chemicals and used as such. Butyl lithium (1.6 M, hexane) was from Sigma-Aldrich.

Chapter 7

7.5.2 Thin-film characterization

D8 advance diffractometer from Bruker (Bragg-Brentano geometry, Cu K α X-ray tube, $\lambda = 1.5406 \text{ \AA}$) was used for thin film and power X-ray diffractograms. Topography and phase AFM images were captured using a CSI Nano observer and data were processed through Gwyddion software. Transmittance and absorption spectra were collected with the help of a UV-vis-IR spectrophotometer (Varian Cary 50 UV/Vis Spectrophotometer). Jeol JEM-1400 transmission electron microscopy (TEM) was used to capture synthesized 2D-TiS₂ flakes. Hitachi S-4800 scanning electron microscopy (SEM) was used for surface and cross-sectional measurements. X-Ray photoelectron spectroscopy (XPS) experiments were carried out on a SPECS system (Berlin, Germany) equipped with a Phoibos 150 1D-DLD analyzer with monochromated Al K α radiation (1486.7 eV). A step energy of 1 eV with a dwell time: 0.1 s and pass energy: 80 eV was acquired for wide scan, and a detailed analysis of the elements was performed using 0.08 eV step energy (dwell time: 0.1 s, pass energy: 30 eV) with an electron exit angle of 90°. The spectra were adjusted using CasaXPS 2.3.16 software, which models Gauss-Lorentzian contributions.

7.5.3 Device fabrication

Prior to device fabrication, substrates were cleaned as mentioned in Chapter 2. UV-Ozone treated cleaned substrates were transferred to the argon-purged glove box. PTAA (1.5 mg mL⁻¹ in toluene) was spin-coated at 6000 rpm for 30 s followed by annealing at 100 °C for 10 min. Once cooled down the layer was washed with DMSO by spin coating at 5000 rpm for 30 s to improve the wettability of the PTAA layer just before the deposition of the perovskite layer. Triple cation perovskite [Cs_{0.1}(FA_{0.9}MA_{0.1})_{0.9}Pb(I_{0.9}Br_{0.1})₃] was deposited according to Chapter 2. The [60]PCBM thin film as an electron transport layer was spin-coated (20 mg mL⁻¹ in CB) at 1200 rpm for 30 s over the perovskite active layer and annealed for 10 min at 80°C. For the modified device, a solution of ETM was prepared by dissolving 15 wt% 2D-TiS₂ and [60]PCBM (3 mg of 2D-TiS₂ with 20 mg of [60]PCBM) in CB. The mixture was spin-coated at 1200 rpm for 30 s followed by annealing at 80°C for 10 min. A thin layer of BCP (0.5 mg mL⁻¹ in IPA) was deposited atop ETL by spin coating at 5000 rpm for 40 s followed by evaporating Ag (100 nm, <1 Å s⁻¹) in a thermal evaporator under low-vacuum conditions (10⁻⁶ Torr).

Chapter 7

7.5.4 Device characterization

The current density-voltage (J - V) studies were performed with Oriel 3A solar simulator (Newport, AM1.5, 1sun) under irradiation of 100 mWcm^{-2} and the generated photocurrent was recorded using a Keithley 2400 source meter at a scan rate of 100 mV/s (pre sweep delay: 10 s , 0.09 cm^2 black metal mas as the active area). The EQE spectra were recorded using a Bentham PVE300 motorized $1/4 \text{ m}$ monochromator attached to a 150 W xenon lamp. EIS measurements were carried out using BioLogic SP-300 Potentiostat using a perturbation of 20 mV , over the frequency range from 2 MHz to 1 Hz , at room temperature. Dark current for the PSCs and electron-only devices were measured with 100 mV/s scan rate at forward scan. Operational stability was performed at $28 \text{ }^\circ\text{C}$ under ambient conditions without encapsulating the devices.

7.6 Bibliography

1. Bai, Y., Yu, H., Zhu, Z., Jiang, K., Zhang, T., Zhao, N., Yang, S., & Yan, H. High performance inverted structure perovskite solar cells based on a PCBM:polystyrene blend electron transport layer. *J. Mater. Chem. A*, 2015, 3(17), 9098–9102.
2. You, J., Hong, Z., Yang, Y. M., Chen, Q., Cai, M., Song, T. B., Chen, C. C., Lu, S., Liu, Y., Zhou, H., & Yang, Y. Low-Temperature Solution-Processed Perovskite Solar Cells with High Efficiency and Flexibility. *ACS Nano*, 2014, 8(2), 1674–1680.
3. Hossain, M. I., Saleque, A. M., Ahmed, S., Saidjafarzoda, I., Shahiduzzaman, M., Qarony, W., Knipp, D., Biyikli, N., & Tsang, Y. H. Perovskite/perovskite planar tandem solar cells: A comprehensive guideline for reaching energy conversion efficiency beyond 30%. *Nano Energy*, 2021, 79, 105400.
4. *Best Research-Cell Efficiency Chart*. (n.d.). Photovoltaic Research | NREL.
5. Saranin, D., Komaricheva, T., Luchnikov, L., Muratov, D. S., Le, T. S., Karpov, Y., Gostishchev, P., Yurchuk, S., Kuznetsov, D., Didenko, S., & Di Carlo, A. Hysteresis-free perovskite solar cells with compact and nanoparticle NiO for indoor application. *Sol. Energy Mater. Sol. Cells*, 2021, 227, 111095.
6. Cao, Q., Li, Y., Zhang, H., Yang, J., Han, J., Xu, T., Wang, S., Wang, Z., Gao, B., Zhao, J., Li, X., Ma, X., Zakeeruddin, S. M., Sha, W. E. I., Li, X., & Grätzel, M. Efficient and stable inverted perovskite solar cells with very high fill factors via incorporation of star-shaped polymer. *Sci. Adv.*, 2021, 7(28).
7. Tian, C., Betancourt-Solis, G., Nan, Z., Liu, K., Lin, K., Lu, J., Xie, L., Echegoyen, L., & Wei, Z. Efficient and stable inverted perovskite solar cells enabled by inhibition of

Chapter 7

- self-aggregation of fullerene electron-transporting compounds. *Sci. Bull.*, 2021, 66(4), 339–346.
8. Xu, C., Liu, Z., & Lee, E. C. High-performance inverted planar perovskite solar cells using a pristine fullerene mixture as an electron-transport layer. *J. Mater. Chem. C*, 2019, 7(23), 6956–6963.
 9. Yang, D., Zhang, X., Wang, K., Wu, C., Yang, R., Hou, Y., Jiang, Y., Liu, S., & Priya, S. Stable Efficiency Exceeding 20.6% for Inverted Perovskite Solar Cells through Polymer-Optimized PCBM Electron-Transport Layers. *Nano Lett.*, 2019, 19(5), 3313–3320.
 10. Younes, E. M., Gurung, A., Bahrami, B., El-Maghraby, E., & Qiao, Q. Highly efficient electron transport based on double-layered PC61BM in inverted perovskite solar cells. *Org. Electron.*, 2022, 100, 106391.
 11. Xie, L., Wang, J., Liao, K., Yang, J. A., Wang, A., Deng, X., Li, C., Li, T., Niu, X., & Hao, F. Low-cost coenzyme Q10 as an efficient electron transport layer for inverted perovskite solar cells. *J. Mater. Chem. A*, 2019, 7(31), 18626–18633.
 12. Wang, Q., Shao, Y., Dong, Q., Xiao, Z., Yuan, Y., & Huang, J. Large fill-factor bilayer iodine perovskite solar cells fabricated by a low-temperature solution-process. *Energy Environ. Sci.*, 2014, 7(7), 2359–2365.
 13. Namkoong, G., Mamun, A. A., & Ava, T. T. Impact of PCBM/C60 electron transfer layer on charge transports on ordered and disordered perovskite phases and hysteresis-free perovskite solar cells. *Org. Electron.*, 2018, 56, 163–169.
 14. H. Dong, Z. Wu, B. Xia, J. Xi, F. Yuan, S. Ning, L. Xiao, X. Hou, Modified deposition process of electron transport layer for efficient inverted planar perovskite solar Cells, *Chem. Commun.*, 2015, 51, 8986–8989.
 15. Zhang, Z., Wang, J., Lang, L., Dong, Y., Liang, J., Zheng, Y., Wu, X., Tian, C., Huang, Y., Zhou, Z., Yang, Y., Wang, L., Kong, L., & Chen, C. C. Size-tunable MoS₂ nanosheets for controlling the crystal morphology and residual stress in sequentially deposited perovskite solar cells with over 22.5% efficiency. *J. Mater. Chem. A*, 2022, 10(7), 3605–3617.
 16. Capasso, A., Matteocci, F., Najafi, L., Prato, M., Buha, J., Cinà, L., Pellegrini, V., Carlo, A. D., & Bonaccorso, F. Few-Layer MoS₂ Flakes as Active Buffer Layer for Stable Perovskite Solar Cells. *Adv. Energy Mater.*, 2016, 6(16), 1600920.

Chapter 7

17. Hemasiri, N. H., Kazim, S., & Ahmad, S. Reduced trap density and mitigating the interfacial losses by placing 2D dichalcogenide material at perovskite/HTM interface in a dopant free perovskite solar cells. *Nano Energy*, 2020, 77, 105292.
18. Sobayel, K., Akhtaruzzaman, M., Rahman, K., Ferdaous, M., Al-Mutairi, Z. A., Alharbi, H. F., Alharthi, N. H., Karim, M. R., Hasmady, S., & Amin, N. A comprehensive defect study of tungsten disulfide (WS_2) as electron transport layer in perovskite solar cells by numerical simulation. *Results Phys.*, 2019, 12, 1097–1103.
19. Malek, N. A. A., Alias, N., Umar, A. A., Zhang, X., Li, X., Saad, S. K. M., Abdullah, N. A., Zhang, H., Weng, Z., Shi, Z., Li, C., Rosli, M. M., & Zhan, Y. Enhanced Charge Transfer in Atom-Thick 2H- WS_2 Nanosheets' electron transport layers of perovskite solar cells. *Solar RRL*, 2020, 4(10), 2000260.
20. Kakavelakis, G., Gouda, L., Tischler, Y., Kaliakatsos, I., & Petridis, K. 2D Transition metal dichalcogenides for solution-processed organic and perovskite solar cells. *Two Dimensional Transition Metal Dichalcogenides*, 2019, 203–239.
21. Marcia, M., Hirsch, A., & Hauke, F. Perylene-based non-covalent functionalization of 2D materials. *FlatChem*, 2017, 1, 89–103.
22. Yin, G., Zhao, H., Feng, J., Sun, J., Yan, J., Liu, Z., Lin, S., & Liu, S. F. Low-temperature and facile solution-processed two-dimensional TiS_2 as an effective electron transport layer for UV-stable planar perovskite solar cells. *J. Mater. Chemis. A*, 6(19), 2018, 9132–9138.
23. Alias, N., Ali Umar, A., Malek, N. A. A., Liu, K., Li, X., Abdullah, N. A., Rosli, M. M., Abd Rahman, M. Y., Shi, Z., Zhang, X., Zhang, H., Liu, F., Wang, J., & Zhan, Y. Photoelectrical dynamics uplift in perovskite solar cells by atoms thick 2D TiS_2 layer passivation of TiO_2 nanograss electron transport layer. *ACS Appl. Mater. Interfaces*, 2021, 13(2), 3051–3061.
24. Chatzimanolis, K., Rogdakis, K., Tsikritzis, D., Tzoganakis, N., Tountas, M., Krassas, M., Bellani, S., Najafi, L., Martín-García, B., Oropesa-Nuñez, R., Prato, M., Bianca, G., Plutnarova, I., Sofer, Z., Bonaccorso, F., & Kymakis, E. Inverted perovskite solar cells with enhanced lifetime and thermal stability enabled by a metallic tantalum disulfide buffer layer. *Nanoscale Adv.*, 2021, 3(11), 3124–3135.
25. Sherrell, P. C., Sharda, K., Grotta, C., Ranalli, J., Sokolikova, M. S., Pesci, F. M., Palczynski, P., Bemmer, V. L., & Mattevi, C. Thickness-Dependent Characterization of Chemically Exfoliated TiS_2 Nanosheets. *ACS Omega*, 2018, 3(8), 8655–8662.

Chapter 7

26. Backes, C., Smith, R. J., McEvoy, N., Berner, N. C., McCloskey, D., Nerl, H. C., O'Neill, A., King, P. J., Higgins, T., Hanlon, D., Scheuschner, N., Maultzsch, J., Houben, L., Duesberg, G. S., Donegan, J. F., Nicolosi, V., & Coleman, J. N. (2014). Edge and confinement effects allow in situ measurement of size and thickness of liquid-exfoliated nanosheets. *Nat. Commun.*, 2014, 5(1).
27. Liu, Y., Liang, C., Wu, J., Sharifi, T., Xu, H., Nakanishi, Y., Yang, Y., Woellne, C. F., Aliyan, A., Martí, A. A., Xie, B., Vajtai, R., Yang, W., & Ajayan, P. M. Atomic Layered Titanium Sulfide Quantum Dots as Electrocatalysts for Enhanced Hydrogen Evolution Reaction. *Adv. Mater. Interfaces*, 2017, 5(1), 1700895.
28. Nguyen, T. P., Choi, S., Jeon, J. M., Kwon, K. C., Jang, H. W., & Kim, S. Y. Transition metal disulfide nanosheets synthesized by facile sonication method for the hydrogen evolution reaction. *J. Phys. Chem. C*, 2016, 120(7), 3929–3935.
29. Jing, H., Cheng, Q., Weller, J. M., Chu, X. S., Wang, Q. H., & Chan, C. K. Synthesis of TiO₂ nanosheet photocatalysts from exfoliation of TiS₂ and hydrothermal treatment. *J. Mater. Res.*, 2018, 33(21), 3540–3548.
30. Hu, Z., Tai, Z., Liu, Q., Wang, S., Jin, H., Wang, S., Lai, W., Chen, M., Li, L., Chen, L., Tao, Z., & Chou, S. (2019). Ultrathin 2D TiS₂ nanosheets for high capacity and long-life sodium ion batteries. *Adv. Energy Mater.*, 2019, 9(8), 1803210.
31. Hemasiri, N. H., Calìò, L., Pegu, M., Kazim, S., & Ahmad, S. Molecular interface engineering via triazatruxene-based moieties/NiO_x as hole-selective bilayers in perovskite solar cells for reliability. *Solar RRL*, 2022, 6(4), 2100793.
32. Bube, R. H. Trap density determination by space-charge-limited currents. *J. Appl. Phys.*, 33(5), 1962, 1733–1737.
33. Murgatroyd, P. N. Theory of space-charge-limited current enhanced by Frenkel effect. *J. Phys. D: Appl. Phys.*, 1970, 3(2), 151–156.
34. Huang, J. Y., Yang, Y. W., Hsu, W. H., Chang, E. W., Chen, M. H., & Wu, Y. R. Influences of dielectric constant and scan rate on hysteresis effect in perovskite solar cell with simulation and experimental analyses. *Sci. Rep.*, 2022, 12(1).
35. Yin, J., Yuan, Y., Ni, J., Guan, J., Zhou, X., Liu, Y., Ding, Y., Cai, H., & Zhang, J. CH₃NH₃PbBr_{3-x}I_x quantum dots enhance bulk crystallization and interface charge transfer for efficient and stable perovskite solar cells. *ACS Appl. Mater. Interfaces*, 2020, 12(43), 48861–48873.
36. Rose, A. Space-Charge-Limited Currents in Solids. *Phys. Rev.*, 1955, 97(6), 1538–1544.

Chapter 7

37. Harindu Hemasiri, N., Kazim, S., & Ahmad, S. 1T-rich 2D-WS₂ as an interfacial agent to escalate photo-induced charge transfer dynamics in dopant-free perovskite solar cells. *J. Mater. Chem. C*, 9(31), 2021, 9865–9873.
38. Raveendhra, D., Kumar, B., Mishra, D., & Mankotia, M. Design of FPGA based open circuit voltage MPPT charge controller for solar PV system. *2013 International Conference on Circuits, Power and Computing Technologies (ICCPCT)*.
39. Bi, Z., Zhang, S., Thandapani, M., Zhu, Y., Zheng, Y., Liem, N. Q., Xiao, X., Xu, G., Guerrero, A., & Xu, X. High Shunt Resistance SnO₂-PbO Electron Transport Layer for Perovskite Solar Cells Used in Low Lighting Applications. *Adv. Sustain. Syst.*, 2021, 5(11), 2100120.
40. Cao, T., Huang, P., Zhang, K., Sun, Z., Zhu, K., Yuan, L., Chen, K., Chen, N., & Li, Y. Interfacial engineering *via* inserting functionalized water-soluble fullerene derivative interlayers for enhancing the performance of perovskite solar cells. *J. Mater. Chem. A*, 2018, 6(8), 3435–3443.
41. Mahapatra, A., Parikh, N., Kumar, P., Kumar, M., Prochowicz, D., Kalam, A., Tavakoli, M. M., & Yadav, P. Changes in the Electrical Characteristics of Perovskite Solar Cells with Aging Time. *Molecules*, 2020, 25(10), 2299.
42. Wetzelaer, G. A. H., Kuik, M., Lenes, M., & Blom, P. W. M. Origin of the dark-current ideality factor in polymer:fullerene bulk heterojunction solar cells. *App. Phys. Lett.*, 2011, 99(15), 153506.
43. Lenes, M., Morana, M., Brabec, C. J., & Blom, P. W. M. (2009). Recombination-limited photocurrents in low bandgap polymer/fullerene solar cells. *Adv. Funct. Mater.*, 2009, 19(7), 1106–1111.
44. Shi, J., Dong, J., Lv, S., Xu, Y., Zhu, L., Xiao, J., Xu, X., Wu, H., Li, D., Luo, Y., & Meng, Q. Hole-conductor-free perovskite organic lead iodide heterojunction thin-film solar cells: High efficiency and junction property. *Appl. Phys. Lett.*, 2014, 104(6), 063901.
45. Troughton, J., Gasparini, N., & Baran, D. Cs_{0.15}FA_{0.85}PbI₃ perovskite solar cells for concentrator photovoltaic applications. *J. Mater. Chem. A*, 2018, 6(44), 21913–21917.
46. Yang, G., Chen, C., Yao, F., Chen, Z., Zhang, Q., Zheng, X., Ma, J., Lei, H., Qin, P., Xiong, L., Ke, W., Li, G., Yan, Y., & Fang, G. Effective carrier-concentration tuning of SnO₂ quantum dot electron-selective layers for high-performance planar perovskite solar cells. *Adv. Mater.*, 2018, 30(14), 1706023.

Chapter 7

47. von Hauff, E. Impedance spectroscopy for emerging photovoltaics. *J. Phys. Chem. C*, 2019, *123*(18), 11329–11346.
48. Khan, M. T., Hemasiri, N. H., Kazim, S., & Ahmad, S. Decoding the charge carrier dynamics in triple cation-based perovskite solar cells. *Sustain. Energy Fuels*, 2021, *5*(24), 6352–6360.

CHAPTER 8

PERORATION & UPCOMINGS

On the road to remarkable success in PSCs, a series of challenges have been overcome during the last decade, while some are yet to be addressed. Despite remarkable progress, PSCs have not yet achieved their full potential owing to the unoptimized photo-charge kinetics. Further enhancement of PV parameters is a prerequisite for achieving highly efficient PSCs in the future. The commercial viability of PSCs is still challenged by their stability compared to the commercially available matured silicon PVs. This thesis focuses on the reliability enhancement of the efficiency and stability in PSCs using low-dimensional materials. At the heart of all investigations lies the critical role of interfaces, responsible for charge-transfer dynamics, non-radiative recombination losses, and ultimately the overall instability of the device. Low-dimensional materials have been introduced to address these interfaces, targeting highly efficient and stable devices above the state-of-the-art.

One of the most promising material classes that have been highly studied in advanced electronic devices is two-dimensional (2D) transition metal dichalcogenides (TMDs). The performance enhancement of PSCs is unveiled upon the insertion of 2D-MoS₂ as an interfacial layer in Chapter 3. In this study, we exfoliated bulk MoS₂ into layered 2D-MoS₂ using liquid-phase assisted alkali-metal (Li) intercalation, targeting effective electron transfer from the valence *s* orbital of the alkali metal atoms to the *d* orbital of the transition metal center. This electron transfer process induces increased electron counts on the transition metal *d* orbital with the density of states at the Fermi level, resulting in a phase transformation of MoS₂ from the thermodynamically stable 2H phase to highly conductive metastable 1T phase. Our synthesis protocol enables us to obtain 1T-predominant 2D-MoS₂ with a few-layer thickness. Indeed the shallow HOMO state of pristine PTAA (-5.1 eV) with respect to the VB minimum of the perovskite (~-5.65 eV) will permit a higher density of holes at the perovskite/PTAA, intensifying charge recombination, meaning that the larger the energy gap between the perovskite and the HTL, the faster the recombination, thus result in lower V_{oc} . Similarly, the lower energy offset between the CB minimum of the perovskite and the deeper LUMO state of HTL activates undesirable electron transfer from the perovskite to HTL, which further induces non-radiative recombination. Better energy level matching was constructed by placing a thin layer of 1T-predominant 2D-MoS₂ between the perovskite and pristine PTAA, which in turn

Chapter 8

reduced the unnecessary charge build-up and charge recombination at the interface of perovskite/PTAA, amplifying the V_{oc} from 0.88 V up to 1.05 V. PSCs with 2H-predominant 2D-MoS₂ as an interfacial layer also gave a moderate improvement in PCE owing to a limited enhancement in V_{oc} only up to 1.01 V. Typically, 1T phase is found to be higher conductive than the 2H phase, which extends the charge extraction ability, benefiting the PV performances of the device. This conclusion was supported by, Y. Li *et. al.*, who evaluated the effect of two phases in 2D-MoS₂-based HTL on the PV performance, and obtained a much higher enhancement in V_{oc} upon 1T-rich rather than 2H-rich 2D-MoS₂.¹

Similarly, the concept was further evaluated with 1T-rich WS₂ in Chapter 4. The high performance was observed upon 1T-rich 2D-TiS₂ as an interface layer, owing to the enhancement of V_{oc} and FF as similar as in 1T-rich MoS₂, however, notable improvement of J_{sc} was also observed, which was not found with 1T-rich MoS₂. This can be then understood, the charge extraction and transportation were intensified upon the 2D-WS₂ interface layer, playing a crucial role in promoting the charge transfer kinetics via suppressing the charge annihilating and overcoming the charge build-up at the interface of the perovskite/PTAA. The query is, to which extend the interfacial energy alignment promotes the J_{sc} , which is still not fully identified. Nevertheless, the device with the 2D-WS₂ interfacial layer shows a rapid approach of saturation of photocurrent density at a relatively low effective voltage explains the prompt-charge extraction to the HTL. On the other hand, surface traps hinder the free mobility of charges, playing the foremost role in governing the overall performance of the PSC. Temperature-dependent admittance spectroscopy is one of the most powerful techniques to investigate the state of trap densities in the devices, where the trap density reduction in the target device upon the 2D-WS₂ interface layer was found to be about 25%. The presented protocol based on the alkali-metal intercalated 2D-TMD interlayer at the interface of the perovskite/PTAA demonstrates a stabilized efficiency in *n-i-p* PSCs. However, between two different 2D-TMDs studied in Chapter 3 and Chapter 4, 2D-WS₂ showed us much higher enhancement in PV performance and stability than 2D-MoS₂, reaching over 19% stabilized PCE.

Among the cost of PSC's components, the expense of the HTM continues to be a major deterrent to possible investments in the field. The expensive HTMs that are frequently utilized in the standard *n-i-p* design could be potentially replaced by the affordable HTLs in the inverted PSCs. Despite the intrinsic NiO_x being a wide-bandgap (>3.5 eV) semiconductor with high hole mobility, it suffers from weak built-in-field strength. The NiO_x/perovskite interface may

Chapter 8

accumulate holes as a result of the significant energy level offset, which raises the possibility of photo-induced charge recombination at the interface. The higher surface roughness with a larger surface wettability commonly found in the NiO_x layer is responsible to create tiny grains with larger grain boundaries in the perovskite, further promoting the charge recombination in the perovskite bulk. To overcome these problematic scenarios, in Chapter 5, a thin layer of molecularly engineered dithieno thiophene-based organic semiconductor (DTT-EHDI₂) was inserted in between the NiO_x nanocrystal layer and the perovskite layer. DTT-EHDI₂ has a lesser wettability, which tends to reduce the number of nucleation sites in the perovskite and creates more room for bigger grain development during crystallization, diminishing the trap states and potential recombination pathways. The π - π intermolecular charge transfer effect of the added organic semiconductor layer advances the hole mobility and conductivity of NiO_x, their existence reduces the energy gap between valence bands of the perovskite and NiO_x, enabling swift and easy charge extraction at the NiO_x/perovskite interface. The development strategy enables to access the quality of the perovskite and reduces the energy loss at the interface, thus ultimately delivering the PCE up to 18.15%. At the core of all these modifications are the fabrication protocols, which should eventually be strengthened even further with other combinations of organic/inorganic compounds.

The operational stability of any PV system is the third pillar for commercial relevance after efficiency and manufacturing cost. Apart from external pertinent variables, the perovskite layer has been demonstrated to degrade under the chemical nature of the adjacent transport layers. Particularly, the volatile nature of the organic cations in the perovskite is considered to be the device weakest point. The ideal interlayer would be able to protect the perovskite layer by blocking harmful conditions while enhancing device performance. Inorganic NiO_x has good inherent stability, but a potential redox reaction at NiO_x/perovskite starts and encourages the deterioration of the active layer, which leads to the instability of the devices. The direct contact of NiO_x with perovskite results in producing a hole extraction barrier of PbI_{2-x}Br_x and deprotonating MA⁺ cations via dual proton and electron-accepting nature of Ni^{>3+} in NiO_x. In Chapter 6, we introduce a metal-free C₃N₄ 2D-polymeric material at the NiO_x/perovskite interface, which is composed of a highly stable architecture of tri-s-triazine, rich in amino (-NH₂) and nitrogen, establishing the π -conjugated electronic structure. The novel interlayer reduces the non-radiative losses and defective charge accumulation at the NiO_x/perovskite interface, thereby allowing higher V_{oc} and FF that are delivering the PCE up to 19.3% with negligible hysteresis. We discovered that the FA⁺ and MA⁺ cations are stabilized at the

Chapter 8

interface as a passivation layer for the perovskite owing to the better coordination of MA^+ cations in the perovskite via H-bonding with the unbound nitrogen electron pairs in the C_3N_4 . The interlayer with the strong interaction along the perovskite layer stabilized 80% of the initial device performances up to 300 h under continuous MPP-tracking in ambient conditions. However, the higher wettability of the 2D- C_3N_4 due to its porous nature indicates the potential for further improvement of this class of materials with better hydrophobicity to control the perovskite nucleation and grain growth for additional enhancement of the performances.

The optoelectronic analyses outlined in Chapters 3, 4, 5, and 6, are based on the remediation at the perovskite/HTL interface, similar focus should be given to the perovskite/ETL interface. The LUMO distribution of PC_{60}BM is crucial since deeper lying states with respect to the CB minimum of the perovskite will increase the density of electrons at the interface, speeding up charge recombination. Further, a surface rough perovskite film can cause the PC_{60}BM layer to disintegrate, promoting the interfacial non-radiative recombination and leakage current. In this sense, it is a prerequisite to eliminating possible parasitic losses that occur in the device by accelerating the conductivity and mobility of the charge-selective layers. Inspired and encouraged by the strategies developed in Chapters 3 and 4, either 2D- TiS_2 was blended with PC_{60}BM and used as an ETL in the devices, or it was applied as an interface layer at the perovskite/ PC_{60}BM interface. We discovered that 2D- TiS_2 had a greater impact on PV performance when combined with PC_{60}BM under optimum addition owing to the suppressed non-radiative recombination at the interface of the perovskite/ETL, leading to V_{oc} as high as 1.057 V and ultimately the PCE up to 17.95%. The addition of 2D- TiS_2 into PC_{60}BM displays a saturation of current density (J_{sat}) at a relatively low V_{eff} , suggesting a greater electron extraction ability in the device and maintaining a high fill factor of ~78%. This work suggests a route for stability enhancement; however, trustworthy stability under different stresses is paramount before attempting a scalability production. Hence, further studies aimed at understanding and determining the behavior of 2D- TiS_2 with other fullerene derivatives on the performance enhancement and the stability of PSCs.

Within the range of low dimensional materials investigated in this thesis, we were able to shed light on the fundamental understanding of the device physics based on the charge carrier kinetics in PSCs under device operating conditions and irrespective of their configuration. With the experimental strategies and device architectural alterations given here, there is potential to further explore the fundamental device physics concerning low dimensional materials and

Chapter 8

perovskite materials for PV applications. The contribution of this work invested in third-generation solar cells, is part of a larger field of research, bringing us one step closer to the widespread application of sustainable energy conversion technology.

These semiconducting materials open new possibilities in advanced technological applications including perovskite solar cells. It is crucial to scale up the device area from the conventional lab size of mm^2 to at least cm^2 when trying to commercialize any solar technology. Although various attempts have been made, the primary obstacle to the commercialization of PSCs remains the drastically decreased efficiency upon scaling-up solar module area, which still lags far behind the performance of the crystalline silicon cells with the same dimensionality. Even though the work focused in this thesis is based on the modification of a single interface (either perovskite/ETL or perovskite/HTL) in PSCs under laboratory scale using low dimensional materials, it is important to study the fundamental device physics and mechanism relative to the PCE loss under dual interface modification in large-scale devices. With the aim of adequate regulation of the homogeneity of these low-dimensional semiconductors and regularity of the crystallization process in large-area perovskite films, significant effort needs to be done. Additionally, the diverse families of other two-dimensional (2D) materials such as MXene enable experimenting with the structure and capabilities of perovskite/MXene interfaces via rational engineering and modifications.²⁻⁵ Realizing rapid and scalable open-air coating of perovskite film is another important yet challenging task for reducing the large-scale module manufacturing cost in the production line. Several methods have been demonstrated to be suitable for scalable film deposition in each layer of PSC; the PCE of large-area solar cells has significantly increased with the use of various techniques and standardization, including precursor engineering and interfacial engineering. Concerns about the environment arise from the use of toxic lead in perovskite, ongoing researches target to find a replacement for toxic lead without sacrificing the performances found in lead-based PSCs.

In contrast to replacing silicon solar cells, the perovskite-on-silicon tandem arrangement offers a more rapid approach to bringing PSCs into the existing photovoltaic market. This also provides an economic strategy to overcome the Shockley and Queisser (SQ) limit for single-junction devices.

After all, the stability of PSCs, however, is where the main issue lies. It is quite challenging to maintain stability throughout while still achieving higher efficiency. The device stability hopes to meet the test criteria for commercialization in the near future with additional advancements

Chapter 8

in encapsulation technology and device optimization. Although there are several obstacles in the way, PSCs are making extraordinary progress toward commercialization, and low-dimensional semiconducting materials impact their progress.

Bibliography

1. Huang, P., Wang, Z., Liu, Y., Zhang, K., Yuan, L., Zhou, Y., Song, B., & Li, Y. Water-soluble 2D transition metal dichalcogenides as the hole-transport layer for highly efficient and stable $p-i-n$ perovskite solar cells. *ACS Appl. Mater. Interfaces*, 2017, 9(30), 25323–25331.
2. Saranin, D., Pescetelli, S., Pazniak, A., Rossi, D., Liedl, A., Yakusheva, A., Luchnikov, L., Podgorny, D., Gostischev, P., Didenko, S., Tameev, A., Lizzit, D., Angelucci, M., Cimino, R., Larciprete, R., Agresti, A., & Di Carlo, A. Transition metal carbides (MXenes) for efficient NiO-based inverted perovskite solar cells. *Nano Energy*, 2021, 82, 105771.
3. Wu, C., Fang, W., Cheng, Q., Wan, J., Wen, R., Wang, Y., Song, Y., & Li, M. MXene-regulated perovskite vertical growth for high-performance solar cells. *Angew. Chem., Int. Ed. Engl.*, 2022, 61(43).
4. Agresti, A., Pazniak, A., Pescetelli, S., Di Vito, A., Rossi, D., Pecchia, A., Auf der Maur, M., Liedl, A., Larciprete, R., Kuznetsov, D. V., Saranin, D., & Di Carlo, A. Titanium-carbide MXenes for work function and interface engineering in perovskite solar cells. *Nat. Mater.*, 2019, 18(11), 1228–1234.
5. Yang, L., Dall’Agnese, C., Dall’Agnese, Y., Chen, G., Gao, Y., Sanehira, Y., Jena, A. K., Wang, X., Gogotsi, Y., & Miyasaka, T. Surface-modified metallic $Ti_3C_2T_x$ MXene as electron transport layer for planar heterojunction perovskite solar cells. *Adv. Funct. Mater.*, 29(46), 1905694.

APPENDICES

APPENDIX A

Additional data of Chapter 3: Mitigation of trap density and interfacial losses by introducing a two-dimensional molybdenum disulfide interface layer in perovskite solar cells.

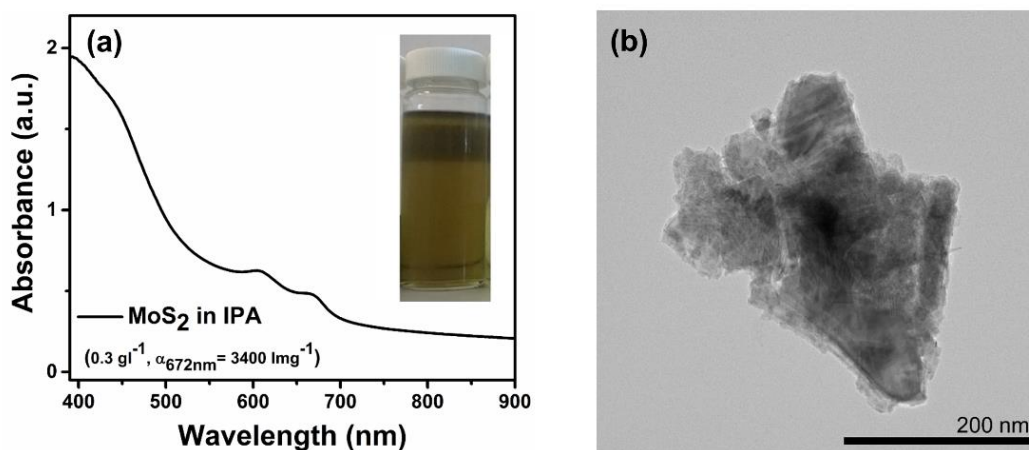


Figure A3.1 (a) UV-Vis absorption spectrum of 2D-MoS₂ solution. Insert shows the stable solution of 2D-MoS₂ in isopropanol (IPA) (b) Transmission electron microscopy (TEM) of 2D-MoS₂ drop-casted on Cu grid.

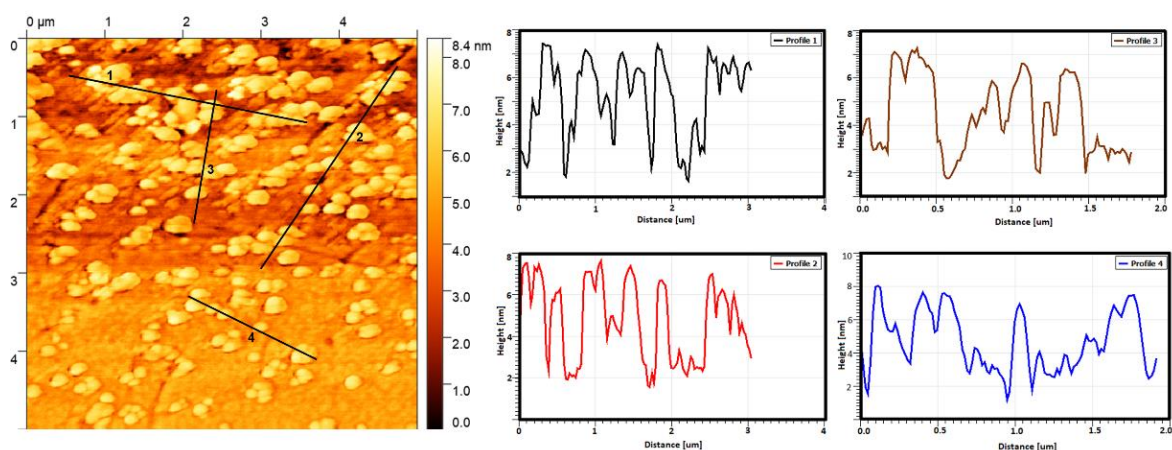


Figure A3.2 AFM height image of 2D-MoS₂ on SiO₂ substrate and thickness profiles.

Appendices

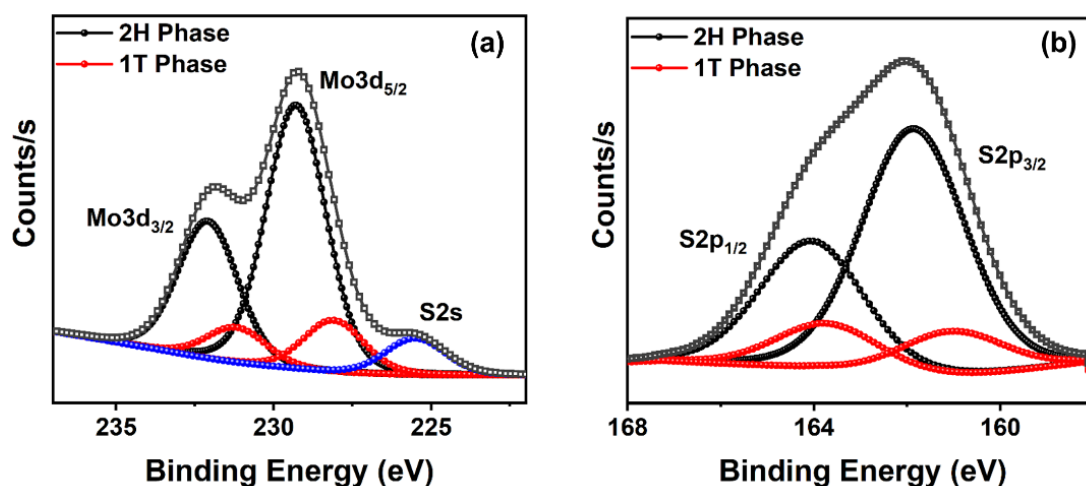


Figure A3.3 XPS narrow spectrum of (a) Mo3d and (b) S2p of spin-coated MoS₂ (synthesized via liquid exfoliation with the absence of lithium intercalation) thin film. Black and red plots respectively represent the 2H and 1T contributions.

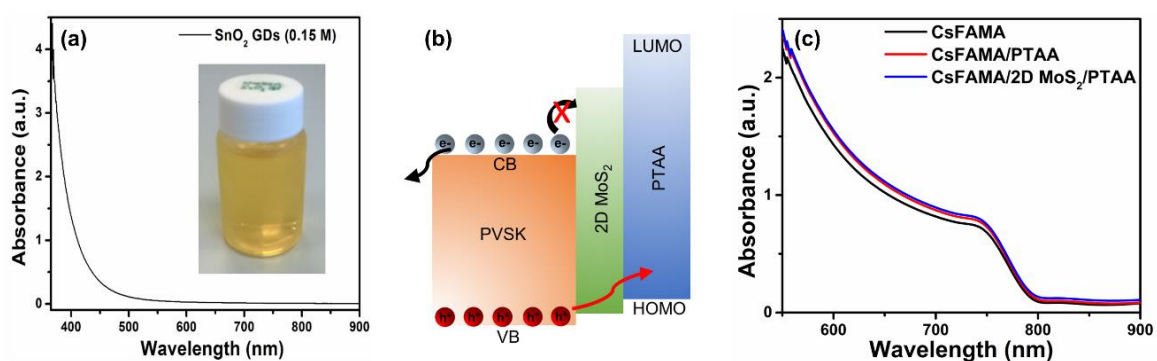


Figure A3.4 (a) UV-Vis absorption spectrum of aqueous SnO₂ QDs solution. Insert shows the stable solution of SnO₂ QDs. (b) Electron blocking at the CsFAMA and PTAA interface due to presence of 2D-MoS₂ interface layer. (c) UV-Vis absorption spectra of CsFAMA, CsFAMA/PTAA and CsFAMA/2D-MoS₂/PTAA.

Table A3.1 Summary of the PV parameters for the PSCs (with 2H-predominant 2D-MoS₂).

Device	Direction	V_{oc} (mV)	J_{sc} (mAcm ⁻²)	FF (%)	PCE (%)	HI
Champion	RS	1018.7	22.22	76.61	17.34	0.018
	FS	1001.0	22.15	75.10	16.65	
Average	RS	1025.4±12.534	22.21±0.0248	75.22±1.569	17.13±0.156	

Appendices

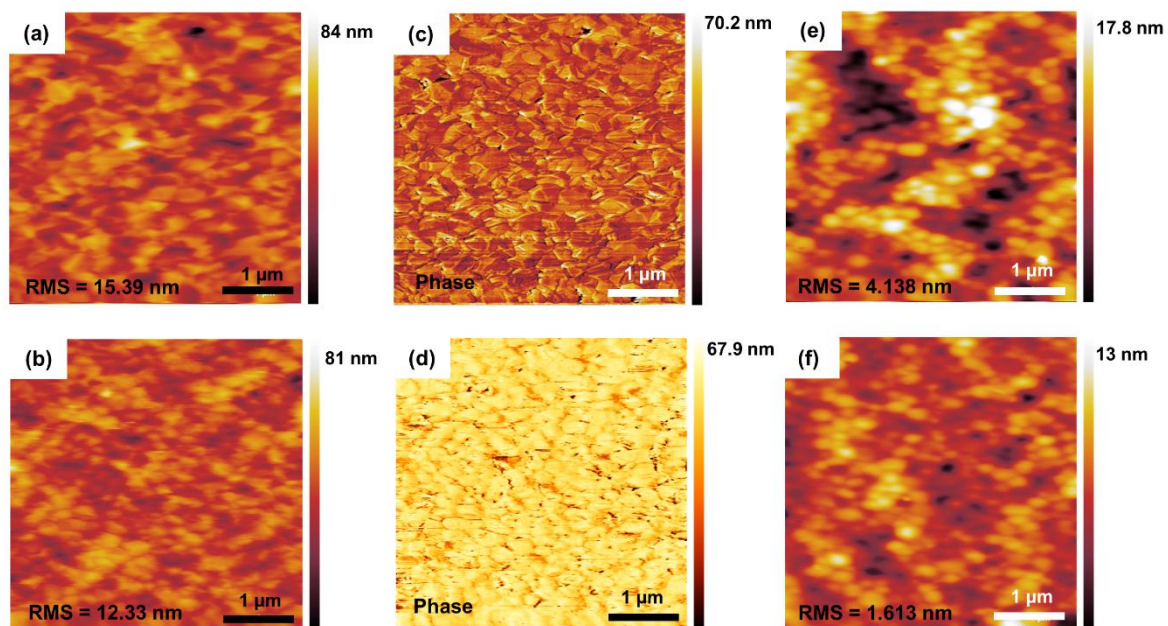


Figure A3.5 AFM topography images of (a) CsFAMA, (b) 2D-MoS₂/CsFAMA, and phase images of (c) CsFAMA, (d) 2D-MoS₂/CsFAMA film, (e) PTAA on CsFAMA film and (f) PTAA on 2D-MoS₂/CsFAMA.

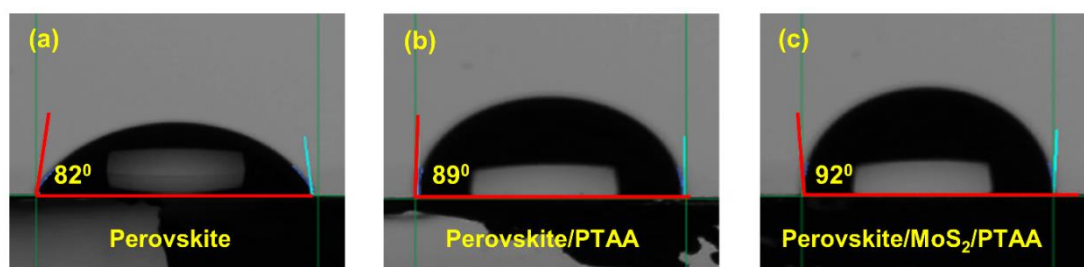


Figure A3.6 The contact angle measurements for (a) CsFAMA, (b) CsFAMA/PTAA, and (c) CsFAMA/2D-MoS₂/PTAA.

Appendices

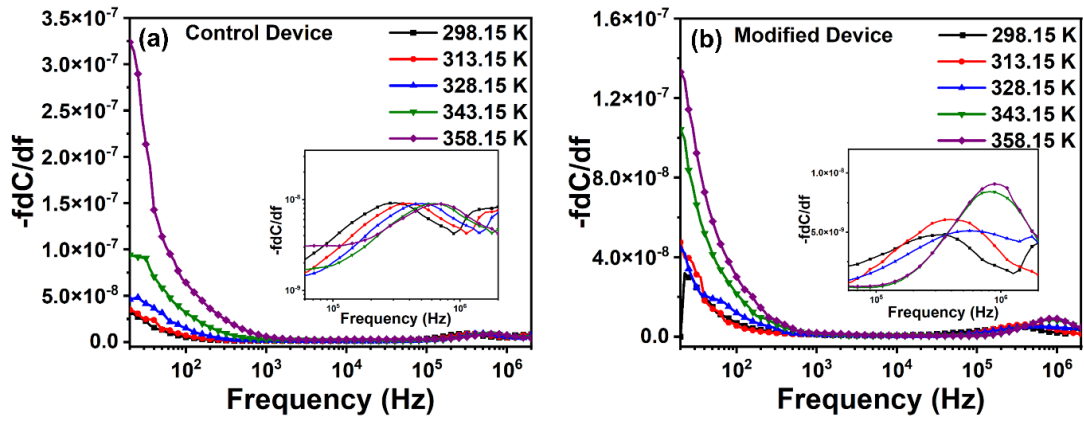


Figure A3.7 $-f dC/df$ versus frequency at variable temperature for (a) control and (b) modified devices.

Appendices

APPENDIX B

Additional data of Chapter 4: Photo-induced charge transfer dynamics in dopant-free perovskite solar cells upon 1T-rich WS₂ interfacial layer.

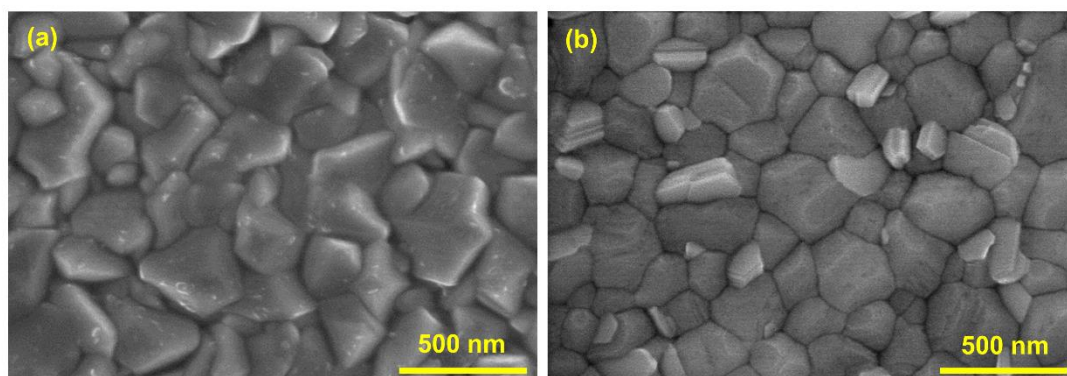


Figure A4.1 SEM images of (a) SnO₂-QD layer on c-TiO₂/FTO, and (b) the triple cation perovskite was grown on SnO₂-QD/c-TiO₂/FTO.

Table A4.1 Photovoltaic statistics of the devices without 2D-WS₂ interface layer.

Device	V_{oc} (mV)	J_{sc} (mAcm ⁻²)	FF (%)	PCE (%)
1	1034.21	23.83	76.99	18.98
2	1049.61	22.98	77.85	18.78
3	1043.02	23.16	75.87	18.32
4	1029.25	23.50	77.79	18.82
5	1051.63	23.59	76.69	19.02
6	1051.07	22.89	77.60	18.67
7	1053.26	23.05	76.79	18.64
8	1029.81	24.09	76.49	18.98
9	1032.49	22.96	75.84	17.96
10	1056.85	23.07	76.68	18.70
Statistics	1043.12 ± 10.15	23.31 ± 0.39	76.86 ± 0.68	18.69 ± 0.31

Appendices

Table A4.2 Photovoltaic statistics of the devices with 2D-WS₂ interface layer.

Device	V_{oc} (mV)	J_{sc} (mAcm ⁻²)	FF (%)	PCE (%)
1	963.42	23.53	68.20	15.46
2	979.52	21.84	73.04	15.63
3	976.73	23.40	68.88	15.74
4	960.96	22.90	70.69	15.56
5	967.65	21.47	71.94	14.94
6	971.38	22.59	71.72	15.74
7	953.88	23.66	64.97	14.66
8	987.65	21.27	72.00	15.13
9	976.93	23.25	68.60	15.58
Statistics	970.90 ± 9.89	22.66 ± 0.86	70.01 ± 2.41	15.38 ± 0.36

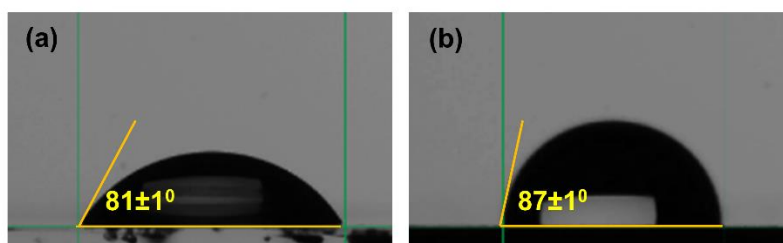


Figure A4.2 The water contact angle of (a) perovskite and with (b) 2D-WS₂/perovskite layer.

Appendices

APPENDIX C

Additional data of Chapter 5: NiO_x nanocrystal assisted interface modulation for the performance boosting of inverted perovskite solar cells.

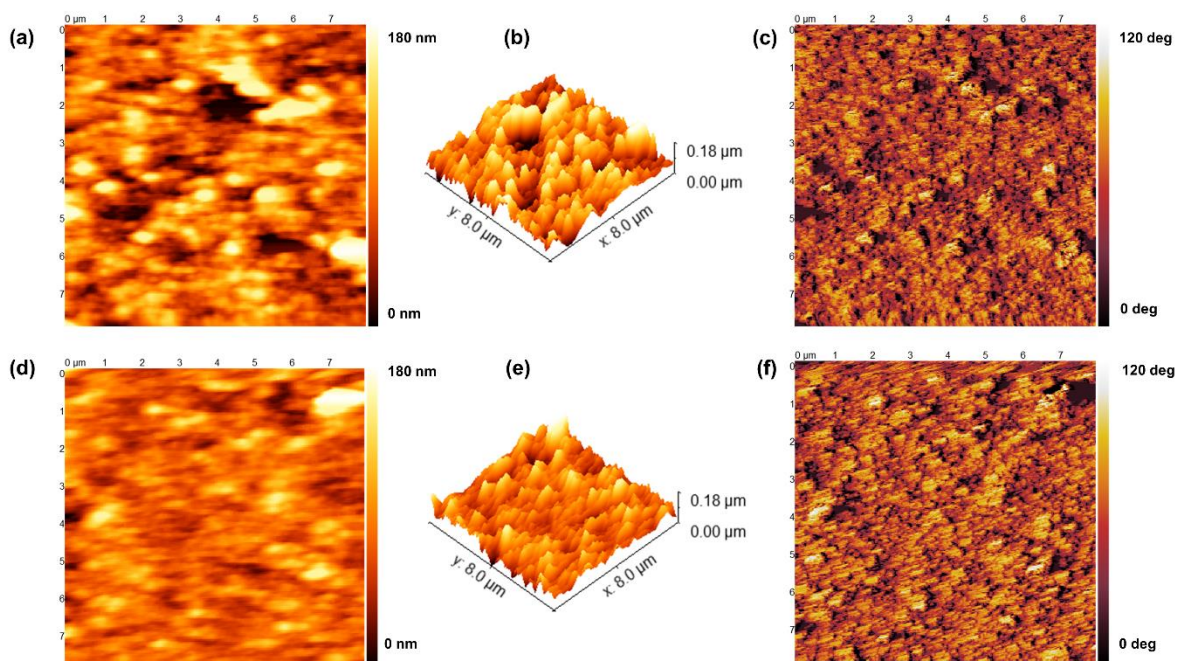


Figure A5.1 AFM Topography, 3D height, and phase images of NiO_x (a, b and c) and DTT-EHDI₂/NiO_x (d, e, and f), respectively.

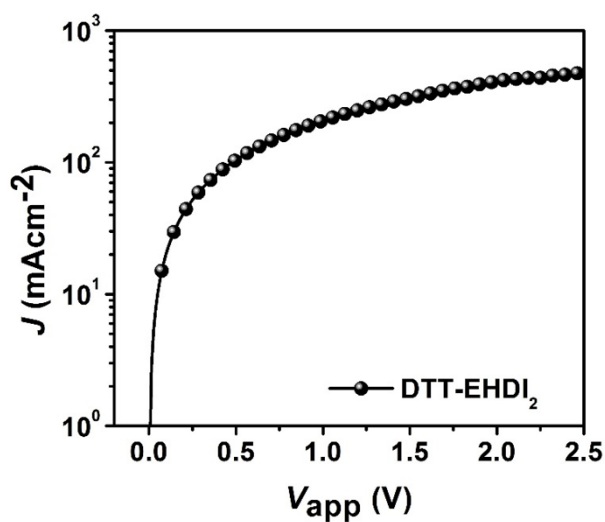


Figure A5.2 J - V curves for hole-mobility measurement of DTT-EHDI₂ with the hole-only device (FTO/PTAA/DTT-EHDI₂/Au) under dark conditions.

Appendices

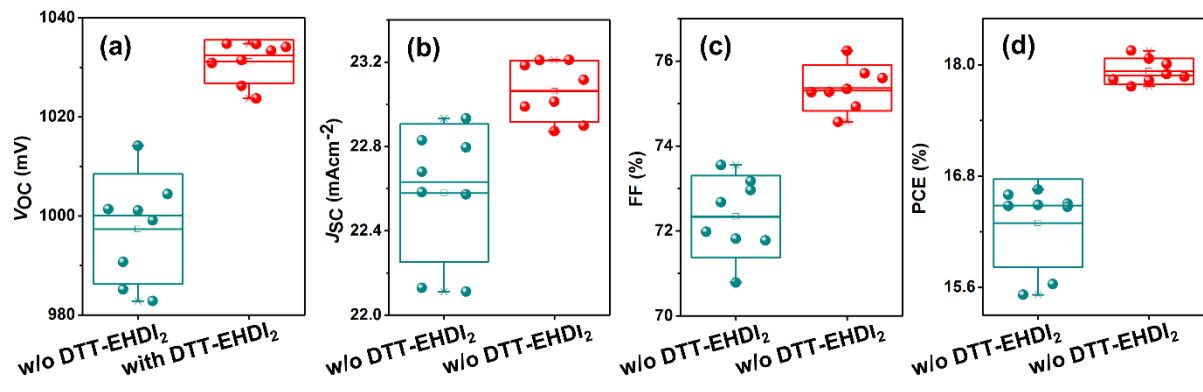


Figure A5.3 The statistical PV parameters of (a) V_{oc} , (b) J_{sc} , (c) FF, and (d) PCE of PSCs w/o and with DTT-EHDI₂ interface layer.

APPENDIX D

Additional data of Chapter 6: Interface tweaking of perovskite solar cells with carbon nitride-based 2D materials

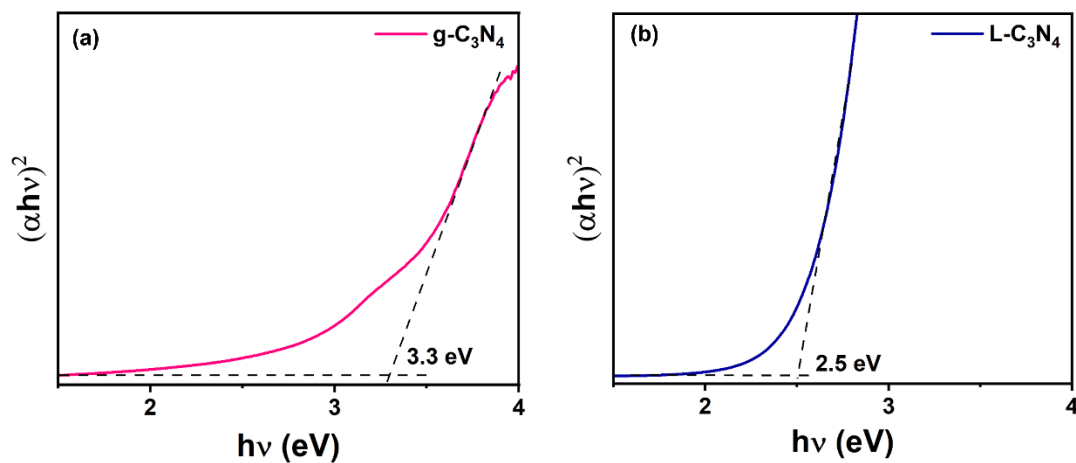


Figure A6.1 $(\alpha hv)^2$ Vs. $h\nu$ plot for exfoliated (a) g-C₃N₄ and (b) L-C₃N₄ in solution (isopropanol/ethanol).

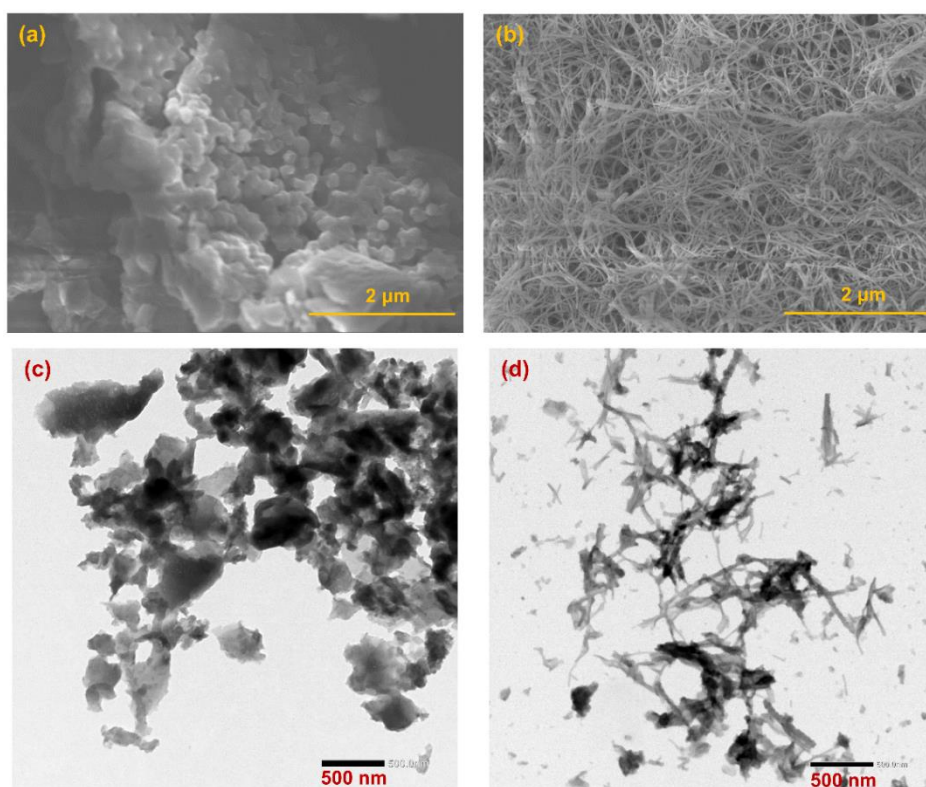


Figure A6.2 Scanning electron microscopy (SEM) of (a) g-C₃N₄ and (b) L-C₃N₄. Transmission electron microscopy (TEM) image of exfoliated (c) g-C₃N₄ and (d) L-C₃N₄.

Appendices

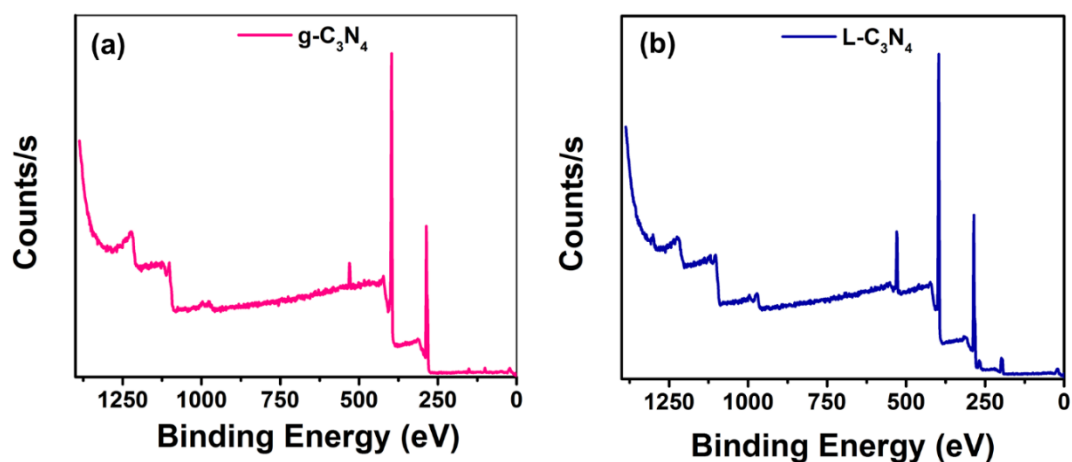


Figure A6.3 Survey XPS of (a) g-C₃N₄ and (b) L-C₃N₄.

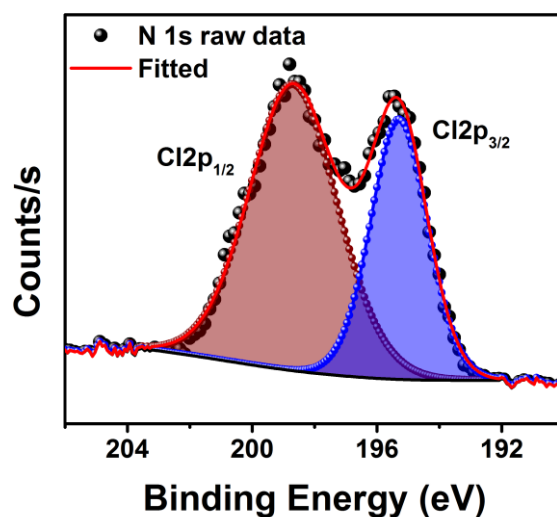


Figure A6.4 High-resolution XPS of Cl 2p in L-C₃N₄.

Table A6.1 Binding energy position of the elemental components.

Component	Binding energy (eV)		
	CsFAMA	CsFAMA/g-C ₃ N ₄	CsFAMA/L-C ₃ N ₄
Pb 4f _{5/2}	142.44	143.17	142.82
Pb 4f _{7/2}	137.57	138.31	137.96
I 3d _{3/2}	629.6	630.6	630.39
I 3d _{5/2}	618.12	619.12	618.9
Cs 3d _{3/2}	737.72	738.79	738.43

Appendices

Cs 3d _{5/2}	723.8	724.74	724.45
N 1s (C-NH ₂)	400.96	402.04	400.23
N1s (C=NH ₂ ⁺)	399.54	400.46	398.85
C1s (C=NH ₂ ⁺)	287.36	288.33	288.3
C1s (C-NH ₂)	285.6	285.95	285.95
C1s (C-C)	284.44	284.57	284.52

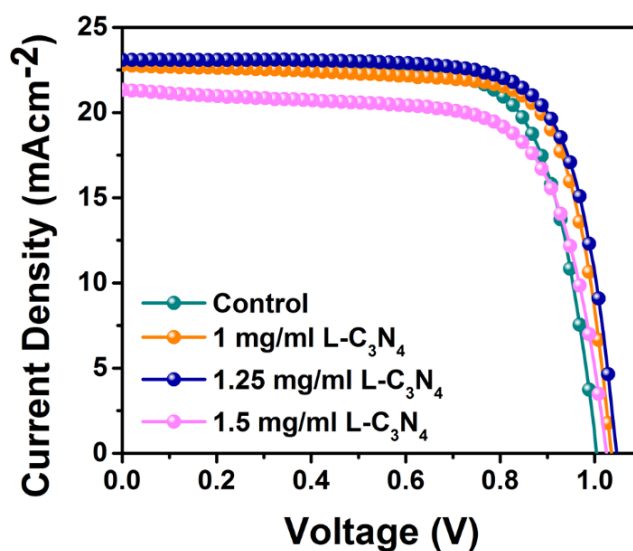


Figure A6.5 *J-V* curve of the devices with different concentrations of L-C₃N₄ interfacial layer.

Table A6.2 Concentration dependent *J-V* parameters (reverse scan) of the PSCs.

Device	V_{oc} (mV)	J_{sc} (mAcm ⁻²)	FF (%)	PCE (%)
Control	1003.81	22.83	73.55	16.85
with 1 mg/ml L-C ₃ N ₄	1035.61	22.80	74.17	17.51
with 1.25 mg/ml L-C ₃ N ₄	1046.46	23.09	75.35	18.21
with 1.5 mg/ml L-C ₃ N ₄	1025.23	21.33	69.46	15.19

Appendices

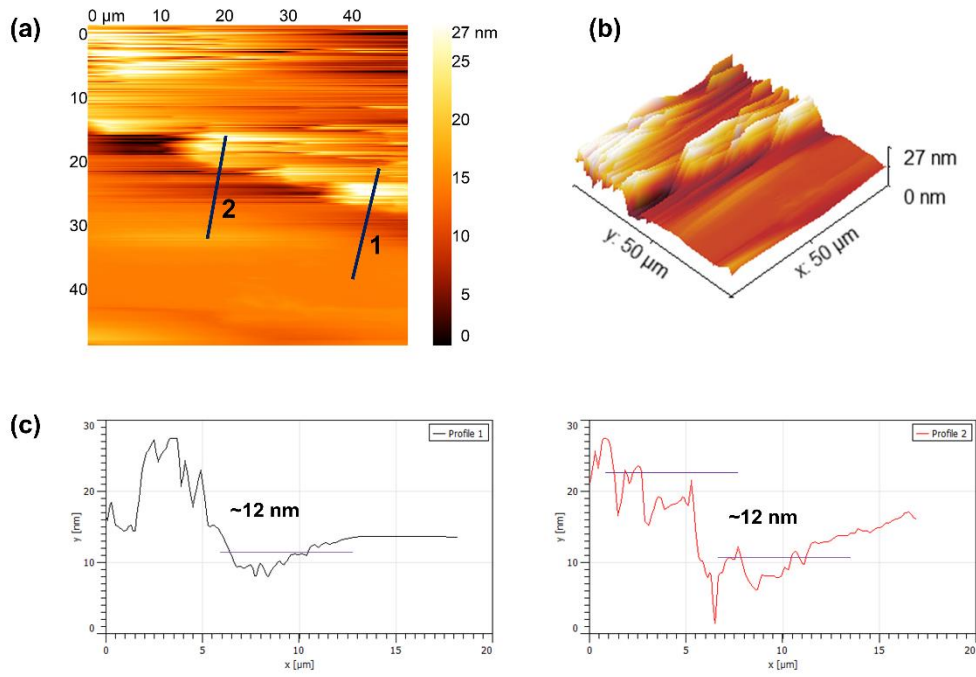


Figure A6.6 AFM height image (a) and (b) 3D image of the partially spin-coated C_3N_4 layer on silicon wafer. (c) The thickness profiles along with 1 and 2.

Table A6.3 R_s , R_{sh} , and HI extracted from J - V curves of PSCs.

Device	Scan direction	R_s (Ω)	R_{sh} ($\text{k}\Omega$)	HI
Control	Reverse	47.24	52.36	0.022
	Forward	52.31	35.47	
with g- C_3N_4	Reverse	38.35	69.74	0.012
	Forward	41.19	57.34	
with L- C_3N_4	Reverse	32.49	82.05	0.005
	Forward	37.41	78.19	

Appendices

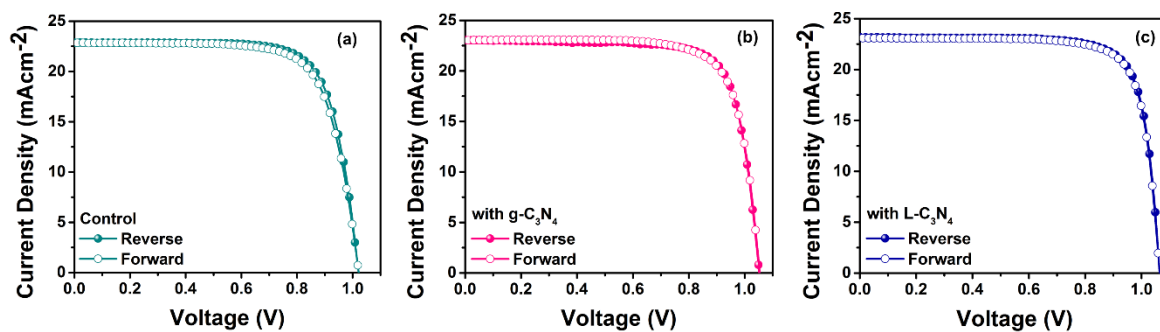


Figure A6.7 Reverse and forward scan J - V curves of PSCs under simulated AM 1.5G illumination.

Table A6.4 Extracted electrochemical parameters of the PSCs at 900 mV applied bias under dark conditions.

Device	$R_{\text{rec}} (\Omega)$	$\tau (\mu\text{s})$
Control	131.3	2.49
with g-C ₃ N ₄	422.8	5.20
with L-C ₃ N ₄	574.5	6.65

Vita

Vita

Naveen Harindu Hemasiri

PhD Candidate

BCMaterials

UPV/EHU Science Park, 48940, Leioa, Spain

University of the Basque Country

Barrio Sarriena, s/n, 48940 Leioa, Biscay

Phone (+34) 632580585

naveen.harindu@bcmaterials.net nbastian001@ikasle.ehu.eus

Orcid: <https://orcid.org/0000-0002-5450-3215>

EDUCATION

- Feb 2019 – Current:* **International PhD in Science & Technology of Materials,**
(Expecting in Feb 2023) University of the Basque Country, UPV/EHU, Spain.
Scientific advisors: Prof. Shahzada Ahmad
- Jun 2021 – Aug 2021:* Research stay (within PhD) at Physics at Interfaces Group,
Max Planck Institute for Polymer Research, Mainz, Germany.
Scientific advisor: Dr. Rüdiger Berger
- Feb 2016 – Feb 2018:* **MEng in Printed Electronics Engineering,**
Nanostructured Materials & Devices Laboratory, Department
of Printed Electronics Engineering, Sunchon National
University, South Korea.
Scientific advisor: Prof. Ji Myon Lee
Graduated with the Achievement Award (GPA: 3.925/4.0)
- May 2015 – Jun 2010:* **BSc (Hons.) in Materials Science & Engineering,**
Faculty of Engineering, University of Moratuwa, Sri Lanka
Graduated with honors (GPA: 3.59/4.0)

RESEARCH & TEACHING EXPERIENCE

- Feb 2019 – Current:* **Pre-Doctoral Researcher,** Basque Center for Materials,
Applications & Nanostructures, UPV/EHU, Spain.
Synthesis, development, and scale-up of a wide range of 2D
materials including graphene and TMDs for perovskite solar
cells. Device fabrication, characterization, and investigation of
photo-induced charge transfer dynamics at interfaces in
perovskite solar cells.
- Jun 2021 – Aug. 2021:* **Visiting Researcher,** Physics at Interfaces, Max Planck
Institute for Polymer Research, Mainz, Germany.

Vita

Focused on Scanning Probe Microscopy methods for characterization of surface and interface properties of perovskite solar cells and 2D materials.

- Feb 2016 – Feb 2018:* **Graduate Research Fellow**, Department of Printed Electronics Engineering, Sunchon National University, South Korea.
Developed new strategy to improve the electronic properties of graphene through the combination of n-type semiconducting materials. Conducted and evaluated research using innovative technology, including CVD, coupled plasma, and Magnetron sputtering.
- May 2015 – Jan 2016:* **Graduate Teaching Assistance**, Faculty of Engineering, University of Moratuwa, Sri Lanka.
Planned, modified, and executed research techniques, procedures and tests in the field of materials engineering.
- Nov 2013 – May 2014:* **Industrial Training-Materials Engineer**, Soil Tech (PVT) LTD, Colombo, Sri Lanka.

AWARDS, HONORS, & FELLOWSHIPS

- **ECOST (European Cooperation in Science & Technology) – STSM fellowship – CA16235-47862** (STSM title - Interface studies by introducing 2D materials for reliability enhancement in perovskite solar cells, Host Institute - Max Planck Institute for Polymer Research, Mainz, Germany), 2021
- **The Outstanding Achievement Award**, Graduate school, Department of Printed Electronics Engineering, Sunchon National University, South Korea, 2018
- **Best poster award in BK (Brain Korea) 21PLUS program**, Sunchon National University, South Korea, 2017
- **Brain Korea (BK) 21+ Scholarship**, South Korea, 2016-2018
- **Dean's List** of best students in the Faculty of Engineering, University of Moratuwa, Sri Lanka, 2010-2015
- **Mahapola Higher Education (Super Merit) Scholarship**, 2010-2015. Awarded for earning an outstanding results in GCE Advanced Level Examination in physical science stream in 2009
- **High Distinction Merit Award** (Senior Division) in Australian National Chemistry Quiz, Royal Australian Chemical Institute, 2005

PUBLICATIONS

Under PhD:

1. **Hemasiri, N. H.**, Calio, L., Pegu, M., Kazim, S., Ahmad, S. Molecular Interface Engineering via Triazatruxene-Based Moieties/NiOx as Hole-Selective Bilayers in Perovskite Solar Cells for Reliability. *Solar RRL*, **2022**, 6(4), 2100793. <https://doi.org/10.1002/solr.202100793>
2. **Hemasiri, N. H.**, Ashraf, M., Kazim, S., Graf, R., Berger, R., Ullah, N., Tahir M. N., Ahmad, S. Interface Tweaking of Perovskite Solar Cells with Carbon Nitride-based 2D Materials. *Nano Energy*, **2022** (Under Revision)
3. **Hemasiri, N. H.**, Kazim, S., Ahmad, S. 1T-Rich 2D-WS₂ as an Interfacial Agent to Escalate Photo-Induced Charge Transfer Dynamics in Dopant-Free Perovskite Solar Cells. *J. Mater. Chem C*, **2021**, 9(31), 9865–9873. <https://doi.org/10.1039/d1tc02307a>
4. **Hemasiri, N. H.**, Kazim, S., Ahmad, S. Reduced Trap Density and Mitigating the Interfacial Losses by Placing 2D Dichalcogenide Material at Perovskite/HTM Interface in a Dopant Free Perovskite Solar Cells. *Nano Energy*, **2020**, 77, 105292. <https://doi.org/10.1016/j.nanoen.2020.105292>
5. **Hemasiri, N. H.**, Kazim, S., Calio, L., Paek, S., Salado, M., Pozzi, G., Lezama, L., Nazeeruddin, M. K., Ahmad, S. Elucidating the Doping Mechanism in Fluorene–Dithiophene-Based Hole Selective Layer Employing Ultrahydrophobic Ionic Liquid Dopant. *ACS Appl. Mater. Interfaces*, **2020**, 12(8), 9395–9403. <https://doi.org/10.1021/acsami.0c00818>
6. Dhifaoui, H. †, **Hemasiri, N. H.** †, Aloui, W., Bouazizi, A., Kazim, S., Ahmad, S. An Approach to Quantify the Negative Capacitance Features in a Triple-Cation based Perovskite Solar Cells. *Adv. Mater. Interfaces*, **2021**, 8(22), 2101002. <https://doi.org/10.1002/admi.202101002> († Equal Authorship)
7. Dhifaoui, H. †, **Hemasiri, N. H.** †, Mehdi, H., Bouazizi, A., Kazim, S., Ahmad, S. Impact of Polymeric Hole Selective Layers on Chemical Inductance in an Inverted Perovskite Solar Cells. *Energy Technol.*, **2022**, 10(11), 2200264. <https://doi.org/10.1002/ente.202200624> († Equal Authorship)
8. Ghaderian, A. †, **Hemasiri, N. H.** †, Kazim, S., Ahmad, S. Amplify the Performance and Stability of Perovskite Solar Cells Using Fluorinated Salt as the Surface Passivator. *Energy Technol.*, **2022**, <https://doi.org/10.1002/ente.202200211> († Equal Authorship)
9. Khan, M. T., **Hemasiri, N. H.**, Kazim, S., Ahmad, S. Decoding the Charge Carrier Dynamics in Triple Cation-Based Perovskite Solar Cells. *Sustain. Energy Fuels*, **2021**, 5(24), 6352–6360. <https://doi.org/10.1039/d1se01398j>
10. Ashraf, M., **Hemasiri, N.H.**, Kazim, S., Ullah, N., Khan, M., Ganiyu, S., Alhooshani, K., Tahir, M. N., Ahmad, S. Hole Transport Layer/Perovskite Interface Engineering with Low Bandgap 2D Carbon Nitrides in Perovskite Solar Cells Fabrication. *Sustain. Energy Fuels*, **2022**. <https://doi.org/10.1039/D2SE01225A>

11. Yildirim, M. O., Gok, E. C., **Hemasiri, N. H.**, Eren, E., Kazim, S., Oksuz, A. U., Ahmad, S. A Machine Learning Approach for Metal Oxide Based Polymer Composites as Charge Selective Layers in Perovskite Solar Cells. *ChemPlusChem*, **2021**, 86(5), 785–793. <https://doi.org/10.1002/cplu.202100132>
12. Ghaderian, A., Pegu, M., **Hemasiri, N. H.**, Huang, P., Ahmad, S., Kazim, S. The impact of Fluorine Atoms on a Triphenylamine-Based Dopant-Free Hole-Selective Layer for Perovskite Solar Cells. *J. Mater. Chem. C*, **2022**, 10(2), 476–484. <https://doi.org/10.1039/d1tc04972k>
13. Gok, E. C., Yildirim, M. O., Haris, M. P. U., Eren, E., Pegu, M., **Hemasiri, N. H.**, Huang, P., Kazim, S., Uygun Oksuz, A., Ahmad, S. Predicting Perovskite Bandgap and Solar Cell Performance with Machine Learning. *Solar RRL*, **2021**, 6(2), 2100927. <https://doi.org/10.1002/solr.202100927>
14. Gassara, M., **Hemasiri, N. H.**, Kazim, S., Costantino, F., Naïli, H., Ahmad, S., Halide doping on lead-free perovskite $(\text{CH}_3\text{NH}_3)_2\text{CuCl}_{4-x}\text{Br}_x$ ($X = 0.3$ and 0.66) and Solar Cells Fabrication. *ChemSusChem*, **2023** (Under Review)

Under MEng:

15. **Hemasiri, B. W. N. H.**, Kim, J. K., Lee, J. M. Synthesis and Characterization of Graphene/ITO Nanoparticle Hybrid Transparent Conducting Electrode. *Nanomicro Lett.*, **2017**, 10(1). <https://doi.org/10.1007/s40820-017-0174-0>
16. **Hemasiri, B. W. N. H.**, Kim, J. K., Lee, J. M. Fabrication of Highly Conductive Graphene/ITO Transparent Bi-Film Through CVD and Organic Additives-Free Sol-Gel Techniques. *Sci. Rep.*, **2017**, 7(1). <https://doi.org/10.1038/s41598-017-18063-w>

SELECTED CONTRIBUTIONS TO CONFERENCES

- Synthetic 2D Materials, Summer School 2022, Collaborative Research Centre (CRC), 19-23 September 2022, Dresden, Germany.
Poster: 2D TMDs: As interfacial layers to promote photo-induced charge transfer dynamics in perovskite solar cells.
- Fortnightly seminar, BCMaterials, 7 June 2021, Leioa, Spain.
Talk: 2D-TMDs: an ideal blockbuster for interfacial layer to promote photo-induced charge transfer dynamics in PSCs.
- The 4th Moscow Autumn Perovskite Photovoltaic International Conference (MAPPIC), 19-21 September 2022, Moscow, Russia.

Vita

Talk (Online): 2D-TMDs: an ideal blockbuster for interfacial layer to promote photo-induced charge transfer dynamics in PSCs.

- The 3rd Moscow Autumn Perovskite Photovoltaic International Conference (MAPPIC), 11-13 October 2021, Moscow, Russia.

Poster: Interface engineering through 2D-transition metal dichalcogenides for reliability enhancement in perovskite solar cells.

- The 22nd RIES-HOKUDAI International Symposium, 6-7 December 2021, Research Institute for Electronic Science (RIES), Hokkaido University, Japan.

Poster: Reduced trap density and energy level alignment of perovskite solar cells using a 2D-MoS₂ interfacial layer.

- MXene: Looking ahead to the Next Ten Years, WILEY, 18 October 2021.
- Global Renewable Energy Researcher Meet, 07-08 May 2021, Australia, Prism Scientific Services.
- International summer school on photovoltaics, Technical University of Denmark, 24-28 August 2020.
- HOPV20 Online Conference on Hybrid and Organic Photovoltaics, 26-29 May 2020.
- ViPerCon (Virtual Perovskite Conference), 23 April 2020, Technical University of Darmstadt.
- The 5th International Conference on Next Generation Solar Energy (NGSE5) 07-09 December 2020.

- NMDC 2017 (The 12th IEEE Nanotechnology Materials and Devices Conference), 2-4 October 2017, Singapore.

Talk: Conductivity improvement of CVD graphene through ITO nanoparticles and Raman characteristics.

- ICEIM 2017 (19th International Conference on Engineering and Innovative Materials), 2-3 February 2017, Melbourne, Australia.

Talk (Online): Fabrication of highly conductive graphene/ITO transparent bi-film through chemical vapour deposition and organic additives-free sol-gel techniques.

- ICAE 2017 (The 4th International Conference on Advanced Electromaterials), 21-24 November 2017, Jeju Island, Korea Rep. of.

Poster: Decoration of CVD grown graphene with ITO NPs; Its effect on conductivity improvement and Raman signatures of graphene.

Vita

- AEPSE 2017 (The 11th Asian-European International Conference on Plasma Surface Engineering), 11-15 September 2017, Jeju Island, Korea Rep. of.
Poster: O₂ plasma treated substrate with enhanced surface free energy for continuous growth of ITO via aqueous sol-gel approach and the synthesis of graphene/ITO bi-film.

MEMBERSHIPS

Institute of Engineers, Sri Lanka (IESL)

Member of Society of Materials Engineering Sri Lanka (SOMESL)

Sri Lankan Student Association – South Korea